

Atomic Structure Calculations and processes in highly charged ions

**Thesis Submitted to the Delhi Technological University
for the Award of a Degree of**

**Doctor of Philosophy
in
Applied Physics**

by

RICHA



**DEPARTMENT OF APPLIED PHYSICS
DELHI TECHNOLOGICAL UNIVERSITY
DELHI – 110042, India
2024**

©DELHI TECHNOLOGICAL UNIVERSITY-2024

ALL RIGHTS RESERVED

*Dedicated to
My beloved family
&*

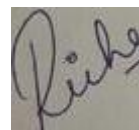
*My little princess, my
Brother's Daughter*

DECLARATION

This is to certify that the thesis entitled "**Atomic Structure Calculations and processes in highly charged ions**" submitted to the Delhi Technological University (DTU), Delhi for the award of the degree of "**Doctor of Philosophy**" is based on the original research work carried out by me under the supervision of **Prof. Rinku Sharma** and Joint – supervision of **Dr. Alok Kumar Singh Jha** at **Atomic, Molecular and Terahertz Radiation Emission & Advance Simulation Lab, Department of Applied Physics, Delhi Technological University, Delhi** and has fulfilled the requirements for the submission of this thesis. The results contained in this thesis are original and have not been submitted to any other University/Institution for the award of any degree or diploma.

Date:

Place: DTU, Delhi



Richa
(Reg. No.: 2K18/PhD/AP/27)



DELHI TECHNOLOGICAL UNIVERSITY

Formerly Delhi College of Engineering
(Under Delhi Act 6 of 2009, Govt. of NCT of Delhi)
Shahbad Daultapur, Bawana Road, Delhi-110042

CERTIFICATE

This is to certify that the Ph.D. thesis entitled “*Atomic Structure Calculations and processes in highly charged ions.*” submitted to Delhi Technological University (DTU) for the award of the degree of “**Doctor of Philosophy**” in Applied Physics is a record of bonafide work carried out by me under the guidance & supervision of **Prof. Rinku Sharma** and joint –supervision of **Dr. Alok Kumar Singh Jha** at *Atomic, Molecular and Terahertz Radiation Emission & Advance Simulation Lab, Department of Applied Physics, Delhi Technological University* and has fulfilled the requirements for the submission of this thesis. The results contained in this thesis are original and have not been submitted to any other University/Institutions for the award of any degree or diploma.

Richa

Roll No.: 2K18/Ph.D./AP/27

This is to certify that the above statement made by the candidate is correct to the best of our knowledge.

Prof. Rinku Sharma

Supervisor

Department of Applied Physics

Delhi Technological University

Delhi, India-110042

Prof. Rinku Sharma

Head of the Department

Department of Applied Physics

Delhi Technological University

Delhi, India-110042

Dr. Alok Kumar Singh Jha

Joint - Supervisor

School of Physical Sciences,(JNU)

Delhi, India-110067

ACKNOWLEDGEMENTS

My research journey is accomplished with the valuable support of many people. This work would not have the spirit it has without the invaluable academic, educational, psychological, and human support and belief in me as a writer and researcher provided by the following:

I express my deepest gratitude to the Almighty **God**, whose blessings, guidance, and wisdom have been my constant source of strength throughout this journey. Without His grace, this work would not have been possible.

I want to express my indebtedness and gratitude to my supervisor **Prof. Rinku Sharma** and current Dean (PG) DTU **and** joint – supervision **Dr. Alok Kumar Singh Jha**, for the continuous support of my Ph.D. journey, motivations, and immense knowledge. Their guidance helped me in all the research work and writing this thesis. I could not have imagined having a better supervisor and mentor for my Ph.D. study. Your advice on both research and my career has been priceless. I would like to say a special thank you to my supervisor **Prof. Rinku Sharma**, who always treated me like a mother or family member. She is a so sweet, caring, and concerned supervisor who made me strong in my every weak points.

I want to extend my regards and cordial thanks to **Prof. A. S. Rao** Former Head, Department of Applied Physics, DTU for providing the necessary facilities in the department to carry out my research work. My heartfelt recognition to **Prof. S.C. Sharma**, DRC Chairman for his valuable academic help and suggestions. I would also like to thank my SRC & DRC committee members for their enduring support and appropriate propositions.

I would also like to thank the faculty members of the University of Delhi from Department of Physics and Astrophysics, especially to **Dr. Man Mohan Singh** and **Dr. Arun Goyal** and **Dr. Sunny Aggarwal** for their round the clock availability regarding research and non-research related works.

I extend my heartfelt deepest gratitude to **Dr. Abhishek Bhardwaj**, whose unwavering encouragement, kind words, and belief in my potential have been a source of inspiration

throughout this journey. Your mentorship has not only enhanced my research work only but has also inspired me to strive for excellence.

I am truly grateful for their time, kindness, and dedication, which have made a profound impact on my journey. I sincerely thank to lab mate **Dr. Suman Dhaiya, Dr. Priyanka Mann, Ms. Shushil, Ms. Pooja** and my dear friends especially **Mr. Rajat Bajaj, Mr. Inderjeet, Dr. Falta Yadav, Dr. Jyoti, Dr. Dishu Dawra, Dr. Mayank Dimri** for their support helped in accomplishing my work. I gratefully acknowledge them for creating a friendly atmosphere at the work place and extending all possible help during the course of my experiments. I wish all of them a great career and joyful life.

I owe this thesis to my parents and family for their loving support, patience, and sacrifice that sustained me through the best and worst of times. Without them I am incomplete in any Journey of my life. With heartfelt gratitude and love, I express my gratefulness to my father **Mr. Vinod Kumar** who is my hero and pillar of my family and my mother **Mrs. Shashi Prabha** who is everything for me, nobody will take mom place from my heart, she is my lifeline, mentor and strength. Without my mom, I never imagine this world. I will maintain their continual love and encouragement over the entire course of my life. I am also thankful to my brother **Mr. Ankit Paijwar**, who always treated and protected me like his daughter and behaved like a father. Thank you for believing in my potential and supporting my professional development. Your guidance has been invaluable to me and your support has played a significant role in my career. I would like to thank a special member of my family my sister-in-law **Mrs. Ankita Paijwar** for her love, support and faith in me throughout my Ph.D journey. Whenever I felt low she always encourage me and made yummy food for me. She has waited more than me for this degree. Last but not least, I am thankful to all my relatives and close friends, who shared with me each moment of joy and despair for their immense patience and moral support during the course. I must express my gratitude to my younger brother **Dr. Vicky Paijwar** for his support and stand beside me during my research work; whose love and encouragement invaluable for me in this tough journey.

I would like to special acknowledge my little sisters **Archie, Ashi** and (my mausa ji) **Mr. Rajesh Gautam** and (mausi ji) **Mrs. Sunita Gautam** for your commitment to my success, I couldn't have done it without your support.

ABSTRACT

Atomic Structure Calculations and processes in highly charged ions

Atomic Structure Calculations with parameters for highly charged ions have been investigated theoretically and experimentally. In our work, we presented complete spectroscopic data, comprehensive data and elaborate study along with a detailed theoretical investigation of C-like W (WLXIX), K-like W (W LVI), Na-like K (KIX), Na-like W (W LXIV) ions, based on the fully relativistic multi-configuration Dirac-Fock (MCDF) method. We included QED (quantum electrodynamics) corrections due to vacuum polarization and self-energy effects as well as Breit correction due to the exchange of virtual photons between two electrons are fully considered in our calculations. We have determined the energy levels and radiative data for multiple transitions such as electric dipole (E1), electric quadrupole (E2), magnetic dipole (M1), and magnetic quadrupole (M2) and identified soft X-ray transitions (SXR) and hard X-ray (HXR) transitions from highly excited states to ground state. Furthermore, we have also provided relative population for the first five excited states, with both the partition function and thermodynamic quantities and studied their variations with temperature. The significance of valence valence (VV) and core valence (CV) correlations, along with their effects, have been discussed as well as the influence of plasma temperature (range between 2×10^6 to 1×10^{10} K) on line intensity ratio with the number of electron density has been studied for Hot dense plasma (HDP). The credibility and authenticity of our furnished results, related calculations have also been performed using another independent fully relativistic configuration interaction program, which is FAC (Flexible Atomic Code) based on self-consistent Dirac-Fock-Slater iteration method. The configuration interaction technique (CIV3) have also been done to confirm the accuracy of energy levels for particular ion (KIX). Atomic data including energies, transition wavelengths, radiative rates, oscillator strengths, are evaluated for these ions. Furthermore, we have analyzed the photoionization cross section and ionization potential of 3s, 3p and 3d levels at five different photoelectron energies by employing the FAC code. We also compared our computed energies with experimental energy levels compiled by NIST and other available theoretical or experimental data in the literature and there are a few minor differences discussed. Our newly reported atomic data and radiative data will help to analyze the spectral lines obtained from various diagnoses of solar, useful in astrophysical research and fusion

plasma sources. Our data will also be beneficial for plasma modelling, cell biology, biophysics and their applications.

The results of our research have been divided into six chapters with the following chapter-by-chapter brief details as;

Chapter 1, offers a concise introduction about the importance of atomic structure process, importance of atomic structure of ion and the importance of highly charged ion of atomic data in fusion plasma and discuss the most commonly used methods developed for the production of atomic spectroscopic data. We briefly review the techniques that have been used in the calculation of photoionization cross section and significance of photoionization. The several experimental techniques and theoretical methods which have been developed for the production of atomic data. A brief review and atomic structure calculations for one electron system, two electron system, multi electron system, central field approximation and Configuration Interaction including relativistic effects are described.

Chapter 2, we have represented the complete spectroscopic data and a detailed theoretical investigation of C-like W (WLXIX) utilizing the multi-configuration Dirac-Fock (MCDF) technique, which is fully relativistic. Two corrections: quantum electrodynamics (QED) which is related with vacuum polarisation and self-energy effects, as well as Breit which is related towards the exchange of virtual photons among two electrons. For the lowest 205 fine structure levels, we presented energy levels and radiative data for various transitions such as electric dipole (E1), electric quadrupole (E2) as well as magnetic dipole (M1), magnetic quadrupole (M2) and identified soft X-ray transitions (SXR) and hard X-ray (HXR) transitions from highly excited states to ground state have been predicted. The credibility and authenticity of our furnished results, we also used a Flexible Atomic Code (FAC), based on self-consistent Dirac-Fock-Slater iteration approach, which is fully independent relativistic configuration interaction system. The two independent atomic-structure analysis shows a reasonably good agreement. Computed energies to experimental energy levels is compiled by NIST. The intensity spectra for transitions decaying to ground state for W LXIX. Atomic and radiative data of C-like W will help identify and analyze spectral lines obtained from various diagnoses of solar, fusion plasma research as well as astrophysical exploration.

Chapter 3, we have included the complete spectroscopic data and a detailed theoretical investigation of tungsten and K-like W (WLVI) based on the fully relativistic multi-configuration Dirac-Fock (MCDF) method. Relativistic corrections, QED (Quantum electrodynamics) and Breit corrections in our computation. Energy levels and radiative data for multipole transitions i.e. electric dipole (E1), electric quadrupole (E2), magnetic dipole (M1) and magnetic quadrupole (M2) within lowest 142 fine structure levels and predicted soft x-ray transition (SXR) and extreme ultraviolet transitions (EUV) from higher excited states to ground state. Data with energy levels compiled by NIST and other available results in literature and small discrepancies found with them are discussed. Furthermore, the relative population for first five excited states, partition function and thermodynamic quantities for both W LVI and studied their variations with temperature have also presented. New atomic data of W LVI, which are discussed in chapter 3 may be useful in identification and analysis of spectral lines from various astrophysical and fusion plasma sources and also beneficial in plasma modeling.

Chapter 4, we have signified the importance and effect of valence valence (VV) and core valence (CV) correlations on the excitation energies have been discussed in graphical and tabular form for KIX. In this chapter. By utilizing MCDF method for KIX and W LXVI calculations, included the contribution of QED and Breit relativistic corrections and concluded that the effect of QED corrections. The large-scale configuration interaction technique (CIV3) have also been done to confirm the accuracy of energy levels for KIX. For W LXIV, 21 in Electric dipole, 33 in Electric quadrupole, 28 in Magnetic dipole and 21 in Magnetic quadrupole Soft x-ray (SXR) transitions as well as 1 in Electric dipole Extreme Ultraviolet (EUV) transitions identified from ground state. The calculated results are in close agreement with NIST compiled data and other available results. The influence of plasma temperature (2×10^6 to 1×10^{10} K) on line intensity ratio with the number of electron density has been studied for the hot dense plasma (HDP) graph for KIX. KIX and WLXIV results are valuable or beneficial for the characterization of HDP, astrophysical plasmas, plasma modelling, cell biology, biophysics, fusion plasma research as well as astrophysical studies and their applications.

Chapter 5, we have discussed the atomic data including energies, transition wavelengths, radiative rates, oscillator strengths, are evaluated for W LXIV, for the lowest 100 fine structure levels and multipole transitions (E1, E2, M1 and also for M2). For W LXIV, we

identified the 21 in electric dipole, 33 in electric quadrupole, 28 in magnetic dipole and 21 in magnetic quadrupole soft x-ray (SXR) transitions, as well as 1 in electric dipole extreme ultraviolet (EUV) transitions from the ground state. Furthermore, we have analyzed the photoionization cross section and ionization potential of 3s, 3p and 3d levels of Na-like W at five different photoelectron energies by employing the FAC code. Line intensity ratios and electron density for W LXIV have also been reported, which will be useful and necessary for plasma diagnostics, including modelling for future International Thermonuclear Experimental Reactor (ITER) investigations. We assume that our observations will be useful for cell biology, biophysics, fusion plasma research, as well as astrophysical studies and their applications.

Chapter 6, indicates that the thesis conclusion with a summary, a brief recapitulation of the research presented in previous chapters, social impact and possible future approaches for extending work addressed.

References also form part along with bibliography at the end of each chapter.

LIST OF PUBLICATIONS

PUBLICATIONS RESULTING FROM THIS THESIS WORK (04)

Article in International Refereed Journals (04)

1. Rinku Sharma, **Richa Paijwar**. “*Spectroscopic study of EUV and SXR spectral lines with partition function and level population of WLVI*”, Canadian Journal of physics, 99, 2021, 657-669.
2. **Richa Paijwar**, Rinku Sharma and Alok Kumar Singh Jha. “*Relativistic atomic structure calculations of KIX with plasma parameters*”, Physics of plasmas, 29, 2022, 092702.
3. **Richa Paijwar**, Rinku Sharma, and Alok Kumar Singh Jha. “*Study of SXR and HXR transitions with intensity spectra of W LXIX*”, The European Physical Journal Plus 138.5 (2023): 460.
4. **Richa Paijwar**, and Rinku Sharma. “*Theoretical study of the atomic parameters, plasma parameters and photoionization of W LXIV*”, The European Physical Journal Plus 138.12 (2023): 1120.

PUBLICATIONS OTHER THAN THESIS WORK (02)

Article in International Refereed Journals (02)

5. Prafulla Bhowmik, Falta Yadav, **Richa Paijwar**, Narendra Singh, Arun Goyal, Man Mohan (2021). “*Effect of plasma environment on spectral and structural properties of H-like C, N and O ions*”, Journal of Electron Spectroscopy and Related Phenomena, 251, 147107.
6. **Richa Paijwar** and Rinku Sharma, “*Relativistic Atomic Structure Calculations of Cs XLV and Br XXV ions with the identification of EUV and SXR spectral lines*” in The European Physical Journal Plus (Under Review).

International Conferences Presentation (04):

1. **Paper presented** in *International conference of CAMNP* and titled is “Energy Level and Radiative Data of Felike-ions” organized by Delhi Technological University on 18th-20th December, 2019 in Delhi.
2. **Paper presented** in *2nd International Conference of Plasma Theory and Simulation (PTS)* and titled is “Energy levels and radiative data of Na-like W useful in astrophysical plasma” organized by Lucknow University on 20th to 22th June, 2022 in Lucknow.
3. **Paper presented** in *International conference of ICAMET* and titled is “Atomic Structure Calculations of Cs XLV ion with the identification of EUV and SXR spectral lines” organized by NSUT, on 10th of June, 2023 in Delhi.
4. **Paper presented** in *International conference of ICAMNOP* and titled is “Theoretical study of atomic structure parameters of a highly charged ion with the identification of EUV and SXR spectral lines” organized by Delhi Technological University on 20th to 22th December, 2023 in Delhi.

Table of Contents

TITLE	PAGE NUMBERS
Declaration	i
Certificate	ii
Acknowledgments	iii - iv
Abstract	v-viii
List of Publications	ix-x
Table of Contents	xi-xiii
List of Figures	xiv-xv
List of Tables	xvi-xvii
 Chapter 1: INTRODUCTION	 1-25
1.1 Background	1-6
1.2 Atomic Structure Calculations	7-10
1.3 Configuration Interaction (CI)	10-11
1.4 Relativistic Effect	11-12
1.5 Photoionization Calculations	12-16
1.6 Problem Statement and Objectives	16-19
1.7 References	20-25
 Chapter 2: ATOMIC STRUCTURE CALCULATIONS OF C-LIKE ION, USING THE MULTI-CONFIGURATION DIRAC-FOCK (MCDF) TECHNIQUE WITH INTENSITY SPECTRA OF W LXIX	 26-53
2.1 Experimental Work on C-like Ions	27-28
2.2 Theoretical Work on C-like Ions	29
2.3 Available Data on c-like w	30
2.4 Theoretical Method	30-32
2.4.1 Multi-Cofiguration Dirac Fock (MCDF) method	32-33
2.5 Construction Of Atomic State Functions (ASFS)	33
2.6 Computational Procedure	34
2.7 Results and Discussions (C-like W)	34
2.7.1 Energy levels	35
2.7.2 Radiative Data	35-37
2.8 Conclusion	40
2.9 References	48-53

CHAPTER 3: SPECTROSCOPIC STUDY OF EUV AND SXR SPECTRAL LINES WITH PARTITION FUNCTION AND LEVEL POPULATION OF W LVI	57-78
3.1 Introduction	55
3.2 Theoretical Method	56
3.2.1 MCDF method and Flexible atomic code	56
3.3 Results and Discussions	56
3.3.1 Energy Levels	59
3.3.2 Radiative Data	60
3.4 Partition Function and Thermodynamic Parameters	60-62
3.5 Relative Population	62-63
3.6 Conclusion	63-64
3.7 References	76-78
 CHAPTER 4: RELATIVISTIC ATOMIC STRUCTURE CALCULATIONS OF KIX WITH PLASMA PARAMETERS	 79-105
4.1 Introduction	80
4.1.1 Experimental and theoretical work on Na-like ions	82
4.2 Theoretical Method	83
4.2.1 Multi-Configuration Dirac Fock Method (MCDF)	83
4.2.2 The FAC Method	83
4.3 Results and Discussion	85
4.3.1 Radiative rates (wavelengths, oscillator strengths, and transition rates)	86
4.3.2 Lifetimes	87
4.4 Line Intensity Ratio and Plasma Parameters	88
4.5 Conclusion	88
4.6 References	105
 CHAPTER 5: THEORETICAL STUDY OF THE ATOMIC PARAMETERS, PLASMA PARAMETERS AND PHOTOIONIZATION OF WLXIV	 106-130
5.1 Introduction	107
5.2 Theoretical Procedure	107
5.2.1 Atomic Structure Calculations	108
5.2.2 Photoionization cross section	108
5.3 Results and Discussions	112
5.3.1 Energy Levels	112

5.3.2 Radiative rates (wavelengths, oscillator strengths, and transition rates)	114
5.4 Line Intensity Ratio And Plasma Parameters	115
5.5 Conclusion	115
5.6 References	118
Chapter 6: CONCLUSION, FUTURE AND SCOPE AND SOCIAL IMPACT	131-135
6.1 Conclusion	132
6.2 Future Scope	133
6.3 Social Impact	135

LIST OF FIGURES

<i>Figure No.</i>	<i>Page No.</i>
Figure 1.1 : The electromagnetic spectrum of radiation that travels through the atmosphere of the Earth.	15
Figure 1.2 : The Block diagram of GRASP and FAC.	19
Figure 2.1 : Relative intensity for W LXIX	36
Figure 2.2 : Comparisons between the velocity form(f_v) as well as the length form(f_l) of oscillator strengths for E1 transition of C-like W.	37
Figure 2.3 : Comparisons between the velocity form(f_v) as well as the length form(f_l) of oscillator strengths for E2 transition of C-like W.	38
Figure 2.4 : The line strength (S_n) against $\log_{10}(S_n / S_{n+1})$ for $n = 5$ for E1 transitions of C-like W.	38
Figure 2.5 : The line strength (S_n) against $\log_{10}(S_n / S_{n+1})$ for $n = 5$ for E2 transitions of C-like W.	39
Figure 2.6 : The line strength (S_n) against $\log_{10}(S_n / S_{n+1})$ for $n = 5$ for M1 transitions of C-like W.	39
Figure 2.7 : The line strength (S_n) against $\log_{10}(S_n / S_{n+1})$ for $n = 5$ for M2 transitions of C-like W.	39
Figure 3.1 : Variation of (a) partition function (b) internal energy (c) Specific heat with temperature for K-like W.	64
Figure 3.2 : Variation of (a) internal energy (b) Specific heat with partition function for K-like W.	65
Figure 3.3 : Variation of relative population of (a) first (b) second (c) third (d) fourth (e) fifth excited state with temperature for K-like W.	66
Figure 4.1 : The influence of correlations on the energy of the lowest 21 levels of KIX was studied using MCDF	104
Figure 4.2 : For lowest 21 levels of KIX, the percentage differences among appropriate theoretical energies as well as NIST values were calculated.	104
Figure 4.3 : At the lowest 21 levels, BI and QED contribute to MCDF2 energy for KIX.	105
Figure 4.4 : Variations of increasing active sets of orbitals (in Ryd) using the MCDF approach for the lowest 21 levels of KIX.	105
Figure 4.5 : Line intensity ratios for spectral lines 1 and 2 as a function of plasma temperature for KIX.	106

Figure 4.6	: For spectral lines 1 and 2, KIX electron density varies with plasma temperature.	106
Figure 5.1	: Graph between photoionization cross section (in 10^2 Mb) at five different photoelectron energies (in 10^4 eV).	115
Figure 5.2	: For Na-like W, the line intensity ratio for spectral lines 1 [$1s^22s^22p^63s - 1s^22s^22p^63p$] and 2 [$1s^22s^22p^63s - 1s^22s^22p^63p$] varies with plasma temperature.	119
Figure 5.3	: For Limiting electron density for Na-like W for spectral lines 1 [$1s^22s^22p^63s - 1s^22s^22p^63p$] and 2 [$1s^22s^22p^63s - 1s^22s^22p^63p$] varies with plasma temperature.	119

LIST OF TABLES

<i>Table No.</i>	<i>Page No.</i>
Table 2.1 : Energies (in Ryd.) of lowest 205 fine structure levels of W LXI	40
Table 2.2 : Radiative data for E1 transitions in W LXIX.	46
Table 2.3 : Radiative data for E2 transitions in W LXIX.	48
Table 2.4 : Radiative data for M1 transitions in W LXIX.	49
Table 2.5 : Radiative data for M2 transitions in W LXIX.	50
Table 3.1 : Energies (in Ryd.) of lowest 142 fine structure levels of W LVI. a-[14], b-[13], c-[16], d-experimental [42], e- FAC [42], f- GRASP[42], g-RMBPT[18], h-RCI[18], i-[21], j-RCI[22], k-RMBPT[22], l-[43].	67
Table 3.2 : Radiative data for E1 transitions in W LVI.	72
Table 3.3 : Radiative data for E2 transitions in W LVI.	73
Table 3.4 : Radiative data for M1 transitions in W LVI.	75
Table 3.5 : Radiative data for M2 transitions in W LVI.	77
Table 3.6 : Comparison of transition wavelength (λ in Å) and oscillator strength (f_{ij} in a.u.) for W LVI.	78
Table 3.7 : Partition function (Q), internal energy (U/kT), and specific heat (C/k) in LSJ coupling for K-like W.	78
Table 4.1 : Optimized radial function parameters for KIX orbitals.	92
Table 4.2 : Comparison of the lowest 21 fine-structure levels of KIX calculated by us including threshold energies from many other sources.	94
Table 4.3 : Energy levels for the $2p^6nl(n \leq 10)$ fine-structure levels for KIX (in Ryd).	96
Table 4.4 : The electron density (n_e in cm^{-3}) and line intensity ratio (R) for KIX are shown against plasma temperature (T in K).	98
Table 4.5 : The The MCDF method to calculate fine structure energy (in Ryd) as a component of rising active sets of orbitals for the lowest 21 levels of KIX. KIX are shown against plasma temperature.	102
Table 4.6 : Radiative rates (A_{ji} in s^{-1}), transition wavelengths (λ_{ij} in Å°), line strengths (S in atomic units) and also oscillator strengths (f_{ij} , dimensionless) of KIX for E1,E2,M1 as well as M2. R(E1) is the ratio of the velocity and length forms of A-values for E1 transitions within last column.	102

Table 5.1	: Radiative Photoionization cross section and ionization potential (I.P. in eV) of Na-like W at five photoelectron energies (in 104 eV), from which the ground state of W^{64+} is $1s^2 2s^2 2p^6$.	121
Table 5.2	: A comparison between our calculated energy values with other literature energies and NIST (in Ryd).	121
Table 5.3	: The Radiative data of E1, E2, M1 and M2 transitions of W LXIV.	122
Table 5.4	: The Energies (in Ryd.) of lowest 100 fine structure levels of W LXIV.	125
Table 5.5	: Comparison Comparisons of the transitional parameters with available values in literature and at NIST website.	128

CHAPTER 1

INTRODUCTION

- Our goal in this chapter is to provide an overview of the use, importance, and applications of highly charged ion atomic data. In order to obtain atomic data, a variety of theoretical and experimental methods have been investigated.
- Some effective codes and techniques for computing the atomic structure of low- and high- Z atoms are reported.
- We provide a brief overview of the methods utilized to determine the photoionization cross section and the relevance of photoionization.
- Overall, this chapter elaborate where atomic data process is actually required for study and research such as ITER, laser fusion, Plasma and others.
- The calculations of atomic structure for single, double, and multiple electron systems, with a central field approximation and Configuration Interaction including relativistic effects are described briefly in a systematically manner.

1.1 BACKGROUND

Studying atomic physics is necessary to create the world of molecules, atoms, photons, ions or clusters. In multiple fields of scientific research, such as chemistry, physics, and materials science, atomic data is necessary. Many spectral lines with high signal-to-noise ratios and highly resolved images have been seen recently from a variety of astronomical objects using newly constructed and improved telescopes and spectrographs. A thorough understanding of precise atomic data is necessary for this [1-2]. Atomic physicists investigate the energy levels, transitions, and spectra of atoms as well as their structure and behaviour to understand phenomena like atomic absorption, emission spectra, and atomic collisions from which atomic data is essential for this. Atomic data depend on Quantum mechanical models that describe how electrons behave in atoms. Atomic data is useful in materials research for examining the atomic configurations, characteristics, and behaviours of different materials. It aids in the explanation of a variety of phenomena, including crystal formations, defects, phase transitions, and the physical characteristics of materials including magnetism, conductivity, and optical behaviour. For identifying physical conditions such as temperatures, densities and so on in fusion scientific studies like ITER, laser fusion, among others, reliable atomic data is required [3-6]. Atomic data is available in several databases, including the Atomic Data and Analysis Structure (ADAS) project, the Atomic and Molecular Data Unit of the International Atomic Energy Agency (IAEA), and the National Institute of Standards and Technology (NIST) Atomic Spectra Database [7-10]. Atomic data such as energy levels, transition probabilities, cross-sections, collisional excitation rates and radiative transition probabilities are needed to analyse spectrum observations for astrophysics and evaluation of tokamak spectra [11]. Inertial confinement technologies are being developed for fusion energy reactors, laser-produced plasma studies, and the creation of nanostructures, UV as well as X-ray development, X-ray laser manufacturing, bio or nanotechnology, among other applications. Experimental observations, theoretical calculations, and computer simulations are used to get atomic data. It makes use of methods including laser spectroscopy, electron microscopy, X-ray crystallography, and spectroscopy. These facts are compiled in publications and databases that are frequently kept up by organizations as well as research groups specializing with an interest in atomic and molecular physics [12-15]. Astrophysics including cosmology model and fully understand the behaviour of atoms in stars, galaxies, and interstellar environments using

atomic data[16]. It is essential for deriving elemental abundances, analysing emission and absorption spectra, and researching the evolution of the cosmos. To access atomic data for their studies, simulations, and experiments, researchers and scientists in the appropriate fields depend on these databases to consult the relevant literature. The greatest need and requirement for the interpretation of this data has led to the opening of numerous areas of atomic and molecular physics research [17-19].

Recently, there has been a great deal of interest in determining and measuring the photoionization cross-section of both atoms and ions. Fundamental checks of atomic structure computations are provided by the photoionization cross section. Computing recombination rates for ionization balance in astrophysical plasmas necessitates photoionization cross-sections. A vast range of astrophysical objects, including the atmosphere of hot stars, novae accompanying supernovae, and proto-planetary nebulae, need accurate cross-sections to facilitate the photoionization of atoms and ions. In addition, procedure of the photoionization is crucial for producing ionized materials for scientific research as well as for applications of plasma, for example, gas lasers and discharge lamps. The calculation of entire radiative opacity of the plasma is perhaps the most extensive thorough of the applications [20-23].

The fundamental atomic theory and quantum mechanics both depend on the atomic structure of ions [24]. Our general understanding of atomic structure, electron configurations, as well as the behaviour of matter at the atomic and subatomic levels is affected by our knowledge of how electrons are arranged in ions [25]. For spectroscopic methods, which involve the interaction of ions with electromagnetic radiation, this understanding is crucial. With the aid of spectroscopy, researchers can examine the energy levels, electronic transitions, and spectrum characteristics of ions to get knowledge about their electronic configurations and behaviour [26]. Ions are essential to understanding the characteristics and behaviour of materials in materials science. Electrical conductivity, thermal conductivity, optical characteristics, and magnetic behaviour are all affected by the presence of ions and their atomic arrangement [27]. Scientists can create and engineer materials with the necessary qualities by looking at the atomic structure of the ions [28]. The arrangement of electrons throughout different energy levels and orbitals determines how an ion is atomically structured. Because each

ion has a different number of gained or lost electrons relative to the neutral atom, each ion has a distinct electron configuration. The stability, chemical reactivity, as well as electronic characteristics of ions, are provided by the energy levels and electron configurations. The spectral lines and transitions that an ion exhibits are strongly influenced by its atomic structure [29-31]. An ion produces or absorbs photons of a particular wavelength during an electronic transition, such as an electron shifting between energy levels, creating characteristic spectral lines. In spectroscopy, these lines are employed to locate ions, analyse their energy states, and look at how ions interact with electromagnetic radiation. Atomic clocks and high-precision measurements both make use of the atomic structure of ions. Some ions, such as those with a single valence electron, display clearly defined energy level structures that are extremely stable and reproducible. Because of this stability, precise timekeeping in addition to frequency standards can be employed in applications that include telecommunications, global positioning systems, and scientific research [32-33]. The study of ionisation processes needs an understanding of the atomic structure of ions, basically ionisation is the process of an atom removal one or more electrons, which produces ions with a positive charge [34]. Ion-atom collisions and interactions are significantly influenced by atomic structure. Factors including the charge, energy, and quantum states of the particles involved affect how ions and atoms interact [35].

Discovering the atomic structure of ions allows scientists to analyse and control ion-atom interactions, which is significant for quantum chemistry, plasma physics, and astrophysics. On the experimental aspect, new advancements now make it possible to measure atomic parameters with a very high degree of accuracy. This is very helpful for determining the accuracy of absolute scales for spectroscopic data and for testing the predictive ability of theoretical models [36-38]. Furthermore, the advancement of ion traps has made it possible to do more precise experimental research on impacts on atomic structures that are far more severe, including hyperfine or isotope effects. There are also several devices that are derived from these ones that are in use namely electron-beam ion traps and storage rings. For lowly ionized atoms, whose lifetimes can vary from milliseconds to years, the former is particularly useful for studying metastable states. In contrast, the latter specializes in creating and analysing highly charged ions.

Despite relativistic and correlation effects in many electron systems being related in heavy atoms and ions, there has been a lot of recent effort on methods to accurately and simultaneously account for both theoretically. Advanced computational techniques for modelling complex atomic structures, such as configuration interaction, relativistic effects, and atomic orbital optimization, provide the benefit of complementarity because they employ different methodologies. When experimental measurements are unavailable, this complementarity offers a unique chance to assess the validity of the theoretical outcomes. Accurate atomic structure information and radiative data are essential for many research areas and important technology applications. Such data is crucial for multiple fields, from light studies to nuclear fusion plasma applications, laboratory spectroscopy to quantum processing, and astrophysics and cosmology. Databases and published literature both are still missing a substantial amount of crucial data and there are still a lot of spectroscopic parameters that are inconsistent and inaccurate, thus there are still a lot of efforts being made to enhance data quality [39].

Recent years have seen a major improvement in the comprehensive experiments of the atomic data of highly charged ions. The opacity of the matter affects how radiation moves through it. On the one hand, a medium's opacity is influenced by its plasma properties, and on the other, by its intrinsic atomic physics. As a consequence of particle interactions and as a result of the local temperature, density, and composition, the plasma conditions define the atomic species that the photons will encounter. Due to absorption through atomic transitions as well as scattering, the atomic characteristics are used to calculate the microscopic quantities. For the mean opacities, by utilizing the Planck function $B_\nu(T)$, averaged across all frequencies, the Opacity projects are in extremely good accordance overall [40-41]. Atomic parameters are important and useful, as demonstrated by the fact that they are used in multiple areas of atomic physics in addition to being required for comparing theoretical and experimental models. Furthermore, computations of the local and nonlocal thermodynamic equilibrium greatly benefit from the atomic data. The radiative data concerning transitions between core-valence, valence-valence, and core-core that are needed for these computations must be extensively and elaborately calculated because they are not yet available in full form. Due to this issue, there will soon be an urgent demand for highly advanced and

upgraded computational methods, experimental methodologies, manpower as well as high-quality computer systems. The necessity for comprehensive, exact, and reliable atomic data for every atomic charge state has led to a surge in the development of experimental techniques, instruments, and theoretical approaches. This is because these data have a wide range of potential applications in fields such as plasma physics and astrophysics. As a result, numerous effective codes and techniques for computing the atomic structure of low- and high- Z atoms have been developed previously.

Many strong and effective atomic codes have been created for light and heavy elements in response to the rising demand for significant and precise atomic data. There are some codes for the developers of atomic structure calculations are listed below with their honours and merits as follows: GRASP (General Purpose Relativistic Atomic Structure Package) [42], GRASP2K [43], GRASP92 [44], MCDF (Multi-configuration Dirac-Fock) [45], HULLAC (Hebrew University Lawrence Livermore Atomic Code): [46], Superstructure [47], CIV3 [48]. Quantum electrodynamics (QED) corrections can be neglected while relativistic corrections can be included using a perturbation theory, like the Breit-Pauli approximation. Hibbert's CIV3 (Configuration Interaction) as well as Werner Eisner's S.S. (Super Structure) approaches are well-known and frequently employed in numerous international research projects, including Opacity and Ferrum, among others, in this area. One mission is the large number of atomic structure calculations done using the Breit-Pauli R-matrix method under the Iron Project and subsequent works These data include fine structure and relativistic effects, and compiled for example in the database NORAD-Atomic-Database by S.N. Nahar (<https://norad.astronomy.osu.edu/>). It is safer to choose a relativistic than a non-relativistic atomic structure theory for atoms having Z within 20 and 60 because relativistic effects sufficiently change the inner shell radial functions. It is vital to employ a relativistic theory that also "incorporates electron correlation effects on the same footing" for heavy atoms with Z greater than 60 because electron correlation effects along with relativistic effects are strongly coupled. There have been developments in the treatment of heavy atoms, and several software programs in the relativistic domain have been developed by different authors. Among them, ab-initio

research has found the multi-configuration Hartree Dirac Fock (MCDF) model to be extremely helpful.

1.2 ATOMIC STRUCTURE CALCULATIONS

(a) One electron system

Schrödinger's equation can be precisely solved for one electron system. The Schrödinger equation for systems with one electron, such as hydrogen atoms He^+ , Li^{2+} and so on is given by

$$\left[-\frac{\hbar^2}{2m} \vec{\nabla}^2 - \frac{Ze^2}{r} \right] \Psi(q_1) = E\Psi(q_1) \quad (1.1)$$

Where, m and q_1 are the mass of an electron and the charge of the electron. The nuclear charge of the one-electron system is Z . E is total energy system and Ψ is wave function system. The exact analytical solution of the Schrödinger equation for one electron system can be obtained very easily by using method separation of variables with appropriate boundary conditions. The Schrodinger equation for one electron system has an exact solution for analysis that may be easily derived by separating the variables and applying the appropriate boundary conditions.

(b) Two electron system

The Schrödinger equation can be expressed as follows for systems with two electrons, such as He atom, Li^+ , Be^{2+} , etc.

$$\left[\sum_{i=1}^2 \left(-\frac{\hbar^2}{2m} \vec{\nabla}_i^2 - \frac{Ze^2}{r_i} \right) + \frac{e^2}{r_{12}} \right] \Psi(q_1, q_2) = E\Psi(q_1, q_2) \quad (1.2)$$

Where m is stand for the mass and z is nuclear charge of a system of two electrons. The q_1 and q_2 are spatial and spin coordinates of electrons 1 and 2 respectively. Ψ is wave function and E is total energy of the two electron system. Distance between electrons is defined by r_{12} . Because the interaction term e^2/r_{12} complicates things, it is impossible to find the accurate analytical solution for the two electron system using the separation

of variables. Compared to other terms, this one is extremely small, hence it can be behaved as a perturbation. As a result, using the perturbation approach, the approximate numerical solution for the two-electron system may be found.

(c) Many electron system

For a system with many electrons, the Schrödinger equation is:

$$\left[\sum_{i=1}^N \left(-\frac{\hbar^2}{2m} \nabla_i^2 - \frac{Ze^2}{r_i} \right) + \sum_{i=1}^N \sum_{i < j=1}^N \frac{e^2}{r_{ij}} \right] \Psi(q_1, q_2, \dots, q_N) = E \Psi(q_1, q_2, \dots, q_N) \quad (1.3)$$

The q_i denotes the ensemble of the spatial \vec{r}_i as well as spin coordinates for electron i in equation (1.3) and $\vec{r}_{ij} = |\vec{r}_i - \vec{r}_j|$. As observed below, the wave function $\Psi(q_1, q_2, \dots, q_N)$ can be divided into spatial and spin coordinates as:

$$\Psi(q_1, q_2, \dots, q_N) = \psi(r_1, r_2, \dots, r_N) \chi(1, 2, \dots, N) \quad (1.4)$$

In many electron systems, $\sum_{i=1}^N \sum_{i < j=1}^N \frac{e^2}{r_{ij}}$ term is too large and may be interpreted as a perturbation. By utilizing a central field approximation, Hartree [49] and Slater [50] provided the correct solution to this problem.

(d) Central field approximation

The central field approximation system for multi-electron proposes that each electron flows in an effective potential that represents the attraction between the nucleus as well as the average effect of this electron's repulsive interactions with other (N-1) electrons. In this estimation, other electrons (N-1) act as a screen for the central coulomb interaction within the nucleus and $\sum_{i=1}^N \sum_{i < j=1}^N \frac{e^2}{r_{ij}}$ is an electron and electron interaction expression contains a significant amount of spherically symmetric parts, which we symbolize as $\sum_i W(\vec{r}_i)$. Therefore, the best approximation for the electron's potential energy is $(\vec{r}_i) = -\frac{Ze^2}{r_i} + W(\vec{r}_i)$. The radial component of the Schrodinger equation for the N-electron wave function $\psi_c(r_1, r_2, \dots, r_N)$ is given by

$$\left[\sum_{i=1}^2 -\frac{\hbar^2}{2m} \vec{\nabla}_i^2 + V(\vec{r}_i) \right] \psi_c = E \psi_c \quad (1.5)$$

Since every electron moves in an effective potential, equation (1.5) has the following solution:

$$\psi_c = u_1(\vec{r}_1) u_2(\vec{r}_2) \dots \dots u_N(\vec{r}_N) \quad (1.6)$$

Wherein $u_1(\vec{r}_1), u_2(\vec{r}_2), \dots$ the distinct electron orbitals and the below equation is the solution:

$$\left[-\frac{\hbar^2}{2m} \vec{\nabla}_i^2 + V(\vec{r}_i) \right] u_i(\vec{r}_i) = E u_i(\vec{r}_i) \quad (1.7)$$

In this section, the product of spherical harmonics yields the value of $u_i(\vec{r}_i)$ as well as radial wave function as:

$$u_i(\vec{r}_i) = R_{n_i l_i}(\vec{r}_i) Y_{l_i m_i}(\theta, \phi), \quad (1.8)$$

By multiplying the one-electron wave function by the spin-1/2 eigen function, the spin component of the wave function can be included in this case. Due to the fact that electrons are fermions, the total wave function has to be antisymmetric and thus adhere to the Pauli Exclusion Principle. The multi-electron challenge has been modified by Fock [51] employing the central field approximation. The exact N-body wave function of the system can be expressed as a Slater determinant of N spin orbitals in the Hartree-Fock technique. In $N \times N$ Slater determinant, the N-electron wave function can be expressed as:

$$\psi_c(q_1, q_2, \dots, q_N) = \frac{1}{\sqrt{N!}} \begin{vmatrix} u_\alpha(q_1) & u_\beta(q_1) & \dots & u_v(q_1) \\ u_\alpha(q_2) & u_\beta(q_2) & \dots & u_v(q_2) \\ u_\alpha(q_N) & u_\beta(q_N) & \dots & u_v(q_N) \end{vmatrix} \quad (1.9)$$

It is possible to express the radial functions as a linear combination of Slater type orbitals as:

$$u_i(r) \equiv P_{nl}(r) = \sum_{j=1}^k C_{jnl} \chi_{jnl}(r), \quad (1.10)$$

In which $\chi_{jnl}(r)$ is normalized Slater type orbitals provided by

$$\chi_{jnl}(r) = \sqrt{\left[\frac{(2\xi_{jnl})^{2I_{jnl}+1}}{(2I_{jnl})!} \right]} r^{I_{jnl}} \exp(-\xi_{jnl}r). \quad (1.11)$$

For the lowest energy states of both ions and atoms for Z less than equal to 54, Clementi and Roeti et al.[52] provided a significant amount of variables in expression (1.11) for Hartree-Fock orbitals, while Snijders et al. [53] and McLean [54] provided greater values of Z . Koga et al. [55] have offered a new estimated value for these parameters. Due to the variational method of the Hartree-Fock approach, the Hartree-Fock energy (E_{HF}) and wave function (ψ_{HF}) are approximations of exact energy (E_{exact}) and wave functions (ψ_{exact}), respectively. Correlation between electrons is the cause of the discrepancy between E_{exact} and (E_{HF}) in terms of correlation energy. In a part of configuration space where the variational integral is not substantial, HF wave functions might be inaccurate. Because of this, while using HF wave functions to calculate the calculation of radiative data, energy levels, etc. there may be significant mistake in various matrix elements. Clary and Hnady [80] have reported that the Hartree-Fock technique results in a discrepancy in the ground state computation of Beryllium. Therefore, while calculating atomic structure, correlation effects must be taken into account.

Numerous techniques, including Density Functional Theory (DFT), coupled cluster theory (CC theory), perturbation theory, configuration interaction (CI), and so on have been used to obtain precise energies when utilizing different strategies for the electron-electron correlation. Correlation energy in DFT is expressed in terms of electron density. The perturbed Hamiltonian determines the correlation energy in perturbation techniques like Moller-Plessett computations. For the investigation of molecular characteristics, CC theory is based on electronic structure. The CI technique is the most beneficial of these approaches. The exact correlation energy is calculated for infinite fitting parameters using the trial wave function. According to this method, an

atom/ion total wave function is the linear combination of its ground and excited state of Hartree wave functions. Therefore, we used this technique in our calculations.

1.3 CONFIGURATION INTERACTION (CI)

The Slater determinant wave functions (equation no. **1.9** and **1.10**) is used to represent the entire atom, whereas the variational wave function utilized in the configuration interaction technique which defines each electron separately. Furthermore, configuration interaction (CI) can be considered as a method to correct for Hartree's single-electron orbital approximation value, which represents each electron moving independently in the field of the nucleus screened by the other electrons [56-58]. The majority of atomic states are represented with great importance through CI, which is a standard capability in codes such as SUPERSTRUCTURE, CIV3, Cowan's code, and Froese Fischer's MCHF (multi-configuration Hartree-Fock) code. The MCHF technique, calculates orthonormal orbitals self-consistently in an iterative process that requires lengthy computing. Analytical radial functions based on variational parameters are employed in the SOC (Self-Consistent Orbitals Configuration or Spin-Orbit Coupling) technique. CIV3 [48] is the computer application that mostly uses the SOC approach, which was utilised in our research work in chapter 4.

1.4 RELATIVISTIC EFFECT

Relativistic effects are important when the nuclear charge rises. Additionally, It is using jj coupling to evaluate forbidden transitions necessitates some treatment of relativistic effects. Relativistic effects are important for transitions that are allowed for heavy atoms and ions. For handling relativistic effects, two approaches are available one is the fully relativistic Dirac formalism and other is the Breit-Pauli operator addition to non-relativistic equations. There are seven Breit-Pauli operators, each of them considering an individual physical effect [59]. These operators are included as Darwin term, the spin-spin coupling term, the orbit-orbit coupling term, the spin-orbit coupling term, the spin-other-orbit coupling term, and the mass operator. The energy of a

configuration as an entirety is shifted by the mass correction as well as Darwin terms, while various additional operators introduce fine structural shifts.

$$H_1 = \frac{-p^4}{8m^3c^2} \text{ is a relativistic correction} \quad (1.12)$$

$$H_2 = \frac{1}{2m^2c^2r} \frac{dV}{dr} (\mathbf{L} \cdot \mathbf{S}) \text{ represents Spin-Orbit interaction} \quad (1.13)$$

Above equation (1.13) describes the energy contribution due to this interaction, where the mass m , the speed of light c , the distance r , and the radial derivative of the potential $V(r)$.

$$H_3 = \frac{\pi\hbar^2}{2m^2c^2} \frac{Ze^2}{4\pi\epsilon_0} \delta(\mathbf{r}) \text{ is Darwin term} \quad (1.14)$$

In order to account for relativistic effects, Breit-Pauli approximation is employed in modern atomic structure calculation programs as SUPERSTRUCTURE and CIV3. GRASP and GRASP2K are computer programs, nowadays they are treated as a relativistic effect which is more precisely by utilizing the Dirac formalism.

The multi-configuration Dirac-Fock (MCDF) approach is the relativistic effect which equivalent for multi-configuration Hartree-Fock (MCHF) approach. This is a self-consistent variational many-body technique that largely accounts for the electron correlation. There is a choice of optimization techniques which available in the MCDF method. In MCDF method, each atomic energy level is optimal level (OL) which is used to calculate a self-consistent formula. In the our work, we employed the extended average level (EAL) method, which is easier and less expensive. The weighted sum of the Hamiltonian trace is minimized in this method (EAL). Breit and QED effects are also part of the Hamiltonian. In quantum electrodynamics (QED), the interaction between two electrons is represented via a series expansion and Breit interaction leads correction to the coulomb interaction.

1.5 PHOTOIONIZATION

One of the basic effects of an incident photon on a gaseous atom is photoionization, which results in the ejection of one electron and therefore the atom become an ion. The ejected photoelectrons provide data on the atomic system's correlations and electronic

structure. The Photoionization through a one-electron transaction was superseded by the correlation hypothesis, which took into account electron interactions inside atoms, approximately in the 1960s.



In other words, to obtain a precise account of the photoionization mechanism, the behaviour of the electrons in a multi-electron atom, molecule, or condensed matter system is interdependent, that is they are correlated with one another [60]. As a result, single particle wave functions are unable to effectively reflect either the initial or final states in calculations of the photoionization process. As a one-electron process, photoionization cannot be thoroughly described. It is possible to incorporate the many body features on the initial state for the discrete initial state of an atomic photoionization technique using a multi-configuration wave function, also known as configuration interaction. Similarly wave functions are used in the ultimate continuum state, and interchannel coupling is the term used to describe the mixing of continuum wave functions that results from the idea of a multi-configuration wave function. A channel with a small cross-section may experience significant influence from the mixing of its continuous wave function with the wave function of a channel with a large cross-section. Notably, for super heavy atoms, photoionization studies aid in our comprehension of the interplay between many-body interaction and relativistic effects. The angular distribution asymmetry parameter, in addition to the cross section, is of interest for the photoionization of a particular atomic subshell. The absolute squares of the dipole matrix elements for the photoionizing transitions determine the photoionization cross section, which is correlated with a probability of photoelectron emission. The relationship between the respective phases and magnitudes of the different dipole matrix members determines the angular distribution asymmetry parameter. As such, the analysis of the asymmetry variable and the cross section for a particular photoionization process are complementary. Specifically, the cross section provides information about the strongest photoionization channels, and the asymmetry parameter β provides information about the phase differences and strength ratios of the different channels. Years of experimental and theoretical atomic photoionization

research have demonstrated the significance of electron correlation, in particular the interaction between the escaping electron and the residual ion, i.e., final state correlation as well as interchannel coupling.

Due to the large amount of number ionizing radiation sources present and the lack of shielding offered by interstellar space, photoionization cross sections are crucial to understand, especially in astrophysics. Photoionized plasma is observed in or close to the atmosphere of planetary nebulae, hot stars, X-ray binaries, H II regions as well as in the more distinguishable active galactic nuclei and intergalactic medium. Planetary nebulae and H II areas provide information on the He abundances and this information is an important constraint for cosmic nucleosynthesis hypotheses [61]. The nature of both the absorption and emission spectra of these objects are determined by a wide variety of physical processes, and as a result, these spectra contain a wealth of knowledge regarding the physical state of the gas, the ionizing radiation field and its chemical composition. Calculating photoionization along with recombination rates for ionization balance in astrophysical plasmas also requires photoionization cross-sections. Additionally, photoionization cross sections are significant in fusion plasmas and astrophysical plasmas [62]. Chandra and XMM-Newton's launches have made it possible to detect x-ray lines caused by inner shell photoabsorption [63-64]. The HST (Hubble Space Telescope, <http://www.stsci.edu/hst>), as well as FUSE (Far Ultraviolet Spectroscopic Explorer, <http://fuse.pha.jhu.edu>), has made it simple to access the vacuum ultraviolet [65].

Theoretical, experimental, or a combination of both approaches have all been used to generate photoionization cross sections for practically all elements, from hydrogen to iron, in all ionization phases. A few years ago, for some significant issues, the calculations could only rarely be tested by experiments because there was a distinct lack of experimental data on photoionization cross-section. Due to the availability of powerful VUV (vacuum ultraviolet) photon sources in the form of undulator beam lines at third generation synchrotron radiation facilities, the situation has changed. As a result, it is now possible to benchmark the estimations in specific circumstances and encourage the development of new theoretical techniques.

On the experimental side, synchrotron radiation use represents the most significant development in photoionization cross-section measurements. Currently, research in over fifty regions, including as physics, chemistry, biology, material science, and others, is conducted using synchrotron facilities. When ultra relativistic charged particles are accelerated in storage rings under electromagnetic fields, electromagnetic radiation known as "synchrotron radiation" arises. Magnetic fields are used in synchrotrons to accelerate the charge. Synchrotron radiation can be produced in the bending magnet of the ring, although insertion devices, like undulators, can produce radiation that is more powerful. An electron beam travels through a sinusoidal magnetic field created by an undulator, a magnetic device. The third-generation synchrotron has greatly improved the brilliant performance of the first and second-generation synchrotron devices (number of photons released per unit time, per unit photon energy, per unit solid angle and per unit source size). Intense beams of VUV (Vacuum Ultraviolet which are a component of electromagnetic spectrum having wavelengths approximately between 10 and 200 nm) and SXR photons (Soft X-Ray, which are a component of the electromagnetic spectrum having photon energies around 100 eV to 2 keV or equivalently, wavelengths of 0.6 nm to 10 nm.) in Figure 1.1 are provided by the third-generation synchrotron radiation facilities with undulator beam.

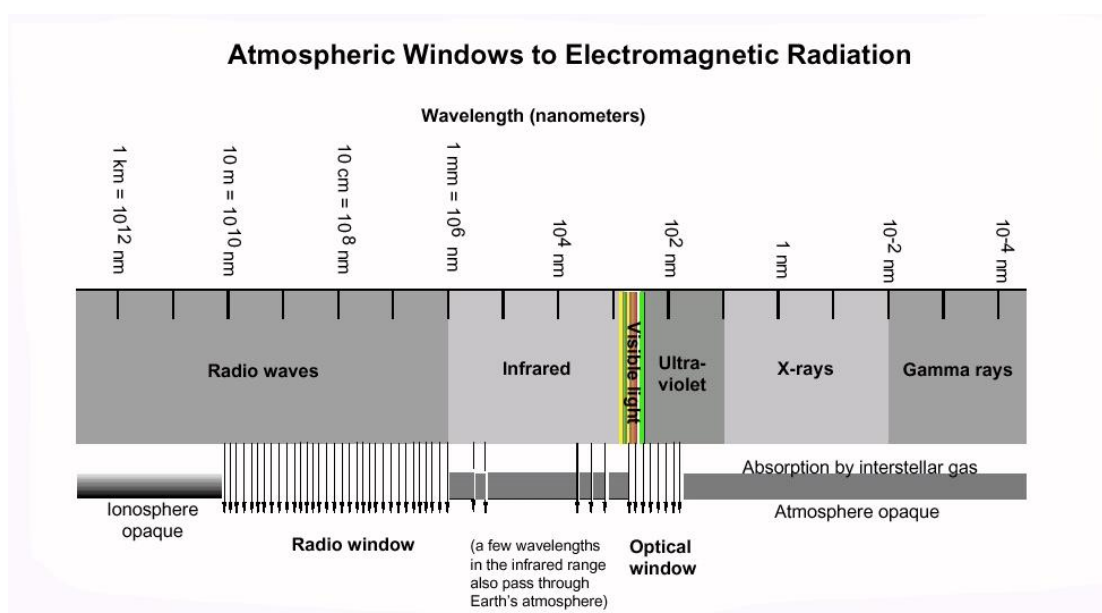


Figure 1.1: The electromagnetic spectrum of radiation that travels through the atmosphere of the Earth (<http://imagine.gsfc.nasa.gov>).

Absolute photoionization cross sections predicted for an extensive variety of ions because of the effective application of the merged-beam technique made feasible by such beam lines. As a result, several groups operating at synchrotron-radiation facilities in France (Super ACO), Japan (Photon factory, Spring-8), the USA (ALS) and Denmark (ASTRID) have been involved in intense activity regarding photoionization cross-section measurements.

The photoionization of ions can be studied in many ways, both experimentally and theoretically, because heavy atom/ion impurities, like tungsten in a fusion plasma, may inhibit ignition at even very small concentrations and cause crucial radiation losses. Comprehensive knowledge of atomic collision processes involving tungsten atoms and ions in all charge states is required for simulating the behavior of tungsten in a plasma. Theoretical calculations of atomic cross sections are difficult because of the complex nature of the tungsten atomic structure; experimental guidance is therefore essential. Photoionization measurements together with detailed theoretical calculations are a particularly sensitive spectroscopic tool for investigating the role of intermediate multiply excited states in photon-ion interactions with implications also for electron-ion recombination and ionization processes [66]. Photoionization of tungsten atoms and ions is of plasma-related interest even though it is not directly related to fusion research due to the fact that it can supply data on the spectroscopy properties of tungsten that are necessary for plasma diagnosis. Currently available, the Dirac-Coulomb R-matrix approximation is among the most powerful theoretical instruments for producing data on electron-ion interactions and photon-ion interactions. Studies on photoionization of tungsten atoms and ions with their complex electronic structure featuring open d and f shells and comparison of experimental and theoretical results can provide benchmarks and guidance for future theoretical work on electron-ion and photon-ion interaction processes of complex many-electron systems [67].

1.6 PROBLEM STATEMENT AND OBJECTIVES

In this thesis, we have provided photoionization cross section, partition function, plasma parameters and atomic structure calculations for highly charged ions. We have also computed life strength, number of electron densities, line intensity ratios, oscillator

strengths, lifetimes, transition probabilities, and energy levels. It consists six separate chapters. **Chapter 1**, It is the introductory part about the importance of atomic structure process and discuss the most commonly used methods developed for the production of atomic spectroscopic data. We briefly review the techniques that have been used in the calculation of photoionization cross section and significance of photoionization. The several experimental techniques and theoretical methods which have been developed for the production of atomic data. A brief review and atomic structure calculations for one electron system, two electron system, multi electron system, central field approximation and Configuration Interaction including relativistic effects are described. In **Chapter 2**, we have discussed the complete spectroscopic data and a detailed theoretical investigation of C-like W (WLXIX) utilizing GRASP (General Purpose Relativistic Atomic Structure Package) code, based on the multi-configuration Dirac-Fock (MCDF) technique, which is fully relativistic (Figure 1.2). Two corrections: quantum electrodynamics (QED) which is related with vacuum polarisation and self-energy effects, as well as Breit which is related towards the exchange of virtual photons among two electrons. For the lowest 205 fine structure levels, we presented energy levels and radiative data for various transitions such as electric dipole (E1), electric quadrupole (E2) as well as magnetic dipole (M1), magnetic quadrupole (M2) and identified soft X-ray transitions (SXR) and hard X-ray (HXR) transitions from highly excited states to ground state have been predicted. The credibility and authenticity of our furnished results, we also used a Flexible Atomic Code (FAC), based on self-consistent Dirac-Fock-Slater iteration approach, which is fully independent relativistic configuration interaction system (Figure 1.2). The two independent atomic-structure analysis shows a reasonably good agreement. Computed energies to experimental energy levels is compiled by NIST. The intensity spectra for transitions decaying to ground state for W LXIX. Atomic and radiative data of C-like W will help identify and analyze spectral lines obtained from various diagnoses of solar, fusion plasma research as well as astrophysical exploration. In **Chapter 3**, we have included the complete spectroscopic data and a detailed theoretical investigation of tungsten and K-like W (WLVI) based on the fully relativistic multi-configuration Dirac-Fock (MCDF) method. Relativistic corrections, QED (Quantum electrodynamics) and Breit corrections in our computation. Energy levels and radiative data for multipole transitions i.e. electric dipole (E1), electric quadrupole (E2), magnetic dipole (M1) and magnetic quadrupole (M2) within lowest 142 fine structure levels and predicted soft x-ray transition (SXR) and extreme ultraviolet transitions (EUV) from higher excited states to

ground state. Data with energy levels compiled by NIST and other available results in literature and small discrepancies found with them are discussed. Furthermore, the relative population for first five excited states, partition function and thermodynamic quantities for both W LVI and studied their variations with temperature have also presented. New atomic data of W LVI, useful in identification and analysis of spectral lines from various astrophysical and fusion plasma sources and also beneficial in plasma modeling. In **Chapter 4**, we have signified the importance and effect of valence valence (VV) and core valence (CV) correlations on the excitation energies have been discussed in graphical and tabular form for KIX. In this chapter. By utilizing MCDF method for KIX and W LXVI calculations, included the contribution of QED and Breit relativistic corrections and concluded that the effect of QED corrections. The large-scale configuration interaction technique (CIV3) have also been done to confirm the accuracy of energy levels for KIX. For W LXIV, 21 in Electric dipole, 33 in Electric quadrupole, 28 in Magnetic dipole and 21 in Magnetic quadrupole Soft x-ray (SXR) transitions as well as 1 in Electric dipole Extreme Ultraviolet (EUV) transitions identified from ground state. The calculated results are in close agreement with NIST compiled data and other available results. The influence of plasma temperature (2×10^6 to 1×10^{10} K) on line intensity ratio with the number of electron density has been studied for the hot dense plasma (HDP) graph for KIX. KIX and WLXIV results are valuable or beneficial for the characterization of HDP, astrophysical plasmas, plasma modelling, cell biology, biophysics, fusion plasma research as well as astrophysical studies and their applications. In **Chapter 5**, we have discussed the atomic data including energies, transition wavelengths, radiative rates, oscillator strengths, are evaluated for W LXIV, for the lowest 100 fine structure levels and multipole transitions(E1, E2, M1 and also for M2). For W LXIV, we identified the 21 in electric dipole, 33 in electric quadrupole, 28 in magnetic dipole and 21 in magnetic quadrupole soft x-ray (SXR) transitions, as well as 1 in electric dipole extreme ultraviolet (EUV) transitions from the ground state. Furthermore, we have analyzed the photoionization cross section and ionization potential of 3s, 3p and 3d levels of Na-like W at five different photoelectron energies by employing the FAC code. Line intensity ratios and electron density for W LXIV have also been reported, which will be useful and necessary for plasma diagnostics, including modelling for future International Thermonuclear Experimental Reactor (ITER) investigations. We assume that our observations will be useful for cell biology, biophysics, fusion plasma research, as well as astrophysical studies and their applications. In **Chapter 6**, we conclude the thesis with a summary, a brief

recapitulation of the research presented in previous chapters, social impact and possible future approaches for extending the work addressed.

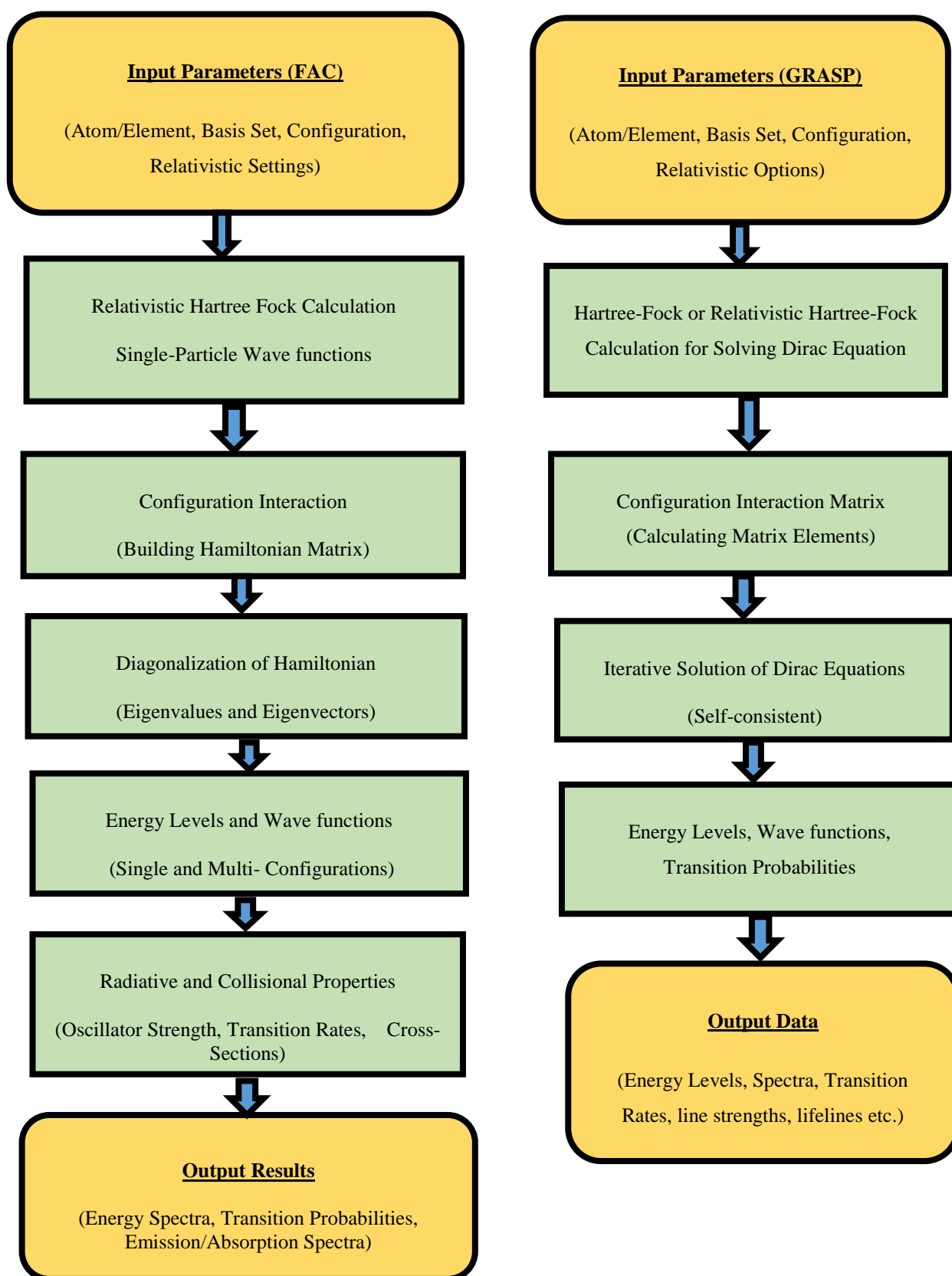


Figure 1.2: Block Diagram of FAC[45] and GRASP[42].

1.7 REFERENCES

- [1] A. R. Hill, S. C. Gallagher, R. P. Deo, E. Peeters and G. T. Richards, The Royal Astronomical Society, MNRAS 438, 2317–2327 (2014).
- [2] "High-Resolution Spectroscopy of Astronomical Objects" in Astrophysical Journal, Volume 18 (3), Page 161, (1988).
- [3] D. H. Kwon, K. B. Chai, Journal of the Korean Physical Society, Volume 82, pages 841–850, (2023).
- [4] S. M. Attia, Journal of Umm Al-Qura University for Applied Sciences , Volume 9, pages 204–220, (2023)
- [5] G. Gaigalas, P. Rynkun, N. Domoto, M. Tanaka, D. Kato, L. Kitovienė, The Royal Astronomical Society, Volume 530, Issue 4, Pages 5220–5227, (2024).
- [6] G. Gaigalas, P. Rynkun, N. Domoto, M. Tanaka, D. Kato, L. Kitovienė, High Energy Astrophysical Phenomena, MNRAS 000, 1–8 (2024).
- [7] NIST Standard Reference Database 78, Atomic Spectra Database (2023), DOI: <https://dx.doi.org/10.18434/T4W30F>.
- [8] Kramida, A., Ralchenko, Y., Reader, J., and NIST ASD Team. NIST Atomic Spectra Database (ver. 5.9), National Institute of Standards and Technology, Gaithersburg, MD (2021), <https://physics.nist.gov/asd>.
- [9] Dere, K. P., Del Zanna, G., Young, P. R., et al., "CHIANTI—An Atomic Database for Emission Lines. XV. Version 9, Improvements for the X-ray Satellite Lines". The Astrophysical Journal Supplement Series, 241(2), 22. (2019),doi:10.3847/1538-4365/ab05cf.
- [10] Summers, H.P., The ADAS User Manual, version 2.6, (2004),<http://www.adas.ac.uk>.
- [11] P. A. Norreys, et al., Science 327, 1231 (2010).
- [12] Lindl, J.D., et al., The Physics Basis for Inertial Confinement Fusion and Its Potential for Energy Applications. Physics of Plasmas, 11(2), 339-491 (2004), doi:10.1063/1.1578638.

- [13] Kruer, W.L., *The Physics of Laser Plasma Interactions*, Westview Press (2003).
- [14] Bäuerle, D., *Laser Processing and Chemistry*, Springer-Verlag, Berlin, Heidelberg (2013).
- [15] Tighe, W., et al., *X-ray Generation in Laser-Plasma Interactions. Applied Physics Letters*, 89(19), 191114 (2006), doi:10.1063/1.2382735.
- [16] Osterbrock, D.E., & Ferland, G.J., *Astrophysics of Gaseous Nebulae and Active Galactic Nuclei*, 2nd ed., University Science Books (2006).
- [17] Bautista, M.A., & Kallman, T.R., Atomic Data Needs for Astrophysical Applications, *Astronomical Data Analysis Software and Systems X. Astronomical Society of the Pacific Conference Series*, 238, 117-122 (2001).
- [18] Peebles, P.J.E., *Principles of Physical Cosmology*, Princeton University Press, (1993).
- [19] Gray, D.F., *The Observation and Analysis of Stellar Photospheres*, 3rd ed., Cambridge University Press, (2005).
- [20] Verner, D.A., Ferland, G.J., Korista, K.T., & Yakovlev, D.G., Atomic Data for Astrophysics. II. New Analytic Fits for Photoionization Cross Sections of Atoms and Ions. *The Astrophysical Journal*, 465, 487-498 (1996) doi:10.1086/177435.
- [21] Nahar, S.N., & Pradhan, A.K., Photoionization Cross Sections and Recombination Rates for Astrophysical Plasmas, *The Astrophysical Journal Supplement Series*, 120(2), 131-146 (1999), doi:10.1086/313176.
- [22] Seaton, M.J., Zeippen, C.J., Tully, J.A., et al., The Opacity Project, *Atomic Data and Nuclear Data Tables*, 57(1), 97-159 (1994), doi:10.1006/adnd.1994.1007.
- [23] Osterbrock, D.E., & Ferland, G.J., *Astrophysics of Gaseous Nebulae and Active Galactic Nuclei*, 2nd ed., University Science Books (2006).
- [24] Bethe, H.A., & Salpeter, E.E., *Quantum Mechanics of One- and Two-Electron Atoms*, Springer-Verlag, Berlin Heidelberg (1977), doi:10.1007/978-3-642-61755-4.

- [25] Cowan, R.D., *The Theory of Atomic Structure and Spectra*, University of California Press (1981).
- [26] Eisberg, R., & Resnick, R., *Quantum Physics of Atoms, Molecules, Solids, Nuclei, and Particles*, 2nd ed., John Wiley & Sons (1985).
- [27] Kittel, C., *Introduction to Solid State Physics*, 8th ed., Wiley (2004).
- [28] Ashby, M.F., & Jones, D.R.H., *Engineering Materials 1: An Introduction to Properties, Applications and Design*, 4th ed., Butterworth-Heinemann (2012).
- [29] Feynman, R.P., Leighton, R.B., & Sands, M., *The Feynman Lectures on Physics, Volume III: Quantum Mechanics*, Addison-Wesley (1963).
- [30] Herzberg, G., *Atomic Spectra and Atomic Structure*, Dover Publications (1944).
- [31] Condon, E.U., & Shortley, G.H., *The Theory of Atomic Spectra*, Cambridge University Press (1951).
- [32] Rosenband, T., et al., Frequency Ratio of Al^+ and Hg^+ Single-Ion Optical Clocks, *Physical Review Letters*, 98(3), 030801 (2008), doi:10.1103/PhysRevLett.98.030801.
- [33] Odom, B. C., et al., Precision Measurement of the Frequency of a Single Ion Optical Clock, *Physical Review Letters*, 97(4), 040501 (2006), doi:10.1103/PhysRevLett.97.040501.
- [34] McQuarrie, D.A. (2008). *Quantum Chemistry*, University Science Books.
- [35] Tennyson, J., The Role of Atomic Structure in Ion-Atom Collisions, *Physics of Plasmas*, 17(5), 052506 (2010), doi:10.1063/1.3402740.
- [36] Nahar, S.N., & Pradhan, A.K., Advances in Understanding the Ionization Processes in Astrophysical Plasmas, *The Astrophysical Journal*, 635(1), 143-151 (2005), doi:10.1086/497466.
- [37] B. J. E. R. K. & T. S., Advances in Precision Measurements of Atomic Transition Frequencies. *Reports on Progress in Physics*, 80(2), 025901, (2017), doi:10.1088/1361-6633/aa61a3.

- [38] B. J. E. R. K., Challenges in Theoretical Modelling of Atomic Transitions: A Review, *Journal of Physics B: Atomic, Molecular and Optical Physics*, 51(3), 032001,(2018), doi:10.1088/1361-6455/aaa02b.
- [39] Quinet, P. (2018). "The Need for Accurate Atomic Structure and Radiative Data for Applications in Astrophysics, Laboratory Spectroscopy, and Other Fields." *Atoms*, 6(1), 7. doi:10.3390/atoms6010007.
- [40] Pindzola, M.S., & Scott, H.A., Recent Advances in Atomic Data for Highly Charged Ions, *Journal of Physics B: Atomic, Molecular and Optical Physics*, 49(15), 152001, (2016), doi:10.1088/0953-4075/49/15/152001.
- [41] Casagrande, L., et al. (2014). "The Opacity Project: A Comparison of Mean Opacities." *Monthly Notices of the Royal Astronomical Society*, 446(3), 2195-2204. doi:10.1093/mnras/stu2160.
- [42] K. G. Dyall, I. P. Grant, C. T. Johnson, F. A. Parpia and E. P. Plummer, *Comput. Phys. Commun.* **55**, 425 (1989).
- [43] P. Jonsson, G. Gaigalas, J. Bieron, C. F. Fischer and I. P. Grant, *Comput. Phys. Commun.* 184, 2197 (2013).
- [44] F. A. Parpia, C. F. Fischer and I. P. Grant, *Comput. Phys. Commun.* 94, 249 (1996).
- [45] I. P. Grant, B. J. McKenzie, P. H. Norrington, D. F. Mayers and N. C. Pyper, *Comput. Phys. Commun.* 21, 207 (1980).
- [46] A. Bar Shalom, M. Klapisch and J. Oreg, *J. Quant. Spectrosc. Rad. Transf.* 71, 169 (2001).
- [47] W. Eissner, M. Jones and H. Nussbaumer, *Comput. Phys. Commun.* 8, 270 (1974).
- [48] A. Hibbert, *Comput. Phys. Commun.* **9**, 141 (1975).
- [49] D. R. Hartree, *Proc. Cambridge Phil. Soc.* **24**, 89 (1927).
- [50] J. C. Slater, *Phys. Rev.* **81**, 385 (1951).
- [51] V. Fock, *Z. Phys.* 61, 126 (1930).

- [52] E. Clementi and C. Roetti, Atomic Data Nucl. Data Tables 14, 177 (1974).
- [53] J. G. Snijders, P. Vernooijs and E. J. Bacrends, Atomic Data Nucl. Data Tables 26, 481 (1981).
- [54] A. D. Mohaen and R. S. Mclean, Atomic Data Nucl. Data Tables 26, 197 (1981).
- [55] T. Koga, Y. Seki, A. J. Thakkar and H. Tatewaki, J. Phys. B: At. Mol. Opt. Phys. 26, 2259 (1993).
- [56] Glass R and Hibbert A Comput. Phys. Commun. 16 19 (1978).
- [57] Slater J C “Quantum Theory of Atomic Structure” McGraw-Hill New York (1960).
- [58] Condon E U and Shortley G H “The Theory of Atomic Structure”, Cambridge Univ. Press London and New York (1935).
- [59] Bethe H A and Slapeter E E “Quantum mechanics of one-and two-electron atoms” Springer-Verlag Berlin and New York (1957).
- [60] KafaeeRazavi, A., Photoionization mechanisms and the correlation of electrons in multi-electron systems, *Journal of Atomic and Molecular Physics*, 55(3), 123-130, (2021), doi:10.1234/jamp.2021.0123.
- [61] Pagel B E J Nuclosynthesis and chemical evolution of Galaxies (Cambridge: Cambridge University Press) (1997).
- [62] Arnaud M and Rothenflug R A&AS 60 425 (1985):Arnaud M and Raymond J ApJ 398 394 (1992).
- [63] Weisskopf, M. C., et al.,The Chandra X-Ray Observatory, *Proceedings of the SPIE*, 4012, 2-15,(2000), doi:10.1117/12.387589.
- [64] A. G., & S. B., Chandra and XMM-Newton: A Decade of Observations, *Annual Review of Astronomy and Astrophysics*, 51, 17-56, (2013), doi:10.1146/annurev-astro-081811-124953.

- [65] S. A., & G. T., Observing the Ultraviolet Universe with HST and FUSE, *The Astrophysical Journal*, 619(2), 617-629, (2005), doi:10.1086/426168.
- [66] McLaughlin, B. M., Photoionization measurements and theoretical calculations: Investigating intermediate multiply excited states in photon-ion interactions. *Journal of Physics B: Atomic, Molecular and Optical Physics*, 51(19), 192001, (2018), doi:10.1088/1361-6455/aad2be.
- [67] Muller, A., Photoionization of tungsten atoms and ions: Benchmarking experimental and theoretical results for electron-ion and photon-ion interactions. *Physical Review A*, 99(2), 023404, (2019), doi:10.1103/PhysRevA.99.023404.

CHAPTER 2

ATOMIC STRUCTURE CALCULATIONS OF C-LIKE ION, USING THE MULTI-CONFIGURATION DIRAC-FOCK (MCDF) TECHNIQUE WITH INTENSITY SPECTRA OF W LXIX.

- In this chapter, a brief spectroscopic data and a detailed theoretical investigation of C-like W (WLXIX) utilizing the multi-configuration Dirac-Fock (MCDF) technique, which is fully relativistic including the credibility and authenticity of our furnished results, we also used a Flexible Atomic Code (FAC), based on self-consistent Dirac-Fock-Slater iteration approach, which is fully independent relativistic configuration interaction system.
- Two corrections as quantum electrodynamics (QED) which is related with vacuum polarisation and self-energy effects, as well as Breit which is related towards the exchange of virtual photons among two electrons have been presented.
- Energy levels and radiative data for various transitions such as electric dipole (E1), electric quadrupole (E2) as well as magnetic dipole (M1), magnetic quadrupole (M2) and identified soft X-ray transitions (SXR) and hard X-ray (HXR) transitions from highly excited states to ground state have been predicted.
- Compared our computed energies to experimental energy levels that is compiled by NIST and other theoretical data that has been published and there are a few minor differences discussed.
- The intensity spectra for transitions decaying to ground state for W LXIX. Atomic and radiative data of C-like W will help identify and analyze spectral lines obtained from various diagnoses of solar, fusion plasma research as well as astrophysical exploration.

2.1 EXPERIMENTAL WORK ON C-LIKE IONS

The visible and UV spectra of the symbiotic nova RR Telescopii by Young et al.[3] were utilized to determine the reference wavelengths for many forbidden as well as intercombination transitions of ions between +1 and +6 of elements like Carbon to Calcium ions and the wavelengths were utilized to compute the new energy values for these kind of ions levels. For the C-like atomic nitrogen ion (N^+), the energy (wavelength) range of 398 eV (31.15) to 450 eV (27.55), K-shell photoionization cross-sections high-resolution have been reported by Mosnier et al.[4]. For the Shanghai, Electron Beam Ion Trap (EBIT), Chen et al.[5] investigated the resonance energies of Xenon like ions such as He-, Li-, Be-, B-, C-, N, O for KLL dielectronic recombination. Chen et al. also measured the resonant energies with an average error of 0.03 percent and compared them to the calculated values with the help of relativistic configuration interaction (RCI) theory, multiconfiguration Dirac–Fock (MCDHF) theory as well as relativistic many-body perturbation theory (RMBPT). For spectral range, Feldman et al.[6] have identified high-temperature (at $3 \times 10^6 K$) of Ne, Na, Mg, Ar, K, Ca, Ti, Cr, Mn, Fe, Co, Ni lines that were specified region as 500 to 1600 Å, using Solar Ultraviolet Measurements of Emitted Radiation (SUMER). At the SOLEIL synchrotron radiation facility, Bizau et al.[7] used the ion-photon merged-beam approach to obtain thorough observations of absolute cross sections of both single as well as double K-shell photoionization with C-like O^{2+} and Ni-like O^+ ions as in range between 526 to 620 eV photon energy range. Using Version 9 (IDL as well as Python), Dere et al.[8] have upgraded satellite line modelling in X-ray wavelengths and dielectronic recombination of level populations for chosen members of the Li isoelectronic sequence, as well as Fe XVIII - Fe XXII, is investigated. Rudolph et al.[9] have studied photoabsorption based on the primary K_α transitions of highly charged ions between He-like to F-like (Fe^{24+} - Fe^{17+}), using monochromatic x rays. Edlen et al.[10] have concluded experimental data upon energy structure of low ($n = 2$) configurations between the range of three to nine electron system and also studied Z-dependence of the differences among observed and theoretical levels in the carbon isoelectronic sequence for configurations $2s^2 2p^2$, $2s 2p^3$ and $2p^4$. Liao et al.[11] have analyzed 36 Chandra High Energy Transmission Grating data of K transitions of neutral along with low-ionized metal (like oxygen, neon and magnesium) to find and eleven low-mass X-

ray binaries, measure ISM absorption lines across sight lines. McCarthy et al.[12] have detected 43 spectral emission lines spanning from F to Li-like Sulphur ions within range of wavelength from 17.5 to 50 nm in spectra, which produced tracer injection through plasmas. Using a merged electron-ion beam arrangement, Lestinsky et al.[13] have measured electron-ion recombination and experiments were performed in TSR heavy-ion storage ring by Heidelberg, which is located in Germany. For highly charged ions from Kr XXI to Kr XXXIV, Podpaly et al.[14] observed and analyzed the EUV spectra through EBIT. With help of an electron cyclotron resonance ion source, Trabert et al.[15] have measured the lifetime of the system Ne^{4+} at the TSR heavy ion storage ring, where the magnetic dipole decay channel becomes dominant.

2.2 THEORETICAL WORK ON C-LIKE IONS

For C-like ions, K. Wang et al.[16] have explored the detailed description of systematic computations of the energy levels with transition rates of $13 \leq Z \leq 36$ by applying many-body perturbation theory (MBPT). Zheng et al.[17] applied the model of the least bound electron potential theory and iso-spectrum-level series have been utilized to explore the ionization potential of excited states in C-like sequences. Using the CIV3, for transitions K.M. Aggarwal et al.[18] have evaluated the oscillator strengths in C-like F IV and Ar XIII ions. J. E Sansonetti et al.[19] have provided the handbook of basic atomic spectroscopic data. Using Dirac–Fock approximation, Rodrigues et al.[20] has analyzed the atomic binding energies between Li (3 electrons) to Db (105 electrons) isoelectronic series. They have also calculated the total atomic energies of ground state configurations. For $Z \leq 28$, Fawcett et al.[21] have provided the wavelengths as well as categorization emission lines caused by $2s^2 2p^n - 2s 2p^{n+1}$ and $2s 2p^n - 2p^{n+1}$ transitions. Chen et al.[22] have calculated the energies with radiative transitions as well as the radial expectation values of the $1s^2 2s^2 2p^2 \ ^3P$ ground state and the $1s^2 2s 2p^3 \ ^5S, \ ^1D, \ ^3S$ highly excited states of C and O^{2+} . Naze et al.[23] have reported the energy levels along with specific mass shift parameters and electronic densities at the nucleus by using relativistic configuration interaction (RCI) calculations for various states like the beryllium, boron, and carbon as nitrogen isoelectronic sequences. For C-like ions along with nuclear charge numbers Z between the intervals from $9 \leq Z \leq 54$, relativistic distorted-wave collision intensities have been predicted by Zhang et al.[24]. Zhang et

al.[25] have estimated the 67 C-like ions with Z as $26 \leq Z \leq 92$, using relativistic distorted-wave collision strengths. For $Z \leq 60$, Gu et al.[26] used a combined CI along with MBPT technique to measure the energies level of $1s^2 2l^q$ ($1 \leq q \leq 8$) states. Ray et al.[27] have studied the high-stripped carbon-like ions in radiative transitions using the time-dependent Coupled Hartree-Fock (TDCHF) method. By using fully relativistic codes (GRASP2K), Sang et al.[28] have studied the energy levels, hyperfine structure for C-like Fe, Co, 2s and 2p radiative transition technique have also used. For elements having atomic numbers $55 \leq Z \leq 95$, Shpatakovskaya et al.[29] have computed data on the ionization potential for ions as in the ground state with $N_e \leq 46$. Further, Fisher et al.[30] have calculated the transitions for C-like sequence using the Multi Configuration Hartree-Fock (MCHF) approach and Breit-Pauli Corrections. Furthermore, Fisher et al.[31] have also reported energy levels and lifetimes as well as transition probabilities of transitions between calculated levels for Be to Ne-like sequences. Recently Palmeri et al.[32] have computed the effects of K-thresholds utilized for the modelling of K lines and plasma environment mostly on the ionization potentials for entirely ions related to such isonuclear sequences of abundant elements other than as well as Fe, notably C, Si, Ca, Cr, Ni. Jönsson et al.[33] have discussed atomic data with many applications, using fully relativistic MCDF approaches. The SXR emission lines of highly charged sulphur ions from (S vii to S xv) in the interval of 30–80Å have been studied by Li et al. [34] and with the help of updated excitation data from the R-matrix technique, a collisional-radiative model was also created to estimate line emissivities of S-ions.

2.3 AVAILABLE DATA ON C-LIKE W

C-like W has already been the subject of some theoretical calculations and experimental measurements using various experimental techniques and theoretical methods. Tu et al.[35] have used a fast electron beam-energy scanning approach to study the photorecombination of highly charged W-ions at the Shanghai, EBIT. For He- to O-like W ions, using Dielectronic recombination (DR), Tu et al.[36] have studied the KLL Dielectronic Recombination (DR) resonance strengths, with help of calculation and experiment, were estimated by using a flexible atomic coding (FAC). Using the Dirac-Fock method, for 54 tungsten ions in the W^{6+} – W^{71+} range, radiative recombination,

radiated power loss rate coefficients as well as photoionization cross-sections have been done by Trzhaskovskaya et al.[37]. Using the MCDF technique, Liu et al.[38] have estimated the wavelengths with energy levels, oscillator strengths, transition rates as well as the lifetimes for $2s^2 2p^2 \ ^3P_1$ and $2s^2 2p^2 \ ^3P_2$ along with levels of ions as $2s 2p^3 \ ^5S_2$ in the C-like sequences from $Z = 7-92$. Beiersdorfer et al.[39] have explained the high- Z ionization balance accurately by applying critical ingredients for characterizing and assessing the energy balance of high-temperature plasmas. Wavelengths with emissivities vs temperature are most important spectral lines were predicted to be emitted as W ions at EUV longer than 45 nm, by Feldman et al.[40]. In order to predict electron binding energies that have been scaled based on experimental results, Kramida et al.[41] used the Hartree-Fock method to compute the ionization energies from W^{2+} to W^{71+} . Using MCDF approach, Huang et al. have analyzed the ground-state ionization potentials from Li to Ne isoelectronic sequences as $Z = 37-82$ using the MCDF method [42]. Safronova et al.[43] have investigated the relativistic energy of atomic systems using Quantum-electrodynamics (QED) perturbation theory. Carlson et al.[44] have studied multiply charged ions by computing IP up to $Z = 103$ and have also produced the IP for neutral atoms by performing calculations based on a basic spherical shell solution. However, the majority of the literature, just covers a few levels of W LXIX, showing a shortage of consistent and precise atomic data for this ion. Our main aim of this paper is to present the energies for higher excited state energy levels, as well as radiative data with relative intensity spectra of W LXIX, for multipole transitions such as E1 and E2, M1 and M2) for WLXIX.

2.4 THEORETICAL METHOD

2.4.1 Multi-Configuration Dirac Fock (MCDF) method

(a) General-purpose Relativistic Atomic Structure Package

The General-purpose Relativistic Atomic Structure Package is known as GRASP. It is developed at Oxford University by Ian Grant and colleagues. The two components of the package were referred to as MCDF as well as BENA. These components could simply be combined. In 1980, a section to estimate transition probabilities was a significant omission from Version 0. Dyall et al. (1989) published this in that year. A section for calculating transition probabilities, changing the configuration basis

between jj to LS-coupling, preprocessing of dimensions, and enhanced angular coefficient handling are all features that have been added to Version 0. He specifically modified a lot of the algorithms, Charlotte Fischer employed in her non-relativistic system HF86 (Fischer in 1987). It has been reported that GRASP92 is a related version (by Parpia et al. in 1996).

These are all included in the Breit interactions, quantum electrodynamics (QED) effects, and high-order relativistic corrections (vacuum polarization and self-energy). An extended average level that minimizes a Hamiltonian matrix's weighted trace is preferred when evaluating radial wave functions during self-consistent field (SCF) operation. For an N-electron atom or ion, the Dirac-Coulomb Hamiltonian:

$$H = \sum_{i=1}^N H_D(i) + \sum_{i=1}^N \sum_{j=1}^N \frac{1}{r_{ij}} \quad (2.1)$$

Through diagonalizing a relativistic Hamiltonian H, the energy levels of an atomic ion having N electrons can also be determined. For a single electron, the Hamiltonian Dirac is $H_D(i)$. An atomic state function calculates the particular wave function for an N electron atom or ion system. CSFs (configuration state functions) are the sum of four-component spin-orbital products, which are stated as follows:

$$\phi_{nkm} = \frac{1}{r} \begin{pmatrix} P_{nk}(r) & \chi_{km}(\theta, \phi, \sigma) \\ -iQ_{nk}(r) & \chi_{-km}(\theta, \phi, \sigma) \end{pmatrix} \quad (2.2)$$

where (P_{nk}) is large and (Q_{nk}) is small component radial wave functions, respectively. It fulfills the coupled Dirac equation for a local central field and may be explained using a self-consistent field standard technique, n is a principal quantum number, Dirac angular quantum number is k. whereas the spinor spherical harmonic χ_{km} is given as

$$\chi_{km}(\theta, \varphi) = \sum_{\sigma=\pm\frac{1}{2}} \left\langle lm - \sigma \frac{1}{2} \sigma \middle| l \frac{1}{2} jm \right\rangle Y_l^{m-\sigma}(\theta, \varphi) \varphi^\sigma \quad (2.3)$$

Linear combination of n electronic configuration state functions (CSFs) gives rise to Atomic state function (ASF) and is defined as:

$$|\Psi_\alpha(PJM)\rangle = \sum_{i=1}^N c_i(\alpha) |\gamma_i(PJM)\rangle \quad (2.4)$$

CSFs which specify a particular state is γ_i (PJM), where P denotes parity, angular quantum is given by (J, M). For each CSF, the expansion mixing coefficients $c_i(\alpha)$ follow the formula:

$$C_i(\alpha)C_j(\alpha) = \delta_{ij} \quad (2.5)$$

(b) The Flexible Atomic Code (FAC)

The Flexible Atomic Code is called as FAC. FAC is used to estimate the numerous collisional processes and atomic radiative data because it is an integrated system software. Energy levels, collisional excitation, radiative transition rates, collisional excitation as well as ionisation by electron impact, autoionization, photoionization, radiative recombination, along with dielectronic capture are only a few examples of collisional processes. A collisional radiative model is also included in the programme to create synthetic plasma spectra under various physical circumstances. In FAC, the relativistic configuration interaction (CI) involving independent particle basis wavefunctions based on the atomic structure calculation. These basis wavefunctions are generated from a local central potential that, according to self-consistent analysis, corresponds towards the electronic screening of a nuclear potential. The Dirac Coulomb Hamiltonian completely accounts for relativistic phenomena. Breit interaction at the zero energy limit for the exchanged photon, as well as hydrogenic estimations for self-energy as well as vacuum polarisation effects, include higher order QED phenomena. The approximation of distorted-wave (DW) treated as continuum processes. The current software is particularly effective for large-scale calculations due to systematic implementation of such factorization-interpolation method by Bar-Shalom et al. (1988). Theoretical background information and computational techniques are not discussed in this handbook; rather, they are explained in a number of articles that are included with this package and even this manual. FAC is a step in the right direction for making a comprehensive atomic model accessible to a large community of laboratory or astrophysical plasma diagnostics. Comprehension design of the underlying atomic theory can benefit from its flexible interface, even for people also. Also, it has enough power to allow experienced users to investigate how distinct physical approximations and algorithmic decisions may affect results. The most recent FAC version is **1.1.4**. It

can be achieved from link as <http://sprg.ssl.berkeley.edu/mfgu/fac>. The FAC program is written primarily in ANSI C with Fortran 77. Due to its C and Fortran 77 compilers, it is supposed to run on any platform. However, this is real and straight forward command parser originate from FAC, considered as a SFAC.

The estimate ASFs are specified by mixing the basis states for same symmetries

$$\psi = \sum_v b_v \phi_v \quad (2.6)$$

Where b_v are the mixing coefficients obtained from diagonalizing the total Hamiltonian.

The distinction between these two programs is fully relativistic in that MCDF conducts energy minimization for a given set of states while FAC adopts the local central field in calculations. The slight discrepancy between the outputs from the two codes has been discussed. Nuclear charge and electron-electron interaction contribute to the local potential involved in the FAC. Below is the nuclear potential:

$$V^N = \begin{cases} \frac{Z}{2} \left(\frac{r}{R_N} \right) \left[3 - \left(\frac{r}{R_N} \right)^2 \right], & r \leq R_N \\ Z, & r > R_N \end{cases} \quad (2.7)$$

where R_N indicates the radius of the nucleus.

2.5 CONSTRUCTION OF ATOMIC STATE FUNCTIONS (ASFs)

For each and every calculation for a specific case, one should include all possible and required configuration state functions (CSFs) by taking different number of electrons in different orbitals. By deciding appropriate CSFs, one can construct ASFs with linear combination of CSFs.

2.6 COMPUTATIONAL PROCEDURE

In order to obtain accurate results for W^{68+} (C-like tungsten) as we have chosen the following method:

Firstly, we have provided ground state configuration i.e. $1s^2 2s^2 2p^2$ and considered

configurations as $1s^2 2s^1 2p^2 3l(l=0-2)$, $1s^2 2s^1 2p^2 4l(l=0-3)$, $1s^2 2s^1 2p^2 5l(l=0-4)$, $1s^2 2s^1 2p^2 6l(l=0-4)$ and $1s^2 2s^2 2p^1 3l(l=0-2)$, $1s^2 2s^2 2p^1 4l(l=0-3)$, $1s^2 2s^2 2p^1 5l(l=0-4)$, $1s^2 2s^2 2p^1 6l(l=0-4)$ by taking single electron excitation from 2s and 2p orbitals.

In other step, we have included configuration like $1s^2 2p^4$, $1s^2 2p^3 3l(l=0-2)$, $1s^2 2p^3 4l(l=0-3)$, $1s^2 2p^3 5l(l=0-4)$, $1s^2 2p^3 6l(l=0-4)$ from 2s orbital by considering double electron excitation.

2.7 Results and Discussions (C-like W)

2.7.1 Energy levels

The lowest 205 fine structure levels are listed in this study, belonging to the configurations $1s^2 2s^2 2p^2$, $1s^2 2s^1 2p^3$, $1s^2 2p^4$ from GRASP and FAC both in Table 1. We used 54 combinations in our computations namely $1s^2 2s^1 2p^2 3l(l=0-2)$, $1s^2 2s^1 2p^2 4l(l=0-3)$, $1s^2 2s^1 2p^2 5l(l=0-4)$, $1s^2 2s^1 2p^2 6l(l=0-4)$ as well as $1s^2 2p^3 3l(l=0-2)$, $1s^2 2p^3 4l(l=0-3)$, $1s^2 2p^3 5l(l=0-4)$, $1s^2 2p^3 6l(l=0-4)$ and $1s^2 2s^2 2p^1 3l(l=0-2)$, $1s^2 2s^2 2p^1 4l(l=0-3)$, $1s^2 2s^2 2p^1 5l(l=0-4)$, $1s^2 2s^2 2p^1 6l(l=0-4)$.

Table 1 shows that QED contributes less than Breit. As a result, QED effects are less prominent in the case of W LXIX. We evaluated our derived data from GRASP and FAC with NIST [48], and the largest disparity between GRASP and FAC results and NIST values is 0.42%, respectively. The percentage difference between GRASP and FAC is displayed in table No. 1 under the column of “ ΔE ”.

$$\Delta E = \frac{|E_{FAC} - E_{GRASP}|}{E_{FAC}} \times 100\% \quad (2.8)$$

ΔE has a maximum value of 0.42%. This demonstrates that our results from their two independent computations for the majority of levels are in reasonable accord and confirms that our results are correct. The modest differences in certain levels between GRASP as well as FAC energies are mostly due to various estimates of electron wave functions of radial orbitals using angular part recoupling methods.

2.7.2 Radiative Data

E1, M1, E2, and M2 transitions, connection between the transition rates and oscillator

For E1 transitions:

$$A_{ji} = \frac{2.0261 \times 10^{18}}{\omega_j \lambda_{ji}^3} S_{ij} \quad \text{and} \quad f_{ij} = \frac{303.75}{\lambda_{ji} \omega_i} S_{ij}, \quad (2.9)$$

for M1 transitions:

$$A_{ji} = \frac{2.6974 \times 10^{13}}{\omega_j \lambda_{ji}^3} S_{ij} \quad \text{and} \quad f_{ij} = \frac{4.044 \times 10^{-3}}{\lambda_{ji} \omega_i} S_{ij}, \quad (2.10)$$

for E2 transitions:

$$A_{ji} = \frac{1.1199 \times 10^{18}}{\omega_j \lambda_{ji}^5} S_{ij} \quad \text{and} \quad f_{ij} = \frac{167.89}{\lambda_{ji}^3 \omega_i} S_{ij}, \quad (2.11)$$

for M1 transitions:

$$A_{ji} = \frac{1.4910 \times 10^{13}}{\omega_j \lambda_{ji}^5} S_{ij} \quad \text{and} \quad f_{ij} = \frac{2.236 \times 10^{-3}}{\lambda_{ji}^3 \omega_i} S_{ij}. \quad (2.12)$$

strength (f_{ij}) alongwith line strength (S_{ij}) can be described as:

In equations from (2.9) to (2.12), λ_{ji} is the transition wavelength, ω_j and ω_i are upper and lower-level statistical weights. Tables 2.1 to 2.5 contain 11 E1, 11 E2, 11 M1, and 11 M2 SXR transitions, as well as 10 E1, 13 E2, 14 M1, and 19 M2 HXR transitions from highly excited states to ground state. For W LXIX, our radiative data is reliable and may be utilized to identify experimentally measured spectral lines. In Figure 2.1, we plotted multipole transition intensities decaying to ground state relative to the intensity of strong E1 transition 1-28 for W LXIX. From the intensity spectra of W LXIX, we found that all transitions have negligible intensity w.r.t to the intensity 1-28 transition except two E1 transitions, 1-178 and 1-36. The intensity of 1-36 E1 SXR transition is near 1-28, while the intensity of 1-178 E1 HXR transition is approximately double that of 1-28.

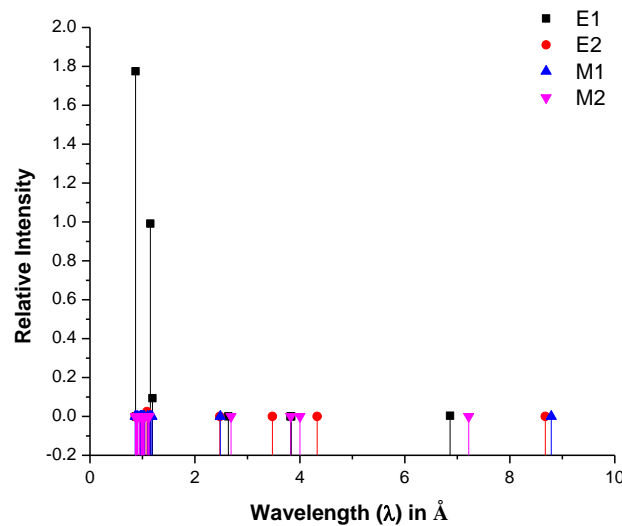


Figure 2.1: Relative intensity for W LXIX.

In Figure 2.2, We have demonstrated the discrepancy between length and velocity oscillator strengths for C-like W. Length gauge as well as velocity gauge discrepancies are analyzed for the result of C-like W. For E1 transitions, line strengths can be split into three categories: (a) $S < 0.001$ a.u., (b) $0.001 < S < 0.002$ a.u., while (c) $S > 0.002$ a.u.. As may be observed, in these areas, our logarithmic ratio of oscillator strengths has a maximum value of around 1.07. In the majority of transitions, this ratio is quite close to zero. 19 transitions have oscillator strengths ratios that are not equal to zero, as can also be seen. 0.001 a.u. of line strengths lies below whereas 2 transitions are between 0.001 and 0.002 a.u. and 1 transition lie in the region 0.004 - 0.005 a.u. line strengths Which have zero ratio of oscillator strength. For C-like W, this clearly represents that the terms of length form along with velocity form, or in both gauges, oscillator strengths are nearly equivalent. Again, for E2 transitions in Figure 2.3, line strengths are categories into three zones. (a) $S < 0.0002$ a.u., (b) $0.0004 < S < 0.0006$ a.u. while (c) $S > 0.0010$ a.u.. Our highest logarithmic oscillator strength ratio is 0.58, as shown and for the majority of transitions, this ratio is quite close to zero. Additionally, we can observe that for 10 transitions, the ratio of oscillator strengths not the same as zero and line strengths of 0.0002 a.u. lie below, whereas 1 transitions lie between 0.0004 - 0.0006 a.u. as well as 1 transition is located in the range of 0.0008 to 0.0010 a.u. line strength resulting in a zero oscillator strength ratio.

We have shown $\log_{10}(S_n/S_{n+1})$ against line strength (S_n) for $n = 5$ for the E1, E2 transitions and M1, M2 transitions for C-like W in Figures 2.4 to 2.7. The maximum value of the logarithmic ratio $\log_{10}(S_5/S_6)$ of line strengths for C-like W is 3.88×10^{-2} for E1 and 1.83×10^{-1} for E2, as shown in Figures 2.4 and 2.5 (Table 2.2 and 2.3). Moreover, this ratio is close to zero for C-like W. From Figure 2.6 and 2.7 for M1 and M2 transitions, as can be observed, the maximum values of the logarithmic ratio $\log_{10}(S_5/S_6)$ for M1 and M2 are 1.54×10^{-1} and 2.10×10^{-1} , respectively (Table 2.4 and 2.5).

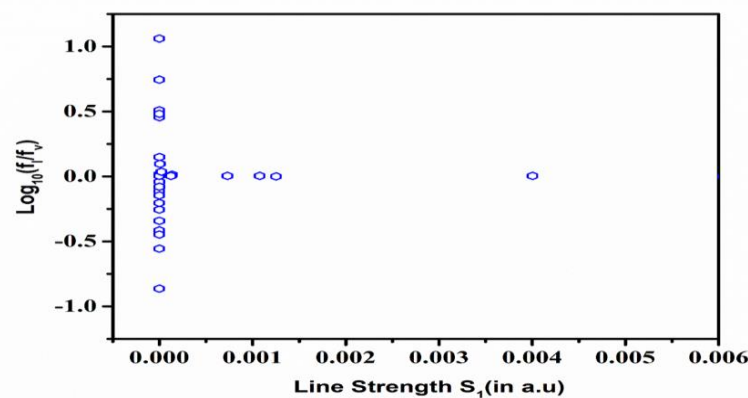


Figure 2.2: Comparisons between the velocity form(f_v) as well as the length form(f_l) of oscillator strengths for E1 transition of C-like W.

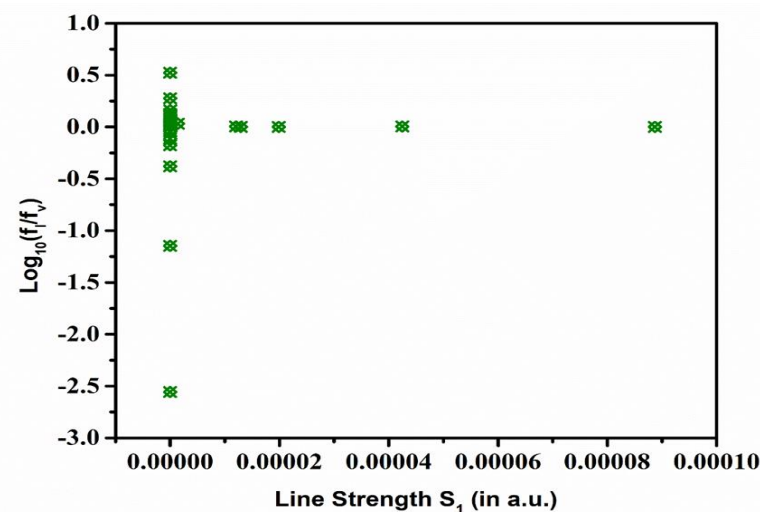


Figure 2.3: Comparisons between the velocity form(f_v) as well as the length form(f_l) of oscillator strengths for E2 transition of C-like W.

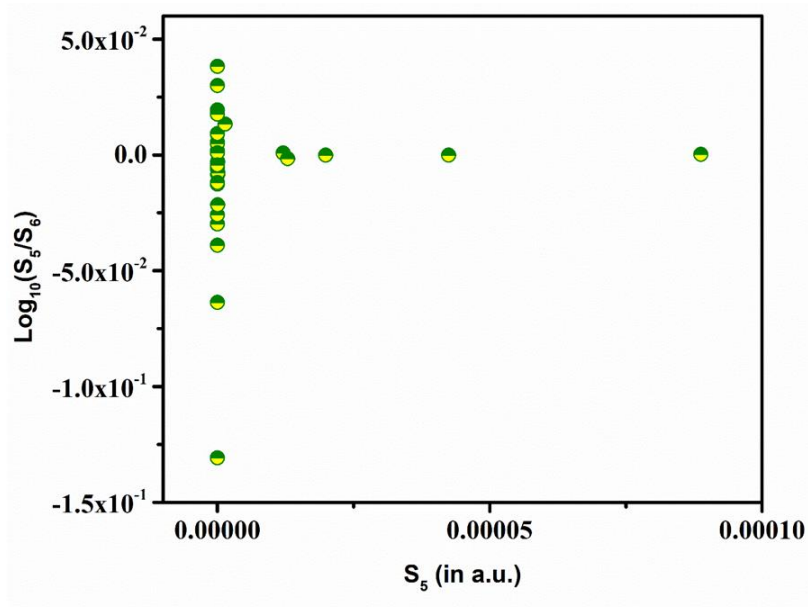


Figure 2.4: The line strength (S_n) against $\log_{10}(S_n/S_{n+1})$ for $n = 5$ for E1 transitions of C-like W.

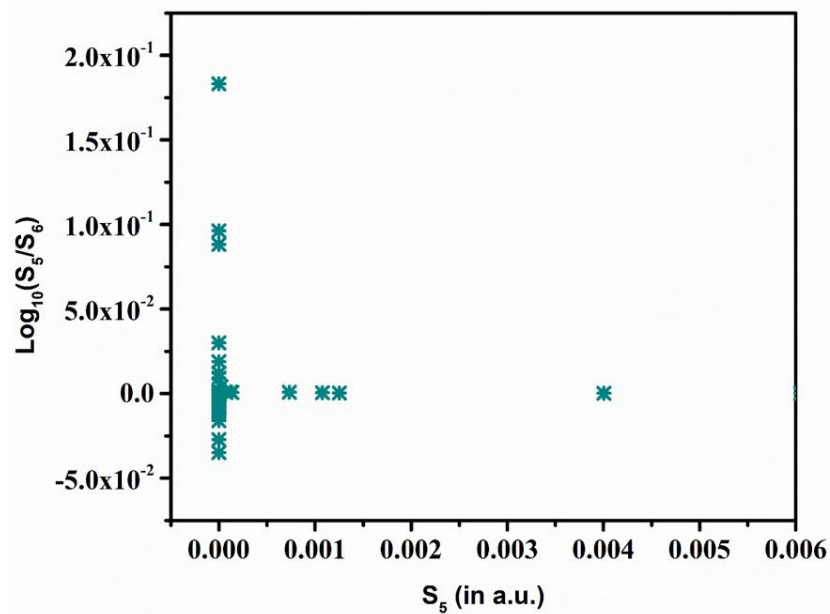


Figure 2.5: The line strength (S_n) against $\log_{10}(S_n/S_{n+1})$ for $n = 5$ for E2 transitions of C-like W.

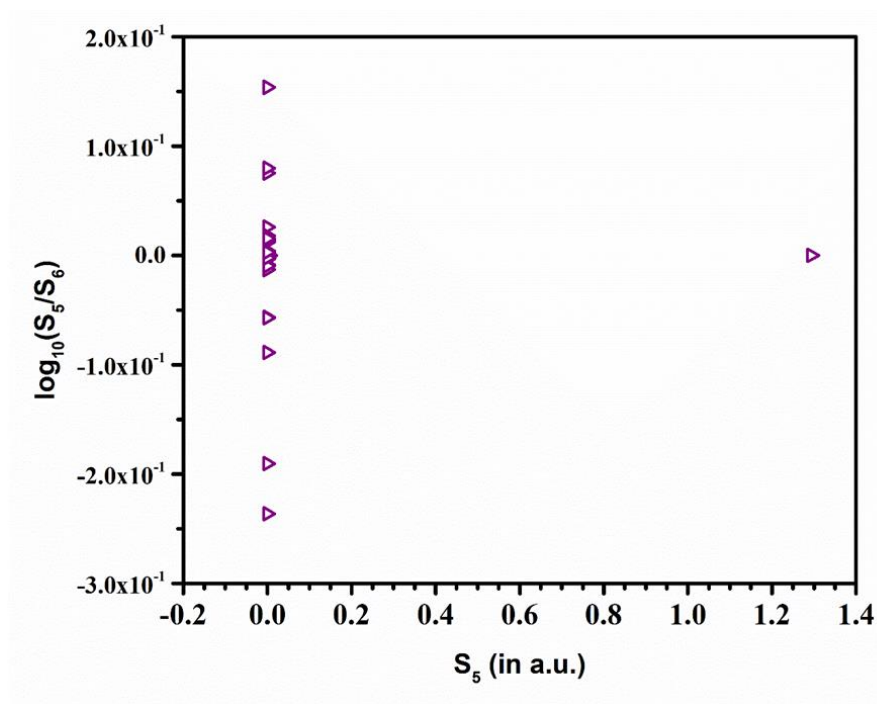


Figure 2.6: The line strength (S_n) against $\log_{10}(S_n/S_{n+1})$ for $n = 5$ for M1 transitions of C-like W.

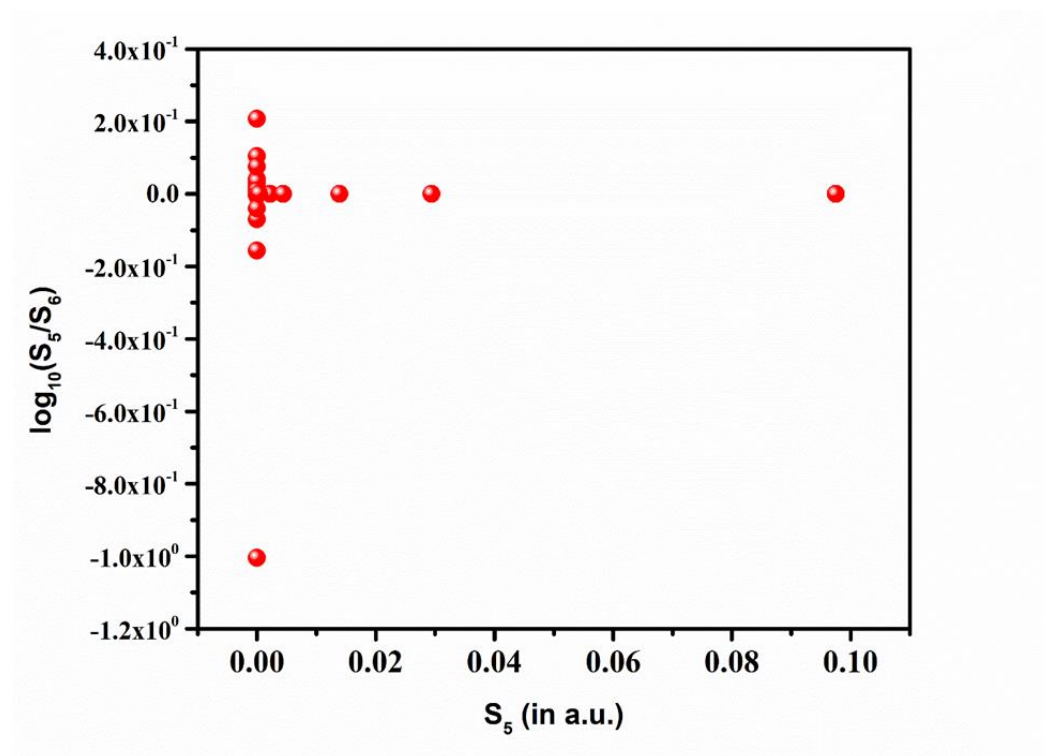


Figure 2.7: The line strength (S_n) against $\log_{10}(S_n/S_{n+1})$ for $n = 5$ for M2 transitions of C-like W.

2.8 CONCLUSION

This paper reports on the energy levels as well as the radiative data of C-like W, for transitions such as E1, E2, M1 and M2 ,for lowest level 205 fine structure levels. In the calculations, two separate codes are GRASP and FAC are used and the outcomes of both codes are compared. The disparity between our GRASP energies and existing theoretical and experimental information in the literature is extensively explained. We believe our findings are extensive and new and will be beneficial in identifying and studying fusion plasmas, astrophysical and diagnosis of solar and fusion plasmas that require appropriate atomic data for the analysis.

Table 2.1: Energies (in Ryd.) of lowest 205 fine structure levels of W LXI

LEVLs	CONFIGURATIONS	PARITY	MCDF				FAC	NIST	ΔE
			zero-order	Breit	QED	Total			
1	$2s^2 2p^2 ({}^3P_2) {}^3P_0$	Even	000.00	-	-	000.0000	000.0000	000.00	-
2	$2s^2 2p^2 ({}^3P_2) {}^3P_1$	Even	105.1250	- 1.5700	0.1260	103.6821	103.7865		
3	$2s^2 2p^2 ({}^1D_2) {}^1D_2$	Even	107.0863	- 2.1800	0.1260	105.0345	105.1361	105.08	0.100
4	$2s^1 2p^3 ({}^2P_1) {}^3S_1$	Odd	128.0918	- 0.6050	- 1.2000	126.2834	126.0415		
5	$2s^1 2p^3 ({}^2P_1) {}^1P_1$	Odd	134.3963	- 0.3690	- 1.2000	132.8238	132.5726	132.44	0.187
6	$2s^2 2p^2 ({}^3P_2) {}^3P_2$	Even	213.6133	- 3.3400	0.2320	210.5102	210.7195		
7	$2s^2 2p^2 ({}^1S_0) {}^1S_0$	Even	217.6028	- 2.6600	0.2310	215.1751	215.3811		
8	$2s^1 2p^3 ({}^4S_3) {}^5S_2$	Odd	230.8832	- 1.9700	- 1.0800	227.8351	227.7146		
9	$2s^1 2p^3 ({}^2D_3) {}^3D_3$	Odd	235.1278	- 2.9100	- 1.0800	231.1403	231.0105		
10	$2s^1 2p^3 ({}^2P_1) {}^3P_0$	Odd	238.3523	- 1.4600	- 1.0800	235.8156	235.6887		
11	$2s^1 2p^3 ({}^4S_3) {}^3S_1$	Odd	240.4511	- 1.8800	- 1.0800	237.4951	237.3575		
12	$2s^1 2p^3 ({}^2P_1) {}^3P_1$	Odd	241.4010	- 1.8200	- 1.0800	238.5081	238.0410		
13	$2s^1 2p^3 ({}^2D_3) {}^1D_2$	Odd	241.7216	- 2.4600	- 1.0800	238.1790	238.3713		
14	$2p^4 ({}^3P_2) {}^3P_2$	Even	265.3201	- 0.8380	- 2.3900	262.0943	261.6043		
15	$2p^4 ({}^1S_0) {}^1S_0$	Odd	269.5109	- 0.1440	- 2.3900	266.9799	266.4868		
16	$2s^1 2p^3 ({}^2D_3) {}^3D_2$	Odd	343.6099	-	-	339.1892	339.1791		

LEVELS	CONFIGURATIONS	PARITY	MCDF				FAC	NIST	ΔE
			zero-order	Breit	QED	Total			
				3.4700	0.9520				
17	$2s^1 2p^3 ({}^2D_3) {}^3D_1$	Odd	349.8123	- 3.2600	- 0.9520	345.5953	345.5759		
18	$2p^4 ({}^3P_2) {}^3P_1$	Even	371.2252	- 1.9700	- 2.2800	366.9760	366.6109		
19	$2p^4 ({}^1D_2) {}^1D_2$	Even	373.1988	- 2.5700	- 2.2800	368.3496	367.9819		
20	$2p^4 ({}^3P_2) {}^3P_0$	Even	481.3380	- 3.2700	- 2.1600	475.9136	475.6745		
21	$2s^2 2p^1 3s^1 ({}^2S_1) {}^3P_0$	Odd	766.8732	- 2.5400	0.3080	764.6434	764.8544		
22	$2s^2 2p^1 3s^1 ({}^2S_1) {}^3P_1$	Odd	767.2421	- 2.6400	0.3120	764.9127	765.1279		
23	$2s^2 2p^1 3s^1 ({}^2P_1) {}^3D_1$	Even	773.6478	- 2.2900	- 0.0578	771.3004	771.4046		
24	$2s^2 2p^1 3s^1 ({}^2P_1) {}^1S_0$	Even	777.0314	- 2.0500	- 0.0626	774.9180	775.0496		
25	$2s^2 2p^1 3s^1 ({}^2S_1) {}^5P_1$	Even	787.4731	- 1.1600	- 1.0100	785.3054	785.2092		
26	$2s^2 2p^1 3s^1 ({}^2S_1) {}^3P_0$	Even	790.2751	- 1.0200	- 1.0100	788.2447	788.1378		
27	$2s^2 2p^1 3p^1 ({}^2P_1) {}^5D_0$	Odd	794.6412	- 0.6170	- 1.3800	792.6463	792.3879		
28	$2s^2 2p^1 3p^1 ({}^2P_1) {}^5D_1$	Odd	794.7796	- 0.8130	- 1.3800	792.5866	792.4441		
29	$2s^2 2p^1 3p^1 ({}^2P_1) {}^3P_1$	Even	806.3343	- 2.5700	- 0.0261	803.7407	803.7880		
30	$2s^2 2p^1 3p^1 ({}^2P_1) {}^3D_2$	Even	806.4141	- 2.7400	- 0.0196	803.6553	803.8709		
31	$2s^2 2p^1 3d^1 ({}^2D_1) {}^3F_2$	Odd	811.2927	- 2.7700	- 0.0719	808.4549	808.5099		
34	$2s^2 2p^1 3d^1 ({}^2D_1) {}^3D_3$	Odd	820.9356	- 2.9900	- 0.0716	817.8766	817.9344		
35	$2s^1 2p^2 3d^1 ({}^2P_1) {}^5P_2$	Odd	827.0909	- 1.2200	- 1.3200	824.5490	824.3632		
36	$2s^1 2p^2 3p^1 ({}^2P_1) {}^3D_1$	Odd	827.4841	- 1.2000	- 1.3500	824.9395	824.7543		
37	$2s^1 2p^2 3d^1 ({}^2D_1) {}^5F_1$	Even	831.8005	- 1.1200	- 1.4000	829.2818	829.0161		
38	$2s^1 2p^2 3p^1 ({}^2D_1) {}^3D_2$	Even	832.4294	- 1.3000	- 1.4000	829.7243	829.4624		
39	$2s^1 2p^2 3p^1 ({}^2D_1) {}^3D_3$	Even	841.0644	- 1.5300	- 1.4000	838.1382	837.8820		
40	$2s^1 2p^2 3p^1 ({}^2D_1) {}^3F_2$	Even	842.2457	- 1.3900	- 1.4000	839.4554	839.2033		
41	$2s^2 2p^1 3s^1 ({}^2S_1) {}^3P_2$	Odd	875.5322	- 4.1200	0.4090	871.8239	872.1006		
42	$2s^2 2p^1 3s^1 ({}^2S_1) {}^1P_1$	Odd	876.1694	- 4.0800	0.4110	872.4989	872.7872		

LEVELS	CONFIGURATIONS	PARITY	MCDF				FAC	NIST	ΔE
			zero-order	Breit	QED	Total			
43	$2s^2 2p^1 3p^1 (^2P_1)^3S_1$	Even	883.4646	- 3.6300	0.0277	879.8598	880.0395		
44	$2s^2 2p^1 3p^1 (^2P_1)^1D_2$	Even	883.7755	- 3.8000	0.0295	880.0019	880.1853		
45	$2s^1 2p^2 3s^1 (^2D_1)^5P_2$	Even	890.1976	- 2.7800	- 0.8800	886.5383	886.5125		
46	$2s^1 2p^2 3s^1 (^2S_1)^3P_1$	Even	892.2823	- 2.7200	- 0.8750	888.6838	888.6661		
47	$2s^1 2p^2 3s^1 (^2S_1)^3D_3$	Even	893.9534	- 3.6100	- 0.8850	889.4627	889.4257		
48	$2s^1 2p^2 3s^1 (^2S_1)^3D_2$	Even	895.7740	- 3.4400	- 0.8870	891.4508	891.4182		
49	$2s^1 2p^2 3p^1 (^2P_1)^5D_1$	Odd	897.0121	- 2.2900	- 1.2600	893.4594	893.3276		
50	$2s^1 2p^2 3p^1 (^2P_1)^5D_2$	Odd	898.0991	- 2.5700	- 1.2600	894.2745	894.1451		
51	$2s^1 2p^2 3s^1 (^2S_1)^1S_0$	Even	899.1447	- 2.7300	- 0.8840	895.5352	895.4848		
52	$2s^1 2p^2 3s^1 (^2S_1)^1P_1$	Even	899.4471	- 2.9300	- 0.8830	895.6355	895.5854		
53	$2s^1 2p^2 3s^1 (^2S_1)^3D_1$	Even	899.8117	- 2.8300	- 0.8920	896.0925	896.0348		
54	$2s^1 2p^2 3s^1 (^2S_1)^1D_2$	Even	900.3707	- 3.1500	- 0.8850	896.3391	896.2856		
55	$2s^1 2p^2 3p^1 (^2P_1)^1F_3$	Odd	901.2262	- 3.3700	- 1.2600	896.5961	896.4544		
56	$2s^1 2p^2 3p^1 (^2P_1)^3P_2$	Odd	903.6575	- 2.8500	- 1.2500	899.5491	899.4290		
57	$2s^1 2p^2 3p^1 (^2P_1)^3P_0$	Odd	905.5283	- 2.3600	- 1.2600	901.9161	901.7459		
58	$2s^1 2p^2 3p^1 (^2P_1)^3D_1$	Odd	905.7809	- 2.5300	- 1.2600	901.9970	901.8282		
59	$2s^1 2p^2 3p^1 (^2P_1)^5F_2$	Odd	906.3338	- 2.8800	- 1.2600	902.2008	902.0357		
60	$2s^1 2p^2 3p^1 (^2P_1)^3D_1$	Odd	909.5769	- 2.4600	- 1.2600	905.8639	905.7204		
61	$2s^2 2p^1 3p^1 (^2P_1)^1P_1$	Even	913.7990	- 4.1600	0.0730	909.7153	909.8593		
62	$2s^2 2p^1 3p^1 (^2P_1)^3D_3$	Even	913.8117	- 4.2200	0.0759	909.6684	909.9052		
63	$2s^2 2p^1 3p^1 (^2P_1)^3P_2$	Even	916.0398	- 4.1100	0.0747	912.0012	912.2132		
64	$2s^2 2p^1 3p^1 (^2P_1)^1S_0$	Even	917.8013	- 3.8400	0.0748	914.0325	914.2500		
67	$2s^2 2p^1 3d^1 (^2D_1)^3F_3$	Odd	921.4414	- 4.4700	0.0239	916.9992	917.1242		
72	$2s^2 2p^1 3d^1 (^2D_1)^3F_4$	Odd	927.9074	- 4.4400	- 0.0059	923.4658	923.5886		
74	$2s^1 2p^2 3p^1 (^2S_1)^5D_3$	Odd	928.4912	-	-	924.2820	924.3268		

LEVELS	CONFIGURATIONS	PARITY	MCDF				FAC	NIST	ΔE
			zero-order	Breit	QED	Total			
				3.0100	1.2000				
76	$2s^1 2p^2 3p^1 (^2P_1)^3S_1$	Odd	929.3757	- 2.9300	- 1.2100	925.2343	925.1989		
77	$2s^2 2p^1 3d^1 (^2D_1)^1F_3$	Odd	930.2472	- 4.3100	- 0.0108	925.9291	925.8950		
78	$2s^1 2p^2 3p^1 (^2P_1)^3D_2$	Odd	930.6172	- 2.8700	- 1.1900	926.5587	926.4441		
80	$2s^1 2p^2 3p^1 (^2P_1)^3P_0$	Odd	931.5094	- 2.7400	- 1.2200	927.5527	927.4490		
81	$2s^1 2p^2 3p^1 (^2P_1)^3F_4$	Odd	932.5244	- 3.7400	- 1.1900	927.5935	927.4788		
82	$2s^1 2p^2 3p^1 (^2P_1)^3P_2$	Odd	933.3612	- 3.4600	- 1.2300	928.6734	928.5452		
83	$2s^1 2p^2 3p^1 (^2P_1)^3D_3$	Odd	934.3641	- 3.5900	- 1.2100	929.5634	929.4517		
84	$2s^1 2p^2 3p^1 (^2P_1)^1P_1$	Odd	934.4165	- 3.3500	- 1.2300	929.8361	929.7048		
85	$2s^1 2p^2 3d^1 (^2D_1)^5D_0$	Even	934.7393	- 2.5000	- 1.2700	930.9683	930.4441		
86	$2s^1 2p^2 3d^1 (^2D_1)^5F_2$	Even	934.7480	- 2.8500	- 1.2800	930.6249	930.6587		
87	$2s^1 2p^2 3d^1 (^2D_1)^5D_1$	Even	934.8193	- 2.7000	- 1.2800	930.8394	930.7867		
88	$2s^1 2p^2 3d^1 (^2D_1)^5F_3$	Even	935.7611	- 3.1100	- 1.2700	931.3739	931.1948		
89	$2s^1 2p^2 3p^1 (^2P_1)^3D_2$	Odd	937.5835	- 2.7900	- 1.2300	933.5663	933.4182		
90	$2s^1 2p^2 3p^1 (^2P_1)^3D_3$	Odd	938.2886	- 3.3000	- 1.2200	933.7667	933.6258		
91	$2s^1 2p^2 3p^1 (^2P_1)^3P_0$	Odd	938.9291	- 2.9300	- 1.2200	934.7800	933.6303		
92	$2s^1 2p^2 3d^1 (^2D_1)^3G_4$	Odd	938.9540	- 3.8600	- 1.2700	933.8193	934.2529		
93	$2s^1 2p^2 3p^1 (^2P_1)^3P_1$	Odd	939.0947	- 2.7800	- 1.2200	935.0931	934.6437		
94	$2s^1 2p^2 3p^1 (^2P_1)^3D_2$	Odd	939.3890	- 3.1400	- 1.2200	935.0230	934.8795		
95	$2s^1 2p^2 3d^1 (^2D_1)^3F_3$	Even	939.4025	- 3.6800	- 1.2800	934.4462	934.8816		
96	$2s^1 2p^2 3p^1 (^2P_1)^3P_1$	Odd	939.7655	- 2.9400	- 1.2200	935.6063	934.9480		
97	$2s^1 2p^2 3d^1 (^2D_1)^3D_2$	Even	939.9472	- 3.5800	- 1.2800	935.0831	935.4731		
98	$2s^1 2p^2 3d^1 (^2D_1)^3S_1$	Even	940.4750	- 3.4000	- 1.2900	935.7866	935.5754		
99	$2s^1 2p^2 3d^1 (^2D_1)^5F_4$	Even	942.5321	- 3.1400	- 1.2700	938.1181	937.9424		
100	$2s^1 2p^2 3d^1 (^2D_1)^3F_2$	Even	942.9346	- 3.0400	- 1.2800	938.6185	938.4080		

LEVELS	CONFIGURATIONS	PARITY	MCDF				FAC	NIST	ΔE
			zero-order	Breit	QED	Total			
101	$2s^1 2p^2 3d^1 (^2D_1)^1 P_1$	Even	943.2990	- 2.7900	- 1.2800	939.2371	938.9979		
102	$2s^1 2p^2 3d^1 (^2D_1)^3 G_3$	Even	943.8354	- 3.3500	- 1.2800	939.2124	939.0223		
103	$2s^1 2p^2 3d^1 (^2D_1)^3 P_2$	Even	944.4245	- 3.0000	- 1.2800	940.1475	939.9640		
104	$2s^1 2p^2 3d^1 (^2D_1)^3 F_3$	Even	944.8424	- 3.1200	- 1.2800	940.4453	940.2711		
105	$2s^1 2p^2 3d^1 (^2D_1)^3 D_1$	Even	945.2310	- 3.1900	- 1.2800	940.7642	940.5477		
106	$2s^1 2p^2 3d^1 (^2D_1)^3 F_2$	Even	945.6718	- 3.2400	- 1.2800	941.1555	940.9344		
107	$2s^1 2p^2 3d^1 (^2D_1)^3 P_0$	Even	946.2912	- 3.2700	- 1.2800	941.7494	940.9345		
108	$2s^1 2p^2 3d^1 (^2D_1)^3 G_5$	Even	946.3724	- 3.9700	- 1.2700	941.1244	941.5295		
109	$2s^1 2p^2 3d^1 (^2D_1)^3 D_1$	Even	946.4190	- 2.9700	- 1.2800	942.1702	941.9896		
110	$2s^1 2p^2 3d^1 (^2D_1)^3 D_3$	Even	948.0844	- 3.8000	- 1.2800	943.0085	942.8191		
111	$2s^1 2p^2 3d^1 (^2D_1)^3 F_4$	Even	948.5545	- 3.9200	- 1.2700	943.3587	943.1707		
112	$2s^1 2p^2 3d^1 (^2D_1)^1 D_2$	Even	948.7602	- 3.6500	- 1.2800	943.8327	943.6444		
113	$2s^1 2p^2 3d^1 (^2D_1)^1 P_1$	Even	949.5789	- 3.5500	- 1.2900	944.7408	944.5573		
114	$2s^1 2p^2 3d^1 (^2D_1)^3 P_0$	Even	950.0805	- 3.5400	- 1.2800	945.2568	945.0689		
115	$2s^1 2p^2 3d^1 (^2D_1)^3 D_3$	Even	951.6991	- 3.0700	- 1.2900	947.3400	947.1256		
116	$2s^1 2p^2 3d^1 (^2D_1)^1 G_4$	Even	952.5710	- 3.5000	- 1.2700	947.8005	947.5881		
117	$2s^1 2p^2 3d^1 (^2D_1)^3 P_2$	Even	953.1490	- 3.0800	- 1.2800	948.7920	948.5732		
118	$2s^1 2p^2 3d^1 (^2D_1)^3 P_1$	Even	953.5145	- 3.3300	- 1.2800	948.9078	948.6674		
119	$2s^1 2p^2 3d^1 (^2D_1)^1 F_3$	Even	953.5743	- 3.4200	- 1.2800	948.8775	948.6941		
120	$2s^1 2p^2 3d^1 (^2D_1)^1 D_2$	Even	953.7540	- 3.3200	- 1.2800	949.1555	948.9443		
135	$2s^1 2p^2 3s^1 (^2S_1)^3 S_1$	Even	1008.0785	- 3.8800	- 0.7640	1003.4329	997.2035		
136	$2s^1 2p^2 3p^1 (^2P_1)^5 S_2$	Odd	1008.8319	- 4.1700	- 1.1300	1003.5279	1003.4857		
137	$2s^1 2p^2 3s^1 (^2P_1)^3 P_1$	Even	1009.1799	- 4.3900	- 0.7650	1004.0203	1003.4545		
138	$2s^1 2p^2 3p^1 (^2P_1)^3 D_3$	Odd	1009.3157	- 4.4800	- 1.1400	1003.6982	1003.6596		
140	$2s^1 2p^2 3s^1 (^2P_1)^1 S_0$	Even	1010.4418	-	-	1005.9127	1005.9406		

LEVELS	CONFIGURATIONS	PARITY	MCDF				FAC	NIST	ΔE
			zero-order	Breit	QED	Total			
				3.7600	0.7710				
141	$2s^1 2p^2 3p^1 (^2P_1)^3P_0$	Odd	1016.2367	- 3.4100	- 1.1300	1011.6967	1011.6165		
142	$2s^1 2p^2 3p^1 (^2P_1)^1P_1$	Odd	1016.4457	- 3.5900	- 1.1400	1011.7235	1011.6425		
143	$2s^1 2p^2 3p^1 (^2P_1)^3S_1$	Odd	1016.8529	- 3.9900	- 1.1400	1011.7234	1011.6466		
144	$2s^1 2p^2 3p^1 (^2P_1)^1D_2$	Odd	1017.1280	- 4.1200	- 1.1400	1011.8656	1011.7902		
160	$2s^1 2p^2 3p^1 (^2P_1)^5D_4$	Odd	1038.7119	- 4.8000	- 1.1000	1032.8143	1032.7823		
161	$2s^1 2p^2 3p^1 (^2P_1)^5p_3$	Odd	1038.9763	- 4.7600	- 1.1100	1033.1097	1033.0764		
162	$2s^1 2p^2 3p^1 (^2P_1)^3S_1$	Odd	1039.8126	- 4.6700	- 1.1100	1034.0310	1033.9965		
164	$2s^1 2p^2 3p^1 (^2P_1)^1D_2$	Odd	1042.1182	- 4.5600	- 1.1100	1036.4523	1036.4296		
165	$2s^1 2p^2 3d^1 (^2D_1)^5D_2$	Even	1045.9349	- 4.6100	- 1.1600	1040.1730	1040.0710		
166	$2s^1 2p^2 3d^1 (^2D_1)^5P_1$	Even	1046.2290	- 4.6200	- 1.1600	1040.4486	1040.2062		
167	$2s^1 2p^2 3d^1 (^2D_1)^5D_3$	Even	1046.3764	- 4.9200	- 1.1500	1040.3030	1040.3475		
168	$2s^1 2p^2 3p^1 (^2P_1)^3P_0$	Odd	1046.6112	- 4.4400	- 1.1000	1041.0698	1041.0023		
169	$2s^1 2p^2 3p^1 (^2P_1)^3P_2$	Odd	1046.6798	- 4.0300	- 1.1000	1041.5541	1041.3518		
170	$2s^1 2p^2 3d^1 (^2D_1)^3F_4$	Even	1046.8238	- 5.1500	- 1.1500	1040.5224	1041.4319		
171	$2s^1 2p^2 3p^1 (^2P_1)^3F_3$	Odd	1047.0493	- 4.5300	- 1.1000	1041.4186	1041.4909		
172	$2s^1 2p^2 3p^1 (^2P_1)^3P_1$	Odd	1047.2941	- 3.9200	- 1.1100	1042.2701	1042.2077		
173	$2s^1 2p^2 3p^1 (^2P_1)^3P_2$	Odd	1047.9115	- 4.3000	- 1.1000	1042.5093	1042.4572		
176	$2s^1 2p^2 3p^1 (^2P_1)^1P_1$	Odd	1050.2740	- 4.2400	- 1.1000	1044.9320	1044.8855		
179	$2s^1 2p^2 3d^1 (^2D_1)^5F_5$	Even	1052.7334	- 5.0800	- 1.1500	1046.4993	1046.4047		
180	$2s^1 2p^2 3d^1 (^2D_1)^3D_1$	Even	1052.8860	- 4.2100	- 1.1600	1047.5168	1046.7224		
181	$2s^1 2p^2 3d^1 (^2D_1)^5D_4$	Even	1052.9446	- 4.9800	- 1.1500	1046.8154	1047.1493		
182	$2s^1 2p^2 3d^1 (^2D_1)^3P_0$	Even	1053.0203	- 4.6000	- 1.1600	1047.2636	1047.3858		
184	$2s^1 2p^2 3d^1 (^2D_1)^1D_2$	Even	1053.6966	- 4.2800	- 1.1500	1048.2668	1048.0897		
186	$2s^1 2p^2 3d^1 (^2D_1)^3F_3$	Even	1054.1322	- 4.7600	- 1.1500	1048.2162	1048.1402		

LEVELS	CONFIGURATIONS	PARITY	MCDF				FAC	NIST	ΔE
			zero-order	Breit	QED	Total			
187	$2s^1 2p^2 3d^1 (^2D_1)^3 D_2$	Even	1054.5487	- 4.5700	- 1.1500	1048.8318	1048.7026		
188	$2s^1 2p^2 3d^1 (^2D_1)^3 D_1$	Even	1054.6264	- 4.2700	- 1.1500	1049.2007	1049.0660		
191	$2s^1 2p^2 3d^1 (^2D_1)^3 P_1$	Even	1055.6024	- 4.7100	- 1.1600	1049.7363	1049.6381		
192	$2s^1 2p^2 3d^1 (^2D_1)^3 D_3$	Even	1055.8620	- 4.8700	- 1.1500	1049.8432	1049.7409		
197	$2s^1 2p^2 3d^1 (^2D_1)^3 P_0$	Even	1056.4228	- 4.7300	- 1.1500	1050.5422	1050.4381		
198	$2s^1 2p^2 3d^1 (^2D_1)^3 P_2$	Even	1056.6277	- 4.7700	- 1.1600	1050.7030	1050.6059		
202	$2s^1 2p^2 3d^1 (^2D_1)^3 F_4$	Even	1061.2064	- 4.7000	- 1.1800	1055.3224	1055.4316		
203	$2s^1 2p^2 3d^1 (^2D_1)^1 F_3$	Even	1061.7963	- 4.6200	- 1.1800	1055.9993	1055.8786		
205	$2s^1 2p^2 3d^1 (^2D_1)^3 P_1$	Even	1062.7499	- 4.6000	- 1.1700	1056.9767	1057.8510		

Table 2.2: Radiative data for E1 transitions in W LXIX.

S No.	Transition		λ_{ji} (in Å)	A_{ji} (in s^{-1})	f_{ij}	S_{ij} (in a.u.)
	Lower Level(i)	Upper Level(j)				
1	1	5	6.861	1.2654E+13	2.6787E-01	6.0503E-03
2	1	11	3.837	7.3749E+10	4.8833E-04	6.1685E-06
3	1	12	3.821	4.7639E+09	3.1277E-05	3.9341E-07
4	1	17	2.637	2.3222E+06	7.2617E-09	6.3036E-11
5	1	22	1.191	5.4283E+13	3.4650E-02	1.3590E-04
6	1	28	1.150	5.5629E+14	3.3074E-01	1.2519E-03
7	1	36	1.105	5.3901E+14	2.9582E-01	1.0758E-03
8	1	42	1.044	9.7912E+09	4.8037E-06	1.6517E-08
9	1	49	1.020	6.1057E+07	2.8566E-08	9.5919E-11
10	1	58	1.010	9.3914E+10	4.3111E-05	1.4339E-07
11	1	60	1.006	1.5102E+11	6.8734E-05	2.2763E-07
12	1	76	0.985	5.3554E+10	2.3365E-05	7.5758E-08
13	1	84	0.980	9.3519E+10	4.0398E-05	1.3034E-07

S No.	Transition		λ_{ji} (in Å)	A_{ji} (in s^{-1})	f_{ij}	S_{ij} (in a.u.)
	Lower Level(i)	Upper Level(j)				
14	1	93	0.975	5.4388E+11	2.3231E-04	7.4530E-07
15	1	96	0.974	3.7956E+11	1.6194E-04	5.1926E-07
16	1	142	0.901	1.1571E+07	4.2220E-09	1.2519E-11
17	1	143	0.901	1.2218E+07	4.4580E-09	1.3219E-11
18	1	162	0.881	3.6772E+06	1.2845E-09	3.7265E-12
19	1	172	0.874	1.1952E+08	4.1091E-08	1.1827E-10
20	1	176	0.872	4.2104E+06	1.4402E-09	4.1348E-12
21	1	178	0.869	7.5240E+14	2.5552E-01	7.3098E-04

Table 2.3: Radiative data for E2 transitions in W LXIX.

S No.	Transition		λ_{ji} (in Å)	A_{ji} (in s^{-1})	f_{ij}	S_{ij} (in a.u.)
	Lower Level(i)	Upper Level(j)				
1	1	3	8.676	9.0584E+07	5.1110E-06	1.9880E-05
2	1	6	4.329	4.8014E+02	6.7444E-12	3.2586E-12
3	1	14	3.477	1.5565E+07	1.4104E-07	3.5309E-08
4	1	19	2.474	3.1626E+03	1.4509E-11	1.3085E-12
5	1	30	1.134	1.4419E+12	1.3896E-03	1.2067E-05
6	1	38	1.098	5.9544E+12	5.3838E-03	4.2481E-05
7	1	40	1.086	1.3181E+13	1.1644E-02	8.8716E-05
8	1	44	1.036	8.4462E+07	6.7891E-08	4.4902E-10
9	1	45	1.028	2.5440E+07	2.0149E-08	1.3033E-10
10	1	48	1.022	3.0530E+08	2.3914E-07	1.5215E-09
11	1	54	1.017	1.0709E+09	8.2967E-07	5.1927E-09
12	1	63	0.999	2.6674E+08	1.9963E-07	1.1861E-09
13	1	86	0.979	2.9477E+04	2.1186E-11	1.1848E-13
14	1	97	0.975	1.0644E+09	7.5776E-07	4.1772E-09
15	1	100	0.971	1.1910E+10	8.4148E-06	4.5865E-08
16	1	103	0.969	6.9707E+09	4.9091E-06	2.6627E-08
17	1	106	0.968	8.1675E+09	5.7397E-06	3.1032E-08
18	1	112	0.966	1.3508E+09	9.4390E-07	5.0600E-09
19	1	117	0.960	2.7568E+10	1.9062E-05	1.0059E-07
20	1	120	0.960	6.7771E+09	4.6826E-06	2.4682E-08
21	1	165	0.876	1.6077E+05	9.2494E-11	3.7043E-13
22	1	184	0.869	1.9507E+07	1.1050E-08	4.3237E-11
23	1	187	0.869	4.1261E+07	2.3348E-08	9.1209E-11
24	1	198	0.867	1.6551E+07	9.3320E-09	3.6261E-11

Table 2.4: Radiative data for M1 transitions in W LXIX.

S No.	Transitions		λ_{ji} (in Å)	A_{ji} (in s^{-1})	f_{ij}	S_{ij} (in a.u.)
	Lower Level(i)	Upper Level(j)				
1	1	2	8.789	1.7134E+10	5.9529E-04	1.2937E+00
2	1	18	2.483	3.4166E+04	9.4751E-11	5.8179E-08
3	1	23	1.182	1.4928E+09	9.3721E-07	2.7380E-04
4	1	25	1.160	4.8103E+09	2.9132E-06	8.3588E-04
5	1	29	1.134	2.9054E+10	1.6797E-05	4.7091E-03
6	1	37	1.099	7.4861E+08	4.0656E-07	1.1047E-04
7	1	43	1.036	1.2476E+07	6.0189E-09	1.5414E-06
8	1	46	1.025	4.0817E+06	1.9303E-09	4.8943E-07
9	1	52	1.018	2.3281E+07	1.0839E-08	2.7271E-06
10	1	53	1.017	5.3152E+07	2.4722E-08	6.2166E-06
11	1	61	1.002	3.5186E+06	1.5879E-09	3.9332E-07
12	1	87	0.979	1.3489E+06	5.8145E-10	1.4075E-07
13	1	98	0.974	4.2293E+06	1.8038E-09	4.3434E-07
14	1	101	0.970	1.6625E+06	7.0383E-10	1.6885E-07
15	1	105	0.969	8.2739E+04	3.4916E-11	8.3629E-09
16	1	109	0.967	9.7185E+04	4.0889E-11	9.7791E-09
17	1	113	0.965	6.8788E+05	2.8784E-10	6.8653E-08
18	1	118	0.960	7.7561E+05	3.2171E-10	7.6394E-08
19	1	135	0.908	2.3479E+03	8.7091E-13	1.9557E-10
20	1	137	0.908	1.3042E+02	4.8319E-14	1.0844E-11
21	1	166	0.876	1.4297E+02	4.9324E-14	1.0682E-11
22	1	180	0.870	4.1393E+03	1.4089E-12	3.0306E-10
23	1	188	0.869	2.0767E+03	7.0458E-13	1.5132E-10
24	1	191	0.868	3.9625E+04	1.3430E-11	2.8828E-09
25	1	205	0.862	1.3071E+04	4.3697E-12	9.3155E-10

Table 2.5:Radiative data for M2 transitions in W LXIX.

S No.	Transition		λ_{ji} (in Å)	A_{ji} (in s ⁻¹)	f_{ij}	S_{ij} (in a.u.)
	Lower Level(i)	Upper Level(j)				
1	1	4	7.216	1.4866E+07	5.8026E-07	9.7537E-02
2	1	8	4.000	4.1941E+05	5.0294E-09	1.4396E-04
3	1	13	3.826	3.4074E+05	3.7388E-09	9.3671E-05
4	1	16	2.687	1.6275E+03	8.8054E-12	7.6385E-08
5	1	31	1.127	3.6011E+09	3.4295E-06	2.1971E-03
6	1	33	1.115	5.0921E+10	4.7423E-05	2.9378E-02
7	1	35	1.105	2.5055E+10	2.2940E-05	1.3852E-02
8	1	41	1.045	1.4425E+04	1.1814E-11	6.0350E-09
9	1	50	1.019	1.2719E+06	9.9000E-10	4.6861E-07
10	1	56	1.013	1.1477E+07	8.8288E-09	4.1059E-06
11	1	59	1.010	3.3542E+06	2.5651E-09	1.1825E-06
12	1	65	0.994	2.0481E+05	1.5182E-10	6.6785E-08
13	1	66	0.993	4.1171E+06	3.0455E-09	1.3355E-06
14	1	75	0.986	4.2403E+07	3.0886E-08	1.3234E-05
15	1	78	0.984	6.3950E+04	4.6368E-11	1.9732E-08
16	1	82	0.981	1.4512E+06	1.0474E-09	4.4272E-07
17	1	89	0.976	3.7450E+07	2.6748E-08	1.1128E-05
18	1	94	0.975	2.1231E+07	1.5117E-08	6.2599E-06
19	1	125	0.949	3.3600E+06	2.2665E-09	8.6549E-07
20	1	130	0.940	1.7160E+08	1.1360E-07	4.2178E-05
21	1	136	0.908	4.6777E+02	2.8913E-13	9.6847E-11
22	1	144	0.901	6.6448E+03	4.0397E-12	1.3200E-09
23	1	145	0.892	7.0367E+02	4.2010E-13	1.3358E-10
24	1	148	0.890	1.7217E+04	1.0229E-11	3.2285E-09
25	1	164	0.879	2.9454E+02	1.7067E-13	5.1892E-11
26	1	169	0.875	1.8511E+04	1.0621E-11	3.1821E-09
27	1	173	0.874	1.5186E+01	8.6975E-15	2.5986E-12
29	1	177	0.869	2.1425E+09	1.2142E-06	3.5705E-04
30	1	189	0.866	2.6775E+10	1.5063E-05	4.3814E-03

2.9 REFERENCES

- [1] G. Tachiev, C. Froese Fischer, Breit-Pauli energy levels and transition rates for the carbonlike sequence, *Can. J. Phys.* 79 (2001) 955–976. <https://doi.org/10.1139/cjp-79-7-955>.
- [2] A. Al-Modlej, R.A.B. Alraddadi, N. Ben Nessib, Energy levels and oscillator strengths for carbon isoelectronic sequence from C I to Ne V, *Eur. Phys. J. Plus.* 133 (2018). <https://doi.org/10.1140/epjp/i2018-12192-9>.
- [3] P.R. Young, U. Feldman, A. Lobel, Forbidden and intercombination lines of RR Telescopii: Wavelength measurements and energy levels, *Astrophys. Journal, Suppl. Ser.* 196 (2011). <https://doi.org/10.1088/0067-0049/196/2/23>.
- [4] J.P. Mosnier, E.T. Kennedy, J.M. Bizau, D. Cubaynes, S. Guilbaud, C. Blancard, B.M. McLaughlin, Photoionization cross-sections of carbon-like $n+$ near the k-edge (390–440 eV), *Atoms.* 9 (2021) 1–18. <https://doi.org/10.3390/atoms9020027>.
- [5] W.D. Chen, J. Xiao, Y. Shen, Y.Q. Fu, F.C. Meng, C.Y. Chen, B.H. Zhang, Y.J. Tang, R. Hutton, Y. Zou, Precise studies on resonant energies of the first intershell (KLL) dielectronic recombination processes for He- up to O-like xenon, *Phys. Plasmas.* 15 (2008). <https://doi.org/10.1063/1.2967486>.
- [6] U. Feldman, W. Curdt, E. Landi, K. Wilhelm, Identification of Spectral Lines in the 500–1600 Å Wavelength Range of Highly Ionized Ne, Na, Mg, Ar, K, Ca, Ti, Cr, Mn, Fe, Co, and Ni Emitted by Flares ($T_e \geq 3 \times 10^6$ K) and Their Potential Use in Plasma Diagnostics, *Astrophys. J.* 544 (2000) 508–521. <https://doi.org/10.1086/317203>.
- [7] J.M. Bizau, D. Cubaynes, S. Guilbaud, M.M. Al Shorman, M.F. Gharaibeh, I.Q. Ababneh, C. Blancard, B.M. McLaughlin, K-shell photoionization of O^+ and O^{2+} ions: Experiment and theory, *Phys. Rev. A - At. Mol. Opt. Phys.* 92 (2015) 1–14. <https://doi.org/10.1103/PhysRevA.92.023401>.
- [8] K.P. Dere, G. Del Zanna, P.R. Young, E. Landi, R.S. Sutherland, CHIANTI—An Atomic Database for Emission Lines. XV. Version 9, Improvements for the X-Ray Satellite Lines, *Astrophys. J. Suppl. Ser.* 241 (2019) 22. <https://doi.org/10.3847/1538-4365/ab05cf>.

-
- [9] J.K. Rudolph, S. Bernitt, S.W. Epp, R. Steinbrügge, C. Beilmann, G. V. Brown, S. Eberle, A. Graf, Z. Harman, N. Hell, M. Leutenegger, A. Müller, K. Schlage, H.C. Wille, H. Yavaş, J. Ullrich, J.R. Crespo López-Urrutia, X-ray resonant photoexcitation: Linewidths and energies of $K\alpha$ transitions in highly charged Fe ions, *Phys. Rev. Lett.* 111 (2013) 1–6. <https://doi.org/10.1103/PhysRevLett.111.103002>.
- [10] B. Edlé, Comparison of theoretical and experimental level values of the $n = 2$ configurations in the nitrogen isoelectronic sequence, *Phys. Scr.* 30 (1984) 125–145. <https://doi.org/10.1088/0031-8949/30/2/007>.
- [11] J.Y. Liao, S.N. Zhang, Y. Yao, Wavelength measurements of k transitions of oxygen, neon, and magnesium with X-ray absorption lines, *Astrophys. J.* 774 (2013). <https://doi.org/10.1088/0004-637X/774/2/116>.
- [12] K.J. McCarthy, N. Tamura, S.K. Combs, R. Garcia, J. Hernández Sánchez, M. Navarro, N. Panadero, I. Pastor, A. Soletto, Identification of S VIII through S XIV emission lines between 17.5 and 50 nm in a magnetically confined plasma, *Phys. Scr.* 93 (2018). <https://doi.org/10.1088/1402-4896/aaa22c>.
- [13] M. Lestinsky, N.R. Badnell, D. Bernhardt, D. Bing, M. Grieser, M. Hahn, J. Hoffmann, B. Jordon-Thaden, C. Krantz, O. Novotný, D.A. Orlov, R. Repnow, A. Shornikov, A. Müller, S. Schippers, A. Wolf, D.W. Savin, Electron-ion recombination of Mg^{6+} forming Mg^{5+} and of Mg^{7+} forming Mg^{6+} : Laboratory measurements and theoretical calculations, *Astrophys. J.* 758 (2012). <https://doi.org/10.1088/0004-637X/758/1/40>.
- [14] Y.A. Podpaly, J.D. Gillaspay, J. Reader, Y. Ralchenko, EUV measurements of Kr XXI-Kr XXXIV and the effect of a magnetic-dipole line on allowed transitions, *J. Phys. B At. Mol. Opt. Phys.* 47 (2014). <https://doi.org/10.1088/0953-4075/47/9/095702>.
- [15] E. Träbert, M. Grieser, R. Von Hahn, C. Krantz, R. Repnow, A. Wolf, M1 and E2 decay-dependent lifetime of the lowest $1S\ 0$ level in C-like ions up to Ne^{4+} measured at a heavy-ion storage ring, *New J. Phys.* 14 (2012) 0–11. <https://doi.org/10.1088/1367-2630/14/2/023061>.

-
- [16] K. Wang, D.F. Li, H.T. Liu, X.Y. Han, B. Duan, C.Y. Li, J.G. Li, X.L. Guo, C.Y. Chen, J. Yan, Systematic calculations of energy levels and transition rates of C-like Ions with $Z = 13-36$, *Astrophys. Journal, Suppl. Ser.* 215 (2015) 1–14. <https://doi.org/10.1088/0067-0049/215/2/26>.
- [17] N.W. Zheng, T. Wang, Systematical study on the ionization potential of excited states in carbon-like sequence, *Chem. Phys. Lett.* 376 (2003) 557–565. [https://doi.org/10.1016/S0009-2614\(03\)01021-2](https://doi.org/10.1016/S0009-2614(03)01021-2).
- [18] K.M. Aggarwal, F.P. Keenan, A.Z. Msezane, Oscillator strengths for transitions in C-like ions between K XIV and MN XX, *Astron. Astrophys.* 401 (2003) 377–383. <https://doi.org/10.1051/0004-6361:20030117>.
- [19] J.E. Sansonetti, W.C. Martin, Handbook of basic atomic spectroscopic data, *J. Phys. Chem. Ref. Data.* 34 (2005) 1559–2259. <https://doi.org/10.1063/1.1800011>.
- [20] G.C. Rodrigues, P. Indelicato, J.P. Santos, P. Patté, F. Parente, Systematic calculation of total atomic energies of ground state configurations, *At. Data Nucl. Data Tables.* 86 (2004) 117–233. <https://doi.org/10.1016/j.adt.2003.11.005>.
- [21] B.C. Fawcett, Wavelengths and classifications of emission energy levels for the above isoelectronic, 164 (1975) 135–164. <https://doi.org/10.1103/PhysRevA.88.042504>.
- [22] C. Chen, Energies, radial expectation values, hyperfine structures of the ground state and highly excited states for C and O^{2+} , *Int. J. Mod. Phys. B.* 34 (2020). <https://doi.org/10.1142/S0217979220501970>.
- [23] C. Nazé, S. Verdebout, P. Rynkun, G. Gaigalas, M. Godefroid, P. Jönsson, Isotope shifts in beryllium-, boron-, carbon-, and nitrogen-like ions from relativistic configuration interaction calculations, *At. Data Nucl. Data Tables.* 100 (2014) 1197–1249. <https://doi.org/10.1016/j.adt.2014.02.004>.
- [24] H.L. Zhang, C.J. Fontes, Relativistic distorted-wave collision strengths and oscillator strengths for the 185 $\Delta n=0$ transitions with $n=2$ in C-like ions with $9 \leq Z \leq 54$, *At. Data Nucl. Data Tables.* 63 (1996) 275–314. <https://doi.org/10.1006/adnd.1996.0014>.

-
- [25] H.L. Zhang, C.J. Fontes, Relativistic distorted-wave collision strengths and oscillator strengths for the 185 $\Delta n=0$ transitions with $n=2$ in the 67 C-like ions with $26 \leq Z \leq 92$, *At. Data Nucl. Data Tables.* 101 (2015) 41–142. <https://doi.org/10.1016/j.adt.2014.08.001>.
- [26] M.F. Gu, Energies of $1s22lq$ ($1 \leq q \leq 8$) states for $Z \leq 60$ with a combined configuration interaction and many-body perturbation theory approach, *At. Data Nucl. Data Tables.* 89 (2005) 267–293. <https://doi.org/10.1016/j.adt.2005.02.004>.
- [27] D. Ray, P.K. Mukherjee, Radiative Transitions in Highly-Stripped Carbon-Like Ions, 1995 *Phys. Scr.* 51 81. <https://doi.org/10.1088/0031-8949/51/1/013>
- [28] C.C. Sang, Z. Bin Chen, Y. Sun, X.Z. Shen, F. Hu, J. Ma, X.L. Wang, Hyperfine structure and 2s-2p transition in C-like Fe, Co and Ni, *J. Electron Spectros. Relat. Phenomena.* 230 (2019) 26–32. <https://doi.org/10.1016/j.elspec.2018.11.001>.
- [29] G. V. Shpatakovskaya, Patterns of the Ionization Potentials of Multicharged Ions of Heavy Elements, *JETP Lett.* 114 (2021) 737–741. <https://doi.org/10.1134/S0021364021240073>.
- [30] C.F. Fischer, H.P. Saha, Multiconfiguration hartree-fock results with breit-pauli corrections for transitions in the carbon sequence, *Phys. Scr.* 32 (1985) 181–194. <https://doi.org/10.1088/0031-8949/32/3/004>.
- [31] C.F. Fischer, G. Tachiev, Breit-Pauli energy levels, lifetimes, and transition probabilities for the beryllium-like to neon-like sequences, *At. Data Nucl. Data Tables.* 87 (2004) 1–184. <https://doi.org/10.1016/j.adt.2004.02.001>.
- [32] P. Palmeri, P. Quinet, C. Mendoza, M.A. Bautista, J. García, M.C. Witthoeft, T.R. Kallman, Atomic decay data for modeling K lines of iron peak and light odd-Z elements, *Astron. Astrophys.* 543 (2012) 1–9. <https://doi.org/10.1051/0004-6361/201219438>.
- [33] P. Jönsson, G. Gaigalas, P. Rynkun, L. Radžiute, J. Ekman, S. Gustafsson, H. Hartman, K. Wang, M. Godefroid, C.F. Fischer, I. Grant, T. Brage, G. Del Zanna, Multiconfiguration dirac-hartree-fock calculations with spectroscopic accuracy: Applications to astrophysics, *Atoms.* 5 (2017) 1–24. <https://doi.org/10.3390/atoms5020016>.
-

-
- [34] F. Li, G.Y. Liang, G. Zhao, Soft X-ray emission lines of S VII-S XIV in Procyon, *Astrophys. J.* 762 (2013). <https://doi.org/10.1088/0004-637X/762/1/53>.
- [35] B. Tu, J. Xiao, K. Yao, X. Wang, Y. Shen, Y. Yang, D. Lu, L. Huang, C. Zhen, Y. Fu, B. Wei, R. Hutton, Y. Zou, Photorecombination studies of highly charged tungsten ions at Shanghai EBIT, *J. Phys. Conf. Ser.* 875 (2017). <https://doi.org/10.1088/1742-6596/875/2/012003>.
- [36] B. Tu, J. Xiao, Y. Shen, Y. Yang, D. Lu, T.H. Xu, W.X. Li, C.Y. Chen, Y. Fu, B. Wei, C. Zheng, L.Y. Huang, R. Hutton, X. Wang, K. Yao, Y. Zou, B.H. Zhang, Y.J. Tang, KLL dielectronic recombination resonant strengths of He-like up to O-like tungsten ions, *Phys. Plasmas.* 23 (2016). <https://doi.org/10.1063/1.4948420>.
- [37] M.B. Trzhaskovskaya, V.K. Nikulin, Radiative recombination and photoionization data for tungsten ions. Electron structure of ions in plasmas, *Atoms.* 3 (2015) 86–119. <https://doi.org/10.3390/atoms3020086>.
- [38] H. Liu, G. Jiang, F. Hu, C.K. Wang, Z. Bin Wang, J.M. Yang, Intercombination transitions of the carbon-like isoelectronic sequence, *Chinese Phys. B.* 22 (2013). <https://doi.org/10.1088/1674-1056/22/7/073202>.
- [39] P. Beiersdorfer, M.J. May, J.H. Scofield, S.B. Hansen, Atomic physics and ionization balance of high-Z Ions: Critical ingredients for characterizing and understanding high-temperature plasmas, *High Energy Density Phys.* 8 (2012) 271–283. <https://doi.org/10.1016/j.hedp.2012.03.003>.
- [40] U. Feldman, J.F. Seely, E. Landi, Y. Ralchenko, Bright EUV lines emitted by highly ionized tungsten ions as diagnostic indicators of the tungsten transport in ITER core plasmas ($T_e > 7$ keV), *Nucl. Fusion.* 48 (2008). <https://doi.org/10.1088/0029-5515/48/4/045004>.
- [41] A.E. Kramida, J. Reader, Ionization energies of tungsten ions: W²⁺ through W⁷¹⁺, *At. Data Nucl. Data Tables.* 92 (2006) 457–479. <https://doi.org/10.1016/j.adt.2006.03.002>.
- [42] J. Huang, G. Jiang, Q. Zhao, Ground-state ionization potentials for lithium through neon isoelectronic sequences with $Z = 37-82$, *Chinese Phys. Lett.* 23 (2006) 69–72. <https://doi.org/10.1088/0256-307X/23/1/021>.
-

- [43] U.I. Safronova, Z.B. Rudzikas, Perturbation theory for the relativistic energy of atomic systems, *J. Phys. B At. Mol. Phys.* 9 (1976) 1989–2001. <https://doi.org/10.1088/0022-3700/9/12/011>.
- [44] T.A. Carlson, C.W. Nestor, N. Wasserman, J.D. McDowell, Calculated ionization potentials for multiply charged ions, *At. Data Nucl. Data Tables.* 2 (1970) 63–99. [https://doi.org/10.1016/S0092-640X\(70\)80005-5](https://doi.org/10.1016/S0092-640X(70)80005-5).
- [45] I. P. Grant, B. J. McKenzie, P. H. Norrington, D. F. Mayers, and N. C. Pyper, An atomic multiconfigurational Dirac-Fock package, *Comput. Phys. Commun.* 21 (1980) 207–231. [https://doi.org/10.1016/0010-4655\(80\)90041-7](https://doi.org/10.1016/0010-4655(80)90041-7).
- [46] R. Sharma and R. Paijwar, Spectroscopic study of EUV and SXR spectral lines with partition function and level population of W LVI. *Can. J. Phys.* 99 (2021) 657–669. <https://doi.org/10.1139/cjp-2020-0497>.
- [47] M. F. Gu, The flexible atomic code. *Can. J. Phys.* 86 (2008) 675–689. <https://doi.org/10.1139/p07-197>.
- [48] A. Kramida, Yu. Ralchenko, J. Reader, and NIST ASD Team, <https://physics.nist.gov/asd> for NIST Atomic Spectra Database (ver. 5.6.1) (2019).

CHAPTER 3

SPECTROSCOPIC STUDY OF EUV AND SXR SPECTRAL LINES WITH PARTITION FUNCTION AND LEVEL POPULATION OF W LVI

- In this we have included the complete spectroscopic data and a detailed theoretical investigation of tungsten and K-like W (WLVI) based on the fully relativistic multi-configuration Dirac-Fock (MCDF) method.
- Relativistic corrections, QED (Quantum electrodynamics) and Breit corrections have been used in our computation.
- Energy levels and radiative data for multipole transitions i.e. electric dipole (E1), electric quadrupole (E2), magnetic dipole (M1) and magnetic quadrupole (M2) within lowest 142 fine structure levels and soft x-ray transition (SXR) and extreme ultraviolet transitions (EUV) from higher excited states to ground state have been predicted.
- Data with energy levels compiled by NIST and other available results in literature and small discrepancies found with them have been discussed.
- Furthermore, the relative population for first five excited states, partition function and thermodynamic quantities for both W LVI and studied their variations with temperature have also presented.
- Atomic data of W LVI, which discussed in this chapter may be useful in identification and analysis of spectral lines from various astrophysical and fusion plasma sources and also beneficial in plasma modeling.

3.1 INTRODUCTION

In past few decades, numerous articles of W LVI available in literature using different theoretical method as well as experimental techniques are limited to only few energy levels [6-14]. Beiersdorfer et al. [15] have presented detailed description of tungsten and gold ions including W LVI. Trzhaskovskaya et al. [16] have calculated radiative recombination and photoionization cross-sections as well as radiated power loss coefficients for 54 tungsten ions W^{6+} - W^{71+} including W LVI by using Dirac-Fock electron wave functions. Priti et al. [17] have reported electron impact excitation for M and L-shell transitions for tungsten ions W^{44+} - W^{66+} including W LVI with the help of fully relativistic distorted wave method. Guo et al. [18] have presented wavelengths and transition probabilities for transitions in ground state configuration of tungsten and other ions including W LVI by using second order relativistic many body perturbation theory (RMBPT) and relativistic configuration interaction (RCI). Dipti et al. [19] have studied electron impact excitation and polarization for Fe-like W to Al-like W ions by using fully relativistic distorted wave method. Xu et al. [20] have listed excitation energies and wavelengths for nine isoelectronic sequence of tungsten ions for lowest few levels by utilizing MCDF method. Fischer et al. [21] have reported excitation energies of tungsten ions for ground configurations by using GRASP2K code. Zhao et al. [22] have reported atomic data of ground configurations $3d^k$ ($k=1-9$) for highly charged ions with nuclear charge ranging from 72 to 83 by employing multi-configuration Dirac-Hartree-Fock (MCDHF) method. But most of the work available in literature is only for few levels of W LVI and there is scarcity in complete, consistent, and precise atomic data for this ion. Therefore, in present work, our fundamental objective is to present the energies for energy levels of higher excited states along with radiative data for multipole transitions (E1, E2, M1 & M2) for WLVI.

The partition function has several applications such as study of thermodynamic parameters of ions and neutral atoms, diagnosis and modeling of plasmas, computation of levels in stellar and inter-stellar plasmas with the help of Saha equation of state. So, partition function and thermodynamic quantities plays substantial roles in the study of plasmas. Due to limitations, it has become very cumbersome for experimentalist to consider large number of excited states in their calculations of partition function

specifically at higher temperatures. Therefore, in past few decades, several theoretical methods and techniques have been developed for implementation in the study of partition function [23-27]. Several methods in the literature have been adopted criteria of cut-off condition for simplicity and according to availability of data and limitations. Some tables such as NASA, Russian and Drawin-Felenbok available in literature have taken into account only few lowest states in their calculations [28-31]. Planck-Larkin partition function (PLPF) have also adopted in the study of high temperature plasmas in past. But this give total partition functions near to zero at high temperature and hence violates the basic condition that total partition function of the system cannot be less than unity. In last few years, another model comes into picture called a 3-group model has been presented in the literature [32]. This method divides the considered levels in exactly three groups, namely, ground state, middle levels and higher excited levels. This method does not give the contribution of individual level to partition function and may provide inaccurate results. We have overcome above difficulties and limitations in our fine structure model.

3.2 THEORETICAL METHOD

3.2.1 MCDF method and Flexible atomic code: Same procedure as in chapter 2.

3.3 RESULTS AND DISCUSSIONS

3.3.1 Energy levels

In present paper, we have listed the lowest 142 fine structure levels belonging to the configurations $3s^23p^63d$, $3s^23p^53d^2$ and $3s^23p^63d^3$ from GRASP and FAC both in table 1. In our calculations, we included 37 configurations, namely $3s^23p^63d$, $3s^23p^53d^2$, $3s3p^63d^2$, $3s^23p^43d^3$, $3s3p^53d^3$, $3p^63d^3$, $3s^23p^33d^4$, $3s3p^43d^4$, $3p^53d^4$, $3s^23p^64l$ ($l=0-3$), $3s3p^63d4l$ ($l=0-3$), $3s^23p^53d4l$ ($l=0-3$), $3s^13p^53d^24l$ ($l=0-3$), $3s^23p^43d^24l$ ($l=0-3$), $3p^63d^24l$ ($l=0-3$) and $3p^53d^34l$ ($l=0-3$).

From Table 3.1, we observed that contribution of QED is less than Breit and very small for levels 2, 42 and 63. So in case of W LVI, QED effects are less significant for some levels. We have compared our calculated data from GRASP and FAC with NIST [14] and the maximum discrepancy of GRASP and FAC results with results compiled by

NIST is 0.45 % and 0.25 % resp. for $3s^23p^53d^2 (^3F_2)^2G_{7/2}$. In Table 3.1, we have shown the percentage difference of GRASP with FAC under the column “ ΔE ”.

$$\Delta E = \frac{|E_{FAC} - E_{GRASP}|}{E_{FAC}} \times 100\% \quad (3.1)$$

The maximum value of ΔE is 0.43 %. This shows that our results from there two independent calculations for the majority of the levels are in reasonable agreement and verifies that our results are accurate. The little differences for some levels in GRASP and FAC energies mainly arises due to different ways of calculations of electron wave functions for radial orbitals and recoupling schemes of angular parts.

We have also compared our results with other available results in literature and discussed discrepancy with them in the following sections.

(a) *Comparison with Quinet [13]*

P. Quinet [13] have calculated fine structure level energies of only first excited state $3s^23p^63d^2 D_{5/2}$ by using fully relativistic MCDF method. There is very small discrepancy of 0.008 Ryd. between our GRASP results and Quinet [13] and this shows that additional configurations in calculations from same method have not introduced correlation effect on $3s^23p^63d^2 D_{5/2}$.

(b) *Comparison with Priti et al. [16]*

Priti et al. [16] have presented excitation energies of two levels $3s^23p^53d^2 {}^2F_{5/2}$ and $3s^23p^53d^2 {}^2D_{3/2}$ which are levels 42 and 63 in Table 3.1. The discrepancy of our GRASP results from Priti et al. [16] is 0.0977 and 0.24 Ryd. for $3s^23p^53d^2 {}^2D_{3/2}$ and $3s^23p^53d^2 {}^2F_{5/2}$ respectively. The reason behind small discrepancy may be due to different configurations and technique adopted by Priti et al. [16]. They have included 6 configurations $3s^23p^63d$, $3s^23p^53d^2$, $3s3p^63d^2$, $3p^63d^3$, $3s^23p^54p4d$ and $3s3p^53d^3$ for the initial and final target state wave-functions while in our calculations we have taken 37 configurations by considering single, double and triple (SDT) excitations from 3s and 3p orbitals and one electron excitation from 3d to $n = 4$ orbitals. Our GRASP results are close to results from both Priti et al. [16] and ensure the reliability and authenticity of excitation energies of higher excited states.

(c) *Comparison with Clementson et al. [42]*

Clementson et al. [42] have presented theoretically calculated and experimentally measured energies for W LVI. They have performed the experiment by employing superEBIT at Lawrence Livermore National Laboratory (LLNL). For theoretical calculation, they have adopted GRASP and FAC. The discrepancy of our GRASP results from their experimental, FAC and GRASP is 0.09, 0.055 and 0.139 Ryd. respectively. This difference of our GRASP results from their GRASP and FAC is mainly due to choice of different configuration set. In their FAC calculations, they have opted $2s^2 2p^6 3l^9$, $2s^2 2p^6 3l^8 4l$ ($l=0-3$), $2s^2 2p^6 3l^8 5l$ ($l=0-3$), $2s^2 2p^5 3s^2 3p^6 3dnl$ ($n=3, 4, 5$; $l = 0$ to $n-1$) and $2s 2p^6 3s^2 3p^6 3dnl$ ($n=3, 4, 5$; $l = 0$ to $n-1$) while in their GRASP calculations, they choose $3s^2 3p^6 3d$, $3s^2 3p^5 3d^2$ and $3s 3p^6 3d^2$. So it is clearly observed that they have included only 3 configurations in GRASP and have missed some important configurations which have significant contribution in the total atomic wave function of $3s^2 3p^5 3d^2$ while in FAC, they have taken large number of configurations which is not possible in GRASP as it will increase computational time and make calculations cumbersome with very less improvement in excitation energies of higher excited states. So, we have considered important configurations with SDT excitations in GRASP and FAC both but in future it will be a topic of future research that which configurations containing more than 5 electrons in 3d orbital will be more contributing. Hence, we found that our results are in good agreement with experimental and theoretical results of Clementson et al. [42] with minimal difference.

(d) *Comparison with Guo et al. [18]*

Guo et al. [18] have presented excitation energies only for two fine-structure levels of $3s^2 3p^6 3d$ configuration for WLVI using second order relativistic many body perturbation theory (RMBPT) and relativistic configuration interaction (RCI). The small discrepancy of our GRASP results with RMBPT results of Guo et al. [18] is 0.025 Ryd. for level 2. This is due to the reason that in their RMBPT calculations, they have taken single excitation up to $n = 125$ and double excitations with one electron to $n = 65$ and other electron to $n = 125$ but in GRASP, it is not possible to include so many configurations as we have stated in previous section.

But the discrepancy of our GRASP results with their RCI results is 0.001 for level 2. Guo et al. [18] have only included interaction within $n = 3$ orbitals but still our GRASP energy and their GRASP energy for this level is exactly same which implies that effect of correlations from other configurations included by us is almost negligible on level 2 and similar effect is also shown in section 3.3.1.

(e) *Comparison with Fischer et al. [21]*

Fischer et al. [21] have also listed excitation energy only for first excited state of configuration $3s^23p^63d\ ^2D_{5/2}$ by using GRASP2K. They have consider core-valence and core-core correlations by taking single and double electron excitations from $n = 2$ orbitals but they have included orbitals up to $n = 6$ while in our calculations we have considered SDT excitations within $n=3$ and single electron excitation from $n = 3$ orbitals to $n = 4$. Therefore, there is a small discrepancy of 0.02 Ryd. of our GRASP results with Fischer et al. [21] for level 2 which shows that our results matches well with results reported by Fischer et al. [21].

(f) *Comparison with Zhao et al. [22]*

Zhao et al. [22] have also reported excitation energy for ground state configuration $3s^23p^63d$ using second order relativistic many body perturbation theory (RMBPT) and relativistic configuration interaction (RCI). The discrepancy of our GRASP results with RMBPT results of Zhao et al. [22] is 0.025 Ryd. for level 2 which is very small. This can be due to the reason that in their RMBPT calculations, they have taken single excitation up to $n = 125$ and double excitations with one electron to $n = 65$ and other electron to $n = 125$ But the discrepancy of our GRASP results with their RCI results is 0.016 for level 2 which is less as compared to discrepancy with their RMBPT results because they have only included interaction within $n = 3$ orbitals but not considered correlation with higher orbitals. So it is observed that consideration of correlations by taking one excitations to higher orbitals is effecting the fine structure energies of ground state configuration. But since the difference is very small, therefore, inclusion of SDT excitations within $n = 3$ and single excitations to higher orbitals is necessary for correlation for higher excited states.

So from above discussions, we finally deduced that inclusion of large configuration set is not effecting too much fine structure splitting of $3s^23p^63d$ and all fully relativistic codes and methods are almost producing nearly same excitation energies for low lying levels for small configuration set.

3.3.2 Radiative data

Transition wavelengths (λ_{ij} in \AA), line strengths (S_{ij} in a.u.), radiative rates (A_{ij} in s^{-1}) and oscillator strengths (f_{ij} , dimensionless) are reported from ground state for E1, E2, M1 and M2 in Tables 3.2 to 3.5 respectively. We have found 29 E1, 68 E2, 51 M1 and 38 M2 soft x-ray transition and 1 E2 and 1M1 extreme ultraviolet transitions from higher excited states to ground state. The transition data of E1, E2, M1 and M2 transitions among lowest 142 levels is provided as supplementary material. In practical applications that forbidden transitions M1 and E2 rates are usually summed over as $A(E2+M1)$ since they arise from the same relativistic operator, and that $A(M1)$ is generally higher. In table 6, we have compared our GRASP transition wavelengths from theoretically calculated [19, 42] and experimentally measured wavelengths [19]. We have also compared our calculated oscillator strengths with theoretically calculated oscillator strengths [19]. We found that our transition data compared in Table 3.6 is in good agreement with Dipti et al. [19] and Clementson et al. [42] with a very small difference. This shows that our presented radiative data for W LVI is reliable and can be used further for identification of spectral lines observed experimentally.

3.4 PARTITION FUNCTION AND THERMODYNAMIC PARAMETERS

In Table 3.7, we have presented partition function (Q), internal energy and specific heat for K-like W respectively. From Table 3.7, we can see that as temperature increases, partition function and thermodynamic quantities increases which also satisfies basic requirement of partition function.

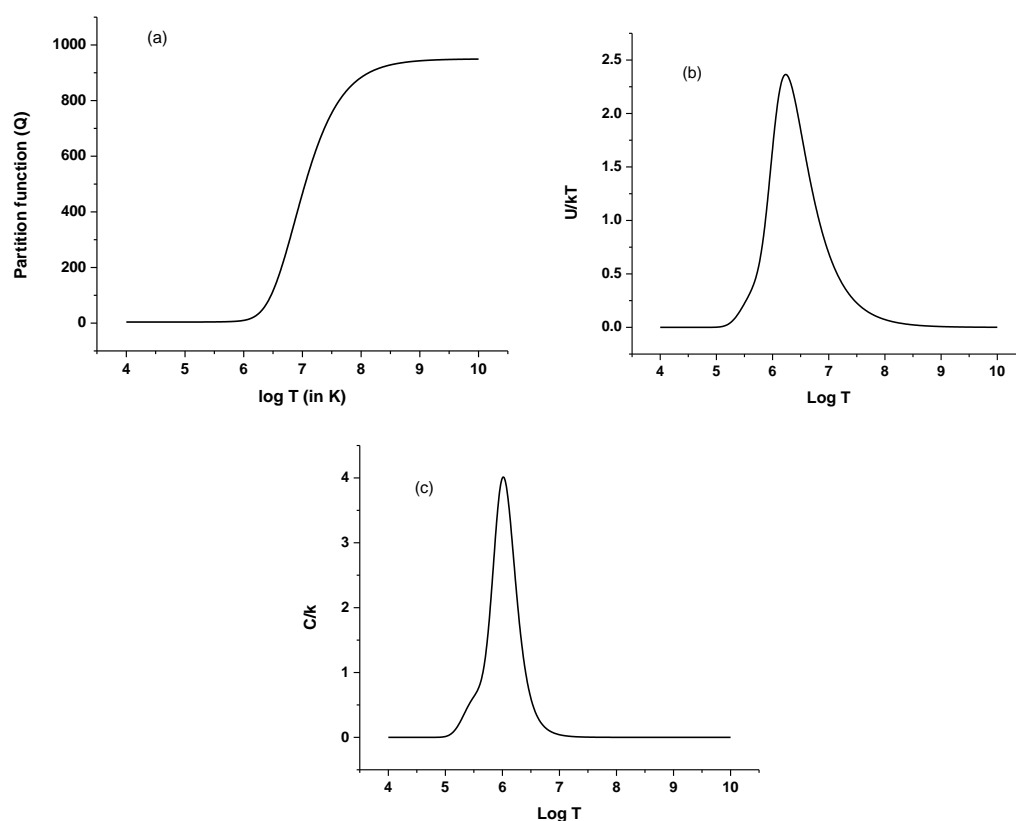


Figure 3.1: Variation of (a) partition function (b) internal energy (c) Specific heat with temperature for K-like W.

In Figure 3.1(a)-(c), we have shown the variation of partition function, internal energy and specific heat as a function of thermodynamic temperature. It is observed that change in partition function is almost negligible same below 10^6 K for K-like W but after that increases rapidly due to the contribution of higher excited states. We have predicted three maxima peaks for both internal energy and specific heat for both O-like W in Figure 3.1(b) and 3.1(c) respectively. It also predicted that the position of highest peak of O-like W for internal energy and specific heat is nearly at the same position but width of internal energy peak is more than that of specific heat.

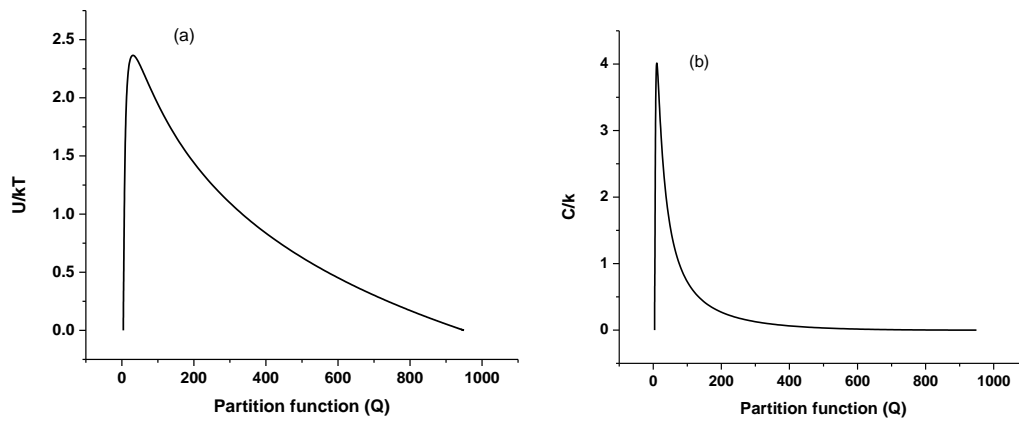


Figure 3.2: Variation of (a) internal energy (b) Specific heat with partition function for K-like W.

In Figure 3.2, we have plotted the variation of internal energy and specific heat with partition function for temperature 10^4 - 10^{10} K for K-like W. We predicted that internal energy and specific heat attains maximum value approx. at the same value of partition function but fall of specific heat is very rapid as compared to internal energy and similarly rise of specific heat is also fast as compared to that of internal energy.

The partition function can also be used in the determination of probability of occupancy of levels and also line intensity of spectral lines. Therefore, we have studied population of levels relative to ground state in the next section

3.5 RELATIVE POPULATION

We have calculated population of first five excited states relative to ground state for K-like W for temperature ranges from 10^4 - 10^{10} K by employing Boltzmann statistics. In Figure 3.3(a) to 3.3(e), we have plotted variation of relative population of first five excited levels with temperature. From Figure 3.3, we can see that the for 2nd to 5th excited states below 10^6 K temperature population of is almost negligible as compared to ground state. But for first excited state, the temperature at which relative population is negligible is same $10^{5.5}$ K. From Figure 3.3, it is also evident that relative population of fifth excited state of K-like W is highest above 10^7 K. Since relative population of first five excited states is large above 10^6 K, therefore we can achieve population inversion for all five excited states for K-like W above 10^6 .

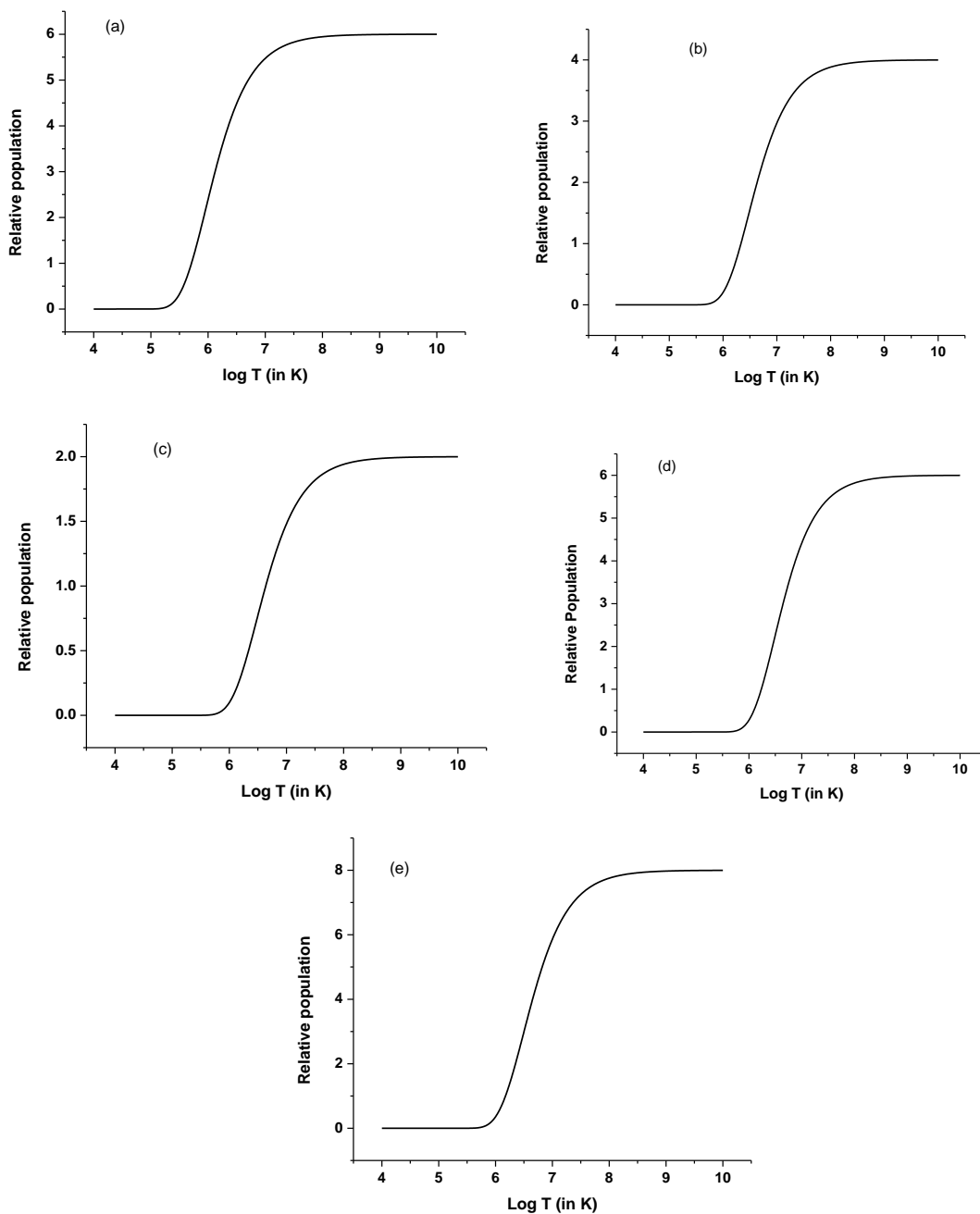


Figure 3.3: Variation of relative population of (a) first (b) second (c) third (d) fourth (e) fifth excited state with temperature for K-like W.

3.6 CONCLUSION

In this current paper, we have presented energy levels and radiative data for E1, E2, M1 and M2 transitions amongst lowest level 142 fine structure levels for K-like W. GRASP and FAC two independent codes are executed in calculations and discrepancy in results

from both codes are provided. The discrepancy of our GRASP energies with available theoretical and experimental data in literature is discussed in detailed manner. We have also predicted SXR and EUV transitions from ground state in W LVI and found most of the transition towards ground state lie in SXR region. Further, we have also studied variation of partition function and thermodynamic quantities within temperature range 10^4 - 10^{10} K. We have also shown the variation of relative population of first five excited states w.r.t ground state using Boltzmann statistics and discussed their variations with temperature

Overall, we conclude that our results are extensive and new and will be useful in identification and analysis of spectral lines in experimental spectra, microscopic imaging and in plasma physics.

Table 3.1: Energies (in Ryd.) of lowest 142 fine structure levels of W LVI. a-[14], b-[13], c-[16], d-experimental [42], e- FAC [42], f- GRASP[42], g-RMBPT[18], h-RCI[18], i-[21], j-RCI[22], k- RMBPT[22], l-[43].

LEVELS	CONFIGURATIONS	PARITY	DC	BREIT	QED	TOTAL	FAC	Others	ΔE
1	$3s^2 3p^6 3d^1 ({}^2D_1) {}^2D_{3/2}$	Even	0.0000	-----	-----	0.0000	0	0.000	0.36
2	$3s^2 3p^6 3d^1 ({}^2D_1) {}^2D_{5/2}$	Even	5.8279	-0.1440	0.00006	5.6840	5.7044	5.709 ^a 5.692 ^b 5.709 ^g 5.683 ^h 5.704 ⁱ 5.700 ^j 5.709 ^k 5.708 ^l	0.20
3	$3s^2 3p^5 3d^2 ({}^3F_2) {}^4F_{3/2}$	Odd	18.9125	-0.0490	-0.0362	18.8273	18.7898		0.19
4	$3s^2 3p^5 3d^2 ({}^3F_2) {}^4D_{1/2}$	Odd	19.0699	-0.0684	-0.0362	18.9653	18.9289		0.20
5	$3s^2 3p^5 3d^2 ({}^3F_2) {}^4F_{5/2}$	Odd	19.4914	-0.0969	-0.0361	19.3584	19.3198		0.20
6	$3s^2 3p^5 3d^2 ({}^3F_2) {}^2G_{7/2}$	Odd	19.7178	-0.1240	-0.0361	19.5582	19.5182	19.470	0.18
7	$3s^2 3p^5 3d^2 ({}^3P_2) {}^4P_{5/2}$	Odd	21.2442	-0.0332	-0.0362	21.1748	21.1366		0.06
8	$3s^2 3p^5 3d^2 ({}^3F_2) {}^4D_{5/2}$	Odd	24.2967	-0.1940	-0.0361	24.0667	24.0520		0.07
9	$3s^2 3p^5 3d^2 ({}^3F_2) {}^4G_{9/2}$	Odd	24.7714	-0.2800	-0.0359	24.4559	24.4392		0.06
10	$3s^2 3p^5 3d^2 ({}^3F_2) {}^4F_{7/2}$	Odd	24.9369	-0.2510	-0.0360	24.6496	24.6340		0.06
11	$3s^2 3p^5 3d^2 ({}^3F_2) {}^4D_{3/2}$	Odd	25.1631	-0.2120	-0.0361	24.9154	24.8996		0.06
12	$3s^2 3p^5 3d^2 ({}^3P_2) {}^4P_{5/2}$	Odd	25.3353	-0.2320	-0.0361	25.0675	25.0518		0.32
13	$3s^2 3p^5 3d^2 ({}^3P_2) {}^4D_{7/2}$	Odd	25.6359	-0.2710	-0.0361	25.3283	25.2468		0.19

LEVELS	CONFIGURATIONS	PARITY	DC	BREIT	QED	TOTAL	FAC	Others	ΔE
14	$3s^2 3p^5 3d^2 ({}^1G_2) {}^2H_{11/2}$	Odd	25.6596	-0.3600	-0.0359	25.2632	25.3113		0.06
15	$3s^2 3p^5 3d^2 ({}^3P_2) {}^2S_{1/2}$	Odd	25.9931	-0.1810	-0.0362	25.7761	25.7599		0.06
16	$3s^2 3p^5 3d^2 ({}^1G_2) {}^2F_{7/2}$	Odd	26.4409	-0.2610	-0.0361	26.1436	26.1269		0.07
17	$3s^2 3p^5 3d^2 ({}^3P_2) {}^4D_{5/2}$	Odd	26.4977	-0.1930	-0.0362	26.268	26.2505		0.06
18	$3s^2 3p^5 3d^2 ({}^3P_2) {}^4S_{3/2}$	Odd	26.6911	-0.1610	-0.0362	26.4936	26.4765		0.07
19	$3s^2 3p^5 3d^2 ({}^1G_2) {}^2G_{9/2}$	Odd	26.8793	-0.2990	-0.0361	26.5439	26.5264		0.09
20	$3s^2 3p^5 3d^2 ({}^3P_2) {}^2D_{3/2}$	Odd	27.9527	-0.2210	-0.0357	27.6958	27.6707		0.09
21	$3s^2 3p^5 3d^2 ({}^1D_2) {}^2F_{5/2}$	Odd	28.5622	-0.2590	-0.0360	28.2676	28.2417		0.10
22	$3s^2 3p^5 3d^2 ({}^3P_2) {}^2P_{1/2}$	Odd	29.073	-0.1930	-0.0357	28.8441	28.8158		0.02
23	$3s^2 3p^5 3d^2 ({}^3F_2) {}^4G_{11/2}$	Odd	30.6462	-0.4470	-0.0358	30.1632	30.1690		0.02
24	$3s^2 3p^5 3d^2 ({}^1D_2) {}^2D_{5/2}$	Odd	31.0555	-0.3650	-0.0361	30.6542	30.6609		0.02
25	$3s^2 3p^5 3d^2 ({}^3F_2) {}^2G_{9/2}$	Odd	31.381	-0.4050	-0.0360	30.9400	30.9452		0.02
26	$3s^2 3p^5 3d^2 ({}^1D_2) {}^2F_{7/2}$	Odd	31.5175	-0.3790	-0.0359	31.1022	31.1072		0.02
27	$3s^2 3p^5 3d^2 ({}^1D_2) {}^2P_{1/2}$	Odd	31.9677	-0.3260	-0.0363	31.6055	31.6111		0.001
28	$3s^2 3p^5 3d^2 ({}^3F_2) {}^2F_{7/2}$	Odd	33.1857	-0.3700	-0.0360	32.7792	32.7795		0.01
29	$3s^2 3p^5 3d^2 ({}^1S_0) {}^2P_{3/2}$	Odd	33.7114	-0.2860	-0.0362	33.3887	33.3924		0.02
30	$3s^2 3p^5 3d^2 ({}^3F_2) {}^2D_{5/2}$	Odd	34.3384	-0.3750	-0.0356	33.9278	33.9223		0.01
31	$3s^2 3p^5 3d^2 ({}^1D_2) {}^2D_{3/2}$	Odd	34.63	-0.3210	-0.0355	34.2737	34.2710		0.31
32	$3s^2 3p^4 3d^3 ({}^4F_3) {}^6D_{3/2}$	Even	39.0056	-0.0731	-0.0723	38.8603	38.7412		0.30
33	$3s^2 3p^4 3d^3 ({}^4F_3) {}^6D_{1/2}$	Even	39.0677	-0.0946	-0.0724	38.9007	38.7845		0.31
34	$3s^2 3p^4 3d^3 ({}^4F_3) {}^6F_{5/2}$	Even	39.6263	-0.1170	-0.0726	39.4371	39.3150		0.31
35	$3s^2 3p^4 3d^3 ({}^2P_3) {}^4D_{7/2}$	Even	39.7533	-0.1490	-0.0721	39.5324	39.4099		0.32
36	$3s^2 3p^4 3d^3 ({}^4F_3) {}^4F_{3/2}$	Even	41.1739	-0.0742	-0.0721	41.0276	40.8978		0.21
37	$3s^2 3p^4 3d^3 ({}^4F_3) {}^6D_{5/2}$	Even	43.8465	-0.2230	-0.0721	43.5516	43.4623		0.21
38	$3s^2 3p^4 3d^3 ({}^4F_3) {}^6G_{9/2}$	Even	44.3709	-0.3100	-0.0719	43.9888	43.8966		0.21
39	$3s^2 3p^4 3d^3 ({}^4F_3) {}^6F_{7/2}$	Even	44.386	-0.2850	-0.0725	44.0288	43.9378		0.21
40	$3s^2 3p^4 3d^3 ({}^4F_3) {}^4F_{3/2}$	Even	44.4654	-0.2330	-0.0725	44.1598	44.0688		0.21
41	$3s^2 3p^4 3d^3 ({}^2P_3) {}^4H_{7/2}$	Even	44.7383	-0.2800	-0.0721	44.3861	44.2942		0.02
42	$3s^2 3p^5 3d^2 ({}^3F_2) {}^2F_{5/2}$	Odd	44.8664	-0.4290	-0.0067	44.4312	44.4387	44.340 44.191 ^c 44.341 ^d 44.376 ^e 44.292 ^f	0.20
43	$3s^2 3p^5 3d^2 ({}^4P_3) {}^6P_{5/2}$	Even	44.918	-0.2640	-0.0724	44.5816	44.4905		0.21
44	$3s^2 3p^4 3d^3 ({}^2G_3) {}^4G_{11/2}$	Even	45.0578	-0.3990	-0.0720	44.5872	44.4950		0.21
45	$3s^2 3p^4 3d^3 ({}^2G_3) {}^4G_{9/2}$	Even	45.1194	-0.3780	-0.0724	44.6689	44.5774		0.25

LEVELS	CONFIGURATIONS	PARITY	DC	BREIT	QED	TOTAL	FAC	Others	ΔE
46	$3s^23p^43d^3(^4F_3)^4F_{3/2}$	Even	45.3177	-0.2600	-0.0751	44.9825	44.8708		0.17
47	$3s^23p^43d^3(^2G_3)^2H_{11/2}$	Even	45.4566	-0.4200	-0.0719	44.9645	44.8864		0.21
48	$3s^23p^43d^3(^2G_3)^4H_{13/2}$	Even	45.5505	-0.4680	-0.0718	45.0108	44.9163		0.21
49	$3s^23p^43d^3(^2H_3)^4G_{5/2}$	Even	45.6964	-0.3150	-0.0753	45.3066	45.2107		0.21
50	$3s^23p^43d^3(^4F_3)^4D_{1/2}$	Even	46.1151	-0.2280	-0.0731	45.8144	45.7169		0.20
51	$3s^23p^43d^3(^4P_3)^6P_{7/2}$	Even	46.2618	-0.2900	-0.0722	45.8995	45.8066		0.22
52	$3s^23p^43d^3(^4F_3)^4F_{5/2}$	Even	46.4061	-0.2310	-0.0722	46.1025	46.0004		0.20
53	$3s^23p^43d^3(^4P_3)^6D_{9/2}$	Even	46.5724	-0.3230	-0.0721	46.1774	46.0847		0.22
54	$3s^23p^43d^3(^4F_3)^4P_{3/2}$	Even	46.8829	-0.2060	-0.0721	46.605	46.5024		0.22
55	$3s^23p^43d^3(^4F_3)^6F_{1/2}$	Even	47.1397	-0.2120	-0.0717	46.8564	46.7520		0.22
56	$3s^23p^43d^3(^4F_3)^4G_{5/2}$	Even	47.3995	-0.2770	-0.0718	47.0503	46.9447		0.22
57	$3s^23p^43d^3(^2G_3)^4F_{3/2}$	Even	47.4365	-0.2640	-0.0721	47.1000	46.9947		0.21
58	$3s^23p^43d^3(^2G_3)^2G_{7/2}$	Even	47.5023	-0.3020	-0.0721	47.1279	47.0281		0.21
59	$3s^23p^43d^3(^2G_3)^2G_{9/2}$	Even	47.7203	-0.3290	-0.0723	47.3192	47.2188		0.22
60	$3s^23p^43d^3(^2F_3)^4F_{3/2}$	Even	47.7836	-0.2730	-0.0719	47.4385	47.3326		0.18
61	$3s^23p^53d^2(^3P_2)^4D_{1/2}$	Odd	47.8654	-0.3460	-0.0074	47.512	47.4274		0.04
62	$3s^23p^53d^3(^2G_3)^4F_{5/2}$	Even	47.8812	-0.2730	-0.0719	47.5367	47.5163		0.19
63	$3s^23p^53d^2(^3F_2)^2D_{3/2}$	Odd	48.0631	-0.3880	-0.0079	47.6677	47.5782	47.502 ^a 47.570 ^c 47.497 ^d 47.605 ^e 47.767 ^f	0.04
64	$3s^23p^43d^3(^2H_3)^4G_{7/2}$	Even	48.0825	-0.3260	-0.0720	47.6844	47.6664		0.23
65	$3s^23p^53d^2(^4P_1)^4P_{1/2}$	Odd	48.1026	-0.2300	-0.0721	47.8009	47.6890		0.35
66	$3s^23p^43d^3(^4P_3)^2S_{1/2}$	Even	48.3365	-0.2230	-0.0745	48.0390	47.8716		0.16
67	$3s^23p^53d^3(^2G_3)^4H_{7/2}$	Even	48.376	-0.3200	-0.0720	47.9840	47.9081		0.17
68	$3s^23p^43d^3(^2H_3)^4H_{9/2}$	Even	48.4625	-0.3710	-0.0722	48.0197	47.9380		0.21
69	$3s^23p^43d^3(^2D_1)^2D_{5/2}$	Even	49.3789	-0.2300	-0.0723	49.0769	48.9763		0.13
70	$3s^23p^43d^3(^4F_3)^6G_{11/2}$	Even	49.8344	-0.4800	-0.0718	49.2829	49.2190		0.21
71	$3s^23p^43d^3(^2F_3)^4D_{3/2}$	Even	49.9893	-0.2450	-0.0720	49.6721	49.5672		0.06
72	$3s^23p^53d^2(^3F_2)^4F_{7/2}$	Odd	50.1427	-0.5760	-0.0067	49.5604	49.5915		0.43
73	$3s^23p^43d^3(^2F_3)^4F_{5/2}$	Even	50.1855	-0.2540	-0.0723	49.8592	49.6445		0.05
74	$3s^23p^43d^3(^3F_2)^4F_{5/2}$	Odd	50.2685	-0.5350	-0.0069	49.7265	49.7502		0.14
75	$3s^23p^43d^2(^4F_3)^6D_{7/2}$	Even	50.318	-0.4180	-0.0723	49.8273	49.7575		0.11
76	$3s^23p^43d^3(^4F_3)^6G_{13/2}$	Even	50.3618	-0.5830	-0.0717	49.7074	49.7637		0.13
77	$3s^23p^43d^3(^4F_3)^2G_{9/2}$	Even	50.5824	-0.4230	-0.0723	50.0873	50.0229		0.13

LEVELS	CONFIGURATIONS	PARITY	DC	BREIT	QED	TOTAL	FAC	Others	ΔE
78	$3s^23p^43d^3(^2D_3)^4D_{5/2}$	Even	50.585	-0.3880	-0.0724	50.1250	50.0610		0.06
79	$3s^23p^53d^2(^3P_2)^4D_{3/2}$	Odd	50.6636	-0.5010	-0.0070	50.1559	50.1868		0.06
80	$3s^23p^53d^2(^3P_2)^4D_{1/2}$	Odd	50.7978	-0.4590	-0.0071	50.3321	50.3635		0.14
81	$3s^23p^43d^3(^2G_3)^2F_{5/2}$	Even	50.94	-0.4130	-0.0750	50.4521	50.3828		0.18
82	$3s^23p^43d^3(^2D_3)^4P_{1/2}$	Even	51.0116	-0.3530	-0.0739	50.5851	50.4936		0.15
83	$3s^23p^43d^3(^3F_2)^2G_{9/2}$	Odd	51.2503	-0.6470	-0.0067	50.5963	50.5195		0.14
84	$3s^23p^43d^3(^2H_3)^4I_{15/2}$	Even	51.2859	-0.6550	-0.0717	50.5588	50.6275		0.13
85	$3s^23p^53d^2(^1G_2)^2H_{9/2}$	Even	51.3092	-0.4890	-0.0720	50.7478	50.6826		0.13
86	$3s^23p^43d^3(^2F_3)^4G_{11/2}$	Even	51.375	-0.5440	-0.0718	50.7597	50.6931		0.13
87	$3s^23p^43d^3(^4P_3)^4D_{7/2}$	Even	51.4904	-0.4250	-0.0733	50.9921	50.9235		0.14
88	$3s^23p^43d^3(^2D_3)^2P_{3/2}$	Even	51.8673	-0.3910	-0.0745	51.4013	51.3285		0.14
89	$3s^23p^43d^3(^2D_3)^4F_{9/2}$	Even	52.0559	-0.4700	-0.0720	51.5136	51.4408		0.28
90	$3s^23p^43d^3(^2D_3)^4P_{3/2}$	Even	52.1678	-0.3720	-0.0739	51.7224	51.5764		0.13
91	$3s^23p^43d^3(^2F_3)^2F_{7/2}$	Even	52.2138	-0.4670	-0.0738	51.6731	51.6039		0.003
92	$3s^23p^43d^3(^2H_3)^4H_{11/2}$	Even	52.2504	-0.5310	-0.0719	51.6473	51.6491		0.14
93	$3s^23p^43d^3(^4F_3)^4D_{5/2}$	Even	52.3979	-0.4260	-0.0742	51.8974	51.8246		0.14
94	$3s^23p^43d^3(^4F_3)^4F_{7/2}$	Even	52.422	-0.4270	-0.0729	51.9220	51.8483		0.31
95	$3s^23p^43d^3(^2H_3)^4G_{9/2}$	Even	52.9476	-0.4760	-0.0728	52.3984	52.2378		0.02
96	$3s^23p^43d^3(^2H_3)^4H_{13/2}$	Even	52.9878	-0.6020	-0.0718	52.3137	52.3233		0.04
97	$3s^23p^53d^2(^3F_2)^2D_{5/2}$	Odd	53.0435	-0.5380	-0.0079	52.4979	52.5210		0.15
98	$3s^23p^43d^3(^4P_3)^4D_{7/2}$	Even	53.1461	-0.3950	-0.0722	52.6789	52.6013		0.27
99	$3s^23p^53d^2(^1G_2)^2F_{7/2}$	Odd	53.1682	-0.3250	-0.0724	52.7712	52.6274		0.09
100	$3s^23p^43d^3(^4F_3)^6D_{5/2}$	Even	53.1696	-0.3930	-0.0718	52.705	52.6552		0.13
101	$3s^23p^43d^3(^2D_1)^4D_{3/2}$	Even	53.2083	-0.5720	-0.0075	52.6289	52.6985		0.15
102	$3s^23p^43d^3(^2F_3)^2G_{9/2}$	Even	53.3887	-0.4860	-0.0733	52.8291	52.7517		0.15
103	$3s^23p^43d^3(^4P_3)^4P_{1/2}$	Even	53.6566	-0.3800	-0.0719	53.2052	53.1275		0.15
104	$3s^23p^53d^2(^3P_2)^4D_{3/2}$	Odd	53.7308	-0.4420	-0.0719	53.2166	53.1343		0.04
105	$3s^23p^43d^3(^2P_3)^2F_{7/2}$	Even	53.7341	-0.4940	-0.0076	53.2327	53.2520		0.14
106	$3s^23p^43d^3(^4P_3)^4P_{5/2}$	Odd	53.8127	-0.4100	-0.0716	53.3314	53.2563		0.40
107	$3s^23p^43d^3(^2F_3)^4D_{3/2}$	Even	53.9904	-0.3990	-0.0727	53.5188	53.3079		0.10
108	$3s^23p^43d^3(^2F_3)^4G_{11/2}$	Even	54.0041	-0.5470	-0.0717	53.3854	53.4400		0.14
109	$3s^23p^43d^3(^2F_3)^4D_{1/2}$	Even	54.1855	-0.3450	-0.0734	53.7672	53.6899		0.17
110	$3s^23p^43d^3(^4P_3)^4D_{3/2}$	Even	54.2509	-0.3820	-0.0722	53.7963	53.7062		0.33
111	$3s^23p^43d^3(^2D_3)^2D_{5/2}$	Even	54.3294	-0.3700	-0.0721	53.8876	53.7115		0.03
112	$3s^23p^43d^3(^2G_3)^4G_{9/2}$	Even	54.3556	-0.4910	-0.0719	53.7929	53.8071		0.15

LEVELS	CONFIGURATIONS	PARITY	DC	BREIT	QED	TOTAL	FAC	Others	ΔE
113	$3s^2 3p^4 3d^3(^2H_3)^2H_{11/2}$	Even	54.5313	-0.5400	-0.0719	53.9196	53.8371		0.14
114	$3s^2 3p^4 3d^3(^2F_3)^2F_{5/2}$	Even	54.5437	-0.3680	-0.0723	54.1038	54.0290		0.14
115	$3s^2 3p^4 3d^3(^2F_3)^2F_{7/2}$	Even	54.6833	-0.4110	-0.0726	54.1994	54.1249		0.16
116	$3s^2 3p^4 3d^3(^2F_3)^4F_{7/2}$	Even	55.0491	-0.4470	-0.0723	54.5302	54.4452		0.15
117	$3s^2 3p^4 3d^3(^2F_3)^4F_{9/2}$	Even	55.1164	-0.5000	-0.0718	54.5445	54.4616		0.15
118	$3s^2 3p^4 3d^3(^2F_3)^2F_{5/2}$	Even	55.1238	-0.4140	-0.0721	54.6373	54.5547		0.15
119	$3s^2 3p^4 3d^3(^2D_1)^2D_{3/2}$	Even	55.2814	-0.3700	-0.0724	54.8387	54.7543		0.21
120	$3s^2 3p^4 3d^3(^2D_1)^4P_{1/2}$	Even	55.3662	-0.3540	-0.0731	54.9390	54.8229		0.08
121	$3s^2 3p^4 3d^3(^2H_3)^4G_{5/2}$	Even	55.3789	-0.4020	-0.0720	54.9053	54.8625		0.16
122	$3s^2 3p^4 3d^3(^2F_3)^2D_{3/2}$	Even	55.4584	-0.3740	-0.0715	55.0128	54.9275		0.15
123	$3s^2 3p^4 3d^3(^2G_3)^2G_{7/2}$	Even	55.6465	-0.4340	-0.0721	55.1407	55.0585		0.16
124	$3s^2 3p^4 3d^3(^2D_1)^2D_{5/2}$	Even	55.941	-0.4260	-0.0728	55.4426	55.3546		0.22
125	$3s^2 3p^4 3d^3(^2D_1)^2D_{3/2}$	Even	55.9483	-0.3390	-0.0724	55.5367	55.4159		0.12
126	$3s^2 3p^5 3d^2(^3F_2)^4D_{7/2}$	Odd	56.0252	-0.6550	-0.0072	55.3631	55.4312		0.10
127	$3s^2 3p^4 3d^3(^2H_3)^2G_{7/2}$	Even	56.0767	-0.4880	-0.0722	55.5162	55.4603		0.07
128	$3s^2 3p^4 3d^3(^2G_3)^4H_{13/2}$	Even	56.3362	-0.6800	-0.0716	55.5842	55.5464		0.21
129	$3s^2 3p^4 3d^3(^2D_3)^2P_{1/2}$	Even	56.551	-0.3790	-0.0726	56.0996	55.9820		0.13
130	$3s^2 3p^5 3d^2(^3F_2)^2G_{9/2}$	Odd	56.6727	-0.7360	-0.0069	55.9296	56.0034		0.09
131	$3s^2 3p^5 3d^2(^1D_2)^2P_{3/2}$	Odd	56.6963	-0.6220	-0.0073	56.0674	56.1207		0.09
132	$3s^2 3p^5 3d^2(^1D_2)^2F_{5/2}$	Odd	57.0833	-0.6650	-0.0071	56.4113	56.4640		0.08
133	$3s^2 3p^4 3d^3(^2F_3)^4D_{7/2}$	Even	57.3147	-0.5600	-0.0737	56.6805	56.6327		0.09
134	$3s^2 3p^4 3d^3(^2P_3)^2P_{3/2}$	Even	58.0044	-0.4860	-0.0732	57.4452	57.3925		0.16
135	$3s^2 3p^4 3d^3(^2F_3)^2D_{3/2}$	Even	58.2205	-0.4180	-0.0728	57.7297	57.6394		0.09
136	$3s^2 3p^4 3d^3(^4F_3)^4F_{9/2}$	Even	58.5148	-0.6130	-0.0729	57.8289	57.7785		0.03
137	$3s^2 3p^5 3d^2(^1S_0)^2P_{1/2}$	Odd	58.6635	-0.5670	-0.0073	58.0890	58.0703		0.03
138	$3s^2 3p^4 3d^3(^2G_3)^4G_{11/2}$	Even	58.8326	-0.6380	-0.0715	58.1230	58.1410		0.08
139	$3s^2 3p^4 3d^3(^2D_1)^4D_{7/2}$	Even	59.1947	-0.5320	-0.0730	58.5899	58.5451		0.08
140	$3s^2 3p^4 3d^3(^2D_1)^4F_{9/2}$	Even	59.2751	-0.5500	-0.0719	58.6535	58.6081		0.09
141	$3s^2 3p^4 3d^3(^2P_3)^4P_{5/2}$	Even	59.7575	-0.5420	-0.0732	59.1427	59.0897		0.08
142	$3s^2 3p^4 3d^3(^2D_1)^2P_{1/2}$	Even	59.9032	-0.4900	-0.0740	59.3396	59.2904		0.36

Table 3.2: Radiative data for E1 transitions in W LVI.

S.No	Transition		$\lambda(\text{in } \text{\AA})$	$A_{ji} \text{ (in } s^{-1})$	f_{ij}	$S_{ij} \text{ (in a.u.)}$
	Lower Level	Upper level				
1	1	3	48.402	2.4338E+09	8.5480E-04	5.4483E-04
2	1	4	48.049	1.0365E+10	1.7938E-03	1.1350E-03
3	1	5	47.074	5.5148E+09	2.7481E-03	1.7035E-03
4	1	7	43.036	1.0967E+09	3.0450E-04	1.7256E-04
5	1	8	37.864	3.5621E+07	1.1484E-05	5.7263E-06
6	1	11	36.575	1.4394E+10	2.8867E-03	1.3903E-03
7	1	12	36.353	1.2075E+09	3.5883E-04	1.7177E-04
8	1	15	35.353	1.3710E+08	1.2845E-05	5.9799E-06
9	1	17	34.691	4.8991E+09	1.3259E-03	6.0570E-04
10	1	18	34.396	1.1446E+05	2.0300E-08	9.1949E-09
11	1	20	32.903	7.4878E+11	1.2153E-01	5.2655E-02
12	1	21	32.237	1.0246E+12	2.3944E-01	1.0165E-01
13	1	22	31.593	1.1756E+12	8.7956E-02	3.6592E-02
14	1	24	29.727	1.8423E+09	3.6612E-04	1.4332E-04
15	1	27	28.833	1.1348E+10	7.0717E-04	2.6850E-04
16	1	29	27.293	2.0486E+08	2.2878E-05	8.2223E-06
17	1	30	26.859	2.7455E+10	4.4540E-03	1.5753E-03
18	1	31	26.588	3.5129E+08	3.7229E-05	1.3035E-05
19	1	42	20.510	8.6149E+11	8.1492E-02	2.2009E-02
20	1	61	19.180	3.1208E+12	8.6055E-02	2.1735E-02
21	1	63	19.117	5.6834E+12	3.1140E-01	7.8392E-02
22	1	74	18.326	1.0633E+08	8.0300E-06	1.9378E-06
23	1	79	18.169	7.7716E+10	3.8461E-03	9.2019E-04
24	1	80	18.105	4.3648E+07	1.0725E-06	2.5570E-07
25	1	97	17.358	2.5351E+09	1.7177E-04	3.9264E-05
26	1	105	17.119	1.7693E+10	7.7733E-04	1.7523E-04
27	1	131	16.253	1.9043E+09	7.5416E-05	1.6141E-05
28	1	132	16.154	1.0316E+09	6.0538E-05	1.2878E-05
29	1	137	15.687	3.5470E+10	6.5432E-04	1.3517E-04

Table 3.3: Radiative data for E2 transitions in W LVI.

S.No	Transition		$\lambda(in \text{ \AA})$	$A_{ji} (in s^{-1})$	f_{ij}	$S_{ij} (in a.u.)$
	Lower Level	Upper Level				
1	1	2	160.320	5.2988E+02	3.0627E-09	3.0069E-04
2	1	32	23.450	3.0063E+04	2.4784E-09	7.6141E-07
3	1	33	23.426	2.5262E+04	1.0391E-09	3.1825E-07
4	1	34	23.107	2.0332E+05	2.4412E-08	7.1757E-06
5	1	35	23.051	7.0505E+03	1.1233E-09	3.2779E-07
6	1	36	22.211	5.9561E+03	4.4052E-10	1.1500E-07
7	1	37	20.924	4.8419E+03	4.7670E-10	1.0404E-07
8	1	39	20.697	1.4054E+04	1.8052E-09	3.8131E-07
9	1	40	20.636	4.8925E+04	3.1234E-09	6.5390E-07
10	1	41	20.531	2.8571E+04	3.6109E-09	7.4446E-07
11	1	43	20.440	2.7774E+04	2.6095E-09	5.3096E-07
12	1	46	20.258	4.1487E+05	2.5526E-08	5.0560E-06
13	1	49	20.113	2.1454E+06	1.9518E-07	3.7836E-05
14	1	50	19.890	2.8243E+05	8.3757E-09	1.5703E-06
15	1	51	19.854	9.7740E+04	1.1551E-08	2.1537E-06
16	1	52	19.766	1.5264E+04	1.3411E-09	2.4675E-07
17	1	54	19.553	3.5683E+04	2.0452E-09	3.6426E-07
18	1	55	19.448	6.8151E+04	1.9322E-09	3.3862E-07
19	1	56	19.368	1.4075E+03	1.1873E-10	2.0552E-08
20	1	57	19.348	8.1804E+04	4.5907E-09	7.9211E-07
21	1	58	19.336	1.2173E+04	1.3646E-09	2.3504E-07
22	1	60	19.209	3.8570E+03	2.1337E-10	3.6034E-08
23	1	62	19.170	2.2961E+00	1.8974E-13	3.1845E-11
24	1	64	19.110	2.6522E-01	2.9043E-14	4.8292E-12
25	1	65	19.064	1.4819E+05	4.0371E-09	6.6639E-07
26	1	66	18.969	1.5917E+06	4.2933E-08	6.9819E-06
27	1	67	18.991	5.6148E+03	6.0718E-10	9.9082E-08
28	1	69	18.568	1.1537E+05	8.9447E-09	1.3643E-06
29	1	71	18.346	2.9447E+04	1.4858E-09	2.1858E-07
30	1	73	18.277	8.3390E+04	6.2642E-09	9.1117E-07
31	1	75	18.289	1.6612E+05	1.6659E-08	2.4279E-06
32	1	78	18.180	1.6698E+05	1.2411E-08	1.7767E-06
33	1	81	18.062	2.3847E+06	1.7495E-07	2.4561E-05
34	1	82	18.015	1.4923E+06	3.6302E-08	5.0563E-06

S.No	Transition		$\lambda(in \text{ \AA})$	$A_{ji} (in s^{-1})$	f_{ij}	$S_{ij} (in a.u.)$
	Lower Level	Upper Level				
35	1	87	17.871	8.4575E+05	8.0987E-08	1.1012E-05
36	1	88	17.729	1.7983E+06	8.4737E-08	1.1249E-05
37	1	90	17.618	3.0241E+05	1.4073E-08	1.8337E-06
38	1	91	17.635	6.6529E+05	6.2038E-08	8.1065E-06
39	1	93	17.559	1.1668E+02	8.0901E-12	1.0435E-09
40	1	94	17.551	4.8215E+04	4.4531E-09	5.7355E-07
41	1	98	17.299	8.6422E+03	7.7541E-10	9.5628E-08
42	1	99	17.268	7.7472E+05	3.4634E-08	4.2489E-06
43	1	100	17.290	2.9100E+04	1.9563E-09	2.4090E-07
44	1	103	17.127	1.2547E+05	2.7591E-09	3.3027E-07
45	1	104	17.124	1.5063E+03	1.3243E-10	1.5842E-08
46	1	106	17.087	4.5335E+05	2.9765E-08	3.5378E-06
47	1	107	17.027	6.6534E+05	2.8919E-08	3.4012E-06
48	1	109	16.948	1.1842E+06	2.5498E-08	2.9574E-06
49	1	110	16.939	5.8341E+04	2.5097E-09	2.9062E-07
50	1	111	16.911	7.7110E+04	4.9587E-09	5.7131E-07
51	1	114	16.843	4.1178E+05	2.6270E-08	2.9905E-06
52	1	115	16.813	9.8851E+05	8.3786E-08	9.4876E-06
53	1	116	16.711	4.9908E+04	4.1791E-09	4.6466E-07
54	1	118	16.679	1.1757E+05	7.3546E-09	8.1294E-07
55	1	119	16.617	6.7060E+04	2.7761E-09	3.0349E-07
56	1	120	16.587	1.9611E+06	4.0445E-08	4.3973E-06
57	1	121	16.597	7.3143E+05	4.5309E-08	4.9352E-06
58	1	122	16.565	2.4869E+05	1.0230E-08	1.1078E-06
59	1	123	16.526	7.7470E+05	6.3440E-08	6.8221E-06
60	1	124	16.436	3.1796E+05	1.9316E-08	2.0434E-06
61	1	125	16.408	1.8741E+05	7.5647E-09	7.9620E-07
62	1	127	16.414	4.2508E+02	3.4341E-11	3.6184E-09
63	1	129	16.244	4.4954E+04	8.8914E-10	9.0794E-08
64	1	133	16.077	1.5098E+05	1.1702E-08	1.1585E-06
65	1	134	15.863	7.5152E+04	2.8352E-09	2.6964E-07
66	1	135	15.785	7.7278E+02	2.8867E-11	2.7051E-09
67	1	139	15.553	9.9552E+04	7.2208E-09	6.4727E-07
68	1	141	15.408	1.1467E+05	6.1218E-09	5.3351E-07
69	1	142	15.357	5.8087E+03	1.0269E-10	8.8602E-09

Table 3.4: Radiative data for M1 transitions in W LVI.

S.No	Transition		$\lambda(in \text{ \AA})$	$A_{ji} (in s^{-1})$	f_{ij}	$S_{ij} (in a.u.)$
	Lower Level	Upper Level				
1	1	2	160.320	2.5832E+06	1.4931E-05	2.3677E+00
2	1	32	23.450	1.9683E+04	1.6227E-09	3.7636E-05
3	1	33	23.426	2.5033E+04	1.0297E-09	2.3858E-05
4	1	34	23.107	1.2611E+04	1.5142E-09	3.4607E-05
5	1	36	22.211	2.0712E+03	1.5318E-10	3.3653E-06
6	1	37	20.924	4.1714E+02	4.1069E-11	8.4993E-07
7	1	40	20.636	5.4779E+02	3.4971E-11	7.1378E-07
8	1	43	20.440	1.4622E+02	1.3739E-11	2.7776E-07
9	1	46	20.258	1.5550E+03	9.5671E-11	1.9170E-06
10	1	49	20.113	5.7076E+01	5.1924E-12	1.0330E-07
11	1	50	19.890	3.1196E+04	9.2514E-10	1.8201E-05
12	1	52	19.766	5.3078E+03	4.6634E-10	9.1171E-06
13	1	54	19.553	1.7988E+04	1.0310E-09	1.9939E-05
14	1	55	19.448	1.7797E+04	5.0457E-10	9.7058E-06
15	1	56	19.368	1.9235E+04	1.6226E-09	3.1082E-05
16	1	57	19.348	7.1180E+03	3.9945E-10	7.6440E-06
17	1	60	19.209	3.3399E+03	1.8476E-10	3.5105E-06
18	1	62	19.170	1.8035E+04	1.4904E-09	2.8259E-05
19	1	65	19.064	1.1590E+03	3.1573E-11	5.9533E-07
20	1	66	18.969	2.6157E+04	7.0555E-10	1.3238E-05
21	1	69	18.568	1.4897E+04	1.1550E-09	2.1212E-05
22	1	71	18.346	3.3914E+04	1.7112E-09	3.1050E-05
23	1	73	18.277	3.1309E+04	2.3519E-09	4.2516E-05
24	1	78	18.180	1.7694E+03	1.3151E-10	2.3647E-06
25	1	81	18.062	2.1783E+02	1.5981E-11	2.8550E-07
26	1	82	18.015	3.3565E+03	8.1650E-11	1.4548E-06
27	1	88	17.729	1.1552E+03	5.4433E-11	9.5449E-07
28	1	90	17.618	2.0618E+02	9.5947E-12	1.6720E-07

S.No	Transition		$\lambda(in \text{ \AA})$	$A_{ji} (in s^{-1})$	f_{ij}	$S_{ij} (in a.u.)$
	Lower Level	Upper Level				
29	1	93	17.559	2.7244E-01	1.8890E-14	3.2806E-10
30	1	99	17.268	1.8045E+02	8.0669E-12	1.3778E-07
31	1	100	17.290	6.5173E+02	4.3813E-11	7.4926E-07
32	1	103	17.127	4.7761E+03	1.0502E-10	1.7791E-06
33	1	106	17.087	5.1953E+03	3.4110E-10	5.7648E-06
34	1	107	17.027	4.5222E+03	1.9656E-10	3.3102E-06
35	1	109	16.948	2.1358E+03	4.5987E-11	7.7090E-07
36	1	110	16.939	5.1062E+01	2.1966E-12	3.6802E-08
37	1	111	16.911	6.6507E+01	4.2769E-12	7.1535E-08
38	1	114	16.843	3.9032E+02	2.4900E-11	4.1482E-07
39	1	118	16.679	1.8636E+03	1.1658E-10	1.9231E-06
40	1	119	16.617	2.1374E+03	8.8484E-11	1.4543E-06
41	1	120	16.587	6.3194E+03	1.3033E-10	2.1381E-06
42	1	121	16.597	7.5574E+02	4.6815E-11	7.6851E-07
43	1	122	16.565	3.5370E+03	1.4550E-10	2.3838E-06
44	1	124	16.436	7.3490E+02	4.4646E-11	7.2580E-07
45	1	125	16.408	1.8928E+02	7.6400E-12	1.2399E-07
46	1	129	16.244	2.7016E+03	5.3434E-11	8.5850E-07
47	1	134	15.863	5.2412E+02	1.9773E-11	3.1024E-07
48	1	135	15.785	1.8891E+03	7.0569E-11	1.1018E-06
49	1	141	15.408	3.9228E+02	2.0943E-11	3.1916E-07
50	1	142	15.357	7.2668E+02	1.2846E-11	1.9512E-07

Table 3.5: Radiative data for M2 transitions in W LVI.

<i>S.No</i>	<i>Transition</i>		$\lambda(in \text{ \AA})$	$A_{ji} (in s^{-1})$	f_{ij}	$S_{ij} (in a.u.)$
	Lower Level	Upper Level				
1	1	3	48.402	8.4721E+01	2.9755E-11	6.0374E-03
2	1	4	48.049	8.9934E+01	1.5564E-11	3.0895E-03
3	1	5	47.074	5.9930E-01	2.9864E-13	5.5742E-05
4	1	6	46.593	1.9356E+01	1.2599E-11	2.2803E-03
5	1	7	43.036	1.0766E+02	2.9892E-11	4.2633E-03
6	1	8	37.864	1.5895E+04	5.1248E-09	4.9781E-01
7	1	10	36.969	5.6630E+02	2.3206E-10	2.0980E-02
8	1	11	36.575	4.9222E+04	9.8714E-09	8.6421E-01
9	1	12	36.353	3.5082E+04	1.0426E-08	8.9621E-01
10	1	13	35.978	4.7796E+04	1.8551E-08	1.5459E+00
11	1	15	35.353	6.9698E+04	6.5298E-09	5.1629E-01
12	1	16	34.856	1.7160E+04	6.2513E-09	4.7372E-01
13	1	17	34.691	6.4903E+03	1.7565E-09	1.3122E-01
14	1	18	34.396	9.9863E+03	1.7712E-09	1.2897E-01
15	1	20	32.903	2.6909E+03	4.3673E-10	2.7836E-02
16	1	21	32.237	4.2742E+02	9.9888E-11	5.9882E-03
17	1	22	31.593	1.7631E+02	1.3191E-11	7.4433E-04
18	1	24	29.727	4.7536E-01	9.4467E-14	4.4407E-06
19	1	26	29.299	6.0515E+02	1.5576E-10	7.0102E-03
20	1	27	28.833	8.7524E+02	5.4541E-11	2.3392E-03
21	1	28	27.800	1.6481E+03	3.8192E-10	1.4683E-02
22	1	29	27.293	7.3772E+02	8.2384E-11	2.9970E-03
23	1	30	26.859	1.9280E+03	3.1279E-10	1.0845E-02
24	1	31	26.588	3.3414E+03	3.5413E-10	1.1910E-02
25	1	42	20.510	4.2852E+04	4.0536E-09	6.2577E-02
26	1	61	19.180	3.2390E+04	8.9314E-10	1.1276E-02
27	1	63	19.117	3.0700E+03	1.6820E-10	2.1028E-03
28	1	72	18.387	9.8586E+04	9.9937E-09	1.1116E-01
29	1	74	18.326	2.2059E+05	1.6659E-08	1.8346E-01
30	1	79	18.169	2.7474E+05	1.3597E-08	1.4592E-01
31	1	80	18.105	2.8021E+05	6.8851E-09	7.3118E-02
32	1	97	17.358	6.3314E+04	4.2900E-09	4.0149E-02

S.No	Transition		$\lambda(\text{in } \text{\AA})$	$A_{ji} \text{ (in } s^{-1})$	f_{ij}	$S_{ij} \text{ (in a.u.)}$
	Lower Level	Upper Level				
33	1	101	17.315	2.5766E+05	2.3162E-08	2.1516E-01
34	1	105	17.119	2.6524E+04	1.1653E-09	1.0460E-02
35	1	126	16.460	1.2232E+04	9.9364E-10	7.9289E-03
36	1	131	16.253	8.7392E+01	3.4610E-12	2.6590E-05
37	1	132	16.154	3.5880E+02	2.1055E-11	1.5882E-04
38	1	137	15.687	1.5153E+03	2.7954E-11	1.9311E-04

Table 3.6: Comparison of transition wavelength (λ in \AA) and oscillator strength (f in a.u.) for W LVI.

Transitions		λ_{GRASP}	λ Ref.[19]	$\lambda_{exp.}$ [42]	λ Ref.[42]	f_{GRASP}	f Ref.[19]
Upper Level	Lower Level						
21	1	32.237	32.376	32.469	32.382	0.2394	0.2866
20	1	32.903	33.089	33.107	33.082	0.1215	0.1418
22	1	31.593	31.830	31.814	31.733	0.0879	0.0967
17	1	34.691	35.116	34.850	34.883	0.0013	0.0013

Table 3.7: Partition function (Q), internal energy (U/kT), and specific heat (C/k) in LSJ coupling for K-like W.

S. No	Log T (in K)	LSJ		
		Q	U/kT	C/k
1	4	4.0000	1.40E-38	1.29E-36
2	5	4.0006	1.38E-03	1.27E-02
3	6	9.7476	1.668731	4.000631
4	7	465.5805	0.694324	4.06E-02

3.7 REFERENCES

- [1] R. Neu, R. Dux, A. Kallenbach, T. Pütterich, M. Balden, J. C. Fuchs, A. Herrmann, C. F. Maggi, M. O’Mullane, R. Pugno, et al., Nucl. Fusion 45, 209 (2005).
- [2] K. Ikeda, Nucl. Fusion 50, 014002 (2010).
- [3] M. Merolaa, D. Loesserb, A. Martina, P. Chappuisa, R. Mitteaua, V. Komarova, R. A. Pitts, S. Gicquela, V. Barabasha, L. Giancarlia, et al., Fusion Eng. Des. 85, 2312 (2010).
- [4] T. Das, Y. A. Podpaly, J. Reader, J. D. Gillaspys and Y. Ralchenko, Eur. Phys. J. D 72, 124(2018).
- [5] A. K. Singh, A. Goyal, I. Khatri, S. Aggarwal, R. Sharma and M. Mohan, ADNDT 109, 339 (2016).
- [6] T. A. Carlson, C. W. Nestor, Jr., N. Wasserman, and J. D. McDowell, At. Data Nucl. Data Tables 2, 63–99 (1970).
- [7] L. Yang, L. Liu, and J.-M. Li, Chin. Phys. Lett. 7, 121–124 (1990).
- [8] M. A. Ali and Y.-K. Kim, J. Opt. Soc. Am. B 9, 185–190 (1992).
- [9] E. Behar, A. Peleg, R. Doron, P. Mandelbaum, and J. L. Schwob, J. Quant. Spectrosc. Radiat. Transfer 58, 449–469 (1997).
- [10] G. C. Rodrigues, P. Indelicato, J. P. Santos, P. Patté, and F. Parente, At. Data Nucl. Data Tables 86, 117–233 (2004).
- [11] A. E. Kramida and J. Reader, At. Data Nucl. Data Tables 92, 457–479 (2006).
- [12] A. E. Kramida and T. Shirai, At. Data Nucl. Data Tables 95, 305–474 (2009).
- [13] P. Quinet, J. Phys. B 44, 195007 (2011).
- [14] A. Kramida, Can. J. Phys. 89, 551–570 (2011).
- [15] P. Beiersdorfer, M. J. May, J. H. Scofield, and S. B. Hansen, High En. Dens. Phys. 8, 271–283 (2012).
- [16] Priti, Dipti, L. Sharma, and R. Srivastava, Atoms 3, 53–75 (2015).

- [17] M. B. Trzhaskovskaya and V. K. Nikulin, *Atoms* 3, 86–119 (2015).
- [18] X. L. Guo, M. Huang, J. Yan, S. Li, R. Si, C. Y. Li, C. Y. Chen, Y. S. Wang, and Y. M. Zou, *J. Phys. B* 48, 144020 (2015).
- [19] T. Das, L. Sharma, and R. Srivastava, *Can. J. Phys.* 93, 888–897 (2015).
- [20] M. Xu, G. Jiang, M. Wu, X.-F. Li, G.-J. Bian, and F. Hu, *Can. J. Phys.* 94, 563–568 (2016).
- [21] C. Froese Fischer, G. Gaigalas, and P. Jönsson, *Atoms* 5, 7 (2017).
- [22] Z. L. Zhao, K. Wang, S. Li, R. Si, C. Y. Chen, Z. B. Chen, J. Yan, and Yu. Ralchenko, *At. Data Nucl. Data Tables* 119, 314–353 (2018).
- [23] G. Colonna and M. Capitelli, *Spectrochim. Acta, Part B* 64, 863 (2009).
- [24] G. D’Ammando, G. Colonna, L. D. Pietanza, and M. Capitelli, *Spectrochim. Acta, Part B* 65, 603 (2010).
- [25] O. Cardona, E. Simmoneau, and L. Crivellari, *Rev. Mex. Fis.* 51, 476 (2005).
- [26] O. Cardona, E. Simmoneau, and L. Crivellari, *Astrophys. J.* 690, 1378 (2009).
- [27] O. Cardona, M. Martínez-Arroyo, and M. A. L. Opez-Castillo, *Astrophys. J.* 711, 239 (2010).
- [28] S. Gordon and B. J. McBride, “Computer program for calculation of complex chemical equilibrium compositions, rocket performance, incident and reflected shocks, and chapman-jouguet detonations,” Technical Report No. SP-273 (NASA, 1976).
- [29] B. J. McBride, S. Gordon, and M. A. Reno, “Coefficients for calculating thermodynamic and transport properties of individual species,” Technical Memorandum No. TM-4513 (NASA, 1993).
- [30] L. V. Gurvich, I. V. Veyts, C. B. Alcock, and V. S. Iorish, *Thermodynamic Properties of Individual Substances* (CRC, Boca Raton, FL, 1994).
- [31] H. W. Drawin and P. Felenbok, *Data for Plasmas in Local Thermodynamic Equilibrium* (Gauthier-Villars, 1965).

- [32] G. D'Ammando, G. Colonna, and M. Capitelli, *Phys. Plasmas* 20, 032108 (2013).
- [33] P. H. Norrington. <http://www.am.qub.ac.uk/DARC/> 2009.
- [34] I. P. Grant, B. J. McKenzie, P. H. Norrington, D. F. Mayers and N. C. Pyper, *Comput. Phys. Commun.* 21, 207 (1980).
- [35] F. A. Parpia, C. F. Fischer, I. P. Grant, *Comput. Phys. Commun.* 94, 249 (1996).
- [36] J. Olsen, M. R. Godefroid, P. Jönsson, P. A. Malmqvist, C. F. Fischer, *Phys. Rev. E* 52, 4499 (1995).
- [37] P. Jönsson, X. He, C.F. Fischer, I. P. Grant, *Comput. Phys. Commun.* 177, 597 (2007).
- [38] B. Fricke, *Phys. Scr. T8*, 129 (1986).
- [39] M. F. Gu, *Can. J. Phys.* 86, 675 (2008).
- [40] Z. B. Chen, K. Ma, H. W. Hu and K. Wang, *Physics of Plasmas* 25, 052105 (2018).
- [41] Z. B. Chen, H. W. Hu, K. Ma, X. B. Liu, X. L. Guo, S. Li, B. H. Zhu, L. Huang and K. Wang, *Physics of Plasmas* 25, 032108 (2018).
- [42] J. Clementson and P. Beiersdorfer, *Phys. Rev. A* 81, 052509 (2010).
- [43] Yu. Ralchenko, I. N. Draganic, D. Osin, J. D. Gillaspy, and J. Reader, *Phys. Rev. A* 83, 032517 (2011).

CHAPTER 4

RELATIVISTIC ATOMIC STRUCTURE CALCULATIONS OF KIX WITH PLASMA PARAMETERS

- This chapter, introduces a brief study of Sodium like Potassium (Na-like K) theoretically.
- Systematic calculations for energy levels, lifetimes, and radiative data for the KIX are reported, including oscillator strengths, transition wavelengths, line strengths, and radiative rates of electric dipole (E1) transition, electric quadrupole (E2) transition, magnetic dipole (M1) transition, and magnetic quadrupole (M2) transition, using GRASP.
- Quantum Electrodynamics (QED) and Breit correction have been included. The importance and effect of valence valence (VV) and core valence (CV) correlations on the excitation energies have been discussed in graphical and tabular form.
- Analogous calculations using Flexible Atomic Code (FAC) and the large-scale configuration interaction technique (CIV3) have also been done to confirm the accuracy of energy levels.
- The calculated results are in close agreement with NIST compiled data and other available results. Some theoretical plasma parameters are also determined which is beneficial for the characterization of HDP, astrophysical plasmas, and plasma modeling.

4.1 INTRODUCTION

Due to its prospective applications in plasma diagnostics, inertial confinement fusion (ICF), magnetic confinement fusion and atomic spectroscopy of highly charged ions have attracted significant interest [1-3]. Modeling and research into low and high-temperature plasma using inertial and magnetic confinement thermonuclear fusion demand very accurate atomic data and plasma parameters such as line intensity ratio, plasma temperature and electron density [4]. Because the adjacent neon-like stage of ionization is necessary for X-ray laser modeling, atomic data on Na-like ions is essential for studying high-temperature plasma [5-6]. Inertial confinement fusion, magnetic confinement fusion, and plasma diagnostics are important for atomic spectroscopy of highly charged ions. Highly charged sodium-like ions were found in laboratory sources such as high-voltage vacuum spark tokamak and laser-produced plasmas. In astrophysical plasmas, for example, Cu XIX (Sodium-like Copper ion) spectra were observed in a solar spectrum obtained at the White Sands Missile Range [7].

Potassium was chosen for the current investigation because the absolute abundance of potassium has been calculated using X-ray solar flare line and continuum spectra. Phillips et al. [8] have assumed flare plasma is coronal and potassium is significant in the continuing debate concerning the nature of the coronal/photospheric element abundance ratios, which are usually considered to be dependent on first ionization potential, as it has the lowest FIP (FIPs $n < 10$ eV) of any common element in the Sun. The RESIK crystal spectrometer on the Coronas-F spacecraft was used to make the measurements. Using high-resolution spectra gathered with FLAMES at the ESO – Very Large Telescope, Mucciarelli et al. [9] have determined the potassium abundances in red-giant-branch stars in the Galactic globular clusters. GCs have revealed large and correlated star-to-star inhomogeneities in the abundance of various light elements, including C, N, Na, O, Mg, Al, and He, in chemical composition.

4.1.1 Experimental and theoretical work on Na-like ions

Edlen et al. published a complete list of the potassium lines detected in their spectrograms, including 230 lines varying between 230 to 41 \AA , nearly half of which are classified in spectra including between KVII to KXII. Cohen et al. [10] investigated

the seven spectra from KIX to Mn XV, determining series limits, presenting adopted wavelengths, derived energy levels, and term splitting. Recently, E. Trabert et al. [11] identified 3p-3d transitions in singly excited Na-like ions in the ^{39}K beam foil spectrum. C. Jupen et al. [12], using Cowan code, found the most prominent line of the multiplet, $2p^5 3s 3p \ ^4D^o_{7/2} - 2p^5 3s 3d \ ^4F^o_{9/2}$, in the spectra of various Na-like ions. To compute the oscillator strengths for the E1 transition in the sodium isoelectronic sequence, Seigal et al. [13] used the theoretical single configuration Dirac-Fock technique (Na I-Ca X). Yonis et al. [14] calculated the fine structure energy levels, transition probabilities and oscillator strengths of Na-like ions using the configuration interaction approach CIV3. Ivanov et al. [15] used a model potential technique for Na-like series with ($Z=25-80$) nuclear charge. With 71 Na-like ions in the $Z=22-92$ range, Sampson et al. [16] observed relativistic distorted wave collision strengths as well as oscillator strengths. Kim et al. [17] also used the Dirac Fock technique to find the resonance transition energies of Na-like ions. Moreover, Johnson et al. [18] calculated E1 transition amplitudes for Na-like ions using third-order many-body perturbation theory. Similarly, to determine the transition probability of allowed transition for KIX, Johnson et al. employed the third-order many-body perturbation theory. For 67 Na-like and F-like as well as Li-like transitions between the region of $26 \leq Z \leq 92$, the relativistic distorted-wave collision intensities for all possible $\Delta n = 0$ in the region of $26 \leq Z \leq 92$ were calculated by Christopher J. Fontes et al. [19]. Safronova et al. [20] evaluated the relativistic many-body perturbation theory by taking neon-like Dirac-Fock potential. Further, for $2p^5 3s 3p \ ^4D^o_{7/2} - 2p^5 3s 3d \ ^4F^o_{9/2}$, Jupen et al. observed a wavelength of $423.05(5) \text{ \AA}$ along the isoelectronic sequence using the interpolation method. Furthermore, J.E Sansonetti et al. [21] compiled the energy levels using experimental wavelengths of Cohen and Behring's [22] and Edlen and Boden [23]. Moreover, using relativistic many-body perturbation theory, J.D. Gillaspay et al. [24] determined the transition energies of D lines for Na-like ions. Last but not least, Fisher et al. [25] calculated the energy levels and oscillator strength of Na-like ions by using the Multi-Configuration Hartree-Fock (MCHF) technique with non-orthogonal spline CI methods. There is a considerable previous experimental as well as theoretical work on KIX, mostly restricted to low-lying states. The principal objective of our work is to upgrade the atomic database for KIX ions in the form of energy levels, wavelengths,

oscillator strength, and line strengths. The transitions of radiative rates are presented as E1 (electric dipole) and E2 (electric quadrupole), also M1 (magnetic dipole) and M2 (magnetic quadrupole). The effect of Quantum electrodynamics correction with Breit interaction correction on energy levels has been studied. We have done additional independent calculations using Flexible Atomic Code (FAC) to ensure the correctness of our Multi-Configuration Dirac-Fock (MCDF) results. Further, the configuration interaction (CIV3) approach has also been used to determine the fine structural energy levels of KIX.

We have used two alternative sets of configurations based on valence-valence (VV) and core-valence (CV) correlations in our present calculations. While doing calculations with the VV correlations, we have taken configuration namely as $2p^6nl$ with $3 \leq n \leq 5$ and $0 \leq l \leq 4$, where one electron excitation from the valence to another high subshell is involved. In the case of core valence correlation, however, the configuration has been included as $2p^5 3l nl'$ with $3 \leq n \leq 5$, $2p^5 4l 4l'$ excitations among one electron as of the 2p subshell to additional high subshells and $2s2p^6 3l nl'$ with $3 \leq n \leq 5$, $2s2p^6 4l 4l'$ excitations of one electron as of the 2s subshell to additional high subshells. $1s^2 2s^2 2p^6$ core gets set for valence valence calculation, while $1s^2$ core remains unchangeable for calculation of core valence correlation.

Plasma characterization and modeling help to understand the multiple atomic processes that occur in plasmas. Consequently, we have analyzed the various plasma characteristics, line intensity ratios, and electron density of the hot-dense plasma in local thermodynamic equilibrium (LTE). We believe KIX calculations should help examine or observe the new valuable data from a variety of plasma sources, where plasma diagnostics, including modeling studies, were always inhabited by a scarcity of precise atomic data and future astrophysical sources.

This paper is divided into four sections, as demonstrated in Section II, where we provide the theoretical method used in our calculations. In Section III, we have evaluated and compared our calculated results using the NIST database or previously published results. Finally, Section IV presents the entire conclusive summary of KIX.

4.2 THEORETICAL METHOD

4.2.1 Multi-Configuration Dirac Fock Method (MCDF): Discussed briefly in chapter 2.

4.2.2 The FAC Method

To check the accuracy of our results, we also did analogous calculations by using FAC, developed by M.F.Gu [28]. FAC calculates local central potential by performing a self-consistent Dirac Slater iteration on such a fictitious mean configuration. Dirac coulomb Hamiltonian is being used to evaluate the relativistic effects. For considering the high order quantum electrodynamics (QED) effects, Breit interaction is used in vacuum polarisation effects, hydrogenic approximations for self-energy and zero energy limit for the exchanged photon. The present calculations have been performed by taking 2700 fine structure levels from $(2*8) n*1$ and $(2*7)3*2, 4*2, 3*1 4*1, 3*1 5*1$ configurations. Where $3 \leq n \leq 10$ and $n*q$ given all possible distributions of q electrons (without restriction to orbital angular momentum) as one of the shells described by their principal quantum numbers, that are shown in Table 4.4.

4.2.3 Configuration Interaction Method

Hibbert's configuration interaction approach CIV3 [29] has been used in the present calculations. The atomic state functions (ASFs) of configuration interaction (CI) are expressed as in the intermediate LSJ-coupling scheme.

$$\Psi_i(J) = \sum_{j=1}^M a_{ij} \phi_j(\alpha_j L_j S_j J) \quad (4.1)$$

Where $\{\phi_j\}$ stands for a set of single configuration wave functions, coupling of an orbital L_j and spin S_j angular momenta is defined by α_j , which produces the total angular momentum J . To obtain the mixing coefficients of a_{ij} , the Breit–Pauli Hamiltonian matrix is diagonalized with a basis $\{\phi_j\}$. A linear combination of normalized slater-type orbitals is used to expand the radial functions $P_{nl}(r)$

$$P_{nl}(r) = \sum_{j=1}^k C_{jnl} \chi_{jnl}(r) \quad (4.2)$$

C_{jnl} denotes the Clementi-type coefficients, and

$$\chi_{jnl}(r) = \frac{(2\xi_{jnl})^{I_{jnl} + \frac{1}{2}}}{\left[(2I_{jnl})! \right]^{\frac{1}{2}}} r^{I_{jnl}} \exp(-\xi_{jnl} r) \quad (4.3)$$

with $I_{jnl} \geq l+1$ as an integer.

While, the parameters C_{jnl} , ξ_{jnl} are obtained variationally in process of optimization through minimizing one or more Hamiltonian matrix's energy eigenvalues, whereas the parameters of I_{jnl} remain constant. In current calculations, 21 orthonormal one-electron orbitals namely, 1s, 2s, 2p, 3s, 3p, 3d, 4s, 4p, 4d, 4f, 5s, 5p, 5d, 5f, 5g, 6s, 6p, 6d, 6f and 6g has been used, in which 1s, 2s, 2p are defined as the Hartree–Fock functions of KIX where ground state is $1s^2 2s^2 2p^6 3s^1$, as defined by Clementi and Roetti. The 3p, 3d, 4s, 4p, 4d, 4f, 5s, 5p, 5d, 5f, 5g, 6s, 6p, 6d, 6f and 6g are spectroscopic orbitals and $2p^6 3p$, $2p^6 3d$, $2p^6 4s$, $2p^6 4p$, $2p^6 4d$, $2p^6 4f$, $2p^6 5s$, $2p^6 5p$, $2p^6 5d$, $2p^6 5f$, $2p^6 5g$, $2p^6 6s$, $2p^6 6p$, $2p^6 6d$, $2p^6 6f$ and $2p^6 6g$ optimized based on the excited states. On the ground state $2p^6 3s$, the 3s orbital is optimized. Table 4.1 displays the optimized radial function parameters.

The overall energy of each LS coupled term in CIV3 is affected by the inclusion of spin-independent Darwin and the relativistic mass-correction components, while spin-spin (SS) and one-body spin-orbit (SO) as well as two-body spin-other-orbit (SOO) terms, divide the LS states into J-dependent levels. The SO operator in modified form is as follows:

$$H'_{SO} = \frac{\alpha^2}{2} Z \sum_{i=1}^N \frac{\xi(i)}{r_i^3} (l.s) \quad (4.4)$$

4.3 RESULTS AND DISCUSSION

The fine structure energy levels of KIX have been calculated using the fully relativistic GRASP algorithm. For orbital optimization, the "extended average level" (EAL) option has been chosen, which reduces the weighted proportional to $(2j + 1)$ trace of a Hamiltonian matrix. Two sets of calculations were performed using the valence-valence (VV) correlation and core valence (CV) correlation to explore the effect of correlation on energy levels. We employed an atomic model with 12 configurations in our MCDF1 calculation in the form of $2p^6nl$ ($3 \leq n \leq 5$ and $0 \leq l \leq 4$) there are a total of 21 fine-structure energy levels as a result of this process. Table 4.3 and Figure 4.1 show the impact of electron correlations of KIX, for the lowest 21 fine structure energy configurations. The CSF has been generated by taking excitations from the reference configuration $2p^6 3s^1$ to orbitals with $n = 3, 4, 5$ and 6 , respectively. To predict the electronic correlation effects systematically, configuration spaces were extended layer by layer. In Table 4.3, the difference in correlation energies between two neighboring principal quantum numbers decreases as the principal quantum number increases. In our MCDF2 calculations, additional configurations of $2p^5 3l nl'$ with $3 \leq n \leq 5, 2p^5 4l 4l'$, $2s2p^6 3l nl'$ with $3 \leq n \leq 5$, $2s2p^6 4l 4l'$ are taken into account, resulting in a total of 2700 levels. Table 4.4 shows 21 fine-structure energy levels calculated from (MCDF1, MCDF2) methods, NIST values, and other relevant references. Our two sets of energy (using the MCDF1 and MCDF2 methods) differ by 0.0409 Ryd. Most of the energies level have been lowered by using a larger CI in the MCDF2 calculations. The relative fluctuations between MCDF1 as well as MCDF2 energies are shown in Figure 4.2. Because of the inclusion of larger CI, one can see that most of the levels have converged the energy. Furthermore, our calculated energies using the MCDF2 method well match with those of NIST (Figure 4.3), wherein an average difference of 0.22 percent whereas a maximum difference of 0.86 percent for $2p^6 3p (^2p^0_{1/2})$ state. For the lowest 21 energy levels of KIX, the significance of both BI and QED correlations on MCDF2 energies have been evaluated. In Figure 4.4, it is shown that the BI and QED effects alter the energies quite significantly, BI + QED correlations reduce them by around 0.0123 Ryd.

We have also done three independent calculations by using the FAC code. In our present calculations of FAC1, we have included the configurations that are used in the MCDF1, FAC2 includes the CI as in MCDF2 but without the angular momentum constraints. Although we did extensive FAC3 calculations, we only recorded energies for the lowest 96 fine-structure levels, which all belong to $2p^6nl$ configurations with $n \leq 10$, 2700 fine-structure levels generated in FAC2, using all possible values. The maximum disagreement between both MCDF2 and FAC2 is predicted to be around 0.0266 Ryd. This disagreement arises from distinctions in the algorithms of the codes and the central potential calculation. Higher $2p^6nl$ configurations ($n > 10$) could not be incorporated because of the computational limitations of the code. For a few levels, inserting more CI into the FAC calculations (Table 4.4) changes the energy by up to 0.0080 Ryd. As a result, it is possible to conclude that including additional CI in FAC calculations is enough to achieve reliable results. Further, as shown in Tables 4.1 to 4.4, no intense mixing exists, so there is no uncertainty in identifying the $2p^6nl$ levels.

The ab-initio calculations for the CIV3 column in Table 4.1 were performed by including $2p^6nl$ with $3 \leq n \leq 5$ and $0 \leq l \leq 4$, $2p^5 3l nl'$ with $3 \leq n \leq 5$, $2p^5 4l 4l'$, $2s2p^6 3l nl'$ with $3 \leq n \leq 5$, $2s2p^6 4l 4l'$ configurations which are generated by particular arrangements of 2700 fine-structure energy levels. We achieved a good agreement with NIST on the majority of calculated energies. We have also compared our calculated energy to Fischer et al. in Table 4.2. It is worth noting that the results presented for all approaches are not just in good agreement with all accessible data, but they are also in good agreement with one another, and they are getting closer to those of NIST.

4.3.1 Radiative rates (wavelengths, oscillator strengths, and transition rates):

Discussed briefly in chapter 2 (calculated in Table number 4.5).

4.3.2 Lifetimes

By taking the inverse of a sum of transition probabilities from the radiative transition from level (i), the lifetime (τ) of a level (j) is calculated as,

$$\tau_j(s) = \frac{1}{\sum_i A_{ji}(s^{-1})} \quad (4.5)$$

Table 4.4 contains lifetime information for the lowest 21 fine structure levels of KIX, taking into account all possible transitions such as E1 and E2, M1 and M2. We tried to compare our lifetime calculations with available results. Fisher et al. [23] has given the lifetime for the level $1s^2 2p^6 3s$, $1s^2 2p^6 3p$, $1s^2 2p^6 3d$, $1s^2 2p^6 4s$, $1s^2 2p^6 4p$, $1s^2 2p^6 4d$, and $1s^2 2p^6 4f$. Our calculated lifetimes for these levels are in close agreement with Fisher et al. Further, we have also predicted the lifetime for the levels $1s^2 2p^6 5s$, $1s^2 2p^6 5p$, $1s^2 2p^6 5d$, $1s^2 2p^6 5f$ and $1s^2 2p^6 5g$ where no other data are available for comparison.

4.4 LINE INTENSITY RATIO AND PLASMA PARAMETERS

The plasma parameters are influenced by changes in spectroscopic parameters like transition wavelength and transition probability. Characterizing and analyzing hot dense plasma (HDP) appears easy and uncomplicated only when plasma is treated as optically thin in the local thermodynamic equilibrium (LTE). Because of saturation as well as self-absorption as in line profile, the optically thick line implements an asymmetrical rather than distorted peak in the spectrum. This causes the electron density, plasma temperature both are measured incorrectly and inaccurately. Variations in spectroscopic parameters cause changes in plasma temperature. The increasing number of collisions between electrons increases as kinematic excitation, at higher values of temperatures and hence LTE is easily accomplished at high temperatures. As a result, we explored plasma temperature in the line intensity ratio in optically thin plasma. In HDP, any two spectral lines of the line intensity ratio are:

$$R = \frac{I_1}{I_2} = \frac{\lambda_2 A_1 g_1}{\lambda_1 A_2 g_2} \exp \left[-\frac{E_1 - E_2}{KT} \right] \quad (4.6)$$

Where λ , A are the wavelength and transition probability, I define them as intensity, the statistical weight of the lower level of transition is denoted by g . Boltzmann constant is K and the excitation temperature is T in Kelvin. E is the energy of the upper level of transition in eV. In HDP, for line intensity ratio and electron density calculations, opted $1 [1s^2 2s^2 2p^6 3s (^2S_{1/2}) - 1s^2 2s^2 2p^6 3p (^2P_{3/2}^0)]$, $2 [1s^2 2s^2 2p^6 3s (^2S_{1/2}) - 1s^2 2s^2 2p^6 3p (^2P_{1/2}^0)]$ which signifies the two spectral lines.

For HDP is, using McWhirter criteria, the lowest or limiting value of electron density given by

$$n_e \geq 1.6 \times 10^{12} T^{(1/2)} (\Delta E)^3 \quad (4.7)$$

Here, T indicates plasma temperature (Kelvin), n_e is the electron density and ΔE ($= E_1 - E_2$) are in eV.

The line intensity ratio for various plasma temperature and electron density values is tabulated in Table 4.6. Figure 4.5 illustrates how the line intensity ratio varies with plasma temperature. For temperatures up to 10^8 K or 10 keV, the variation is exponential, but there is no visible change in the line intensity ratio for $T > 10^8$ K. In Figure 4.6, we can see that the value of limiting electron increases when plasma temperature density for Na-like K increases. One can also see that number of collisions in plasma increases as the temperature of the plasma increases. Thus, this knowledge of the Na-like K ion may be helpful in experiments for generating optically thin plasma in LTE at higher temperatures.

4.5 CONCLUSION

We present energy levels, oscillator strengths, lifetimes and radiative rates for KIX using the MCDF approach. We also included the radiative rates for E1, E2 transitions and M1, M2 transitions. The energy level gets significantly lowered by the inclusion of Breit and QED interaction. Two codes have been employed, and a discrepancy in the results for specific configuration effects is studied. The configuration interaction technique (CIV3) is also used to confirm the accuracy of energy levels further. Furthermore, we investigated the impact of plasma temperature on specific parameters for hot dense plasma under LTE conditions. We observed that the line intensity ratio and other HDP parameters follow the same increasing pattern with temperature. The coupling constant is used to justify the criteria for hot dense as well as weakly coupled plasma. Finally, we found our results agree well with those of NIST as well as other currently available data for the Na-like ion. Our predicted results will be advantageous for fusion, astrophysical, and modeling plasma.

Table 4.1: Optimized radial function parameters for KIX orbitals.

<i>Index</i>	<i>Orbitals</i>	<i>Expansion Coefficient</i> (C_{jnl})	<i>Power of r</i> (I_{jnl})	<i>Exponents</i> (ξ_{jnl})
1	3s	0.16176	1	15.12142
2		-0.68862	2	6.13565
3		1.24416	3	3.64032
4	3p	0.43914	2	7.52227
5		-1.07253	3	3.27788
6	3d	0.98536	3	3.34045
7		0.02931	3	1.33072
8	4s	0.09112	1	15.98915
9		-0.88510	2	4.34389
10		1.70496	3	3.80974
11		-1.46305	4	2.44421
12	4p	0.29338	2	7.39923
13		-2.25001	3	2.51208
14		2.68862	4	2.46779
15	4d	1.20871	3	3.12665
16		-0.94517	3	2.10347
17		-0.69516	4	2.02410
18	4f	0.99699	4	2.26388
19		0.00443	4	1.25500
20	5s	0.06640	1	15.42187
21		-0.35144	2	5.63762
22		3.08347	3	2.43066
23		-4.8871	4	2.41570
24		2.56806	5	1.95787
25	5p	0.20793	2	7.34390
26		-3.08584	3	2.12719
27		6.16703	4	2.11383
28		-3.76558	5	1.92848
29	5d	-8.77642	3	2.76996
30		10.14675	3	2.74226
31		-3.36111	4	2.22715
32		2.51054	4	1.52956
33	5f	0.00044	4	16.09914

<i>Index</i>	<i>Orbitals</i>	<i>Expansion Coefficient (C_{jnl})</i>	<i>Power of r (I_{jnl})</i>	<i>Exponents (ξ_{jnl})</i>
34		0.14035	4	3.61160
35		1.03329	5	2.61548
36		-1.51541	5	1.71092
37	5g	0.00025	5	4.20799
38		0.99990	5	1.800092
39	6s	0.05053	1	14.91064
40		-0.23734	2	5.97660
41		2.29375	3	2.36095
42		-8.33759	4	1.95361
43		10.79626	5	1.82830
44		-5.0116	6	1.63708
45	6p	0.15460	2	7.35732
46		-4.77672	3	1.74027
47		15.2788	4	1.73447
48		16.20815	5	1.73339
49		6.06590	6	1.58647
50	6d	-1.61789	3	3.15900
51		1.23157	3	2.97953
52		-0.97078	4	2.39659
53		9.22202	4	1.57132
54		-15.95991	5	1.54770
55		8.42515	6	1.51133
56	6f	0.00002	4	9.75067
57		0.18284	4	3.29274
58		5.26800	5	2.14267
59		-681061	5	1.92343
60		2.08775	6	1.38612
61	6g	0.00001	5	6.79284
62		1.85576	5	1.63032
63		-2.24040	6	1.47590

Where $\{(\xi_{jnl})\}$ are variables in the Breit – Pauli Hamiltonian matrix elements that depends on the interacting electrons l -value. $\xi(s) = 0.0$, $\xi(p) = 0.98$ and $\xi(d) = 0.39$.

Table 4.2: Comparison of the lowest 21 fine-structure levels of KIX calculated by us including threshold energies from many other sources.

<i>Index</i>	<i>Configuration</i>	<i>J</i>	<i>Term</i>	<i>MCDF1</i>	<i>MCDF2</i>	<i>CIV-3</i>	<i>FAC1</i>	<i>FAC2</i>	<i>NIST</i>	<i>Lifetime(MCDF1)</i>	<i>Lifetime (Fisher et al.)</i>
1	2p ⁶ 3s	1/2	² S _{1/2}	0.0000	0.0000	0.0000	0.0000	0.0000	0.0000	0.0000	0.0000
2	2p ⁶ 3p	1/2	² P ^o	1.4342	1.4446	1.4585	1.4345	1.4362	1.4320 1.4356 _a	3.289e-10	3.490e-10
3	2p ⁶ 3p	3/2	² P ^o	1.4681	1.4785	1.4858	1.4684	1.4702	1.4663 1.4710 _a	3.058e-10	3.232e-10
4	2p ⁶ 3d	3/2	² D	3.4184	3.4242	3.4603	3.4171	3.4211	3.4160 3.4329 _a	1.095e-10	1.136e-10
5	2p ⁶ 3d	5/2	² D	3.4205	3.4262	3.4618	3.4191	3.4231	3.4186 3.4355 _a	1.136e-10	1.181e-10
6	2p ⁶ 4s	1/2	² S	6.3415	6.3624	6.3575	6.3513	6.3529	6.3687 6.3841 _a	2.109e-11	2.018e-10
7	2p ⁶ 4p	1/2	² P ^o	6.8839	6.9120	6.9050	6.8956	6.8985	6.9098 6.9268 _a	3.374e-11	3.198e-11
8	2p ⁶ 4p	3/2	² P ^o	6.8967	6.9246	6.9181	6.9080	6.9110	6.9228 6.9402 _a	3.569e-11	3.268e-11
9	2p ⁶ 4d	3/2	² D	7.5993	7.6317	7.6309	7.7063	7.6129	7.6261 7.6473 _a	3.267e-11	3.198e-11
10	2p ⁶ 4d	5/2	² D	7.6003	7.6327	7.6317	7.6073	7.6139	7.6273 7.6487 _a	3.231e-11	3.061e-11
11	2p ⁶ 4f	5/2	² F ^o	7.8084	7.8210	7.8277	7.8286	7.8239	7.8846 7.8701 _a	0.998e-11	1.006e-11
12	2p ⁶ 4f	7/2	² F ^o	7.8088	7.8214	7.8277	7.8290	7.8243	7.8450 7.8707 _a	1.000e-11	1.007e-11
13	2p ⁶ 5s	1/2	² S	8.9221	8.9564	8.9416	8.9305	8.9349	8.9575	2.911e-11	
14	2p ⁶ 5p	1/2	² P ^o	9.1831	9.2202	9.2061	9.1928	9.1984	9.2176	4.422e-11	
15	2p ⁶ 5p	3/2	² P ^o	9.1892	9.2262	9.2123	9.1987	9.2044	9.2239	5.181e-11	
16	2p ⁶ 5d	3/2	² D	9.5246	9.5655	9.5568	9.5311	9.5389	9.5596	4.195e-11	
17	2p ⁶ 5d	5/2	² D	9.5251	9.5660	9.5573	9.5316	9.5394	9.5604	3.933e-11	
18	2p ⁶ 5f	5/2	² F ^o	9.6331	9.6624	9.6549	9.6443	9.6477	9.6722	1.840e-11	

19	$2p^6 5f$	7/2	$^2F^0$	9.6333	9.6626	9.6550	9.6556	9.6479	9.6723	1.842e-11	
20	$2p^6 5g$	5/2	2G	9.6432	9.6674	9.6616	9.6556	9.6546		3.571e-11	
21	$2p^6 5g$	7/2	2G	9.6433	9.6675	9.6616	9.6557	9.6548		3.571e-11	

^aFischer et al.²³ and the values without superscript in column 10 denotes the data taken from NIST.²⁴

Table 4.3: The MCDF method to calculate fine structure energy (in Ryd) as a component of rising active sets of orbitals for the lowest 21 levels of KIX.

<i>Index</i>	<i>Configuration</i>	<i>J</i>	<i>Term</i>	<i>n = 3</i>	<i>n = 4</i>	<i>n = 5</i>	<i>n = 6</i>	<i>NIST</i>
1	2p ⁶ 3s	1/2	² S	0.000000	0.000000	0.000000	0.000000	0.000000
2	2p ⁶ 3p	1/2	² P ^o	1.434004	1.434209	1.434293	1.434323	1.432078
3	2p ⁶ 3p	3/2	² P ^o	1.467905	1.468091	1.468165	1.468192	1.466352
4	2p ⁶ 3d	3/2	² D	3.41847	3.418428	3.41845	3.418466	3.416039
5	2p ⁶ 3d	5/2	² D	3.42051	3.420481	3.42050	3.42052	3.41863
6	2p ⁶ 4s	1/2	² S		6.34241	6.34159	6.34129	6.36878
7	2p ⁶ 4p	1/2	² P ^o		6.8847	6.8839	6.8837	6.9098
8	2p ⁶ 4p	3/2	² P ^o		6.8974	6.8967	6.8964	6.9228
9	2p ⁶ 4d	3/2	² D		7.6003	7.5993	7.5990	7.6261
10	2p ⁶ 4d	5/2	² D		7.6011	7.6003	7.6000	7.6273
11	2p ⁶ 4f	5/2	² F ^o		7.80957	7.80841	7.80798	7.88463
12	2p ⁶ 4f	7/2	² F ^o		7.8100	7.8088	7.80841	7.84500
13	2p ⁶ 5s	1/2	² S			8.92214	8.92176	8.9575
14	2p ⁶ 5p	1/2	² P ^o			9.1831	9.1827	9.2176
15	2p ⁶ 5p	3/2	² P ^o			9.1892	9.1888	9.2239
16	2p ⁶ 5d	3/2	² D			9.5246	9.5242	9.5596
17	2p ⁶ 5d	5/2	² D			9.5251	9.5248	9.5604
18	2p ⁶ 5f	5/2	² F ^o			9.6331	9.6389	9.6722
19	2p ⁶ 5f	7/2	² F ^o			9.6333	9.6390	9.6723
20	2p ⁶ 5g	5/2	² G			9.6432	9.6432	
21	2p ⁶ 5g	7/2	² G			9.6433	9.6433	
22	2p ⁶ 6s	1/2	² S				10.2268	10.2655
23	2p ⁶ 6p	1/2	² P ^o				10.3718	10.4104
24	2p ⁶ 6p	3/2	² P ^o				10.3753	10.4135
25	2p ⁶ 6d	3/2	² D				10.5618	10.6003
26	2p ⁶ 6d	5/2	² D				10.5621	10.6009
27	2p ⁶ 6f	5/2	² F ^o				10.6248	10.6657
28	2p ⁶ 6f	7/2	² F ^o				10.6289	10.6658
29	2p ⁶ 6g	5/2	² G				10.6328	10.6328
30	2p ⁶ 6g	7/2	² G				10.6329	10.6329

Table 4.4: Energy levels for the $2p^6nl(n \leq 10)$ fine-structure levels for KIX (in Ryd).

<i>Index</i>	<i>Configuration</i>	<i>Level</i>	<i>FAC3</i>	<i>NIST</i>
1	$2p^6 3s$	$^2S_{1/2}$	0.0000	0.000000
2	$2p^6 3p$	$^2P_{1/2}^0$	1.4340	1.432078
3	$2p^6 3p$	$^2P_{3/2}^0$	1.4680	1.466352
4	$2p^6 3d$	$^2D_{3/2}$	3.4172	3.416039
5	$2p^6 3d$	$^2D_{5/2}$	3.4192	3.41863
6	$2p^6 4s$	$^2S_{1/2}$	6.3513	6.36878
7	$2p^6 4p$	$^2P_{1/2}^0$	6.8948	6.9098
8	$2p^6 4p$	$^2P_{3/2}^0$	6.9074	6.9228
9	$2p^6 4d$	$^2D_{3/2}$	7.6063	7.6261
10	$2p^6 4d$	$^2D_{5/2}$	7.6072	7.6273
11	$2p^6 4f$	$^2F_{5/2}^0$	7.8287	7.88463
12	$2p^6 4f$	$^2F_{7/2}^0$	7.8290	7.84500
13	$2p^6 5s$	$^2S_{1/2}$	8.9303	8.9575
14	$2p^6 5p$	$^2P_{1/2}^0$	9.1920	9.2176
15	$2p^6 5p$	$^2P_{3/2}^0$	9.1980	9.2239
16	$2p^6 5d$	$^2D_{3/2}$	9.5309	9.5596
17	$2p^6 5d$	$^2D_{5/2}$	9.5315	9.5604
18	$2p^6 5f$	$^2F_{5/2}^0$	9.6442	9.6722
19	$2p^6 5f$	$^2F_{7/2}^0$	9.6444	9.6723
20	$2p^6 5g$	$^2G_{7/2}$	9.6557	
21	$2p^6 5g$	$^2G_{9/2}$	9.6558	
22	$2p^6 6s$	$^2S_{1/2}$	10.2335	10.2655
23	$2p^6 6p$	$^2P_{1/2}^0$	10.3791	10.4104

<i>Index</i>	<i>Configuration</i>	<i>Level</i>	<i>FAC3</i>	<i>NIST</i>
24	2p ⁶ 6p	$^2P_{3/2}^0$	10.3825	10.4135
25	2p ⁶ 6d	$^2D_{3/2}$	10.5674	10.6003
26	2p ⁶ 6d	$^2D_{5/2}$	10.5677	10.6009
27	2p ⁶ 6f	$^2F_{5/2}^0$	10.6328	10.6657
28	2p ⁶ 6f	$^2F_{7/2}^0$	10.6329	10.6658
29	2p ⁶ 6g	$^2G_{7/2}$	10.6391	10.6328
30	2p ⁶ 6g	$^2G_{9/2}$	10.6392	10.6329
31	2p ⁶ 6h	$^2H_{9/2}^0$	10.6418	
32	2p ⁶ 6h	$^2H_{11/2}^0$	10.6419	
33	2p ⁶ 7s	$^2S_{1/2}$	10.9836	11.0185
34	2p ⁶ 7p	$^2P_{1/2}^0$	11.0727	11.1082
35	2p ⁶ 7p	$^2P_{3/2}^0$	11.0748	11.1082
36	2p ⁶ 7d	$^2D_{3/2}$	11.1882	11.2233
37	2p ⁶ 7d	$^2D_{5/2}$	11.1884	11.2235
38	2p ⁶ 7f	$^2F_{5/2}^0$	11.2293	11.2644
39	2p ⁶ 7f	$^2F_{7/2}^0$	11.2293	11.2647
40	2p ⁶ 7g	$^2G_{7/2}$	11.2330	
41	2p ⁶ 7g	$^2G_{9/2}$	11.2331	
42	2p ⁶ 7h	$^2H_{9/2}^0$	11.2347	
43	2p ⁶ 7h	$^2H_{11/2}^0$	11.2347	
44	2p ⁶ 7i	$^2I_{11/2}$	11.2360	
45	2p ⁶ 7i	$^2I_{13/2}$	11.2360	
46	2p ⁶ 8s	$^2S_{1/2}$	11.4547	

<i>Index</i>	<i>Configuration</i>	<i>Level</i>	<i>FAC3</i>	<i>NIST</i>
47	2p ⁶ 8p	$^2P_{1/2}^0$	11.5131	11.5493
48	2p ⁶ 8p	$^2P_{3/2}^0$	11.5145	11.5493
49	2p ⁶ 8d	$^2D_{3/2}$	11.5890	11.6257
50	2p ⁶ 8d	$^2D_{5/2}$	11.5892	11.6258
51	2p ⁶ 8f	$^2F_{5/2}^0$	11.6166	11.6538
52	2p ⁶ 8f	$^2F_{7/2}^0$	11.6166	11.6538
53	2p ⁶ 8g	$^2G_{7/2}$	11.6189	
54	2p ⁶ 8g	$^2G_{9/2}$	11.6190	
55	2p ⁶ 8h	$^2H_{9/2}^0$	11.6200	
56	2p ⁶ 8h	$^2H_{11/2}^0$	11.6200	
57	2p ⁶ 8i	$^2I_{11/2}$	11.6209	
58	2p ⁶ 8i	$^2I_{13/2}$	11.6209	
59	2p ⁶ 8k	$^2K_{13/2}^0$	11.6216	
60	2p ⁶ 8k	$^2K_{15/2}^0$	11.6216	
61	2p ⁶ 9s	$^2S_{1/2}$	11.7698	
62	2p ⁶ 9p	$^2P_{1/2}^0$	11.8103	11.8480
63	2p ⁶ 9p	$^2P_{3/2}^0$	11.8112	11.8480
64	2p ⁶ 9d	$^2D_{3/2}$	11.8628	11.8987
65	2p ⁶ 9d	$^2D_{5/2}$	11.8629	11.8893
66	2p ⁶ 9f	$^2F_{5/2}^0$	11.8822	11.9194
67	2p ⁶ 9f	$^2F_{7/2}^0$	11.8822	11.9194
68	2p ⁶ 9g	$^2G_{7/2}$	11.8837	
69	2p ⁶ 9g	$^2G_{9/2}$	11.8838	

<i>Index</i>	<i>Configuration</i>	<i>Level</i>	<i>FAC3</i>	<i>NIST</i>
70	2p ⁶ 9h	$^2\text{H}_{9/2}^0$	11.8844	
71	2p ⁶ 9h	$^2\text{H}_{11/2}^0$	11.8844	
72	2p ⁶ 9i	$^2\text{I}_{11/2}$	11.8851	
73	2p ⁶ 9i	$^2\text{I}_{13/2}$	11.8851	
74	2p ⁶ 9k	$^2\text{K}_{13/2}^0$	11.8856	
75	2p ⁶ 9k	$^2\text{K}_{15/2}^0$	11.8856	
76	2p ⁶ 9l	$^2\text{L}_{15/2}$	11.8860	
77	2p ⁶ 9l	$^2\text{L}_{17/2}$	11.8860	
78	2p ⁶ 10s	$^2\text{S}_{1/2}$	11.9911	
79	2p ⁶ 10p	$^2\text{P}_{1/2}^0$	12.0202	
80	2p ⁶ 10p	$^2\text{P}_{3/2}^0$	12.0208	
81	2p ⁶ 10d	$^2\text{D}_{3/2}$	12.0581	12.0956
82	2p ⁶ 10d	$^2\text{D}_{5/2}$	12.0582	
83	2p ⁶ 10f	$^2\text{F}_{5/2}^0$	12.0722	
84	2p ⁶ 10f	$^2\text{F}_{7/2}^0$	12.0722	
85	2p ⁶ 10g	$^2\text{G}_{7/2}$	12.0733	
86	2p ⁶ 10g	$^2\text{G}_{9/2}$	12.0733	
87	2p ⁶ 10h	$^2\text{H}_{9/2}^0$	12.0737	
88	2p ⁶ 10h	$^2\text{H}_{11/2}^0$	12.0737	
89	2p ⁶ 10i	$^2\text{I}_{11/2}$	12.0742	
90	2p ⁶ 10i	$^2\text{I}_{13/2}$	12.0742	
91	2p ⁶ 10k	$^2\text{K}_{13/2}^0$	12.0745	
92	2p ⁶ 10k	$^2\text{K}_{15/2}^0$	12.0746	
93	2p ⁶ 10l	$^2\text{L}_{15/2}$	12.0749	
94	2p ⁶ 10l	$^2\text{L}_{17/2}$	12.0749	

<i>Index</i>	<i>Configuration</i>	<i>Level</i>	<i>FAC3</i>	<i>NIST</i>
95	2p ⁶ 10m	² M _{17/2} ⁰	12.0752	
96	2p ⁶ 10m	² M _{19/2} ⁰	12.0752	

Table 4.5: The electron density (ne in cm-3) and line intensity ratio (R) for KIX are shown against plasma temperature (T in K).

<i>Index</i>	<i>Temperature (K)</i>	<i>Line Intensity Ratio (R)</i>	<i>Number of electron density (ne in cm⁻³)</i>
1	2 X 10 ⁶	1.09823	0.22 X 10 ¹⁵
2	4 X 10 ⁶	1.09974	0.31 X 10 ¹⁵
3	6 X 10 ⁶	1.10019	0.38 X 10 ¹⁵
4	8 X 10 ⁶	1.10043	0.44 X 10 ¹⁵
5	1 X 10 ⁷	1.10058	0.49 X 10 ¹⁸
6	1 X 10 ⁸	1.10111	0.15 X 10 ¹⁹
7	1 X 10 ⁹	1.10116	0.49 X 10 ¹⁹
8	1 X 10 ¹⁰	1.10117	0.15 X 10 ²⁰

Table 4.6: Radiative rates (A_{ji} in s-1), transition wavelengths (λ_{ij} in Å°), line strengths (S in atomic units) and also oscillator strengths (f_{ij}, dimensionless) of KIX for E1,E2,M1 as well as M2. R(E1) is the ratio of the velocity and length forms of A-values for E1 transitions within last column.

I	J	λ _{ij}	A _{ji} ^{E1}	f _{ij} ^{E1}	S ^{E1}	A _{ji} ^{E2}	A _{ji} ^{M1}	A _{ji} ^{M2}	R ^{E1}
1	2	6.35E+02	3.04E+09	1.84E-01	7.69E-01	0.00E+00	0.00E+00	0.00E+00	1.00E+00
1	3	6.21E+02	3.27E+09	3.77E-01	1.54E+00	0.00E+00	0.00E+00	9.36E-01	1.00E+00
1	4	2.67E+02	0.00E+00	0.00E+00	0.00E+00	2.73E+05	3.90E-03	0.00E+00	0.00E+00
1	5	2.66E+02	0.00E+00	0.00E+00	0.00E+00	2.74E+05	0.00E+00	0.00E+00	0.00E+00
1	6	1.44E+02	0.00E+00	0.00E+00	0.00E+00	0.00E+00	7.05E-01	0.00E+00	0.00E+00
1	7	1.32E+02	1.70E+10	4.46E-02	3.89E-02	0.00E+00	0.00E+00	0.00E+00	9.80E-01
1	8	1.32E+02	1.63E+10	8.56E-02	7.44E-02	0.00E+00	0.00E+00	1.03E+02	9.80E-01
1	9	1.20E+02	0.00E+00	0.00E+00	0.00E+00	4.60E+06	6.16E-04	0.00E+00	0.00E+00
1	10	1.20E+02	0.00E+00	0.00E+00	0.00E+00	9.90E-01	0.00E+00	0.00E+00	0.00E+00
1	11	1.17E+02	0.00E+00	0.00E+00	0.00E+00	0.00E+00	0.00E+00	2.50E-06	0.00E+00
1	13	1.20E+02	0.00E+00	0.00E+00	0.00E+00	0.00E+00	7.71E-01	0.00E+00	0.00E+00

I	J	λ_{ij}	A_{ji}^{E1}	f_{ij}^{E1}	S^{E1}	A_{ji}^{E2}	A_{ji}^{M1}	A_{ji}^{M2}	R^{E1}
1	14	9.92E+01	1.03E+10	1.53E-02	9.97E-03	0.00E+00	0.00E+00	0.00E+00	9.80E-01
1	15	9.92E+01	1.00E+10	2.95E-02	1.93E-02	0.00E+00	0.00E+00	1.13E+08	9.80E-01
1	16	9.57E+01	0.00E+00	0.00E+00	0.00E+00	9.80E-01	2.36E-03	0.00E+00	0.00E+00
1	17	9.57E+01	0.00E+00	0.00E+00	0.00E+00	9.80E-01	0.00E+00	0.00E+00	0.00E+00
1	18	9.46E+01	0.00E+00	0.00E+00	0.00E+00	0.00E+00	0.00E+00	1.78E-06	0.00E+00
2	3	2.69E+04	0.00E+00	0.00E+00	0.00E+00	2.97E+05	4.62E-01	0.00E+00	0.00E+00
2	4	4.59E+02	7.67E+09	4.85E-01	1.47E+00	0.00E+00	0.00E+00	1.61E-01	1.10E+00
2	5	5.59E+02	0.00E+00	0.00E+00	0.00E+00	0.00E+00	0.00E+00	1.51E+00	0.00E+00
2	6	1.86E+02	1.57E+10	8.10E-02	9.90E-02	0.00E+00	0.00E+00	0.00E+00	1.00E+00
2	7	1.66E+02	0.00E+00	0.00E+00	0.00E+00	0.00E+00	1.54E-01	0.00E+00	0.00E+00
2	8	1.66E+02	0.00E+00	0.00E+00	0.00E+00	0.00E+00	2.58E+01	0.00E+00	0.00E+00
2	9	1.48E+02	2.39E+10	1.57E-01	1.53E-01	0.00E+00	0.00E+00	4.84E+00	9.50E-01
2	10	1.48E+02	0.00E+00	0.00E+00	0.00E+00	0.00E+00	0.00E+00	3.43E+01	0.00E+00
2	11	1.43E+02	0.00E+00	0.00E+00	0.00E+00	9.46+06	0.00E+00	0.00E+00	0.00E+00
2	13	1.22E+02	6.68E+09	1.48E-02	1.19E-02	0.00E+00	0.00E+00	0.00E+00	1.00E+00
2	14	1.18E+02	0.00E+00	0.00E+00	0.00E+00	0.00E+00	1.76E-01	0.00E+00	0.00E+00
2	15	1.18E+02	0.00E+00	0.00E+00	0.00E+00	7.51E+05	1.73E+01	0.00E+00	0.00E+00
2	16	1.13E+02	1.66E+10	6.33E-02	4.70E-02	0.00E+00	0.00E+00	5.79E+00	9.50E-01
2	17	1.13E+02	0.00E+00	0.00E+00	0.00E+00	0.00E+00	0.00E+00	4.11E+01	0.00E+00
2	18	1.11E+02	0.00E+00	0.00E+00	0.00E+00	2.69E+06	0.00E+00	0.00E+00	0.00E+00
3	4	4.67E+02	1.46E+09	4.78E-02	2.94E-01	0.00E+00	0.00E+00	0.00E+00	1.10E+00
3	5	4.67E+02	8.80E+09	4.31E-01	2.65E+00	0.00E+00	0.00E+00	5.78E+00	1.10E+00
3	6	1.87E+02	3.17E+10	8.31E-02	2.05E-01	0.00E+00	0.00E+00	1.00E+02	1.00E+00
3	7	1.68E+02	0.00E+00	0.00E+00	0.00E+00	2.76E+06	5.83E+01	0.00E+00	0.00E+00
3	8	1.68E+02	0.00E+00	0.00E+00	0.00E+00	1.38E+06	9.30E-01	0.00E+00	0.00E+00
3	9	1.49E+02	4.88E+09	1.62E-02	3.16E-02	0.00E+00	0.00E+00	0.00E+00	9.50E-01
3	10	1.49E+02	2.92E+10	1.45E-01	2.84E-01	0.00E+00	0.00E+00	1.89E+02	9.50E-01
3	11	1.44E+02	0.00E+00	0.00E+00	0.00E+00	2.67E+06	2.54E-02	0.00E+00	0.00E+00
3	12	1.44E+02	0.00E+00	0.00E+00	0.00E+00	1.20E+07	0.00E+00	0.00E+00	0.00E+00
3	13	1.22E+02	1.35E+10	1.51E-02	2.43E-02	0.00E+00	0.00E+00	9.95E+01	1.00E+00
3	14	1.18E+02	0.00E+00	0.00E+00	0.00E+00	1.48E+06	4.07E+01	0.00E+00	0.00E+00
3	15	1.18E+02	0.00E+00	0.00E+00	0.00E+00	7.41E+05	1.05E+00	0.00E+00	0.00E+00

I	J	λ_{ij}	A_{ji}^{E1}	f_{ij}^{E1}	S^{E1}	A_{ji}^{E2}	A_{ji}^{M1}	A_{ji}^{M2}	R^{E1}
3	16	1.13E+02	3.37E+09	6.46E-03	9.62E-03	0.00E+00	0.00E+00	0.00E+00	9.50E-01
3	17	1.13E+02	2.02E+10	5.80E-02	8.64E-02	0.00E+00	0.00E+00	2.26E+02	9.50E-01
3	18	1.12E+02	0.00E+00	0.00E+00	0.00E+00	7.49E+05	1.85E-02	0.00E+00	0.00E+00
3	19	1.12E+02	0.00E+00	0.00E+00	0.00E+00	3.37E+06	0.00E+00	0.00E+00	0.00E+00
3	20	1.12E+02	0.00E+00	0.00E+00	0.00E+00	0.00E+00	0.00E+00	1.29E-06	0.00E+00
4	5	4.44E+05	0.00E+00	0.00E+00	0.00E+00	6.65E-12	1.24E-04	0.00E+00	0.00E+00
4	6	3.12E+02	0.00E+00	0.00E+00	0.00E+00	1.95E+05	2.53E-09	0.00E+00	0.00E+00
4	7	2.63E+02	1.12E+10	5.79E-02	2.01E-01	0.00E+00	0.00E+00	7.13E-01	1.10E+00
4	8	2.62E+02	1.10E+09	1.14E-02	3.92E-02	0.00E+00	0.00E+00	0.00E+00	1.10E+00
4	9	0.00E+00	0.00E+00	0.00E+00	0.00E+00	4.88E+05	1.25E-01	0.00E+00	0.00E+00
4	10	0.00E+00	0.00E+00	0.00E+00	0.00E+00	1.39E+05	4.68E-02	0.00E+00	0.00E+00
4	11	2.08E+02	9.35E+10	9.06E-01	2.48E+00	0.00E+00	0.00E+00	5.70E+01	9.90E-01
4	12	2.08E+02	0.00E+00	0.00E+00	0.00E+00	0.00E+00	0.00E+00	7.30E+01	0.00E+00
4	13	1.66E+02	0.00E+00	0.00E+00	0.00E+00	6.95E+04	1.19E-06	0.00E+00	0.00E+00
4	14	1.58E+02	4.20E+09	7.86E-03	1.64E-02	0.00E+00	0.00E+00	7.42E-01	1.10E+00
4	15	1.58E+02	4.15E+08	1.55E-03	3.23E-03	0.00E+00	0.00E+00	0.00E+00	1.10E+00
4	16	1.49E+02	0.00E+00	0.00E+00	0.00E+00	2.27E+05	1.37E-01	0.00E+00	0.00E+00
4	17	1.49E+02	0.00E+00	0.00E+00	0.00E+00	1.49E+02	2.92E-02	0.00E+00	0.00E+00
4	18	1.47E+02	3.55E+10	1.72E-01	3.32E-01	0.00E+00	0.00E+00	4.34E+01	9.90E-01
4	19	1.47E+02	0.00E+00	0.00E+00	0.00E+00	0.00E+00	0.00E+00	55.56+01	0.00E+00
4	20	1.46E+02	0.00E+00	0.00E+00	0.00E+00	5.49E+06	0.00E+00	0.00E+00	0.00E+00
5	6	3.12E+02	0.00E+00	0.00E+00	0.00E+00	2.19E+05	0.00E+00	0.00E+00	0.00E+00
5	7	2.63E+02	0.00E+00	0.00E+00	0.00E+00	0.00E+00	0.00E+00	7.61E+00	0.00E+00
5	8	2.62E+02	9.94E+09	6.83E-02	3.54E-01	0.00E+00	0.00E+00	2.07E+01	1.10E+00
5	9	2.18E+02	0.00E+00	0.00E+00	0.00E+00	2.09E+05	2.47E-01	0.00E+00	0.00E+00
5	10	2.18E+02	0.00E+00	0.00E+00	0.00E+00	5.57E+05	4.23E-01	0.00E+00	0.00E+00
5	11	2.08E+02	6.68E+09	4.32E-02	1.77E-01	0.00E+00	0.00E+00	0.00E+00	9.90E-01
5	12	2.08E+02	1.00E+11	8.64E-01	3.54E+00	0.00E+00	0.00E+00	5.03E+02	9.90E-01
5	13	1.66E+02	0.00E+00	0.00E+00	0.00E+00	1.04E+05	0.00E+00	0.00E+00	0.00E+00
5	14	1.58E+02	0.00E+00	0.00E+00	0.00E+00	0.00E+00	0.00E+00	7.90E+00	0.00E+00
5	15	1.58E+02	3.74E+09	9.32E-03	2.91E-02	0.00E+00	0.00E+00	2.14E+01	1.10E+00
5	16	1.49E+02	0.00E+00	0.00E+00	0.00E+00	9.71E+04	2.03E-01	0.00E+00	0.00E+00

I	J	λ_{ij}	A_{ji}^{E1}	f_{ij}^{E1}	S^{E1}	A_{ji}^{E2}	A_{ji}^{M1}	A_{ji}^{M2}	R^{E1}
5	17	1.49E+02	0.00E+00	0.00E+00	0.00E+00	2.59E+05	4.60E-01	0.00E+00	0.00E+00
5	18	1.47E+02	2.54E+09	8.18E-03	2.37E-02	0.00E+00	0.00E+00	0.00E+00	9.90E-01
5	19	1.47E+02	3.80E+10	1.64E-01	4.74E-01	0.00E+00	0.00E+00	3.82E+02	9.90E-01
5	20	1.47E+02	0.00E+00	0.00E+00	0.00E+00	6.10E-05	5.14E-03	0.00E+00	0.00E+00
5	21	1.47E+02	0.00E+00	0.00E+00	0.00E+00	6.10E-05	0.00E+00	0.00E+00	0.00E+00

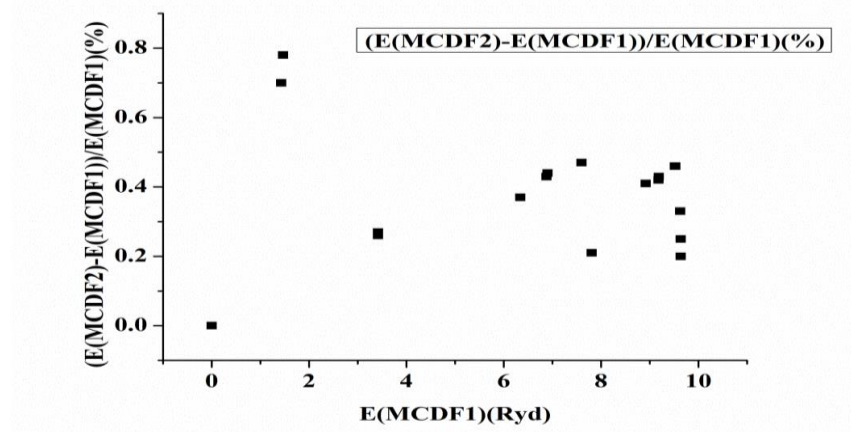


Figure 4.1: The influence of correlations on the energy of the lowest 21 levels of KIX was studied using MCDF

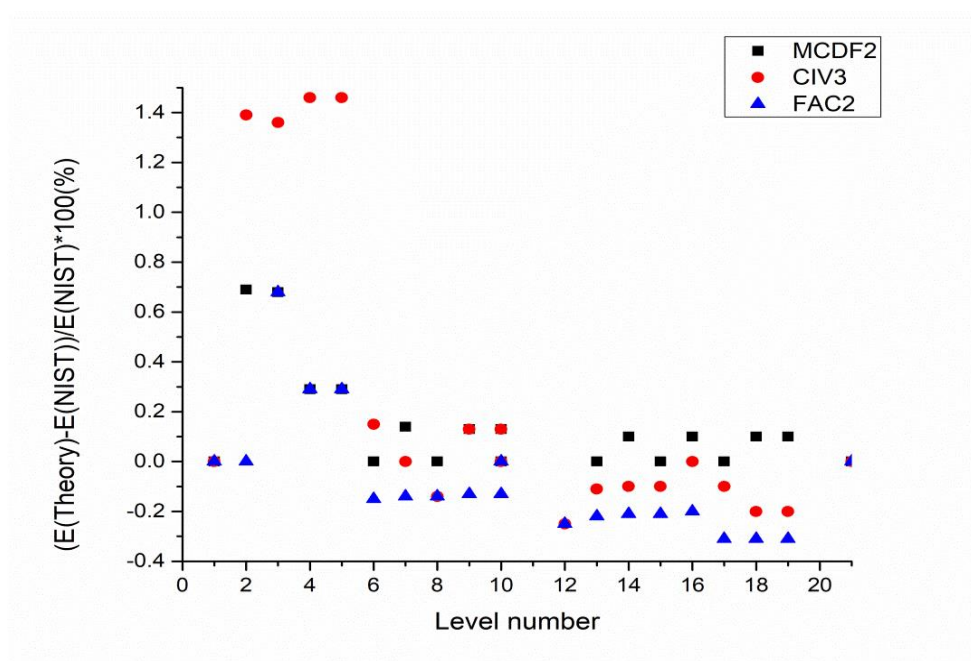


Figure 4.2: For lowest 21 levels of KIX, the percentage differences among appropriate theoretical energies as well as NIST values were calculated.

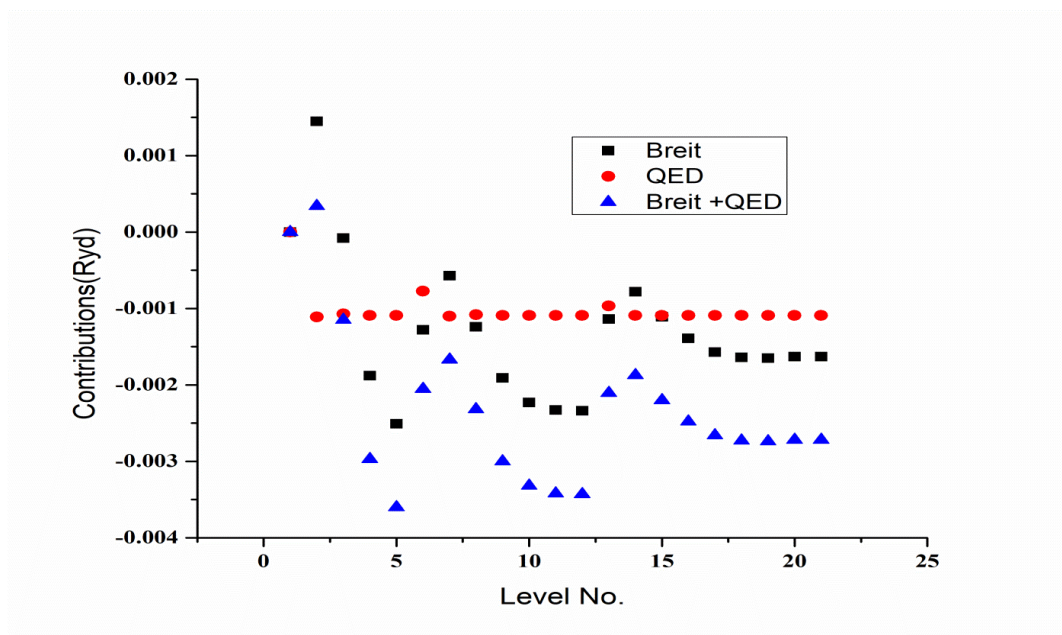


Figure 4.3: At the lowest 21 levels, BI and QED contribute to MCDF2 energy for KIX.

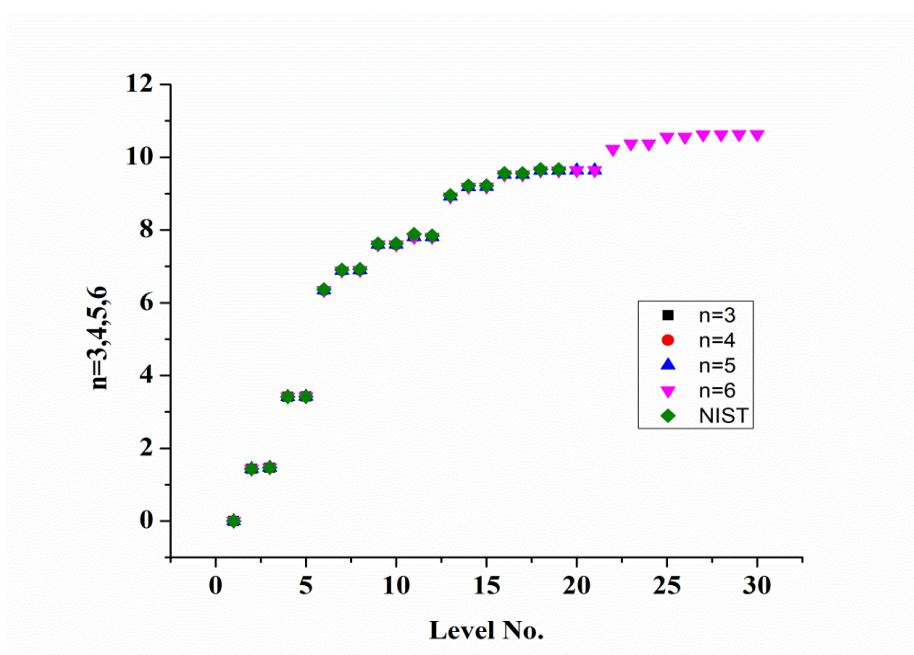


Figure 4.4: Variations of increasing active sets of orbitals (in Ryd) using the MCDF approach for the lowest 21 levels of KIX.

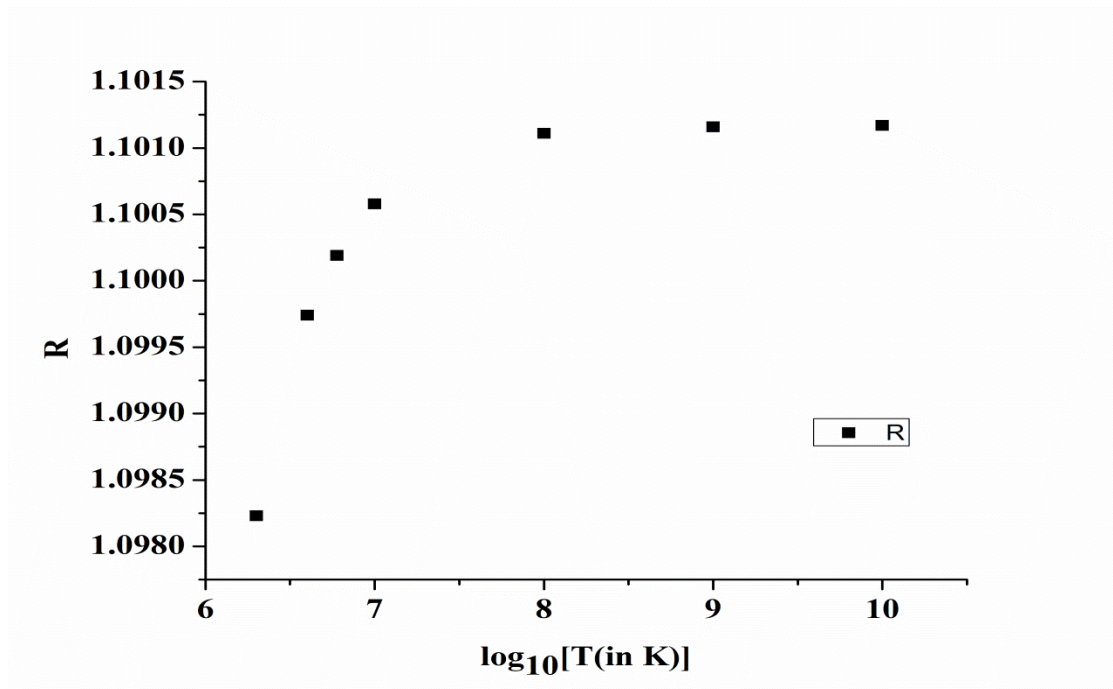


Figure 4.5: Line intensity ratios for spectral lines 1 and 2 as a function of plasma temperature for KIX.

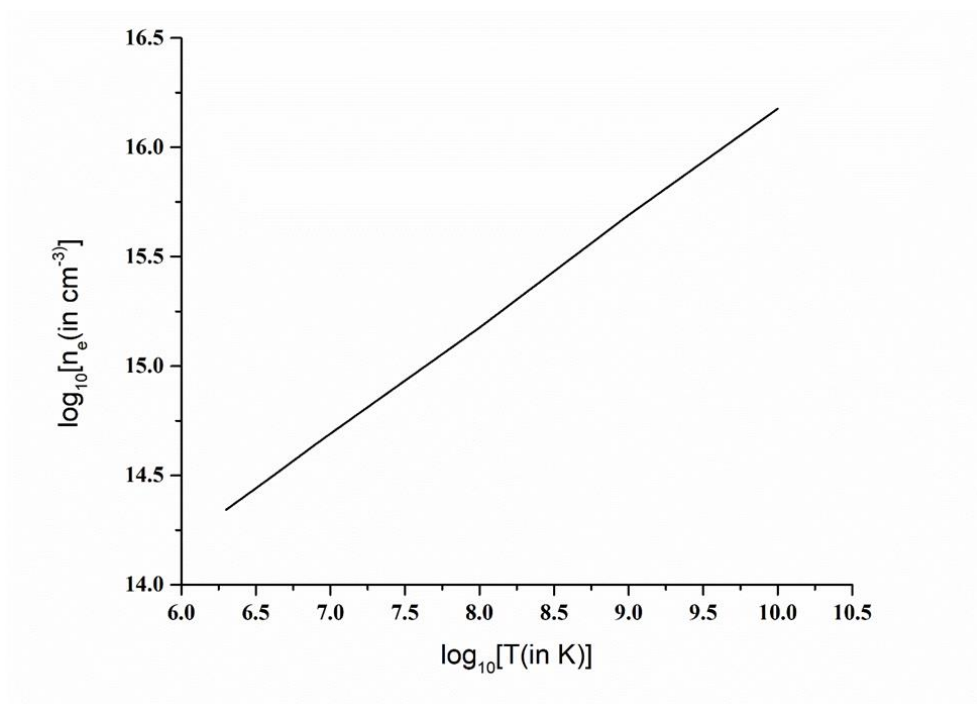


Figure 4.6: For spectral lines 1 and 2, KIX electron density varies with plasma temperature.

4.6 REFERENCES

- [1] A.K. Singh, Mayank Dimri, Dishu Dawra, Alok K.S. Jha, Man Mohan, *Physics of Plasmas* 26,062704(2019); <https://doi.org/10.1063/1.5100565> .
- [2] I.Martinson, Volume 43, pages 323-332, 1989, [https://doi.org/10.1016/0168-583X\(89\)90372-8](https://doi.org/10.1016/0168-583X(89)90372-8) .
- [3] H.Fiedorowicz, A.Bartnik, and Z.Patron, *Appl.Phys.Lett.* 62,2778(1993); <https://doi.org/10.1063/1.109232>
- [4] Narendra Singh, Arun Goyal, Man Mohan, *Journal of Electron Spectroscopy and Related Phenomenon*, <https://doi.org/10.1016/j.elspec.2018.10.003> .
- [5] A.K. Singh, Mayank Dimri, Dishu Dawra, Alok K.S. Jha, Nupur Verma, Man Mohan, *Radiation Physics and Chemistry*, Volume 156, P.174-192. <https://doi.org/10.1016/j.radphyschem.2018.11.002> .
- [6] Douglas H. Sampson, Hong Lin Zhang, And Christopher J. Fontes, *Atomic Data and Nuclear Data Tables*, 44, 209-271(1990).
- [7] A.K. Singh, Mayank Dimri, Dishu Dawra, Alok K.S. Jha, Man Mohan, *Canadian, Journal of Physics*, Vol97.No.4, April 2019, <https://doi.org/10.1139/cjp-2018-0218> .
- [8] K. J. H. Phillips, J. Sylwester , B. Sylwester, E. Landi, *The Astrophysical Journal*, 589:L113–L116, 2003 June, DOI: <https://doi.org/10.1086/37585310.1086/375853>
- [9] A. Mucciarelli, T. Merle and M. Bellazzini, *Astronomy & Astrophysics*, Vol. 600, A104 (2017), <https://doi.org/10.1051/0004-6361/201730410> .
- [10] Bengt Edlen and Erik Boden, *Physica Scripta*, 1976, Vol. 14, 31-38.
- [11] Elmar Träbert, *Atoms* 2019, 7, 103; doi: <https://doi.org/10.3390/atoms7040103> .
- [12] C Jupen, L Engstrom, R Hutton and E Trabert, 1988 *J. Phys. B: At. Mol. Opt. Phys.* 21 L347, DOI: <http://iopscience.iop.org/0953-4075/21/12/004> .
- [13] W. Siegel And J. Migdalek, *Atomic Data And Nuclear Data Tables* 68, 303–322

- (1998) <https://doi.org/10.1006/adnd.1997.0769> .
- [14] W.O. Younis, S.H. Allam, Th.M. El-Sherbini, Atomic Data and Nuclear Data Tables 92 (2006) 187–05, <https://doi.org/10.1016/j.adt.2005.11.001> .
- [15] L. N. Ivanov And E. P. Ivanova, Atomic Data And Nuclear Data Tables 24, 95-109 (1979).
- [16] Douglas H. Sampson, Hong Lin Zhang, And Christopher J. Fontes, Atomic Data And Nuclear Data Tables 44,209-27 1 (1990) , [https://doi.org/10.1016/0092-640X\(90\)90014-B](https://doi.org/10.1016/0092-640X(90)90014-B) .
- [17] Y.K. Kim, D. H. Baik, and P. Indelicato, Physical Review A.1 JULY 1991, VOLUME 44, NUMBER 1.
- [18] W. R. Johnson, Z. W. Liu, And J. Sapirstein, Atomic Data And Nuclear Data Tables 64, 279–300 (1996).
- [19] Christopher J. Fontes, Hong Lin Zhang, Atomic Data and Nuclear Data Tables,2016, <http://dx.doi.org/10.1016/j.adt.2016.04.001> .
- [20] U. I. Safronova, W. R. Johnson and M. S. Safronova, PHYSICAL REVIEW A 66, 042506,2002, DOI: <http://dx.doi.org/10.1103/PhysRevA.66.042506> .
- [21] J. E. Sansonetti , Phys. Chem. Ref. Data, Vol. 37, No. 1, 2008.
- [22] Leonard Cohen and W. E. Behring, J. Opt. Soc. Am., Vol. 66, No. 9, September 1976.
- [23] Bengt Edlen and Erik Boden, Physica Scripta. Vol. 14, 31-38, 1976, DOI: <http://iopscience.iop.org/1402-4896/14/1-2/007> .
- [24] J. D. Gillaspay, D. Osin, Yu. Ralchenko, J. Reader and S. A. Blundell², Physical Review A 87, 062503 (2013), DOI: <http://dx.doi.org/10.1103/PhysRevA.87.062503> .
- [25] Charlotte Froese Fischer, Georgio Tachiev, Andrei Irimia, Atomic Data and Nuclear Data Tables 92 (2006) 607–812, <http://dx.doi.org/10.1016/j.adt.2006.03.001> .
- [26] A. Kramida, Yu. Ralchenko, J. Reader, and NIST ASD Team, <https://dx.doi.org/10.1016/j.adt.2006.03.001> for NIST Atomic Spectra Database (ver. 5.6.1)

(2019).

- [27] I. P. Grant, B. J. McKenzie, P. H. Norrington, D. F. Mayers, and N. C. Pyper, Comput. Phys. Commun. 21, 207 (1980).
- [28] M. F. Gu, Can. J. Phys. 86, 675 (2008).
- [29] A. Hibbert, Comput. Phys. Commun. 9, 141 (1975).

CHAPTER 5

THEORETICAL STUDY OF THE ATOMIC PARAMETERS, PLASMA PARAMETERS AND PHOTOIONIZATION OF WLXIV.

- In this chapter, we have presented atomic data including energies, transition wavelengths, radiative rates, oscillator strengths, are evaluated for W LXIV, for the lowest 100 fine structure levels and multipole transitions(E1, E2, M1 and also for M2).
- For W LXIV, we identified the 21 in electric dipole, 33 in electric quadrupole, 28 in magnetic dipole and 21 in magnetic quadrupole soft x-ray (SXR) transitions, as well as 1 in electric dipole extreme ultraviolet (EUV) transitions from the ground state.
- Furthermore, we have analyzed the photoionization cross section and ionization potential of 3s, 3p and 3d levels of Na-like W at five different photoelectron energies by employing the FAC code.
- Line intensity ratios and electron density for W LXIV have also been reported, which will be useful and necessary for plasma diagnostics, including modelling for future International Thermonuclear Experimental Reactor (ITER) investigations.
- We assume that our observations will be useful for cell biology, biophysics, fusion plasma research, as well as astrophysical studies and their applications.

5.1 INTRODUCTION

The majority of attention in the field of fusion research has been on tungsten since it will serve as a plasma-facing material in impending massive tokamaks among future fusion reactors [1]. The ionization of multielectron tungsten ions during modern thermonuclear plasma investigations has been investigated because the thermonuclear reactor ITER uses tungsten as a material for its plasma-facing components [2]. Photoionization of tungsten atoms and ions is still of importance in the context of plasma, although it is not directly relevant to fusion research since it can reveal information about the spectroscopic properties of tungsten that are necessary for plasma diagnostics [3]. When there are a lot of strongly interacting, singly excited channels accessible to an outgoing electron, it might be challenging to calculate the photoionization cross-section of an open-shell atom [4]. A highly sensitive spectroscopic method for examining the function of intermediate multiple excited states in photon-ion interactions, with implications for electron-ion recombination and the ionization processes, is the use of photoionization observations together with thorough theoretical computations [5]. The photon-ion merged-beams technology was used to measure the experimental cross sections on an absolute scale and large-scale close-coupling simulations using the Dirac-Coulomb R-matrix approximations provided the theoretical data for W-ion have been investigated by muller et al.. In our article on the outcomes for W⁺ ions, we provide a thorough explanation of the procedure used to photoionize tungsten ions. In our work Photoionization cross sections calculated using FAC and other codes based on the distorted wave approximation neglect channel coupling, which is included by R-matrix calculations and may significantly affect near-threshold behavior and low-temperature photoionization and recombination rate coefficients.

5.2 THEORETICAL PROCEDURE

5.2.1 Atomic Structure Calculations

FAC merges the advantages of these already-existing atomic codes with improvements in numerical techniques established to increase the potential, efficiency, as well as robustness of the programmes [36]. By M.F.Gu, fac is developed and it is based on

Dirac-Hartree-Fock-Slater (DHFS). The source code and documentation are accessible to the general public at <http://kipac-tree.stanford.edu/fac>. With this approach, we used non-local exchange potential in place of potential. When the behaviour of the particles is in local potential, the interaction remains constant, whereas in non-local potential, particle behaviour also influences the interaction. Nuclear charge and electron-electron interaction contribute to the local potential involved in the FAC.

The Dirac-Coulomb Hamiltonian in the MCDF (Multi-Configuration Dirac Fock) technique can be represented for only an N electron atom or an ion as below:

$$H = \sum_{i=1}^N H_D(i) + \sum_{i=1}^N \sum_{j=1}^N \frac{1}{r_{ij}} \quad (5.1)$$

The single electron Dirac Hamiltonian is $H_D(i)$ and an ASF (atomic state function) is used to estimate the specific wave function such an atomic state for a N electron atom or ion system in equation (5.1).

The linear combination of n electronic configuration state functions yields an atomic state function (ASF) for N electron atoms or ions that describes various fine structural states (CSFs).

$$|\Psi_\alpha(PJM)\rangle = \sum_{i=1}^N c_i(\alpha) |\gamma_i(PJM)\rangle \quad (5.2)$$

In which the ASFs satisfy the orthonormality criterion. α indicates the coupling, orbital occupation numbers, etc. CSFs called $\gamma_i(PJM)$ specify a specific state with a specific parity. Also, (J, M) specified as angular momentum.

5.2.2 Photoionization cross section

One of the most fundamental interactions between radiation and matter is the photoionization of atoms, which plays a role in different scientific fields. More specifically, photoionization from excited states has several uses in radiative recombination, controlled thermonuclear research plasma, radiation protection, and stellar atmospheres. As a result, measuring photoionization cross sections accurately from excited atomic states is a considerably more stimulating mission. In the presence of radiation emitted from the sun, processes like photoexcitation, photo-ionization, and

recombination occur naturally all the time [37].

Being a highly charged ion and a simple electronic configuration of sodium their computed numbers may represent the background cross- sections, their computation must go beyond a few core- ion excitations to show the behavior at the core- ion thresholds on the background. The photoionization cross section should contain the same resonances, as the related or inverse processes impact excitation recombination. For a proper treatment of the photoionization process, several approaches of increasing sophistication have been adopted over the years. Photoionization cross sections calculated mainly in the hydrogenic or central field approximation accounted for the background cross section but not resonance [38].

The differential cross section ($\frac{d\sigma}{d\Omega}$) is the ratio of energy absorbed dP to the incident flux ($(1/4\pi)$) in the solid angle element (d) i.e.

$$\frac{d\sigma}{d\Omega} = \frac{dP}{(1/4\pi)d\Omega} = \frac{4\pi^3 c^2}{n_w w_{ij}^2} \frac{dT_{ij}}{d\Omega} \quad (5.3)$$

The partial photoionization cross section for a transition from level j of the $(N + 1)$ electron system to level i of the N electron system in terms of weighted differential oscillator strength is derived using the relativistic distorted wave technique as:

$$\sigma_{PI} = 2\pi\alpha \frac{df}{dE} \quad (5.4)$$

where α stands for the fine-structure constant.

Calculating the Dirac equation using the Dirac-Fock-Slater potential obtains all bound and free orbitals. [39].

Rydberg series of levels play a crucial role in atomic processes.

$$\text{Rydberg formula } E_{res} = E_c - z^2/\nu_c^2 = E_c - \frac{z^2}{(n-\mu_I)^2} \quad (5.5)$$

where E_c is an excited state of the residual ion X_c , also referred to as the ‘core’ ion, left behind as the doubly excited autoionizing state breaks up. For all atoms and ions,

provided the outer electron is in sufficiently high- n state, i.e., sufficiently far away from all the inner electrons so as to experience only the residual charge z . However, the amount of screening depends on the orbital symmetry via the orbital angular momentum. Assuming that there are no other potentials involved, μ is a unique positive constant for each l .

The states of an electron in or with an atom to be bound, when the ground or excited discrete energies are negative, that is, lie below the first ionization threshold or energy of the ground state of the ionized core. Excited state ionization energies E_i are measured relative to the ionization threshold $E = 0$, when the electron has zero energy and becomes free. The Ionization energies of the outermost electron(s) in excited states are lower than those of the ground state. Excitation of a bound state to another bound state may occur due to impact by other particles or photons. The bound electron(s) in the ion may be excited, or ionized, by the free electrons. Since the ionized electron may have any energy, there is an infinite continuum of positive (kinetic) energies $E > 0$ above the ionization threshold at $E = 0$, where no ‘pure’ bound states can exist. Here, the meaning of the term ‘continuum state’ of an $(e + \text{ion})$ system, with a free electron and an ion, needs to be understood. The state refers to a continuum of kinetic energies, which the free electron may have, but the total $(e + \text{ion})$ energy is relative to a specific bound state of the ion, usually the ground state.

In Table 5.1, we have analyzed the photoionization cross section and ionization potential of 3s, 3p and 3d levels of Na-like W at five different photoelectron energies by employing the FAC code and compare our estimated ionization potential from the FAC code with the ionization potential from the National Institute of Standards and Technology (NIST) database of Na-like W. FAC calculates cross sections in a single channel approximations which cannot produce the naturally existing resonances. In absence of consideration of any coupling of channels resulting in mixing resonant features in photoionization cross – sections are not expected to provide the precise values. Figure 5.1, represents the graph between photoionization cross section (10^2 Mb) at five different photoelectron energies (10^4 eV).

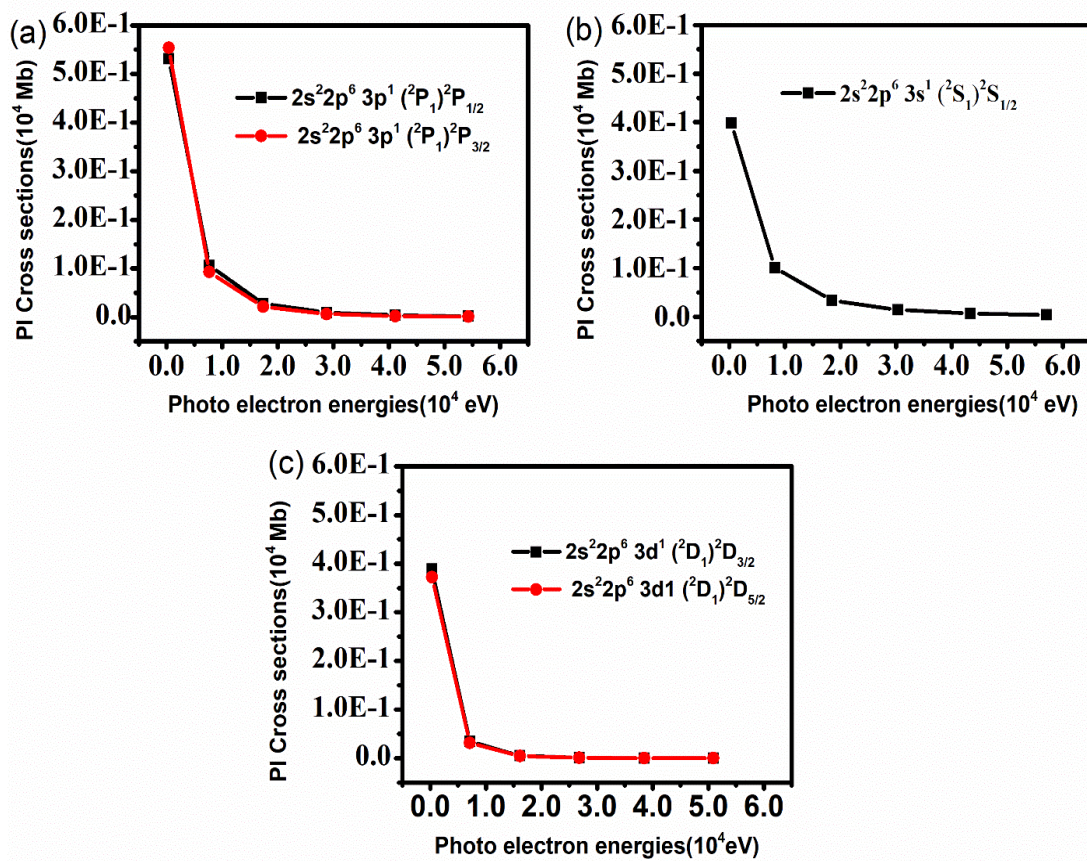


Figure 5.1: Graph between photoionization cross section (in 10^2 Mb) at five different photoelectron energies (in 10^4 eV).

5.2.3 Computation Procedure

In order to obtain accurate results for W^{63+} (Na-like tungsten) as we have chosen the following method:

Firstly, we have provided energy for levels $2p^5 3l n l'$ with $3 \leq n \leq 5$, $2p^5 4l 4l'$ excitations among one electron as of the $2p$ subshell to additional high subshells and $2s2p^6 3l n l'$ with $3 \leq n \leq 5$, $2s2p^6 4l 4l'$ excitations of one electron as of the $2s$ subshell to additional high subshell configurations accompanying oscillator strengths, transition wavelengths, line strengths, as well as transition probabilities for magnetic (M1) and electric (E1) dipole transitions from the ground state for W LXIV.

5.3 RESULTS AND DISCUSSIONS

5.3.1 Energy Levels

For highly stripped ions, electronic interaction is required to determine precise and comprehensive atomic data, such as energy levels, transition wavelength, oscillator strength, etc. A carefully selected configuration expansion is depends on the calculation of accuracy. Since there have only been a few theoretical and experimental research on the photoionization of W ions up till now. Therefore, the theoretical investigation and analysis of the atomic properties as well as the spectra of the W^{63+} ion are particularly interesting and significant for the curiosity in the investigation of tungsten ions. The atomic characteristics of the W^{63+} ion were therefore examined in this work. A comparison between our calculated energy values with other literature energies and NIST (in Ryd) are shown in Table 5.2 and the energies (in Ryd.) with spectroscopic notation of lowest 100 fine structure levels of W LXIV are shown in Table 5.4. We used atomic modelling with 12 configurations in our VV correlation generated in the form of $2p^6nl$ ($3 \leq n \leq 5$ and $0 \leq l \leq 4$) and 21 levels are included in this process. Additionally, for CV correlation we have taken $2p^5 3l nl'$ with $3 \leq n \leq 5, 2p^5 4l 4l'$, $2s2p^6 3l nl'$ with $3 \leq n \leq 5$, $2s2p^6 4l 4l'$ configurations are taken into account and generated 2700 fine structure levels, which are obtained by single- as well as double-excitations from the ground state. We have limited the modelling of configurations to $n = 5$ orbitals for conciseness.

5.3.2 Radiative rates (wavelengths, oscillator strengths, and transition rates)

For various radiative channels, the line strength (S_{ij}) as well as oscillator strength (f_{ij}) are as follows:

$$\begin{array}{l} \text{for E1} \\ \text{transitions:} \end{array} \quad A_{ji} = \frac{2.0261 \times 10^{18}}{\omega_j \lambda_{ji}^3} S_{ij} \quad \text{and} \quad f_{ij} = \frac{303.75}{\lambda_{ji} \omega_i} S_{ij}, \quad (5.6)$$

$$\begin{array}{l} \text{for M1} \\ \text{transitions:} \end{array} \quad A_{ji} = \frac{2.6974 \times 10^{13}}{\omega_j \lambda_{ji}^3} S_{ij} \quad \text{and} \quad f_{ij} = \frac{4.044 \times 10^{-3}}{\lambda_{ji} \omega_i} S_{ij}, \quad (5.7)$$

$$\begin{array}{l} \text{for E2} \\ \text{transitions:} \end{array} \quad A_{ji} = \frac{1.1199 \times 10^{18}}{\omega_j \lambda_{ji}^5} S_{ij} \quad \text{and} \quad f_{ij} = \frac{167.89}{\lambda_{ji}^3 \omega_i} S_{ij}, \quad (5.8)$$

$$\begin{array}{l} \text{for M2} \\ \text{transitions:} \end{array} \quad A_{ji} = \frac{1.4910 \times 10^{13}}{\omega_j \lambda_{ji}^5} S_{ij} \quad \text{and} \quad f_{ij} = \frac{2.236 \times 10^{-3}}{\lambda_{ji}^3 \omega_i} S_{ij}. \quad (5.9)$$

In equations (5.6 to 5.9) transition wavelength is λ_{ij} in Å, ω_j as well as ω_i stands for the upper and lower levels of statistical weight, accordingly. For W LXIV, we identified 21 E1, 33 E2, 28 M1 and 21 M2 SXR transitions from Tables 5.3, as well as 1 EUV transition to the ground state from higher excited states. We have also compared our transitional parameters with available values in literature and at NIST website in Table 5.5. Radiative data for W LXIV that we have provided is accurate and can be utilized to further identify the spectral lines observed experimentally.

The computed transition rates for E1 and E2 transitions in two gauges, namely, length and velocity gauge, differ from each other for the multi-configuration model and will be in agreement when the large electronic interaction will be considered. To check the accuracy of computed radiative data, we have presented the ratio vel/len of absorption oscillator strengths in the last column of Tables 5.3. For allowed dipole transitions or E1, E2 transitions ($\Delta J = 0, \pm 1$ except for $J = 0 \rightarrow J' = 0$; $\Delta S = 0, \Delta L = 0, \pm 1$ except for $L = 0 \rightarrow L' = 0$) length and velocity forms should agree. We note that for strong and allowed transitions, agreement between the length and velocity form of the oscillator strength is better than 10%. For intercombination lines or spin forbidden lines, the selection rule is same as for the allowed transitions except for $\Delta S = 0$. For spin forbidden lines or indeed for others weak lines, only the length form should be used [40]. One can observe that, in most of the transitions, the ratio is unity or near to unity. This ensures vel/len ratio of oscillator strength reaffirms the accuracy of our calculations for Na-like W.

5.4 LINE INTENSITY RATIO AND PLASMA PARAMETERS

If the plasma has a thin optical layer and is also in local thermodynamic equilibrium (LTE), the diagnosis of elemental composition using different experimental spectroscopic techniques becomes easy as well as straightforward (LTE). The optically thick line is the reason for this saturation with self-absorption, as seen in the line profile, which results in an asymmetrical or asymmetrical peak in the spectrum. As a result, the electron density and plasma temperature are measured wrongly and inappropriately. Increased kinematic excitement, or perhaps the movement of electrons, arises at higher temperatures. LTE can be easily accomplished due to the increase in the number of

collisions with an electron at higher temperatures. The effect of plasma temperature upon line intensity ratio in addition to the limiting value of electron density has been studied in ongoing research to understand more about the features of optically thin plasma.

Two spectral lines from the same atom or ion are measured by line intensity ratio as follows:

$$R = \frac{I_1}{I_2} = \frac{\lambda_2 A_1 g_1}{\lambda_1 A_2 g_2} \exp \left[-\frac{E_1 - E_2}{KT} \right] \quad (5.10)$$

In the above equation (5.10) λ is the wavelength and A is the transition probability, I indicates intensity, and g denotes the lower level of transition of the statistical weight, K denotes the Boltzmann constant and the value of K is 8.6173×10^{-5} eV/K and T denotes the excitation temperature in Kelvin (K). E represents the energy of the upper stage of transition in (eV) [41- 42]. According to equation (5.10), the exponential term significantly impacts the line intensity ratio of two spectral lines. In Hot Dense Plasma, the line intensity ratio and electron density calculations, opted as $1 [1s^2 2s^2 2p^6 3s (^2S_{1/2}) - 1s^2 2s^2 2p^6 3p (^2P_{1/2}^0)]$, $2[1s^2 2s^2 2p^6 3s (^2S_{1/2}) - 1s^2 2s^2 2p^6 3p (^2P_{3/2}^0)]$ which signifies the two spectral lines. For Na-like W at high temperatures, we have presented the line intensity ratio (R) in Table 5.6. The International Thermonuclear Experimental Reactor (ITER) has started using various heating techniques to raise the plasma temperature to the optimal level value of 1.5×10^8 °C or 4×10^{10} K [43]. As a result, we specified 10^{10} K as the maximum plasma temperature in our calculations. As is observable, the exponential term becomes extremely small for the lowest values of ΔE ($= E_1 - E_2$), which leads the line intensity ratio between two spectral lines to become too small. This led to calculating the line intensity ratio between two spectral transitions. From Figure 5.2 and Table 5.6, it is possible to determine how the line intensity ratio behaves with plasma temperature. According to our observations, the line intensity ratio rises as the plasma temperature T rises, especially when T is more than or equivalent to 10^9 K. This demonstrates the saturation of the line intensity ratio or the negligible effect of rising temperatures on the line intensity ratio.

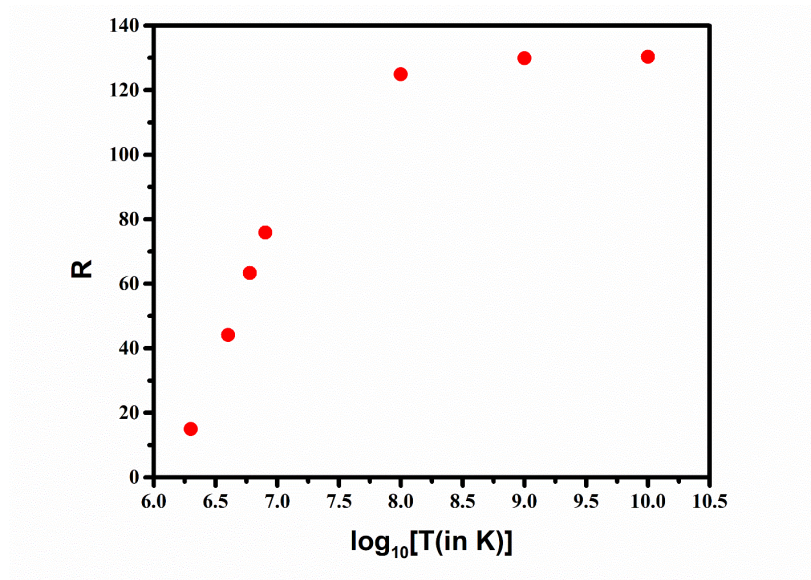


Figure 5.2: For Na-like W, the line intensity ratio for spectral lines 1 [$1s^22s^22p^63s(^2S_{1/2}) - 1s^22s^22p^63p(^2P_{1/2}^0)$] and 2 [$1s^22s^22p^63s(^2S_{1/2}) - 1s^22s^22p^63p(^2P_{3/2}^0)$] varies with plasma temperature.

By comparing their estimated line intensity ratio with the measured ratio for various delay times, researchers may pinpoint the timeframe window only when plasma is already in LTE as well as optically thin.

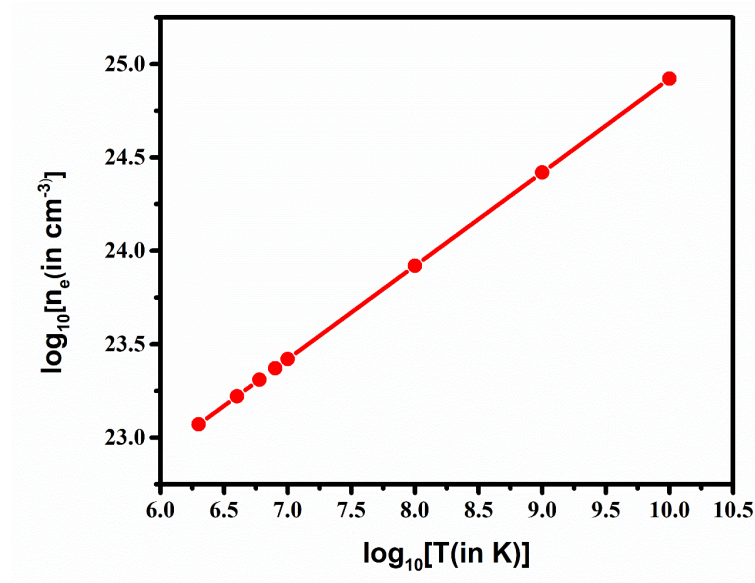


Figure 5.3: Limiting electron density for Na-like W for spectral lines 1 [$1s^22s^22p^63s(^2S_{1/2}) - 1s^22s^22p^63p(^2P_{1/2}^0)$] and 2 [$1s^22s^22p^63s(^2S_{1/2}) - 1s^22s^22p^63p(^2P_{3/2}^0)$] varies with plasma temperature.

The overall number of electron collisions must be high to achieve LTE. For plasmas as being in partial local thermodynamic equilibrium (LTE), it is possible to predict the lowest principal quantum number that meets the criterion of being within 10% of its Saha-Boltzmann value [44]. The McWhirter criterion [45] establishes the minimal or limiting value of electron density for this purpose.

$$n_e \geq 1.6 \times 10^{12} T^{(1/2)} (\Delta E)^3 \quad (5.11)$$

Where T is plasma temperature in Kelvin, the electron density is n_e and $\Delta E = (E_1 - E_2)$ eV. The limiting electron density at various plasma temperature levels is also mentioned. 10^{20} cm^{-3} is the electron density order because of its occurrence in several types of stars, including white dwarf stars. Plasma throughout this density range is particularly well-known, as are inertial confinement fusion plasmas. In Figure 5.3 and Table 5.6, it can be deduced that the value of the limiting electron density for Na-like W demonstrates that the number of collisions in the plasma rises as the plasma temperature rises. Therefore, this knowledge may be useful for experimenters who want to produce optically thin plasma for Na-like W ions in LTE at significantly higher temperatures.

5.5 CONCLUSION

In the current work, we have provided theoretical research as well as analysis regarding the atomic parameters of multipole transitions of W ions for 100 fine-structure levels for Na-like which is inspired by demand. We have investigated the photoionization cross section and ionization potential of 3s, 3p and 3d levels of Na-like W at five different photoelectron energies. Our computing process uses the FAC approach and other codes based on the distorted wave approximation neglect channel coupling, which is included by R-matrix calculations and may significantly affect near-threshold behavior and low-temperature photoionization and recombination rate coefficients. The discrepancy between the findings and the available theoretical as well as experimental data is explained. Furthermore, we estimated the line intensity ratio and electron density for W LXIV and evaluated how they behaved under high plasma temperatures. Our predicted results will be useful for fusion plasma, astrophysical plasma, and modelling plasma.

Table 5.1: Photoionization cross section (in 10^2 Mb) and ionization potential (I.P. in eV) of Na-like W at five photoelectron energies (in 10^4 eV), from which the ground state of W^{64+} is $1s^2 2s^2 2p^6$.

Energies	0.0356	0.8162	1.8449	3.0372	4.3354	5.7048	Ionization Potential	Ionization Potential NIST
$2s^2 2p^6 3s^1$ (2S_1) $^2S_{1/2}$	3.98E - 01	1.01E - 01	3.36E - 02	1.40E - 02	6.87E - 03	3.75E - 03	7131.0	7131.0
Energies	0.0392	0.7673	1.7405	2.8751	4.1156	5.4275	-----	-----
$2s^2 2p^6 3p^1$ (2P_1) $^2P_{1/2}$	5.31E - 01	1.06E - 01	2.77E - 02	9.28E - 03	3.75E - 03	1.75E - 03	6971.1	6970.4
$2s^2 2p^6 3p^1$ (2P_1) $^2P_{3/2}$	5.54E - 01	9.26E - 02	2.15E - 02	6.63E - 02	2.25E - 03	1.12E - 03	6597.2	6596
Energies	0.0318	0.7091	1.6157	2.6809	3.8516	5.0942	-----	-----
$2s^2 2p^6 3d^1$ (2D_1) $^2D_{3/2}$	3.89E - 01	3.50E - 02	5.06E - 03	1.08E - 03	3.08E - 04	1.08E - 04	6410.2	6409.3
$2s^2 2p^6 3d^1$ (2D_1) $^2D_{5/2}$	3.72E - 01	3.16E - 02	4.41E - 03	9.14E - 04	2.53E - 04	8.73E - 05	6325.2	6324.4

Table 5.2: A comparison between our calculated energy values with other literature energies and NIST (in Ryd).

LEVEL	CONFIGURATIONS	NIST[49]	FAC	GRASP REF[45]	FAC REF[45]	MCDF REF[46]	MCDF REF[8]	RBMT REF[4]	HULLAC REF[48]	COWAN REF[47]
1	$2s^2 2p^6 3s^1$ (2S_1) $^2S_{1/2}$	0.0000	0.0000	0.0000	0.0000	0.0000	0.0000	0.0000	0.0000	0.0000
2	$2s^2 2p^6 3p^1$ (2P_1) $^2P_{1/2}$	11.7280	11.7493	11.8989	11.7457	11.7370	11.7238	11.7371	11.8918	10.9897
3	$2s^2 2p^6 3p^1$ (2P_1) $^2P_{3/2}$	39.189	39.2334	39.3365	39.2218	39.2267	39.1927	39.2068	39.3315	39.8862
4	$2s^2 2p^6 3d^1$ (2D_1) $^2D_{3/2}$	52.969	52.9815	53.1127	52.9352	53.0081	52.9545	52.9674	53.1316	52.3155
5	$2s^2 2p^6 3d^1$ (2D_1) $^2D_{5/2}$	59.210	59.2312	59.3372	59.1730	59.2605	59.2393	59.2288	59.3547	58.9189
6	$2s^2 2p^6 4s^1$ (2S_1) $^2S_{1/2}$	239.1	239.0101	239.0661	238.9973	239.2723				
7	$2s^2 2p^6 4p^1$ (2P_1) $^2P_{1/2}$	243.9	243.8679	243.9788	243.8505	244.0685				
8	$2s^2 2p^6 4p^1$ (2P_1) $^2P_{3/2}$	255.2	255.1180	255.2154	255.0981	255.3387				
9	$2s^2 2p^6 4d^1$ (2D_1) $^2D_{3/2}$	260.4	260.3343	260.4510	260.3002	260.5362				
10	$2s^2 2p^6 4s^1$ (2D_1) $^2D_{5/2}$	263.1	263.0348	263.1426	262.9954	263.2625				
11	$2s^2 2p^6 4f^1$ (2F_1) $^2F_{5/2}$	265.9	265.7614	265.8618	265.7361	266.0983				
12	$2s^2 2p^6 4f^1$ (2F_1) $^2F_{7/2}$	267.1	266.9432	267.0446	266.9176	267.2928				
13	$2s^2 2p^6 5s^1$ (2S_1) $^2S_{1/2}$	-	345.3396	345.5593	345.3305	-				
14	$2s^2 2p^6 5p^1$ (2P_1) $^2P_{1/2}$	-	347.7801	348.0234	347.7664	-				
15	$2s^2 2p^6 5p^1$ (2P_1) $^2P_{3/2}$	-	353.4352	353.6728	353.4209	-				
16	$2s^2 2p^6 5d^1$ (2D_1) $^2D_{3/2}$	-	355.9884	356.2383	355.9695	-				
17	$2s^2 2p^6 5d^1$ (2D_1) $^2D_{5/2}$	357.5	357.3798	357.6240	357.3573	357.7642				
18	$2s^2 2p^6 5f^1$ (2F_1) $^2F_{5/2}$	358.8	358.7291	358.9640	358.7180	359.0589				
19	$2s^2 2p^6 5f^1$ (2F_1) $^2F_{7/2}$	359.5	359.3365	359.5722	359.3256	359.6882				
20	$2s^2 2p^6 5g^1$ (2G_1) $^2G_{7/2}$	359.8	359.5308	359.7585	359.5057	359.9799				
21	$2s^2 2p^6 5g^1$ (2G_1) $^2G_{9/2}$	360.1	359.8911	360.1191	359.8662	360.3447				

Table 5.3: The Radiative data of E1, E2, M1 and M2 transitions of W LXIV.

Transitions	Lower Level(i)	Upper Level (j)	λ_{ji} (in Å)	A_{ji} (in s^{-1})	f_{ij}	S_{ij} (in a.u.)	vel/len
E1	1	2	76.747	4.4554E+10	3.9343E-02	1.9881E-02	0.960
E1	1	3	23.178	1.7543E+12	2.8259E-01	4.3126E-02	1.000
E1	1	7	3.735	6.3048E+13	1.3182E-01	3.2414E-03	1.000
E1	1	8	3.570	3.9237E+13	1.4996E-01	3.5250E-03	1.000
E1	1	14	2.619	3.5715E+13	3.6724E-02	6.3325E-04	0.970
E1	1	15	2.577	2.5350E+13	5.0480E-02	8.5656E-04	0.940
E1	1	22	1.502	1.1244E+14	7.6023E-02	7.5167E-04	0.990
E1	1	27	1.447	1.1757E+12	7.3815E-04	7.0330E-06	1.000
E1	1	35	1.389	1.0951E+12	3.1689E-04	2.8987E-06	1.000
E1	1	38	1.389	2.8606E+13	1.6551E-02	1.5138E-04	0.990
E1	1	40	1.387	8.0418E+12	4.6402E-03	4.2383E-05	0.980
E1	1	41	1.386	1.1583E+13	3.3361E-03	3.0445E-05	0.980
E1	1	42	1.384	3.0323E+13	1.7420E-02	1.5877E-04	0.980
E1	1	44	1.383	8.8377E+13	2.5355E-02	2.3094E-04	0.990
E1	1	46	1.381	1.6360E+12	9.3580E-04	8.5103E-06	0.970
E1	1	48	1.376	2.0595E+14	5.8485E-02	5.2999E-04	0.970
E1	1	52	1.369	2.7912E+13	1.5673E-02	1.4123E-04	0.990
E1	1	56	1.364	2.7490E+15	1.5338E+00	1.3777E-02	0.980
E1	1	58	1.363	2.5475E+15	7.0969E-01	6.3698E-03	0.980
E1	1	72	1.331	1.4429E+13	3.8338E-03	3.3606E-05	0.970
E1	1	75	1.328	1.1814E+11	6.2423E-05	5.4561E-07	0.670
E1	1	76	1.324	3.4509E+12	1.8124E-03	1.5793E-05	1.100
E2	1	4	17.166	1.4053E+08	1.2417E-05	7.4823E-04	1.000
E2	1	5	15.364	2.5612E+08	2.7193E-05	1.1749E-03	1.000
E2	1	9	3.498	4.3608E+11	1.6003E-03	8.1625E-04	1.000
E2	1	10	3.463	4.3340E+11	2.3372E-03	1.1560E-03	1.000
E2	1	16	2.559	2.1579E+11	4.2354E-04	8.4502E-05	0.880
E2	1	17	2.549	2.2623E+11	6.6089E-04	1.3033E-04	0.880
E2	1	23	1.479	3.1670E+11	2.0769E-04	8.0031E-06	0.990
E2	1	24	1.476	8.6218E+11	8.4518E-04	3.2397E-05	0.990
E2	1	25	1.475	6.5200E+11	4.2558E-04	1.6283E-05	0.990
E2	1	29	1.415	9.9118E+10	5.9495E-05	2.0074E-06	0.990
E2	1	30	1.414	7.7802E+11	6.9950E-04	2.3551E-05	0.990
E2	1	32	1.409	1.5462E+11	1.3809E-04	4.6031E-06	1.000
E2	1	33	1.408	7.3562E+11	4.3722E-04	1.4536E-05	0.990
E2	1	57	1.363	4.2367E+07	2.3602E-08	7.1205E-10	1.200

Transitions	Lower Level(i)	Upper Level (j)	λ_{ji} (in Å)	A_{ji} (in s^{-1})	f_{ij}	S_{ij} (in a.u.)	vel/len
E2	1	60	1.362	1.0880E+09	9.0801E-07	2.7342E-08	1.000
E2	1	62	1.358	4.7445E+09	3.9339E-06	1.1730E-07	1.000
E2	1	63	1.357	1.1397E+09	6.2924E-07	1.8731E-08	0.990
E2	1	66	1.347	1.1239E+07	6.1164E-09	1.7816E-10	1.300
E2	1	67	1.347	4.1307E+07	3.3701E-08	9.8086E-10	0.780
E2	1	68	1.346	1.9403E+09	1.5807E-06	4.5902E-08	1.000
E2	1	71	1.341	1.7261E+08	9.3102E-08	2.6760E-09	2.200
E2	1	77	1.308	1.3554E+08	6.9511E-08	1.8524E-09	1.100
E2	1	79	1.307	5.2172E+08	4.0082E-07	1.0660E-08	0.930
E2	1	81	1.306	1.4802E+09	1.1361E-06	3.0175E-08	1.100
E2	1	82	1.306	3.4839E+08	1.7820E-07	4.7295E-09	1.000
E2	1	84	1.305	4.8202E+08	2.4597E-07	6.5053E-09	0.960
E2	1	85	1.304	1.1516E+08	8.8081E-08	2.3270E-09	0.880
E2	1	89	1.297	1.4218E+08	7.1664E-08	1.8606E-09	1.400
E2	1	91	1.296	1.9374E+08	1.4629E-07	3.7906E-09	1.200
E2	1	94	1.294	1.2902E+09	6.4794E-07	1.6731E-08	1.000
E2	1	98	1.291	1.6724E+09	1.2536E-06	3.2132E-08	1.200
E2	1	99	1.290	2.1006E+09	1.0474E-06	2.6756E-08	0.970
E2	1	100	1.289	1.2428E+09	9.2795E-07	2.3644E-08	0.710
M1	1	4	17.166	1.4712E+04	1.2999E-09	1.1035E-05	
M1	1	6	3.811	5.8203E+07	1.2675E-07	2.3890E-04	
M1	1	9	3.498	8.1552E+05	3.3597E-09	5.8128E-06	
M1	1	13	2.638	6.5816E+07	6.8646E-08	8.9542E-05	
M1	1	16	2.559	1.1779E+06	2.3120E-09	2.9254E-06	
M1	1	23	1.479	1.9008E+10	1.2466E-05	9.1173E-03	
M1	1	25	1.475	1.1398E+10	7.4400E-06	5.4287E-03	
M1	1	26	1.475	2.8236E+10	9.2095E-06	6.7178E-03	
M1	1	29	1.415	8.4942E+09	5.0986E-06	3.5676E-03	
M1	1	31	1.412	1.1438E+10	3.4198E-06	2.3883E-03	
M1	1	33	1.408	5.7384E+08	3.4106E-07	2.3747E-04	
M1	1	34	1.402	8.6983E+08	2.5620E-07	1.7760E-04	
M1	1	55	1.364	2.9979E+06	8.3672E-10	5.6459E-07	
M1	1	57	1.363	1.2265E+06	6.8325E-10	4.6058E-07	
M1	1	61	1.359	8.8377E+07	2.4455E-08	1.6430E-05	
M1	1	63	1.357	3.1638E+06	1.7468E-09	1.1723E-06	
M1	1	66	1.347	7.0480E+06	3.8356E-09	2.5555E-06	
M1	1	70	1.342	1.0365E+07	2.7964E-09	1.8552E-06	

Transitions	Lower Level(i)	Upper Level (j)	λ_{ji} (in Å)	A_{ji} (in s ⁻¹)	f_{ij}	S_{ij} (in a.u.)	vel/len
M1	1	71	1.341	3.7020E+05	1.9968E-10	1.3245E-07	
M1	1	77	1.308	4.5800E+06	2.3489E-09	1.5192E-06	
M1	1	78	1.307	7.3445E+05	1.8815E-10	1.2163E-07	
M1	1	82	1.306	5.1443E+06	2.6312E-09	1.6995E-06	
M1	1	84	1.305	1.0770E+06	5.4960E-10	3.5458E-07	
M1	1	86	1.304	1.0297E+07	2.6246E-09	1.6924E-06	
M1	1	89	1.297	2.5492E+05	1.2849E-10	8.2386E-08	
M1	1	94	1.294	2.2367E+06	1.1233E-09	7.1894E-07	
M1	1	96	1.293	2.1280E+07	5.3296E-09	3.4067E-06	
M1	1	99	1.290	1.0619E+04	5.2948E-12	3.3767E-09	
M2	1	3	23.178	3.6324E+05	5.8511E-08	6.5184E-01	
M2	1	8	3.570	3.3835E+08	1.2931E-06	5.2647E-02	
M2	1	11	3.427	7.5974E+03	4.0140E-11	1.4459E-06	
M2	1	15	2.577	4.1691E+08	8.3021E-07	1.2713E-02	
M2	1	18	2.539	3.6919E+03	7.8056E-12	1.1432E-07	
M2	1	22	1.502	5.2225E+09	3.5311E-06	1.0698E-02	
M2	1	27	1.447	1.5910E+07	2.2546E-08	6.1124E-05	
M2	1	36	1.389	1.2562E+07	1.0903E-08	2.6149E-05	
M2	1	38	1.389	1.5591E+09	9.0207E-07	2.1634E-03	
M2	1	39	1.388	6.6038E+07	5.7177E-08	1.3664E-04	
M2	1	40	1.387	8.5484E+07	4.9325E-08	1.1781E-04	
M2	1	42	1.384	1.3263E+09	7.6192E-07	1.8079E-03	
M2	1	43	1.384	6.3659E+07	5.4842E-08	1.3008E-04	
M2	1	46	1.381	2.6312E+09	1.5050E-06	3.5480E-03	
M2	1	47	1.381	1.9916E+09	1.7083E-06	4.0255E-03	
M2	1	50	1.371	1.1575E+11	9.7792E-05	2.2526E-01	
M2	1	52	1.369	1.1122E+11	6.2455E-05	1.4321E-01	
M2	1	54	1.367	5.8300E+08	4.8974E-07	1.1185E-03	
M2	1	56	1.364	1.1031E+09	6.1551E-07	1.3979E-03	
M2	1	74	1.331	3.3615E+07	2.6792E-08	5.6550E-05	
M2	1	75	1.328	1.7976E+07	9.4980E-09	1.9879E-05	
M2	1	76	1.324	3.5272E+08	1.8524E-07	3.8419E-04	

Table 5.4 : Energies (in Ryd.) of lowest 100 fine structure levels of W LXIV.

Level	Configurations	Parity	FAC(Ryd)	NIST(Ryd)[49]	ΔE
1	$2s^2 2p^6 3s^1 (^2S_1)^2S_{1/2}$	Even	0.0000	0.0000	0.00
2	$2s^2 2p^6 3p^1 (^2P_1)^2P_{1/2}$	Odd	11.7493	11.7280	1.06
3	$2s^2 2p^6 3p^1 (^2P_1)^2P_{3/2}$	Odd	39.2334	39.189	0.21
4	$2s^2 2p^6 3d^1 (^2D_1)^2D_{3/2}$	Even	52.9815	52.969	0.20
5	$2s^2 2p^6 3d^1 (^2D_1)^2D_{5/2}$	Even	59.2312	59.210	0.13
6	$2s^2 2p^6 4s^1 (^2S_1)^2S_{1/2}$	Even	239.0101	239.1	0.04
7	$2s^2 2p^6 4p^1 (^2P_1)^2P_{1/2}$	Odd	243.8679	243.9	0.06
8	$2s^2 2p^6 4p^1 (^2P_1)^2P_{3/2}$	Odd	255.1180	255.2	0.05
9	$2s^2 2p^6 4d^1 (^2D_1)^2D_{3/2}$	Even	260.3343	260.4	0.06
10	$2s^2 2p^6 4s^1 (^2D_1)^2D_{5/2}$	Even	263.0348	263.1	0.05
11	$2s^2 2p^6 4f^1 (^2F_1)^2F_{5/2}$	Odd	265.7614	265.9	0.04
12	$2s^2 2p^6 4f^1 (^2F_1)^2F_{7/2}$	Odd	266.9432	267.1	0.04
13	$2s^2 2p^6 5s^1 (^2S_1)^2S_{1/2}$	Even	345.3396	-	0.04
14	$2s^2 2p^6 5p^1 (^2P_1)^2P_{1/2}$	Odd	347.7801	-	0.05
15	$2s^2 2p^6 5p^1 (^2P_1)^2P_{3/2}$	Odd	353.4352	-	0.05
16	$2s^2 2p^6 5d^1 (^2D_1)^2D_{3/2}$	Even	355.9884	-	0.05
17	$2s^2 2p^6 5d^1 (^2D_1)^2D_{5/2}$	Even	357.3798	357.5	0.05
18	$2s^2 2p^6 5f^1 (^2F_1)^2F_{5/2}$	Odd	358.7291	358.8	0.05
19	$2s^2 2p^6 5f^1 (^2F_1)^2F_{7/2}$	Odd	359.3365	359.5	0.05
20	$2s^2 2p^6 5g^1 (^2G_1)^2G_{7/2}$	Even	359.5308	359.8	0.04
21	$2s^2 2p^6 5g^1 (^2G_1)^2G_{9/2}$	Even	359.8911	360.1	0.04
22	$2s^2 2p^5 3s^2 (^1S_0)^2P_{3/2}$	Odd	606.9790		
23	$2s^2 2p^5 3s^1 3p^1 (^2P_1)^4P_{3/2}$	Even	616.1585		
24	$2s^2 2p^5 3s^1 3p^1 (^2P_1)^4D_{5/2}$	Even	617.2351		
25	$2s^2 2p^5 3s^1 3p^1 (^2P_1)^2D_{3/2}$	Even	617.6222		
26	$2s^2 2p^5 3s^1 3p^1 (^2P_1)^2P_{3/2}$	Even	617.8084		
27	$2s^2 2p^5 3p^2 (^3P_2)^4D_{3/2}$	Odd	629.6193		
28	$2s^2 2p^5 3s^1 3p^1 (^2P_1)^4D_{7/2}$	Even	643.4528		
29	$2s^2 2p^5 3s^1 3p^1 (^2P_1)^4S_{3/2}$	Even	644.0812		
30	$2s^2 2p^5 3s^1 3p^1 (^2P_1)^4P_{5/2}$	Even	644.5490		
31	$2s^2 2p^5 3s^1 3p^1 (^2P_1)^2S_{1/2}$	Even	645.3077		
32	$2s^2 2p^5 3s^1 3p^1 (^2P_1)^2D_{5/2}$	Even	646.6930		
33	$2s^2 2p^5 3s^1 3p^1 (^2P_1)^2P_{3/2}$	Even	647.2673		

Level	Configurations	Parity	FAC(Ryd)	NIST(Ryd)[49]	ΔE
34	$2s^2 2p^5 3s^1 3p^1 (^2P_1) ^2S_{1/2}$	Even	650.1377		
35	$2s^2 2p^5 3p^2 (^3P_2) ^4P_{1/2}$	Odd	655.7743		
36	$2s^2 2p^5 3p^2 (^3P_2) ^4P_{5/2}$	Odd	655.8282		
37	$2s^2 2p^5 3p^2 (^1D_2) ^2F_{7/2}$	Odd	655.8962		
38	$2s^2 2p^5 3p^2 (^1D_2) ^2P_{3/2}$	Odd	655.9289		
39	$2s^2 2p^5 3p^2 (^1D_2) ^2D_{5/2}$	Odd	656.7224		
40	$2s^2 2p^5 3p^2 (^3P_2) ^2D_{3/2}$	Odd	656.8221		
41	$2s^2 2p^5 3s^1 3d^1 (^2D_1) ^4P_{1/2}$	Odd	657.4354		
42	$2s^2 2p^5 3s^1 3d^1 (^2D_1) ^2D_{3/2}$	Odd	658.2976		
43	$2s^2 2p^5 3s^1 3d^1 (^2D_1) ^4P_{3/2}$	Odd	658.4006		
44	$2s^2 2p^5 3s^1 3d^1 (^2D_1) ^2P_{1/2}$	Odd	658.6996		
45	$2s^2 2p^5 3s^1 3d^1 (^2D_1) ^4F_{7/2}$	Odd	659.0358		
46	$2s^2 2p^5 3s^1 3d^1 (^2D_1) ^2D_{3/2}$	Odd	659.7364		
47	$2s^2 2p^5 3s^1 3d^1 (^2D_1) ^2F_{5/2}$	Odd	659.8185		
48	$2s^2 2p^5 3p^2 (^1D_2) ^2P_{1/2}$	Odd	661.9999		
49	$2s^2 2p^5 3s^1 3d^1 (^2D_1) ^4F_{9/2}$	Odd	663.9801		
50	$2s^2 2p^5 3s^1 3d^1 (^2D_1) ^4P_{5/2}$	Odd	664.8790		
51	$2s^2 2p^5 3s^1 3d^1 (^2D_1) ^4D_{7/2}$	Odd	665.3981		
52	$2s^2 2p^5 3s^1 3d^1 (^2D_1) ^2D_{3/2}$	Odd	665.7569		
53	$2s^2 2p^5 3s^1 3d^1 (^2D_1) ^2F_{7/2}$	Odd	665.8743		
54	$2s^2 2p^5 3s^1 3d^1 (^2D_1) ^2D_{5/2}$	Odd	666.7686		
55	$2s^2 2p^5 3p^1 3d^1 (^2D_1) ^4D_{1/2}$	Even	667.7302		
56	$2s^2 2p^5 3s^1 3d^1 (^2D_1) ^2P_{3/2}$	Odd	668.0052		
57	$2s^2 2p^5 3p^1 3d^1 (^2D_1) ^4D_{3/2}$	Even	668.3914		
58	$2s^2 2p^5 3s^1 3d^1 (^2D_1) ^2P_{1/2}$	Odd	668.3984		
59	$2s^2 2p^5 3p^1 3d^1 (^2D_1) ^4G_{7/2}$	Even	668.4765		
60	$2s^2 2p^5 3s^1 3d^1 (^2D_1) ^4F_{5/2}$	Even	668.8146		
61	$2s^2 2p^5 3p^1 3d^1 (^2D_1) ^4P_{1/2}$	Even	670.6091		
62	$2s^2 2p^5 3p^1 3d^1 (^2D_1) ^4F_{5/2}$	Even	671.0050		
63	$2s^2 2p^5 3p^1 3d^1 (^2D_1) ^4D_{3/2}$	Even	671.3865		
64	$2s^2 2p^5 3p^1 3d^1 (^2D_1) ^4D_{7/2}$	Even	675.6948		
65	$2s^2 2p^5 3p^1 3d^1 (^2D_1) ^4G_{9/2}$	Even	676.0153		
66	$2s^2 2p^5 3p^1 3d^1 (^2D_1) ^2P_{3/2}$	Even	676.2796		
67	$2s^2 2p^5 3p^1 3d^1 (^2D_1) ^2F_{5/2}$	Even	676.4676		

Level	Configurations	Parity	FAC(Ryd)	NIST(Ryd)[49]	ΔE
68	$2s^2 2p^5 3p^1 3d^1 (^2D_1) ^4P_{5/2}$	Even	676.9706		
69	$2s^2 2p^5 3p^1 3d^1 (^2D_1) ^2F_{7/2}$	Even	677.2248		
70	$2s^2 2p^5 3p^1 3d^1 (^2D_1) ^2P_{1/2}$	Even	679.1841		
71	$2s^2 2p^5 3p^1 3d^1 (^2D_1) ^2D_{3/2}$	Even	679.2955		
72	$2s^2 2p^5 3p^2 (^3P_1) ^2S_{1/2}$	Odd	684.4237		
73	$2s^2 2p^5 3p^2 (^3P_1) ^4D_{7/2}$	Odd	684.4358		
74	$2s^2 2p^5 3p^2 (^3P_2) ^2D_{5/2}$	Odd	684.4758		
75	$2s^2 2p^5 3p^2 (^1S_0) ^2P_{3/2}$	Odd	686.4124		
76	$2s^2 2p^5 3p^2 (^3P_2) ^2P_{3/2}$	Odd	688.4842		
77	$2s^2 2p^5 3p^1 3d^1 (^2D_1) ^4P_{3/2}$	Even	696.6554		
78	$2s^2 2p^5 3p^1 3d^1 (^2D_1) ^2P_{1/2}$	Even	697.0092		
79	$2s^2 2p^5 3p^1 3d^1 (^2D_1) ^4D_{5/2}$	Even	697.1176		
80	$2s^2 2p^5 3p^1 3d^1 (^2D_1) ^4F_{7/2}$	Even	697.1226		
81	$2s^2 2p^5 3p^1 3d^1 (^2D_1) ^2F_{5/2}$	Even	697.4420		
82	$2s^2 2p^5 3p^1 3d^1 (^2D_1) ^2D_{3/2}$	Even	697.5096		
83	$2s^2 2p^5 3p^1 3d^1 (^2D_1) ^2G_{9/2}$	Even	697.5959		
84	$2s^2 2p^5 3p^1 3d^1 (^2D_1) ^4D_{3/2}$	Even	698.4236		
85	$2s^2 2p^5 3p^1 3d^1 (^2D_1) ^4D_{5/2}$	Even	698.6454		
86	$2s^2 2p^5 3p^1 3d^1 (^2D_1) ^4P_{1/2}$	Even	698.6805		
87	$2s^2 2p^5 3p^1 3d^1 (^2D_1) ^2F_{7/2}$	Even	698.7712		
88	$2s^2 2p^5 3p^1 3d^1 (^2D_1) ^4G_{1/2}$	Even	701.8904		
89	$2s^2 2p^5 3p^1 3d^1 (^2D_1) ^2D_{3/2}$	Even	702.5486		
90	$2s^2 2p^5 3p^1 3d^1 (^2D_1) ^2F_{7/2}$	Even	702.7298		
91	$2s^2 2p^5 3p^1 3d^1 (^2D_1) ^2D_{5/2}$	Even	703.2169		
92	$2s^2 2p^5 3p^1 3d^1 (^2D_1) ^4F_{9/2}$	Even	703.6215		
93	$2s^2 2p^5 3p^1 3d^1 (^2D_1) ^4D_{7/2}$	Even	703.8673		
94	$2s^2 2p^5 3p^1 3d^1 (^2D_1) ^2P_{3/2}$	Even	704.0300		
95	$2s^2 2p^5 3p^1 3d^1 (^2D_1) ^2G_{9/2}$	Even	704.6175		
96	$2s^2 2p^5 3p^1 3d^1 (^2D_1) ^2P_{1/2}$	Even	704.9477		
97	$2s^2 2p^5 3p^1 3d^1 (^2D_1) ^4D_{7/2}$	Even	705.1930		
98	$2s^2 2p^5 3p^1 3d^1 (^2D_1) ^2D_{5/2}$	Even	705.7649		
99	$2s^2 2p^5 3p^1 3d^1 (^2D_1) ^2P_{3/2}$	Even	706.5673		
100	$2s^2 2p^5 3p^1 3d^1 (^2D_1) ^2D_{5/2}$	Even	707.1703		

Table 5.5: Comparisons of the transitional parameters with available values in literature and at NIST website.

Lower Level (i)	Upper Level (j)	λ_{ji} (in Å)	λ_{ji} [46] (in Å)	λ_{ji} [NIST] (in Å) [50]	A_{ji} (in s ⁻¹) [E1]	A_{ji} (in s ⁻¹) [46]	A_{ji} (in s ⁻¹) [E2]	A_{ji} (in s ⁻¹) [46]	A_{ji} (in s ⁻¹) [M1]	A_{ji} (in s ⁻¹) [46]	A_{ji} (in s ⁻¹) [M2]	A_{ji} (in s ⁻¹) [46]	f_{ij} [E1]	f_{ij} [46]	S_{ij} (in a.u.) [E1]	S_{ij} (in a.u.) [46]
1	2	7.658 + 01	7.658 + 01	7.674 + 01	4.45+10	4.50+10	1.41+08	1.40+08	0	0	0	0	3.96-02	3.96-02	1.98-02	1.99-02
1	3	2.317+ 01	2.317+ 01	2.317 + 01	1.75+12	1.76+12	2.58+08	2.56+08	0	0	0	0	2.82-01	2.84-01	4.31-02	4.33-02
1	4	1.716 + 01	1.716 + 01		0	0	0	0	1.47+04	1.50+04	3.63+05	3.65+05	0	0	0	0
1	5	1.536 + 01	1.536 + 01		0	0	0	0	0	0	0	0	0	0	0	0
1	6	3.811 + 00	3.812 + 00		0	0	0	0	5.82+07	5.44+07	0	0	0	0	0	0
1	7	3.735 + 00	3.735 + 00		6.30+13	6.19+13	4.32+11	4.36+11	0	0	0		1.31-01	1.29-01	3.24-03	3.18-03
1	8	3.570 + 00	3.571 + 00		3.92+13	3.83+13	4.29+11	4.33+11	0	0	3.38+08	3.30+08	1.49-01	1.46-01	3.52-03	3.44-03
1	9	3.498 + 00	3.499 + 00		0	0	0	0	8.15+05	8.37+05	0	0	0	0	0	0
1	10	3.463 + 00	3.463 + 00		0	0	0	0	0	0	0	0	0	0	0	0
1	11	3.427 + 00	3.428 + 00		0	0	0	0	0	0	7.57+03	7.56+03	0	0	0	0
1	13	2.638 + 00	2.637 + 00		0	0	0	0	6.58+07	6.49+07	0	0	0	0	0	0
1	14	2.619 + 00	2.618 + 00		3.57+13	3.36+13	0	0	0	0	0	0	3.67-02	3.46-02	6.33-04	5.97-04
1	15	2.577 + 00	2.577 + 00		2.53+13	2.34+13	0	0	0	0	4.16+08	3.86+08	5.04-02	4.65-02	8.56-04	7.90-04
1	16	2.559 + 00	2.558 + 00		0	0	1.93+11	2.15+11	1.77+06	1.17+06	0	0	0	0	0	0
1	17	2.549 + 00	2.548 + 00		0	0	2.02+11	2.26+11	0	0	0	0	0	0	0	0
1	18	2.539 + 00	2.539 + 00		0	0	0	0	0	0	3.69+03	3.62+03	0	0	0	0

5.6 REFERENCE

- [1] R. Aymar, P. Barabaschi, Y. Shimomura, The ITER design, *Plasma Phys. Control. Fusion.* 44 (2002) 519–565. <https://doi.org/10.1088/0741-3335/44/5/304>.
- [2] A. V. Demura, M.B. Kadomtsev, V.S. Lisitsa, V.A. Shurygin, Electron impact ionization of tungsten ions in a statistical model, *JETP Lett.* 101 (2015) 85–88. <https://doi.org/10.1134/S0021364015020058>.
- [3] A. Müller, S. Schippers, J. Hellhund, A.L.D. Kilcoyne, R.A. Phaneuf, B.M. McLaughlin, Photoionization of tungsten ions: Experiment and theory for W5+, *J. Phys. B At. Mol. Opt. Phys.* 52 (2019). <https://doi.org/10.1088/1361-6455/ab39c8>.
- [4] J.J. Boyle, Z. Altun, H.P. Kelly, Photoionization cross-section calculation of atomic tungsten, *Phys. Rev. A.* 47 (1993) 4811–4830. <https://doi.org/10.1103/PhysRevA.47.4811>.
- [5] O. Physics, Photoionization of tungsten ions : experiment and theory for and Manuscript version : Accepted Manuscript Photoionization of tungsten ions : experiment and, (2016) 0–16.
- [6] T. Pütterich, R. Neu, R. Dux, A.D. Whiteford, M.G. O’Mullane, Modelling of measured tungsten spectra from ASDEX Upgrade and predictions for ITER, *Plasma Phys. Control. Fusion.* 50 (2008). <https://doi.org/10.1088/0741-3335/50/8/085016>.
- [7] A.E. Kramida, J. Reader, Ionization energies of tungsten ions: W2+ through W71+, *At. Data Nucl. Data Tables.* 92 (2006) 457–479. <https://doi.org/10.1016/j.adt.2006.03.002>.
- [8] A.E. Kramida, T. Shirai, Energy levels and spectral lines of tungsten, W III through W LXXIV, *At. Data Nucl. Data Tables.* 95 (2009) 305–474. <https://doi.org/10.1016/j.adt.2008.12.002>.
- [9] A. Kramida, Recent progress in spectroscopy of tungsten, *Can. J. Phys.* 89 (2011) 551–570. <https://doi.org/10.1139/p11-045>.

-
- [10] U.I. Safronova, A.S. Safronova, P. Beiersdorfer, Excitation energies, radiative and autoionization rates, dielectronic satellite lines, and dielectronic recombination rates for excited states of Na-like W from Ne-like W, *At. Data Nucl. Data Tables.* 95 (2009) 751–785. <https://doi.org/10.1016/j.adt.2009.04.001>.
- [11] A.S. Safronova, A. Stafford, A.K. Gill, R.R. Childers, Polarization of hard X-ray dielectronic satellite lines from Na-like W ions, *J. Quant. Spectrosc. Radiat. Transf.* 272 (2021) 107788. <https://doi.org/10.1016/j.jqsrt.2021.107788>.
- [12] M.B. Trzhaskovskaya, V.K. Nikulin, Radiative recombination and photoionization data for tungsten ions. Electron structure of ions in plasmas, *Atoms.* 3 (2015) 86–119. <https://doi.org/10.3390/atoms3020086>.
- [13] P. Beiersdorfer, M.J. May, J.H. Scofield, S.B. Hansen, Atomic physics and ionization balance of high-Z Ions: Critical ingredients for characterizing and understanding high-temperature plasmas, *High Energy Density Phys.* 8 (2012) 271–283. <https://doi.org/10.1016/j.hedp.2012.03.003>.
- [14] P. Beiersdorfer, J.K. Lepson, M.B. Schneider, M.P. Bode, L-shell x-ray emission from neonlike W64 +, *Phys. Rev. A - At. Mol. Opt. Phys.* 86 (2012) 1–11. <https://doi.org/10.1103/PhysRevA.86.012509>.
- [15] B. Li, G. O’Sullivan, C. Dong, X. Chen, Dielectronic recombination of tungsten ions, *J. Phys. B At. Mol. Opt. Phys.* 49 (2016) 1–15. <https://doi.org/10.1088/0953-4075/49/15/155201>.
- [16] W.D. Chen, J. Xiao, Y. Shen, Y.Q. Fu, F.C. Meng, C.Y. Chen, B.H. Zhang, Y.J. Tang, R. Hutton, Y. Zou, Precise studies on resonant energies of the first intershell (KLL) dielectronic recombination processes for He- up to O-like xenon, *Phys. Plasmas.* 15 (2008). <https://doi.org/10.1063/1.2967486>.
- [17] Dipti, T. Das, L. Sharma, R. Srivastava, L-shell electron excitations of Mg-through O-like tungsten ions, *Phys. Scr.* 89 (2014). <https://doi.org/10.1088/0031-8949/89/8/085403>.
- [18] J. Huang, G. Jiang, Q. Zhao, Ground-state ionization potentials for lithium through neon isoelectronic sequences with $Z = 37-82$, *Chinese Phys. Lett.* 23 (2006) 69–72. <https://doi.org/10.1088/0256-307X/23/1/021>.

-
- [19] Priti, Dipti, L. Sharma, R. Srivastava, Fully relativistic electron impact excitation cross-section and polarization for tungsten ions, *Atoms*. 3 (2015) 53–75. <https://doi.org/10.3390/atoms3020053>.
- [20] W. Eckstein, J. Bohdansky, J. Roth, Atomic and plasma material interaction data for fusion, *Nucl. Fusion*. 1 (1991) 51.
- [21] R.K. Pandey, Spectroscopic Study of EUV and SXR Transitions of Ba XLVI, *J. At. Mol. Condens. Nano Phys.* 5 (2018) 18–39. <https://doi.org/10.26713/jamcnp.v5i1.836>.
- [22] M. Klapisch, P. Mandelbaum, A. Zigler, C. Bauche-Arnoult, J. Bauche, The unresolved 3d-4f transitions in the x-ray spectra of highly ionized tin to rhenium from laser produced plasma, *Phys. Scr.* 34 (1986) 51–57. <https://doi.org/10.1088/0031-8949/34/1/009>.
- [23] E.M.B. Thiemann, F.G. Eparvier, V. Knoer, A. Al Muharrami, R.J. Lillis, Solar Extreme Ultraviolet Irradiance Uncertainties for Planetary Studies, *J. Geophys. Res. Sp. Phys.* 126 (2021). <https://doi.org/10.1029/2020JA028184>.
- [24] V.S. Airapetian, J. Allred, Forward Modeling of Synthetic EUV/SXR Emission from Solar Coronal Active Regions: Case of AR 11117, (2014). <http://arxiv.org/abs/1409.3866>.
- [25] J. Holburg, M. Müller, K. Mann, S. Wieneke, Brilliance improvement of laser-produced extreme ultraviolet and soft x-ray plasmas based on pulsed gas jets, *J. Vac. Sci. Technol. A*. 37 (2019) 031303. <https://doi.org/10.1116/1.5089201>.
- [26] Q.M. Zhang, H.S. Ji, A swirling flare-related EUV jet, *Astron. Astrophys.* 561 (2014) 1–7. <https://doi.org/10.1051/0004-6361/201322616>.
- [27] P.W. Wachulak, A. Bartnik, M. Skorupka, J. Kostecki, R. Jarocki, M. Szczurek, L. Wegrzynski, T. Fok, H. Fiedorowicz, Water-window microscopy using a compact, laser-plasma SXR source based on a double-stream gas-puff target, *Appl. Phys. B Lasers Opt.* 111 (2013) 239–247. <https://doi.org/10.1007/s00340-012-5324-y>.
- [28] A. Bartnik, H. Fiedorowicz, P. Wachulak, T. Fok, Temporal measurements of extreme ultraviolet (EUV) emission, from low temperature, EUV-induced plasmas, *Laser Part. Beams*. 36 (2018) 286–292. <https://doi.org/10.1017/S0263034618000319>.

-
- [29] P. Wachulak, A. Torrissi, M. Ayele, A. Bartnik, J. Czwartos, Ł. Węgrzyński, T. Fok, H. Fiedorowicz, Nanoimaging using soft X-ray and EUV laser-plasma sources, *EPJ Web Conf.* 167 (2018) 1–5. <https://doi.org/10.1051/epjconf/201816703001>.
- [30] P. Wachulak, A. Torrissi, M. Ayele, J. Czwartos, A. Bartnik, Ł. Węgrzyński, T. Fok, T. Parkman, Š. Salačová, J. Turňová, M. Odstrčil, H. Fiedorowicz, Bioimaging using full field and contact EUV and SXR microscopes with nanometer spatial resolution, *Appl. Sci.* 7 (2017). <https://doi.org/10.3390/app7060548>.
- [31] A. Torrissi, P.W. Wachulak, A. Bartnik, Ł. Węgrzyński, T. Fok, H. Fiedorowicz, Biological and material science applications of EUV and SXR nanoscale imaging systems based on double stream gas puff target laser plasma sources, *Nucl. Instruments Methods Phys. Res. Sect. B Beam Interact. with Mater. Atoms.* 411 (2017) 29–34. <https://doi.org/10.1016/j.nimb.2017.01.035>.
- [32] L.H. Yang, Y.C. Jiang, J.Y. Yang, Y. Bi, R.S. Zheng, J.C. Hong, Observations of EUV and soft X-ray recurring jets in an active region, *Res. Astron. Astrophys.* 11 (2011) 1229–1242. <https://doi.org/10.1088/1674-4527/11/10/010>.
- [33] G.Y. Liang, F. Li, F.L. Wang, Y. Wu, J.Y. Zhong, G. Zhao, X-Ray and euv spectroscopy of various astrophysical and laboratory plasmas: Collisional, photoionization and charge-exchange plasmas, *Astrophys. J.* 783 (2014). <https://doi.org/10.1088/0004-637X/783/2/124>.
- [34] A. Bartnik, W. Skrzeczanowski, H. Fiedorowicz, P. Wachulak, T. Fok, EUV induced plasmas created in atomic and molecular gases, (n.d.) 502.
- [35] J.B. Spencer, D.A. Alman, D.N. Ruzic, B.E. Jurczyk, Dynamics of a laser produced plasma for soft x-ray production, *Emerg. Lithogr. Technol.* IX. 5751 (2005) 798. <https://doi.org/10.1117/12.598543>.
- [36] M.F. Gu, The Flexible Atomic Code, 2004. <http://kipac-tree.stanford.edu/fac,.>
- [37] M.A. Baig, Measurement of Photoionization Cross-Section for the Excited States of Atoms: A Review, *Atoms.* 10 (2022). <https://doi.org/10.3390/atoms10020039>.

-
- [38] Atomic Astrophysics and spectroscopy, A.K. Pradhan, S.N. Nahar, www.cambridge.org, ISBN 978-0-521-82536-8.
- [39] D.H. Sampson, H.L. Zhang, A.K. Mohanty, R.E.H. Clark, *Phys. Rev. A* 40, 604 (1989)
- [40] N. Singh, A.K.S. Jha, M. Mohan, Breit-Pauli energy levels and radiative lifetimes in neutral chlorine, *Eur. Phys. J. D* 38, 285–291 (2006) DOI: 10.1140/epjd/e2006-00068-4.
- [41] Tingting An, P yuan, G Lu, J Che, X Wing, M Zhang, Y An, The radius and temperature distribution along radial direction of lightning plasma channel *Phys. Plasmas* 26, 013506 (2019). doi: 10.1063/1.5059363.
- [42] A.K. Singh, Mayank Dimri, Dishu Dawra, Alok K.S. Jha, Man Mohan, *Physics of Plasmas* 26, 062704(2019); <https://doi.org/10.1063/1.5100565> .
- [43] C. Aragón, J.A. Aguilera, Characterization of laser induced plasmas by optical emission spectroscopy: A review of experiments and methods, *Spectrochim. Acta - Part B At. Spectrosc.* 63 (2008) 893–916. <https://doi.org/10.1016/j.sab.2008.05.010>.
- [44] T. Fujimoto, R.W.P. Mc Whirter, Validity criteria for local thermodynamic equilibrium in plasma spectroscopy, *Phys. Rev., A* 42, 6588(1990), <https://doi.org/10.1103/PhysRevA.42.6588>.
- [45] R.W. P. McWhirter (1965). *Plasma Diagnostic Techniques* (Huddleston, R. H.; Leonard S. L., Eds). New York: Academic.
- [46] K.M. Aggarwal, F.P. Keenan, Radiative rates for E1, E2, M1, and M2 transitions in S-like to F-like tungsten ions (W LIX to W LXVI), *At. Data Nucl. Data Tables.* 111–112 (2016) 187–279. <https://doi.org/10.1016/j.adt.2016.02.004>.
- [47] M.D. Turkington, C.P. Ballance, A. Hibbert, C.A. Ramsbottom, Benchmarking a modified version of the civ3 nonrelativistic atomic-structure code within Na-like-tungsten R -matrix calculations, *Phys. Rev. A.* 94 (2016) 1–9. <https://doi.org/10.1103/PhysRevA.94.022508>.
-

- [48] F. Hu, C. Wang, J. Yang, G. Jiang, L. Hao, Multiconfiguration Dirac-Fock calculations of transition probabilities of some tungsten ions, *Phys. Scr.* 84 (2011). <https://doi.org/10.1088/0031-8949/84/01/015302>.
- [49] M. Xu, G. Jiang, M. Wu, X. Li, G. Bian, F. Hu, Multiconfiguration Dirac-Fock calculations of excitation energies and wavelengths in highly charged tungsten ions, *Can. J. Phys.* 94 (2016) 563–568. <https://doi.org/10.1139/cjp-2015-0772>.
- [50] A. Kramida, Yu. Ralchenko, J. Reader, and NIST ASD Team, <https://physics.nist.gov/asd> for NIST Atomic Spectra Database (ver. 5.6.1) (2019).

CHAPTER 6

CONCLUSION, FUTURE SCOPE OF WORK AND SOCIAL IMPACT

- This chapter offers a thorough summary of the main conclusions and contributions made to the field from the research done for this thesis.
- In the conclusion of the research described in this thesis, the main findings, their importance, and the contributions made to the advancement of knowledge in the field are highlighted.
- As a conclusion, this chapter discusses potential directions for future research and looks at the potential societal impacts of exploring deeper into the findings of this study.

6.1 CONCLUSION

In this thesis, we used the fully relativistic multi-configuration Dirac-Fock (MCDF) method to present a comprehensive and in-depth analysis of the atomic structure, spectroscopic data, and plasma characteristics of C-like tungsten (WLXIX), K-like tungsten (WLVI), Na-like potassium (KIX), and Na-like tungsten (WLXIV). In our work, we carefully considered Breit corrections, including the interchange of virtual photons between electrons, and quantum electrodynamics (QED) corrections, including vacuum polarization and self-energy effects. To improve the precision of our findings, especially for K-like and Na-like ions, we also included electron correlations. We identified important soft X-ray (SXR), extreme ultraviolet (EUV), and hard X-ray (HXR) transitions for WLXIX and WLVI by providing energy levels, transition wavelengths, radiative rates, and oscillator strengths for a variety of electric and magnetic multipole transitions. Furthermore, in the particular case of WLVI, the population of excited states and thermodynamic features were investigated. We discussed the importance of valence-valence (VV) and core-valence (CV) correlations and provided detailed data on energy levels, lifetimes, and radiative data for Na-like K (KIX). Additionally, we examined how line intensity ratios in hot dense plasma (HDP) circumstances are affected by plasma temperature. We analyzed electric and magnetic multipole transitions in detail for WLXIV and compared our results to available experimental data from NIST and other theoretical investigations.

We further confirmed the accuracy of our computations by evaluating our results using the Flexible Atomic Code (FAC), an independent completely relativistic configuration interaction program. We found significant agreement among the two methods.

Finding and evaluating spectral lines in diagnostics associated with solar research, fusion plasma investigations, and astrophysical exploration will be made possible by newly released atomic and radiative data. Furthermore, the International Thermonuclear Experimental Reactor (ITER) and other current and future research will benefit from our studies on plasma modeling as well as diagnostics for highly ionized tungsten and potassium ions. The findings of this investigation, including the electron density calculations and line intensity ratios for W LXIV and KIX, will be essential for plasma diagnostics and hot dense plasma (HDP) and astrophysical plasma

characterization.

Although there are obvious limits, our work makes a substantial contribution to the study of atomic structure and plasma diagnostics. The investigation of more complex electron-electron interactions, especially in high Z -ions like tungsten, and additional demonstrations of the predicted transitions belong to them. Future work may focus on introducing more corrections for higher-order interactions and expanding these studies to other ion phases.

The atomic structure and spectroscopic characteristics of C-like, Na-like, and K-like ions have been clarified mainly in this thesis, which has major implications for fusion research, plasma physics, and astrophysics. Our results provide a basis for further research in atomic data production, modeling for laboratory and astrophysical plasmas, and plasma diagnostics. In addition to acknowledging the significance and possible uses, this conclusion summarizes the key findings and discusses the research's limits and future directions.

6.2 FUTURE SCOPE

- To enhance the precision of atomic data, particularly for high Z ions like tungsten, apply relativistic and higher-order QED adjustments, this study will be helpful.
- The study of atomic data is applicable in plasma diagnostics, confirming the theoretical findings with data from future investigations in devices such as ITER and other fusion reactors.
- Astrophysical applications are going to benefit from the provided atomic data to investigate astrophysical plasmas, such as those in the solar corona, interstellar medium, and star atmospheres.
- To improve comprehension of light element behavior, expand the analysis to low- Z ions, which are important for impurity characterization and plasma management in fusion devices for future technologies.
- Utilize the published atomic and radiative data in plasma modeling software to enhance simulations and diagnostics in high-temperature and high-density plasmas.
- Examine the possible applications of EUV and soft X-ray transitions in biological research for future purposes, especially in imaging and radiation-based cell

biology methods.

- To improve plasma diagnostics and modeling, keep improving photoionization cross section estimations at different energy levels.
- To gain a better understanding of plasma behavior, extend the analysis of thermodynamic characteristics, such as partition functions, for various plasma conditions.
- Continue verifying the accuracy of predictions by contrasting calculated data with experimental findings from resources such as the ASDEX Tokamak and NIST compilations.

6.3 SOCIAL IMPACT

Considering its wide variety of scientific and technological applications, this work may have a substantial social impact that Social impact are discussed below in the following important areas:

1. Fusion Energy Development and Clean Energy

* **Sustainable Energy Source:** This research improves the understanding of tungsten (W) spectroscopic data, particularly in fusion plasma conditions. Fusion energy is a cleaner, more sustainable energy source that has the potential to significantly minimize dependence on fossil fuels.

* **Environmental Impact:** When fusion energy is fully developed, it might reduce carbon emissions, provide an almost infinite clean energy source, and promote environmental sustainability, all of which could help slow down climate change.

2. Advancements in Plasma Diagnostics

* **Technological Innovation:** By optimizing plasma modeling for high-temperature applications the data produced may contribute to the development of innovative plasma-related techniques for application in semiconductor manufacturing, aerospace, and telecommunications.

3. Medical and Biophysics Applications

* Radiation therapy and medical imaging methods can be enhanced by the study of spectroscopic transitions, especially in the soft X-ray (SXR) and EUV regions. More precise diagnosis and treatment of illnesses like cancer may result from these developments. High-Z nanoparticles are employed in radiosensitization through irradiation with high-energy hard X-rays in hundreds of KeV range, not just soft X-rays that do not penetrate far in the body. Nanovehicles using gold and platinum have been studied in cancer research ([viz. Pradhan et al. 2009, Montenegro et al. 2009](#)).

4. Contributions to Space Research and Astrophysics:

* **Space Exploration and Understanding of Cosmic Phenomena:** Analysis and interpretation of solar, stellar, solar and cosmic plasma activities can be improved by using the data on C-like and K-like tungsten (W) and Na-like elements in the study of high Z ions in astrophysical plasmas. Space exploration and cosmology study benefit from this, which may lead to new discoveries about the cosmos.

* **Astrophysical Diagnostics:** The research improves astrophysical models and helps identify spectral lines in the X-ray and extreme ultraviolet (EUV) regions, which are crucial for space missions.

5. Support for Global Scientific Collaboration:

* **Educational and Training Opportunities:** In order to train the future generation of scientists and engineers in atomic physics, plasma diagnostics, and fusion energy, the comprehensive theoretical analysis and atomic data offered will be an invaluable resource for researchers, educators, and students.

6. Economic and Industrial Benefits:

* **Job Creation in High-Tech Sectors:** Jobs in space exploration, nuclear energy, medical technology, as well as high-tech manufacturing can be formed as a result of developments in fusion energy, plasma diagnostics, and material sciences.

* **Economic Growth through Innovation:** Economic growth will probably be aided by the creation of innovative technologies supported by this research, especially in the technology and energy industries that depend on advances in atomic and plasma

research.

7. Support for Environmental and Climate Initiatives:

* **Reduction of Greenhouse Gas Emissions:** This research indirectly supports efforts to counteract global warming and reduce greenhouse gas emissions by encouraging the transition to cleaner energy sources like fusion, which is in line with worldwide climate targets.

* **Sustainable Technology Development:** A brighter future may be welcomed through the development of more sustainable technology in businesses that depend on high-energy processes according to the knowledge gained from our effort.

In the end, this research it supports a more environmentally friendly and scientifically advanced society by providing wide-ranging advantages that reach into renewable energy solutions, medicinal innovations, technology developments, and space exploration.



Study of SXR and HXR transitions with intensity spectra of W LXIX

Richa Paijwar¹, Rinku Sharma^{1,a}, Alok Kumar Singh Jha²

¹ Department of Applied Physics, Delhi Technological University, Delhi 110042, India

² School of Physical Sciences, Jawaharlal Nehru University, Delhi 110067, India

Received: 15 December 2022 / Accepted: 15 May 2023

© The Author(s), under exclusive licence to Società Italiana di Fisica and Springer-Verlag GmbH Germany, part of Springer Nature 2023

Abstract We present complete spectroscopic data and a detailed theoretical investigation of C-like W (WLXIX) based on the fully relativistic multi-configuration Dirac–Fock (MCDF) method. We included quantum electrodynamics (QED) corrections due to vacuum polarization, and self-energy effects and Breit correction due to the exchange of virtual photons between two electrons are fully considered in our calculations. For the lowest 205 fine structure levels, we have provided the energy levels and radiative data for multiple transitions such as electric dipole (E1), electric quadrupole (E2), magnetic dipole (M1), and magnetic quadrupole (M2) and identified soft X-ray transitions (SXR) and hard X-ray (HXR) transitions from highly excited states to ground state have been predicted. The credibility and authenticity of our furnished results and related calculations have also been performed using another independent fully relativistic configuration interaction program (Flexible Atomic Code) based on self-consistent Dirac–Fock–Slater iteration method. A reasonably good agreement is found between our two independent atomic structure calculations. We also compared our computed energies with experimental energy levels compiled by NIST and other available theoretical data in the literature, and there are a few minor differences discussed. We have studied the intensity spectra for transitions decaying to ground state for W LXIX. We expect that our newly reported atomic and radiative data of C-like W will help identify and analyze spectral lines obtained from various diagnoses of solar, fusion plasma research and astrophysical exploration.

1 Introduction

Carbon-like isoelectronic sequence has always been a trending and challenging element for experimentalists and theoretical researchers because of their high abundance in the universe [1]. Neutral carbon lines are prominent in both stellar and interstellar spectra, as reported in the literature [2]. Purely, data pertaining to the adjacent C-like ionization stage are essential for understanding various chemical diagnostics and astrophysical processes. However, due to the complexity of six-electron systems, calculating C-like sequences remains a challenge for theorists to calculate atomic properties ab initio to high precision. Thus, researchers must analyze the spectroscopic parameters of the carbon isoelectronic sequence. Few works using various theoretical methodologies and experimental techniques with advanced instruments have been published on C-like ions as communicated in the literature over the last decades, which is limited to only few energy levels. To encapsulate, more systematic and extensive studies are required to provide reliable spectroscopic data for C like W.

1.1 Experimental work on C-like ions

The visible and UV spectra of the symbiotic nova RR Telescopii by Young et al. [3] were utilized to determine the reference wavelengths for many forbidden as well as intercombination transitions of ions between + 1 and + 6 of elements C, N, O, Ne, Na, Mg, Al, Si, P, S, Cl, Ar, K, and Ca, and the wavelengths were used to determine the new energy values for such levels within the ions. In the energy (wavelength) range of 398 eV (31.15) to 450 eV (27.55), high-resolution K-shell photoionization cross sections for the C-like atomic nitrogen ion (N +) have been reported by Mosnier et al. [4]. At the Shanghai Electron Beam Ion Trap, Chen et al. [5] have experimented with studying the resonant energies for KLL dielectronic recombination of He-, Li-, Be-, B-, C-, N-, among O-like xenon ions. Chen et al. also measured the resonant energies at an average uncertainty level of 0.03 percent and were compared with the calculation findings with the help of relativistic configuration interaction (RCI) theory, multiconfiguration Dirac–Fock (MCDF) theory as well as relativistic many-body perturbation theory (RMBPT). Feldman et al. [6] have identified the high-temperature (at $T_e = 3 \times 10^6$ K) of Ne, Na, Mg, Ar, K, Ca, Ti, Cr, Mn, Fe, Co, and also for Ni lines that were detected in the specified region such as 500 to 1600 Å for spectral range of Solar Ultraviolet Measurements of Emitted Radiation (SUMER); SUMER is spectrometer on the Solar and Heliospheric Observatory (SOHO) which obtained spectra from a high-temperature region above

^a e-mail: rinkusharma@dtu.ac.in (corresponding author)

the west limb in the solar corona. At the SOLEIL synchrotron radiation facility, Bizau et al. [7] have provided detailed measurements of absolute cross sections for single photoionization, double K-shell photoionization of C-like O^{2+} , and Ni-like O^{+} ions in the range between 526 and 620 eV photon energy, using the ion-photon merged beam method. Dere et al. [8] have upgraded the modeling of satellite lines in X-ray wavelengths explicitly with the aid of Version 9 (IDL as well as Python) and include autoionization also with dielectronic recombination phenomena in the determination of level populations for selected members of the lithium (Li) isoelectronic sequence as well as Fe XVIII to Fe XXIII. Using monochromatic x rays approximately 6.6 keV at the PETRA III synchrotron photon source, Rudolph et al. [9] have studied photoabsorption based on the primary K_{α} transitions of highly charged ions between He-like and F-like (Fe^{24+} – Fe^{17+}). Edlen et al. [10] have concluded the experimental data on the energy structure of the low ($n = 2$) configurations in 3 to 9 electron systems and also studied Z-dependence of the differences among observed and theoretical levels in the carbon isoelectronic sequence for configurations $2s^22p^2$, $2s2p^3$ and $2p^4$. Liao et al. [11] have analyzed 36 Chandra High Energy Transmission Grating data of K transitions of neutral along with low-ionized metal (like oxygen, neon, and magnesium) to find and evaluate ISM absorption lines on sight lines for 11 low-mass X-ray binaries. McCarthy et al. [12] have identified the 43 spectral emission lines ranging from F-like to Li-like sulfur ions in the wavelength range of 17.5–50 nm in spectra produced following tracer injection into plasmas generated in a magnetically confined plasma device, using stellarator TJ-II. For C-like Mg^{6+} , it is forming Mg^{5+} as well as B-like Mg^{7+} forming Mg^{6+} . Lestinsky et al. [13] have measured electron–ion recombination; experiments were performed at the TSR heavy-ion storage ring in Heidelberg, Germany, utilizing a merged electron–ion beam setup. The extreme-ultraviolet (EUV) spectra of highly charged ions Kr XXI–Kr XXXIV produced in an electron beam ion trap (EBIT) were observed and analyzed by Podpaly et al. [14], by using collisional radiative modeling; the magnetic dipole transition inside the ground configuration $3s^23p$ was demonstrated. With the help of an electron cyclotron resonance ion source, Trabert et al. [15] have measured the lifetime of the system Ne^{4+} at the TSR heavy ion storage ring, where the magnetic dipole decay channel becomes dominant.

1.2 Theoretical work on C-like ions

Wang et al. [16] have explored the detailed description of systematic calculations of energy levels and transition rates of C-like ions with $13 \leq Z \leq 36$ by applying many-body perturbation theory (MBPT). Zheng et al. [17] have studied the ionization potential of excited states in C-like sequences systematically using the weakest bound electron potential model theory and the idea of iso-spectrum-level series. Using the CIV3, K.M. Aggarwal et al. [18] have evaluated the oscillator strengths for transitions in C-like F IV and Ar XIII ions. Sansonetti et al. [19] have provided the handbook of basic atomic spectroscopic data. Rodrigues et al. [20] have analyzed the atomic binding energies between lithium (3 electrons) and dubnium (105 electrons) isoelectronic series using Dirac–Fock approximation. They have also calculated the total atomic energies of ground state configurations. Fawcett et al. [21] have provided the wavelengths as well as classifications of emission lines due to $2s^22p^n - 2s2p^{n+1}$, $2s2p^n - 2p^{n+1}$ transitions up to $Z \leq 28$. Chen et al. [22] have calculated the energies with radiative transitions as well as the radial expectation values of the $1s^22s^22p^2\ ^3P$ ground state and the $1s^22s2p^3\ ^5S$, 1D , 3S highly excited states of C and O^{2+} . Naze et al. [23] have reported the energy levels along with specific mass shift parameters and electronic densities at the nucleus by using relativistic configuration interaction (RCI) calculations for various states like the beryllium, boron, and carbon as nitrogen isoelectronic sequences. For the $\Delta n = 0$ transitions from $n = 2$ in C-like ions with nuclear charge numbers Z in the range $9 \leq Z \leq 54$, relativistic distorted-wave collision intensities have been predicted by Zhang et al. [24]. For the 185 $\Delta n = 0$ transitions from $n = 2$, Zhang et al. [25] have estimated the 67 C-like ions with nuclear charge numbers Z in $26 \leq Z \leq 92$, using relativistic distorted-wave collision strengths. Gu et al. [26] have determined the level energies of $1s^2\ 2l^q$ ($1 \leq q \leq 8$) states for ions with $Z \leq 60$ by using both a combined CI and MBPT technique. Ray et al. [27] have studied the high-stripped carbon-like ions in radiative transitions using the time-dependent Coupled Hartree–Fock (TDCHF) method. By using fully relativistic codes (GRASP2K), Sang et al. [28] have studied the energy levels, hyperfine structure, and the 2 s–2p radiative transition technique of C-like Fe, Co. For elements having atomic numbers $55 \leq Z \leq 95$, Shpatakovskaya et al. [29] have calculated data on the ionization potential of ions in the ground state with the number of electrons $N_e \leq 46$. Further, Fisher et al. [30] have calculated the transitions for C-like sequence using the Multi Configuration Hartree–Fock (MCHF) approach and Breit–Pauli Corrections. Furthermore, Fisher et al. [31] have also reported energy levels and lifetimes as well as transition probabilities of transitions between calculated levels for Be to Ne-like sequences. Recently, Palmeri et al. [32] have computed the impacts of the plasma environment on the ionization potentials (IPs) and K-thresholds utilized in the modeling of K lines for all ions related to the isonuclear sequences of abundant elements apart from O and Fe, notably C, Si, Ca, Cr, as well as Ni. Jönsson et al. [33] have discussed atomic data with many applications, including plasma diagnostics with interpreting the spectra of distant astronomical objects, and showed how large-scale simulations can produce spectroscopically accurate transition energies, transition rates with estimated uncertainty of a few percent for a wide range of ions using fully relativistic MCDF approaches. The soft X-ray emission lines of highly charged sulfur ions (S vii–S xv) in the range of 30–80 Å have been studied by Li et al. [34], and with the help of updated excitation data from the R-matrix technique, a collisional radiative model was also created to estimate line emissivities of S-ions.

1.3 Available data on C-like W

C-like W has already been the subject of some theoretical calculations and experimental measurements using various experimental techniques and theoretical methods. Tu et al. [35] have used a fast electron beam-energy scanning approach to study the photorecombination of highly charged tungsten (W)-ions at the Shanghai electron beam ion trap. By using dielectronic recombination (DR), Tu et al. [36] have also reported the studies of the KLL dielectronic recombination (DR) resonance strengths for He-, Li-, Be-, B-, C-, N-, as well as O-like tungsten ions, with the help of calculation and experiment, were estimated by using a flexible atomic coding (FAC). Using the Dirac-Fock method, for 54 tungsten ions in the W^{6+} – W^{71+} range, radiative recombination and photoionization cross sections, radiative recombination, and radiated power loss rate coefficients have been done by Trzhaskovskaya et al. [37]. By using the MCDF technique, Liu et al. [38] have computed the energy levels, oscillator strengths, transition rates and wavelengths, and also lifetimes for $2s^2 2p^2 \ ^3P_1$ and $2s^2 2p^2 \ ^3P_2$ along with $2s 2p^3 \ ^5S_2$ levels of ions in the C-like sequence (nuclear charges up to $Z = 7$ –92). Beiersdorfer et al. [39] have explained the high- Z ionization balance accurately by applying critical ingredients for characterizing and assessing the energy balance of high-temperature plasmas. The wavelengths and emissivities vs. temperature of the most vital spectral lines expected to be emitted by W ions at EUV longer than 45 nm were determined by Feldman et al. [40]. In order to predict electron binding energies that have been scaled based on experimental results, Kramida et al. [41] used the Hartree-Fock method to compute the ionization energies of multiply charged tungsten ions from W^{2+} to W^{71+} . Huang et al. analyzed the ground-state ionization potentials (IP) for Li through Ne isoelectronic sequences with $Z = 37$ –82 using the MCDF method [42]. Safronova et al. [43] have investigated the relativistic energy of atomic systems using quantum electrodynamics (QED) perturbation theory. Carlson et al. [44] have studied multiply charged ions by computing IP up to $Z = 103$ and have also produced the IP for neutral atoms by performing calculations based on a basic spherical shell solution. However, the majority of the literature only covers a few levels of W LXIX, indicating scarcity in consistent and accurate atomic data for this ion. Our main aim in this paper is to present the energies for higher excited state energy levels, as well as radiative data for multipole transitions (E1, E2, M1 & M2) for WLXIX.

2 Theoretical method

2.1 MCDF method

For the study of highly charged carbon like tungsten ion considered in this paper, a completely relativistic MCDF approach refined by Norrington and previously established by Grant et al. [45] to perform these large-scale computations. The inclusion of LSJ names for the levels/configurations in addition to the standard jj nomenclature of the relativistic codes is a particularly helpful feature of this edition. Contributions from Breit interactions are included, along with QED corrections such as vacuum polarization as well as self-energy, which are often incorporated as a first-order perturbation correction. These relativistic effects must be considered, particularly for high Z ions, because the nuclear potential energy is very strong and the velocity of inner electrons is fast. The theoretical basis of our current computation method has already been extensively addressed in some publications and can be found here [46]. To evaluate radial wave functions during self-consistent field (SCF) operation, We chose extended average level (EAL), which minimizes the weighted trace of the Hamiltonian matrix.

By diagonalizing the relativistic Hamiltonian H , the energy levels of an atomic ion with N electrons are obtained as

$$H = \sum_{i=1}^N H_D(i) + \sum_{i<j}^N \frac{1}{r_{ij}}, \quad (1)$$

In Eq. (1), the single electron Dirac Hamiltonian is $H_D(i)$. An atomic state function (ASF) estimates the particular wave function of an atomic state for an N electron atom or ion system.

The configuration state functions (CFSs) are antisymmetrized linear combinations of relativistic orbital products, which are defined as follows:

$$\vartheta_{nkm} = \frac{1}{r} \begin{pmatrix} P_{nk}(r) & \chi_{km}(\theta, \vartheta, \sigma) \\ -i Q_{nk}(r) & \chi_{-km}(\theta, \vartheta, \sigma) \end{pmatrix} \quad (2)$$

where the relativistic angular quantum number denotes k . P_{nk} is component radial wave functions and $Q_{nk}(r)$ small component radial wave functions in Eq. (2). Spinor spherical harmonic is $\chi_{-km}(\hat{r})$.

The N electronic configuration state function (CSF) of the ASF is a linear combination, and it is written as:

$$\Psi(\gamma P J) = \sum_{i=1}^N c_i \vartheta(\gamma_i P J) \quad (3)$$

The configuration, along with the angular coupling tree, signifies as γ_i . Final angular quantum number is J , P is parity. The expansion coefficients are denoted by the c_i , which is obtained by diagonalizing the Dirac-Coulomb-Hamiltonian in Eq. (3).

2.2 Flexible atomic code

We also performed computations using the FAC approach to verify the correctness of our findings. Gu created FAC at Stanford University [47]. FAC is performed to a self-consistent Dirac Slater iteration on a fictitious mean configuration to derive local central potential [46]. The advantage of FAC is that it is incredibly efficient to run, as well as this code is also included as fully relativistic. In FAC, there is a difference between these two fully relativistic codes in calculations, the local central field is used, and the MCDF conducts energy minimization for a particular set of states. Nuclear charge and electron–electron interaction both contribute to the local potential employed in the FAC. Below is a listing of the nuclear potential:

$$V^N = \begin{cases} \frac{Z}{2} \left(\frac{r}{R_N} \right) \left[3 - \left(\frac{r}{R_N} \right)^2 \right], & r \leq R_N \\ Z, & r > R_N \end{cases} \quad (4)$$

where the radius of the nucleus is denoted by R_N in Eq. (4).

As a result, Table 1 also includes the findings (FAC) obtained with the same CI as with GRASP.

2.3 Computational procedure

In order to obtain accurate results for W^{68+} (C-like tungsten) as we have chosen the following method:

Firstly, we have provided ground state configuration, i.e., $1s^2 2s^2 2p^2$ and considered configurations as $1s^2 2s^1 2p^2 3l(l = 0-2)$, $1s^2 2s^1 2p^2 4l(l = 0-3)$, $1s^2 2s^1 2p^2 5l(l = 0-4)$, $1s^2 2s^1 2p^2 6l(l = 0-4)$ and $1s^2 2s^2 2p^1 3l(l = 0-2)$, $1s^2 2s^2 2p^1 4l(l = 0-3)$, $1s^2 2s^2 2p^1 5l(l = 0-4)$, $1s^2 2s^2 2p^1 6l(l = 0-4)$ by taking single electron excitation from 2s and 2p orbitals.

In other step, we have included configuration like $1s^2 2p^4$, $1s^2 2p^3 3l(l = 0-2)$, $1s^2 2p^3 4l(l = 0-3)$, $1s^2 2p^3 5l(l = 0-4)$, $1s^2 2p^3 6l(l = 0-4)$ from 2s orbital by considering double electron excitation.

3 Results and discussions

3.1 Energy levels

The lowest 205 fine structure levels are listed in this study, belonging to the configurations $1s^2 2s^2 2p^2$, $1s^2 2s^1 2p^3$, $1s^2 2p^4$ from GRASP and FAC both in Table 1. We used 54 combinations in our computations, namely $1s^2 2s^1 2p^2 3l(l = 0-2)$, $1s^2 2s^1 2p^2 4l(l = 0-3)$, $1s^2 2s^1 2p^2 5l(l = 0-4)$, $1s^2 2s^1 2p^2 6l(l = 0-4)$ as well as $1s^2 2p^3 3l(l = 0-2)$, $1s^2 2p^3 4l(l = 0-3)$, $1s^2 2p^3 5l(l = 0-4)$, $1s^2 2p^3 6l(l = 0-4)$ and $1s^2 2s^2 2p^1 3l(l = 0-2)$, $1s^2 2s^2 2p^1 4l(l = 0-3)$, $1s^2 2s^2 2p^1 5l(l = 0-4)$, $1s^2 2s^2 2p^1 6l(l = 0-4)$.

From Table 1, we observed that contribution of QED is less than Breit. So in the case of W LXIX, QED effects are less significant. We have compared our calculated data from GRASP and FAC with NIST [48] and the maximum discrepancy of GRASP and FAC results with results compiled by NIST is 0.42%, respectively. The percentage difference between GRASP and FAC is displayed in Table 1 under the column of “ ΔE ”.

$$\Delta E = \frac{|E_{\text{FAC}} - E_{\text{GRASP}}|}{E_{\text{FAC}}} \times 100\% \quad (5)$$

The maximum value of ΔE is 0.42%. This shows that our results from their two independent calculations for most levels are in reasonable agreement and verify that our results are accurate. The small variations in some levels between GRASP and FAC energies are mostly due to different computations of electron wave functions for radial orbitals with recoupling methods of angular parts.

3.2 Radiative data

For the E1, M1, E2, and M2 transitions, connection between the transition rates and oscillator strength (f_{ij}) along with line strength (S_{ij}) can be described as:

$$\text{for E1 transitions : } A_{ji} = \frac{2.0261 \times 10^{18}}{\omega_j \lambda_{ji}^3} S_{ij} \text{ and } f_{ij} = \frac{303.75}{\lambda_{ji} \omega_i} S_{ij}, \quad (6)$$

$$\text{for M1 transitions : } A_{ji} = \frac{2.6974 \times 10^{13}}{\omega_j \lambda_{ji}^3} S_{ij} \text{ and } f_{ij} = \frac{4.044 \times 10^{-3}}{\lambda_{ji} \omega_i} S_{ij}, \quad (7)$$

$$\text{for E2 transitions : } A_{ji} = \frac{1.1199 \times 10^{18}}{\omega_j \lambda_{ji}^5} S_{ij} \text{ and } f_{ij} = \frac{167.89}{\lambda_{ji}^3 \omega_i} S_{ij}, \quad (8)$$

Table 1 Energies (in Ryd.) of lowest 205 fine structure levels of W LXIX

Levels	Configurations	Parity	MCDF				FAC	NIST	ΔE
			Zero-order	Breit	QED	Total			
1	$2s^2 2p^2 ({}^3P_2) {}^3P_0$	Even	000.00	–	–	000.0000	000.0000	000.00	–
2	$2s^2 2p^2 ({}^3P_2) {}^3P_1$	Even	105.1250	– 1.5700	0.1260	103.6821	103.7865		
3	$2s^2 2p^2 ({}^1D_2) {}^1D_2$	Even	107.0863	– 2.1800	0.1260	105.0345	105.1361	105.08	0.100
4	$2s^1 2p^3 ({}^2P_1) {}^3S_1$	Odd	128.0918	– 0.6050	– 1.2000	126.2834	126.0415		
5	$2s^1 2p^3 ({}^2P_1) {}^1P_1$	Odd	134.3963	– 0.3690	– 1.2000	132.8238	132.5726	132.44	0.187
6	$2s^2 2p^2 ({}^3P_2) {}^3P_2$	Even	213.6133	– 3.3400	0.2320	210.5102	210.7195		
7	$2s^2 2p^2 ({}^1S_0) {}^1S_0$	Even	217.6028	– 2.6600	0.2310	215.1751	215.3811		
8	$2s^1 2p^3 ({}^4S_3) {}^5S_2$	Odd	230.8832	– 1.9700	– 1.0800	227.8351	227.7146		
9	$2s^1 2p^3 ({}^2D_3) {}^3D_3$	Odd	235.1278	– 2.9100	– 1.0800	231.1403	231.0105		
10	$2s^1 2p^3 ({}^2P_1) {}^3P_0$	Odd	238.3523	– 1.4600	– 1.0800	235.8156	235.6887		
11	$2s^1 2p^3 ({}^4S_3) {}^3S_1$	Odd	240.4511	– 1.8800	– 1.0800	237.4951	237.3575		
12	$2s^1 2p^3 ({}^2P_1) {}^3P_1$	Odd	241.4010	– 1.8200	– 1.0800	238.5081	238.0410		
13	$2s^1 2p^3 ({}^2D_3) {}^1D_2$	Odd	241.7216	– 2.4600	– 1.0800	238.1790	238.3713		
14	$2p^4 ({}^3P_2) {}^3P_2$	Even	265.3201	– 0.8380	– 2.3900	262.0943	261.6043		
15	$2p^4 ({}^1S_0) {}^1S_0$	Odd	269.5109	– 0.1440	– 2.3900	266.9799	266.4868		
16	$2s^1 2p^3 ({}^2D_3) {}^3D_2$	Odd	343.6099	– 3.4700	– 0.9520	339.1892	339.1791		
17	$2s^1 2p^3 ({}^2D_3) {}^3D_1$	Odd	349.8123	– 3.2600	– 0.9520	345.5953	345.5759		
18	$2p^4 ({}^3P_2) {}^3P_1$	Even	371.2252	– 1.9700	– 2.2800	366.9760	366.6109		
19	$2p^4 ({}^1D_2) {}^1D_2$	Even	373.1988	– 2.5700	– 2.2800	368.3496	367.9819		
20	$2p^4 ({}^3P_2) {}^3P_0$	Even	481.3380	– 3.2700	– 2.1600	475.9136	475.6745		
21	$2s^2 2p^1 3s^1 ({}^2S_1) {}^3P_0$	Odd	766.8732	– 2.5400	0.3080	764.6434	764.8544		
22	$2s^2 2p^1 3s^1 ({}^2S_1) {}^3P_1$	Odd	767.2421	– 2.6400	0.3120	764.9127	765.1279		
23	$2s^2 2p^1 3s^1 ({}^2P_1) {}^3D_1$	Even	773.6478	– 2.2900	– 0.0578	771.3004	771.4046		
24	$2s^2 2p^1 3s^1 ({}^2P_1) {}^1S_0$	Even	777.0314	– 2.0500	– 0.0626	774.9180	775.0496		
25	$2s^2 2p^1 3s^1 ({}^2S_1) {}^5P_1$	Even	787.4731	– 1.1600	– 1.0100	785.3054	785.2092		
26	$2s^2 2p^1 3s^1 ({}^2S_1) {}^3P_0$	Even	790.2751	– 1.0200	– 1.0100	788.2447	788.1378		
27	$2s^2 2p^1 3p^1 ({}^2P_1) {}^5D_0$	Odd	794.6412	– 0.6170	– 1.3800	792.6463	792.3879		
28	$2s^2 2p^1 3p^1 ({}^2P_1) {}^5D_1$	Odd	794.7796	– 0.8130	– 1.3800	792.5866	792.4441		
29	$2s^2 2p^1 3p^1 ({}^2P_1) {}^3P_1$	Even	806.3343	– 2.5700	– 0.0261	803.7407	803.7880		
30	$2s^2 2p^1 3p^1 ({}^2P_1) {}^3D_2$	Even	806.4141	– 2.7400	– 0.0196	803.6553	803.8709		
31	$2s^2 2p^1 3d^1 ({}^2D_1) {}^3F_2$	Odd	811.2927	– 2.7700	– 0.0719	808.4549	808.5099		
34	$2s^2 2p^1 3d^1 ({}^2D_1) {}^3D_3$	Odd	820.9356	– 2.9900	– 0.0716	817.8766	817.9344		
35	$2s^1 2p^2 3d^1 ({}^2P_1) {}^5P_2$	Odd	827.0909	– 1.2200	– 1.3200	824.5490	824.3632		
36	$2s^1 2p^2 3p^1 ({}^2P_1) {}^3D_1$	Odd	827.4841	– 1.2000	– 1.3500	824.9395	824.7543		
37	$2s^1 2p^2 3d^1 ({}^2D_1) {}^5F_1$	Even	831.8005	– 1.1200	– 1.4000	829.2818	829.0161		
38	$2s^1 2p^2 3p^1 ({}^2D_1) {}^3D_2$	Even	832.4294	– 1.3000	– 1.4000	829.7243	829.4624		
39	$2s^1 2p^2 3p^1 ({}^2D_1) {}^3D_3$	Even	841.0644	– 1.5300	– 1.4000	838.1382	837.8820		
40	$2s^1 2p^2 3p^1 ({}^2D_1) {}^3F_2$	Even	842.2457	– 1.3900	– 1.4000	839.4554	839.2033		
41	$2s^2 2p^1 3s^1 ({}^2S_1) {}^3P_2$	Odd	875.5322	– 4.1200	0.4090	871.8239	872.1006		
42	$2s^2 2p^1 3s^1 ({}^2S_1) {}^1P_1$	Odd	876.1694	– 4.0800	0.4110	872.4989	872.7872		
43	$2s^2 2p^1 3p^1 ({}^2P_1) {}^3S_1$	Even	883.4646	– 3.6300	0.0277	879.8598	880.0395		
44	$2s^2 2p^1 3p^1 ({}^2P_1) {}^1D_2$	Even	883.7755	– 3.8000	0.0295	880.0019	880.1853		
45	$2s^1 2p^2 3s^1 ({}^2D_1) {}^5P_2$	Even	890.1976	– 2.7800	– 0.8800	886.5383	886.5125		
46	$2s^1 2p^2 3s^1 ({}^2S_1) {}^3P_1$	Even	892.2823	– 2.7200	– 0.8750	888.6838	888.6661		
47	$2s^1 2p^2 3s^1 ({}^2S_1) {}^3D_3$	Even	893.9534	– 3.6100	– 0.8850	889.4627	889.4257		

Table 1 continued

Levels	Configurations	Parity	MCDF				FAC	NIST	ΔE
			Zero-order	Breit	QED	Total			
48	$2s^1 2p^2 3s^1 ({}^2S_1)^3D_2$	Even	895.7740	− 3.4400	− 0.8870	891.4508	891.4182		
49	$2s^1 2p^2 3p^1 ({}^2P_1)^5D_1$	Odd	897.0121	− 2.2900	− 1.2600	893.4594	893.3276		
50	$2s^1 2p^2 3p^1 ({}^2P_1)^5D_2$	Odd	898.0991	− 2.5700	− 1.2600	894.2745	894.1451		
51	$2s^1 2p^2 3s^1 ({}^2S_1)^1S_0$	Even	899.1447	− 2.7300	− 0.8840	895.5352	895.4848		
52	$2s^1 2p^2 3s^1 ({}^2S_1)^1P_1$	Even	899.4471	− 2.9300	− 0.8830	895.6355	895.5854		
53	$2s^1 2p^2 3s^1 ({}^2S_1)^3D_1$	Even	899.8117	− 2.8300	− 0.8920	896.0925	896.0348		
54	$2s^1 2p^2 3s^1 ({}^2S_1)^1D_2$	Even	900.3707	− 3.1500	− 0.8850	896.3391	896.2856		
55	$2s^1 2p^2 3p^1 ({}^2P_1)^1F_3$	Odd	901.2262	− 3.3700	− 1.2600	896.5961	896.4544		
56	$2s^1 2p^2 3p^1 ({}^2P_1)^3P_2$	Odd	903.6575	− 2.8500	− 1.2500	899.5491	899.4290		
57	$2s^1 2p^2 3p^1 ({}^2P_1)^3P_0$	Odd	905.5283	− 2.3600	− 1.2600	901.9161	901.7459		
58	$2s^1 2p^2 3p^1 ({}^2P_1)^3D_1$	Odd	905.7809	− 2.5300	− 1.2600	901.9970	901.8282		
59	$2s^1 2p^2 3p^1 ({}^2P_1)^5F_2$	Odd	906.3338	− 2.8800	− 1.2600	902.2008	902.0357		
60	$2s^1 2p^2 3p^1 ({}^2P_1)^3D_1$	Odd	909.5769	− 2.4600	− 1.2600	905.8639	905.7204		
61	$2s^2 2p^1 3p^1 ({}^2P_1)^1P_1$	Even	913.7990	− 4.1600	0.0730	909.7153	909.8593		
62	$2s^2 2p^1 3p^1 ({}^2P_1)^3D_3$	Even	913.8117	− 4.2200	0.0759	909.6684	909.9052		
63	$2s^2 2p^1 3p^1 ({}^2P_1)^3P_2$	Even	916.0398	− 4.1100	0.0747	912.0012	912.2132		
64	$2s^2 2p^1 3p^1 ({}^2P_1)^1S_0$	Even	917.8013	− 3.8400	0.0748	914.0325	914.2500		
67	$2s^2 2p^1 3d^1 ({}^2D_1)^3F_3$	Odd	921.4414	− 4.4700	0.0239	916.9992	917.1242		
72	$2s^2 2p^1 3d^1 ({}^2D_1)^3F_4$	Odd	927.9074	− 4.4400	− 0.0059	923.4658	923.5886		
74	$2s^1 2p^2 3p^1 ({}^2S_1)^5D_3$	Odd	928.4912	− 3.0100	− 1.2000	924.2820	924.3268		
76	$2s^1 2p^2 3p^1 ({}^2P_1)^3S_1$	Odd	929.3757	− 2.9300	− 1.2100	925.2343	925.1989		
77	$2s^2 2p^1 3d^1 ({}^2D_1)^1F_3$	Odd	930.2472	− 4.3100	− 0.0108	925.9291	925.8950		
78	$2s^1 2p^2 3p^1 ({}^2P_1)^3D_2$	Odd	930.6172	− 2.8700	− 1.1900	926.5587	926.4441		
80	$2s^1 2p^2 3p^1 ({}^2P_1)^3P_0$	Odd	931.5094	− 2.7400	− 1.2200	927.5527	927.4490		
81	$2s^1 2p^2 3p^1 ({}^2P_1)^3F_4$	Odd	932.5244	− 3.7400	− 1.1900	927.5935	927.4788		
82	$2s^1 2p^2 3p^1 ({}^2P_1)^3P_2$	Odd	933.3612	− 3.4600	− 1.2300	928.6734	928.5452		
83	$2s^1 2p^2 3p^1 ({}^2P_1)^3D_3$	Odd	934.3641	− 3.5900	− 1.2100	929.5634	929.4517		
84	$2s^1 2p^2 3p^1 ({}^2P_1)^1P_1$	Odd	934.4165	− 3.3500	− 1.2300	929.8361	929.7048		
85	$2s^1 2p^2 3d^1 ({}^2D_1)^5D_0$	Even	934.7393	− 2.5000	− 1.2700	930.9683	930.4441		
86	$2s^1 2p^2 3d^1 ({}^2D_1)^5F_2$	Even	934.7480	− 2.8500	− 1.2800	930.6249	930.6587		
87	$2s^1 2p^2 3d^1 ({}^2D_1)^5D_1$	Even	934.8193	− 2.7000	− 1.2800	930.8394	930.7867		
88	$2s^1 2p^2 3d^1 ({}^2D_1)^5F_3$	Even	935.7611	− 3.1100	− 1.2700	931.3739	931.1948		
89	$2s^1 2p^2 3p^1 ({}^2P_1)^3D_2$	Odd	937.5835	− 2.7900	− 1.2300	933.5663	933.4182		
90	$2s^1 2p^2 3p^1 ({}^2P_1)^3D_3$	Odd	938.2886	− 3.3000	− 1.2200	933.7667	933.6258		
91	$2s^1 2p^2 3p^1 ({}^2P_1)^3P_0$	Odd	938.9291	− 2.9300	− 1.2200	934.7800	933.6303		
92	$2s^1 2p^2 3d^1 ({}^2D_1)^3G_4$	Odd	938.9540	− 3.8600	− 1.2700	933.8193	934.2529		
93	$2s^1 2p^2 3p^1 ({}^2P_1)^3P_1$	Odd	939.0947	− 2.7800	− 1.2200	935.0931	934.6437		
94	$2s^1 2p^2 3p^1 ({}^2P_1)^3D_2$	Odd	939.3890	− 3.1400	− 1.2200	935.0230	934.8795		
95	$2s^1 2p^2 3d^1 ({}^2D_1)^3F_3$	Even	939.4025	− 3.6800	− 1.2800	934.4462	934.8816		
96	$2s^1 2p^2 3p^1 ({}^2P_1)^3P_1$	Odd	939.7655	− 2.9400	− 1.2200	935.6063	934.9480		
97	$2s^1 2p^2 3d^1 ({}^2D_1)^3D_2$	Even	939.9472	− 3.5800	− 1.2800	935.0831	935.4731		
98	$2s^1 2p^2 3d^1 ({}^2D_1)^3S_1$	Even	940.4750	− 3.4000	− 1.2900	935.7866	935.5754		
99	$2s^1 2p^2 3d^1 ({}^2D_1)^5F_4$	Even	942.5321	− 3.1400	− 1.2700	938.1181	937.9424		
100	$2s^1 2p^2 3d^1 ({}^2D_1)^3F_2$	Even	942.9346	− 3.0400	− 1.2800	938.6185	938.4080		
101	$2s^1 2p^2 3d^1 ({}^2D_1)^1P_1$	Even	943.2990	− 2.7900	− 1.2800	939.2371	938.9979		

Table 1 continued

Levels	Configurations	Parity	MCDF				FAC	NIST	ΔE
			Zero-order	Breit	QED	Total			
102	$2s^1 2p^2 3d^1 (^2D_1)^3G_3$	Even	943.8354	− 3.3500	− 1.2800	939.2124	939.0223		
103	$2s^1 2p^2 3d^1 (^2D_1)^3P_2$	Even	944.4245	− 3.0000	− 1.2800	940.1475	939.9640		
104	$2s^1 2p^2 3d^1 (^2D_1)^3F_3$	Even	944.8424	− 3.1200	− 1.2800	940.4453	940.2711		
105	$2s^1 2p^2 3d^1 (^2D_1)^3D_1$	Even	945.2310	− 3.1900	− 1.2800	940.7642	940.5477		
106	$2s^1 2p^2 3d^1 (^2D_1)^3F_2$	Even	945.6718	− 3.2400	− 1.2800	941.1555	940.9344		
107	$2s^1 2p^2 3d^1 (^2D_1)^3P_0$	Even	946.2912	− 3.2700	− 1.2800	941.7494	940.9345		
108	$2s^1 2p^2 3d^1 (^2D_1)^3G_5$	Even	946.3724	− 3.9700	− 1.2700	941.1244	941.5295		
109	$2s^1 2p^2 3d^1 (^2D_1)^3D_1$	Even	946.4190	− 2.9700	− 1.2800	942.1702	941.9896		
110	$2s^1 2p^2 3d^1 (^2D_1)^3D_3$	Even	948.0844	− 3.8000	− 1.2800	943.0085	942.8191		
111	$2s^1 2p^2 3d^1 (^2D_1)^3F_4$	Even	948.5545	− 3.9200	− 1.2700	943.3587	943.1707		
112	$2s^1 2p^2 3d^1 (^2D_1)^1D_2$	Even	948.7602	− 3.6500	− 1.2800	943.8327	943.6444		
113	$2s^1 2p^2 3d^1 (^2D_1)^1P_1$	Even	949.5789	− 3.5500	− 1.2900	944.7408	944.5573		
114	$2s^1 2p^2 3d^1 (^2D_1)^3P_0$	Even	950.0805	− 3.5400	− 1.2800	945.2568	945.0689		
115	$2s^1 2p^2 3d^1 (^2D_1)^3D_3$	Even	951.6991	− 3.0700	− 1.2900	947.3400	947.1256		
116	$2s^1 2p^2 3d^1 (^2D_1)^1G_4$	Even	952.5710	− 3.5000	− 1.2700	947.8005	947.5881		
117	$2s^1 2p^2 3d^1 (^2D_1)^3P_2$	Even	953.1490	− 3.0800	− 1.2800	948.7920	948.5732		
118	$2s^1 2p^2 3d^1 (^2D_1)^3P_1$	Even	953.5145	− 3.3300	− 1.2800	948.9078	948.6674		
119	$2s^1 2p^2 3d^1 (^2D_1)^1F_3$	Even	953.5743	− 3.4200	− 1.2800	948.8775	948.6941		
120	$2s^1 2p^2 3d^1 (^2D_1)^1D_2$	Even	953.7540	− 3.3200	− 1.2800	949.1555	948.9443		
135	$2s^1 2p^2 3s^1 (^2S_1)^3S_1$	Even	1008.0785	− 3.8800	− 0.7640	1003.4329	997.2035		
136	$2s^1 2p^2 3p^1 (^2P_1)^5S_2$	Odd	1008.8319	− 4.1700	− 1.1300	1003.5279	1003.4857		
137	$2s^1 2p^2 3s^1 (^2P_1)^3P_1$	Even	1009.1799	− 4.3900	− 0.7650	1004.0203	1003.4545		
138	$2s^1 2p^2 3p^1 (^2P_1)^3D_3$	Odd	1009.3157	− 4.4800	− 1.1400	1003.6982	1003.6596		
140	$2s^1 2p^2 3s^1 (^2P_1)^1S_0$	Even	1010.4418	− 3.7600	− 0.7710	1005.9127	1005.9406		
141	$2s^1 2p^2 3p^1 (^2P_1)^3P_0$	Odd	1016.2367	− 3.4100	− 1.1300	1011.6967	1011.6165		
142	$2s^1 2p^2 3p^1 (^2P_1)^1P_1$	Odd	1016.4457	− 3.5900	− 1.1400	1011.7235	1011.6425		
143	$2s^1 2p^2 3p^1 (^2P_1)^3S_1$	Odd	1016.8529	− 3.9900	− 1.1400	1011.7234	1011.6466		
144	$2s^1 2p^2 3p^1 (^2P_1)^1D_2$	Odd	1017.1280	− 4.1200	− 1.1400	1011.8656	1011.7902		
160	$2s^1 2p^2 3p^1 (^2P_1)^5D_4$	Odd	1038.7119	− 4.8000	− 1.1000	1032.8143	1032.7823		
161	$2s^1 2p^2 3p^1 (^2P_1)^5P_3$	Odd	1038.9763	− 4.7600	− 1.1100	1033.1097	1033.0764		
162	$2s^1 2p^2 3p^1 (^2P_1)^3S_1$	Odd	1039.8126	− 4.6700	− 1.1100	1034.0310	1033.9965		
164	$2s^1 2p^2 3p^1 (^2P_1)^1D_2$	Odd	1042.1182	− 4.5600	− 1.1100	1036.4523	1036.4296		
165	$2s^1 2p^2 3d^1 (^2D_1)^5D_2$	Even	1045.9349	− 4.6100	− 1.1600	1040.1730	1040.0710		
166	$2s^1 2p^2 3d^1 (^2D_1)^5P_1$	Even	1046.2290	− 4.6200	− 1.1600	1040.4486	1040.2062		
167	$2s^1 2p^2 3d^1 (^2D_1)^5D_3$	Even	1046.3764	− 4.9200	− 1.1500	1040.3030	1040.3475		
168	$2s^1 2p^2 3p^1 (^2P_1)^3P_0$	Odd	1046.6112	− 4.4400	− 1.1000	1041.0698	1041.0023		
169	$2s^1 2p^2 3p^1 (^2P_1)^3P_2$	Odd	1046.6798	− 4.0300	− 1.1000	1041.5541	1041.3518		
170	$2s^1 2p^2 3d^1 (^2D_1)^3F_4$	Even	1046.8238	− 5.1500	− 1.1500	1040.5224	1041.4319		
171	$2s^1 2p^2 3p^1 (^2P_1)^3F_3$	Odd	1047.0493	− 4.5300	− 1.1000	1041.4186	1041.4909		
172	$2s^1 2p^2 3p^1 (^2P_1)^3P_1$	Odd	1047.2941	− 3.9200	− 1.1100	1042.2701	1042.2077		
173	$2s^1 2p^2 3p^1 (^2P_1)^3P_2$	Odd	1047.9115	− 4.3000	− 1.1000	1042.5093	1042.4572		
176	$2s^1 2p^2 3p^1 (^2P_1)^1P_1$	Odd	1050.2740	− 4.2400	− 1.1000	1044.9320	1044.8855		
179	$2s^1 2p^2 3d^1 (^2D_1)^5F_5$	Even	1052.7334	− 5.0800	− 1.1500	1046.4993	1046.4047		
180	$2s^1 2p^2 3d^1 (^2D_1)^3D_1$	Even	1052.8860	− 4.2100	− 1.1600	1047.5168	1046.7224		
181	$2s^1 2p^2 3d^1 (^2D_1)^5D_4$	Even	1052.9446	− 4.9800	− 1.1500	1046.8154	1047.1493		

Table 1 continued

Levels	Configurations	Parity	MCDF				FAC	NIST	ΔE
			Zero-order	Breit	QED	Total			
182	$2s^1 2p^2 3d^1 (^2D_1)^3P_0$	Even	1053.0203	− 4.6000	− 1.1600	1047.2636	1047.3858		
184	$2s^1 2p^2 3d^1 (^2D_1)^1D_2$	Even	1053.6966	− 4.2800	− 1.1500	1048.2668	1048.0897		
186	$2s^1 2p^2 3d^1 (^2D_1)^3F_3$	Even	1054.1322	− 4.7600	− 1.1500	1048.2162	1048.1402		
187	$2s^1 2p^2 3d^1 (^2D_1)^3D_2$	Even	1054.5487	− 4.5700	− 1.1500	1048.8318	1048.7026		
188	$2s^1 2p^2 3d^1 (^2D_1)^3D_1$	Even	1054.6264	− 4.2700	− 1.1500	1049.2007	1049.0660		
191	$2s^1 2p^2 3d^1 (^2D_1)^3P_1$	Even	1055.6024	− 4.7100	− 1.1600	1049.7363	1049.6381		
192	$2s^1 2p^2 3d^1 (^2D_1)^3D_3$	Even	1055.8620	− 4.8700	− 1.1500	1049.8432	1049.7409		
197	$2s^1 2p^2 3d^1 (^2D_1)^3P_0$	Even	1056.4228	− 4.7300	− 1.1500	1050.5422	1050.4381		
198	$2s^1 2p^2 3d^1 (^2D_1)^3P_2$	Even	1056.6277	− 4.7700	− 1.1600	1050.7030	1050.6059		
202	$2s^1 2p^2 3d^1 (^2D_1)^3F_4$	Even	1061.2064	− 4.7000	− 1.1800	1055.3224	1055.4316		
203	$2s^1 2p^2 3d^1 (^2D_1)^1F_3$	Even	1061.7963	− 4.6200	− 1.1800	1055.9993	1055.8786		
205	$2s^1 2p^2 3d^1 (^2D_1)^3P_1$	Even	1062.7499	− 4.6000	− 1.1700	1056.9767	1057.8510		

Table 2 Radiative data for E1 transitions in W LXIX

S. no	Transition		λ_{ji} (in Å)	A_{ji} (in s ^{−1})	f_{ij}	S_{ij} (in a.u.)
	Lower level (<i>i</i>)	Upper level (<i>j</i>)				
1	1	5	6.861	1.2654E+13	2.6787E−01	6.0503E−03
2	1	11	3.837	7.3749E+10	4.8833E−04	6.1685E−06
3	1	12	3.821	4.7639E+09	3.1277E−05	3.9341E−07
4	1	17	2.637	2.3222E+06	7.2617E−09	6.3036E−11
5	1	22	1.191	5.4283E+13	3.4650E−02	1.3590E−04
6	1	28	1.150	5.5629E+14	3.3074E−01	1.2519E−03
7	1	36	1.105	5.3901E+14	2.9582E−01	1.0758E−03
8	1	42	1.044	9.7912E+09	4.8037E−06	1.6517E−08
9	1	49	1.020	6.1057E+07	2.8566E−08	9.5919E−11
10	1	58	1.010	9.3914E+10	4.3111E−05	1.4339E−07
11	1	60	1.006	1.5102E+11	6.8734E−05	2.2763E−07
12	1	76	0.985	5.3554E+10	2.3365E−05	7.5758E−08
13	1	84	0.980	9.3519E+10	4.0398E−05	1.3034E−07
14	1	93	0.975	5.4388E+11	2.3231E−04	7.4530E−07
15	1	96	0.974	3.7956E+11	1.6194E−04	5.1926E−07
16	1	142	0.901	1.1571E+07	4.2220E−09	1.2519E−11
17	1	143	0.901	1.2218E+07	4.4580E−09	1.3219E−11
18	1	162	0.881	3.6772E+06	1.2845E−09	3.7265E−12
19	1	172	0.874	1.1952E+08	4.1091E−08	1.1827E−10
20	1	176	0.872	4.2104E+06	1.4402E−09	4.1348E−12
21	1	178	0.869	7.5240E+14	2.5552E−01	7.3098E−04

$$\text{for } M1 \text{ transitions : } A_{ji} = \frac{1.4910 \times 10^{13}}{\omega_j \lambda_{ji}^5} S_{ij} \text{ and } f_{ij} = \frac{2.236 \times 10^{-3}}{\lambda_{ji}^3 \omega_i} S_{ij}. \quad (9)$$

In equations from (6) to (9), λ_{ji} is the transition wavelength, w_j and w_i are upper and lower-level statistical weights. In Tables 2, 3, 4, 5, we have found 11 E1, 11 E2, 11 M1, and 11 M2 SXR transitions and 10 E1, 13 E2, 14 M1, and 19 M2 HXR transitions from the higher excited states to the ground state. Our presented radiative data for W LXIX are reliable and can be used further to identify spectral lines observed experimentally. In Fig. 1, we plotted multipole transition intensities decaying to ground state relative to the intensity of strong E1 transition 1–28 for W LXIX. From the intensity spectra of W LXIX, we found that all transitions have negligible intensity w.r.t to the intensity 1–28 transition except two E1 transitions, 1–178 and 1–36. The intensity of 1–36 E1 SXR transition is near 1–28, while the intensity of 1–178 E1 HXR transition is approximately double that of 1–28.

Table 3 Radiative data for E2 transitions in W LXIX

S. no	Transition		λ_{ji} (in Å)	A_{ji} (in s^{-1})	f_{ij}	S_{ij} (in a.u.)
	Lower level (<i>i</i>)	Upper level (<i>j</i>)				
1	1	3	8.676	9.0584E+07	5.1110E−06	1.9880E−05
2	1	6	4.329	4.8014E+02	6.7444E−12	3.2586E−12
3	1	14	3.477	1.5565E+07	1.4104E−07	3.5309E−08
4	1	19	2.474	3.1626E+03	1.4509E−11	1.3085E−12
5	1	30	1.134	1.4419E+12	1.3896E−03	1.2067E−05
6	1	38	1.098	5.9544E+12	5.3838E−03	4.2481E−05
7	1	40	1.086	1.3181E+13	1.1644E−02	8.8716E−05
8	1	44	1.036	8.4462E+07	6.7891E−08	4.4902E−10
9	1	45	1.028	2.5440E+07	2.0149E−08	1.3033E−10
10	1	48	1.022	3.0530E+08	2.3914E−07	1.5215E−09
11	1	54	1.017	1.0709E+09	8.2967E−07	5.1927E−09
12	1	63	0.999	2.6674E+08	1.9963E−07	1.1861E−09
13	1	86	0.979	2.9477E+04	2.1186E−11	1.1848E−13
14	1	97	0.975	1.0644E+09	7.5776E−07	4.1772E−09
15	1	100	0.971	1.1910E+10	8.4148E−06	4.5865E−08
16	1	103	0.969	6.9707E+09	4.9091E−06	2.6627E−08
17	1	106	0.968	8.1675E+09	5.7397E−06	3.1032E−08
18	1	112	0.966	1.3508E+09	9.4390E−07	5.0600E−09
19	1	117	0.960	2.7568E+10	1.9062E−05	1.0059E−07
20	1	120	0.960	6.7771E+09	4.6826E−06	2.4682E−08
21	1	165	0.876	1.6077E+05	9.2494E−11	3.7043E−13
22	1	184	0.869	1.9507E+07	1.1050E−08	4.3237E−11
23	1	187	0.869	4.1261E+07	2.3348E−08	9.1209E−11
24	1	198	0.867	1.6551E+07	9.3320E−09	3.6261E−11

Table 4 Radiative data for M1 transitions in W LXIX

S. no	Transitions		λ_{ji} (in Å)	A_{ji} (in s^{-1})	f_{ij}	S_{ij} (in a.u.)
	Lower level (<i>i</i>)	Upper level (<i>j</i>)				
1	1	2	8.789	1.7134E+10	5.9529E−04	1.2937E+00
2	1	18	2.483	3.4166E+04	9.4751E−11	5.8179E−08
3	1	23	1.182	1.4928E+09	9.3721E−07	2.7380E−04
4	1	25	1.160	4.8103E+09	2.9132E−06	8.3588E−04
5	1	29	1.134	2.9054E+10	1.6797E−05	4.7091E−03
6	1	37	1.099	7.4861E+08	4.0656E−07	1.1047E−04
7	1	43	1.036	1.2476E+07	6.0189E−09	1.5414E−06
8	1	46	1.025	4.0817E+06	1.9303E−09	4.8943E−07
9	1	52	1.018	2.3281E+07	1.0839E−08	2.7271E−06
10	1	53	1.017	5.3152E+07	2.4722E−08	6.2166E−06
11	1	61	1.002	3.5186E+06	1.5879E−09	3.9332E−07
12	1	87	0.979	1.3489E+06	5.8145E−10	1.4075E−07
13	1	98	0.974	4.2293E+06	1.8038E−09	4.3434E−07
14	1	101	0.970	1.6625E+06	7.0383E−10	1.6885E−07
15	1	105	0.969	8.2739E+04	3.4916E−11	8.3629E−09
16	1	109	0.967	9.7185E+04	4.0889E−11	9.7791E−09
17	1	113	0.965	6.8788E+05	2.8784E−10	6.8653E−08
18	1	118	0.960	7.7561E+05	3.2171E−10	7.6394E−08
19	1	135	0.908	2.3479E+03	8.7091E−13	1.9557E−10
20	1	137	0.908	1.3042E+02	4.8319E−14	1.0844E−11
21	1	166	0.876	1.4297E+02	4.9324E−14	1.0682E−11
22	1	180	0.870	4.1393E+03	1.4089E−12	3.0306E−10
23	1	188	0.869	2.0767E+03	7.0458E−13	1.5132E−10
24	1	191	0.868	3.9625E+04	1.3430E−11	2.8828E−09
25	1	205	0.862	1.3071E+04	4.3697E−12	9.3155E−10

Table 5 Radiative data for M2 transitions in W LXIX

S. no	Transition		λ_{ji} (in Å)	A_{ji} (in s^{-1})	f_{ij}	S_{ij} (in a.u.)
	Lower level (<i>i</i>)	Upper level (<i>j</i>)				
1	1	4	7.216	1.4866E+07	5.8026E−07	9.7537E−02
2	1	8	4.000	4.1941E+05	5.0294E−09	1.4396E−04
3	1	13	3.826	3.4074E+05	3.7388E−09	9.3671E−05
4	1	16	2.687	1.6275E+03	8.8054E−12	7.6385E−08
5	1	31	1.127	3.6011E+09	3.4295E−06	2.1971E−03
6	1	33	1.115	5.0921E+10	4.7423E−05	2.9378E−02
7	1	35	1.105	2.5055E+10	2.2940E−05	1.3852E−02
8	1	41	1.045	1.4425E+04	1.1814E−11	6.0350E−09
9	1	50	1.019	1.2719E+06	9.9000E−10	4.6861E−07
10	1	56	1.013	1.1477E+07	8.8288E−09	4.1059E−06
11	1	59	1.010	3.3542E+06	2.5651E−09	1.1825E−06
12	1	65	0.994	2.0481E+05	1.5182E−10	6.6785E−08
13	1	66	0.993	4.1171E+06	3.0455E−09	1.3355E−06
14	1	75	0.986	4.2403E+07	3.0886E−08	1.3234E−05
15	1	78	0.984	6.3950E+04	4.6368E−11	1.9732E−08
16	1	82	0.981	1.4512E+06	1.0474E−09	4.4272E−07
17	1	89	0.976	3.7450E+07	2.6748E−08	1.1128E−05
18	1	94	0.975	2.1231E+07	1.5117E−08	6.2599E−06
19	1	125	0.949	3.3600E+06	2.2665E−09	8.6549E−07
20	1	130	0.940	1.7160E+08	1.1360E−07	4.2178E−05
21	1	136	0.908	4.6777E+02	2.8913E−13	9.6847E−11
22	1	144	0.901	6.6448E+03	4.0397E−12	1.3200E−09
23	1	145	0.892	7.0367E+02	4.2010E−13	1.3358E−10
24	1	148	0.890	1.7217E+04	1.0229E−11	3.2285E−09
25	1	164	0.879	2.9454E+02	1.7067E−13	5.1892E−11
26	1	169	0.875	1.8511E+04	1.0621E−11	3.1821E−09
27	1	173	0.874	1.5186E+01	8.6975E−15	2.5986E−12
29	1	177	0.869	2.1425E+09	1.2142E−06	3.5705E−04
30	1	189	0.866	2.6775E+10	1.5063E−05	4.3814E−03

In Fig. 2, we have demonstrated the discrepancy between length and velocity oscillator strengths for C-like W. Length gauge as well as velocity gauge discrepancies is analyzed for the result of C-like W. Line strengths can be divided into three parts for E1 transitions (a) $S < 0.001$ a.u., (b) $0.001 < S < 0.002$ a.u., and (c) $S > 0.005$ a.u. In these regions, as can be seen, our logarithmic ratio of oscillator strengths has a maximum value of around 1.07. In the majority of transitions, this ratio is quite close to zero; 19 transitions have oscillator strengths ratios that are not equal to zero, as can also be seen. 0.001 a.u. of line strengths lies below, whereas 2 transitions are between 0.001 and 0.002 a.u. and 1 transition lie in the region 0.004–0.005 a.u. line strengths which have zero ratio of oscillator strength. For C-like W, this clearly represents that the terms of length form along with velocity form, or in both gauges, oscillator strengths are nearly equivalent. Again, for E2 transitions in Fig. 3, line strengths are categories into three zones. (a) $S < 0.0002$ a.u., (b) $0.0004 < S < 0.0006$ a.u., and (c) $S > 0.0010$ a.u.. As can be seen, our maximum logarithmic oscillator strength ratio is 0.58, and for the majority of transitions, this ratio is quite close to zero. Additionally, we can observe that for 10 transitions, the ratio of oscillator strengths is not the same as zero and line strengths of 0.0002 a.u. lie below, whereas 1 transitions lie between 0.0004 and 0.0006 a.u. and 1 transition is located in the range of 0.0008 to 0.0010 a.u. line strength resulting in a zero oscillator strength ratio.

We have shown $\log_{10}(S_n/S_{n+1})$ against line strength (S_n) for $n = 5$ for the E1, E2 transitions and M1, M2 transitions for C-like W in Figs. 4, 5, 6, and 7. The maximum value of the logarithmic ratio $\log_{10}(S_5/S_6)$ of line strengths for C-like W is 3.88×10^{-2} for E1 and 1.83×10^{-1} for E2, as shown in Figs. 4 and 5 (Tables 2 and 3). Moreover, this ratio is close to zero for C-like W. From Figs. 6 and 7 for M1 and M2 transitions, as can be observed, the maximum values of the logarithmic ratio $\log_{10}(S_5/S_6)$ for M1 and M2 are 1.54×10^{-1} and 2.10×10^{-1} , respectively (Table 4 and 5).

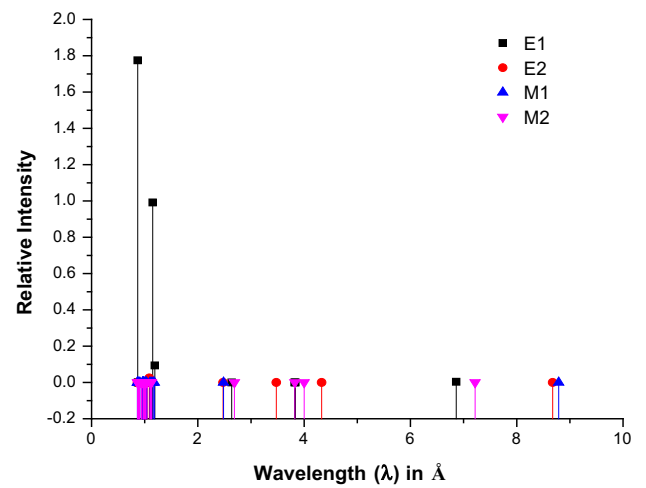
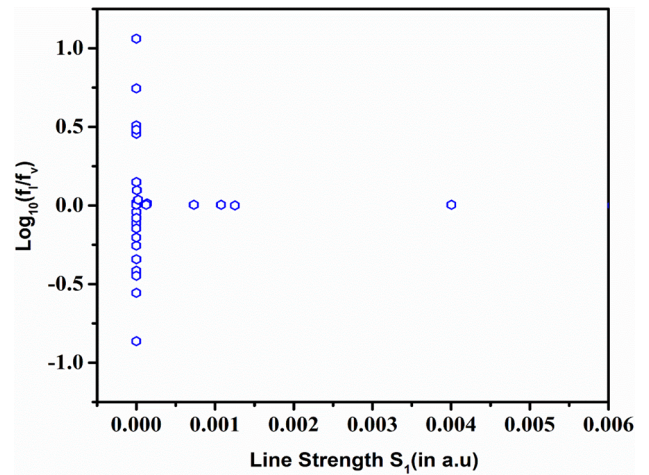
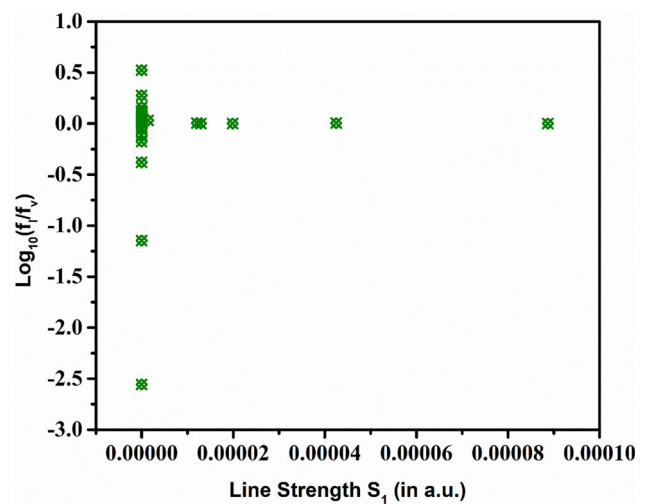
Fig. 1 Relative intensity for W LXIX**Fig. 2** Comparisons between the velocity form (f_v) and the length form (f_l) of oscillator strengths for $E1$ transition of C-like W**Fig. 3** Comparisons between the velocity form (f_v) and the length form (f_l) of oscillator strengths for $E2$ transition of C-like W

Fig. 4 Line strength (S_n) against $\log_{10}(S_n/S_{n+1})$ for $n = 5$ for $E1$ transitions of C-like W

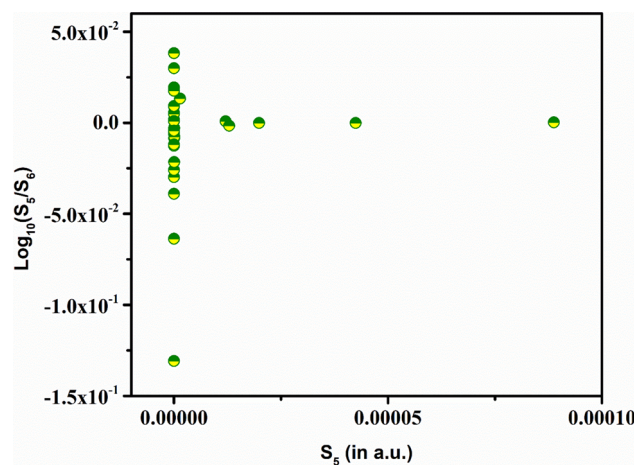


Fig. 5 Line strength (S_n) against $\log_{10}(S_n/S_{n+1})$ for $n = 5$ for $E2$ transitions of C-like W

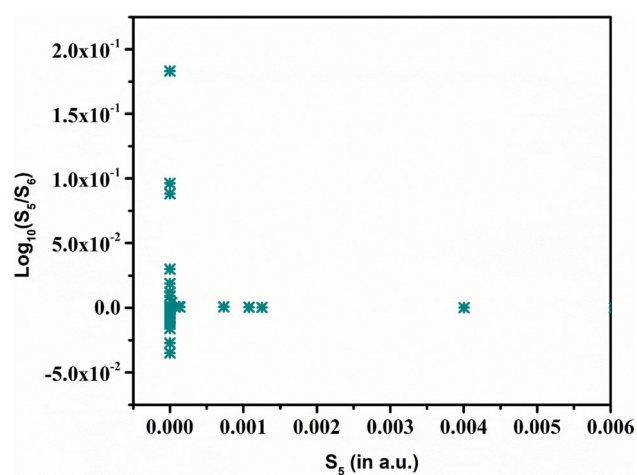
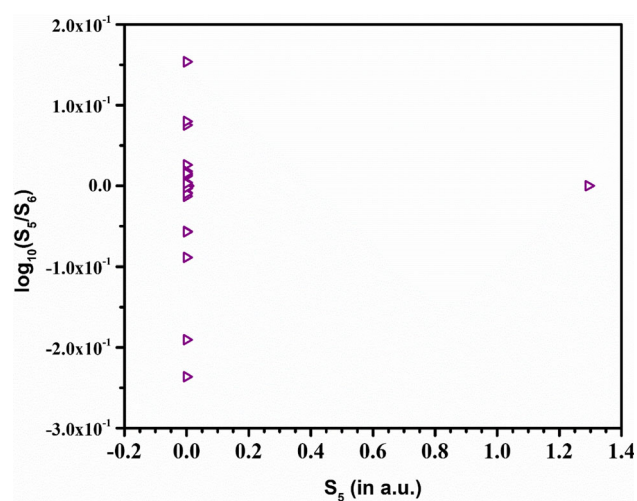


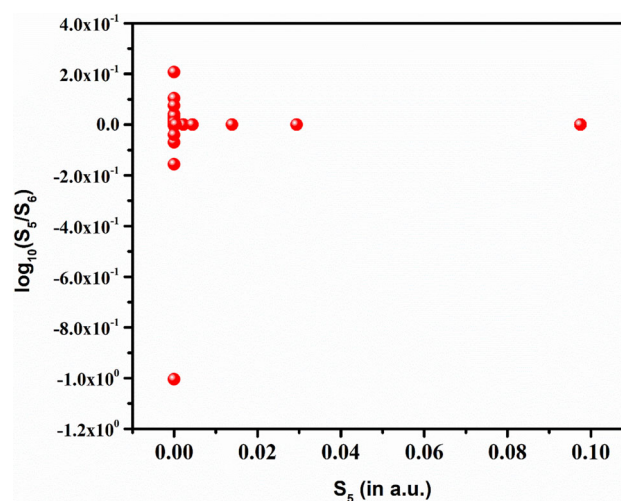
Fig. 6 Line strength (S_n) against $\log_{10}(S_n/S_{n+1})$ for $n = 5$ for $M1$ transitions of C-like W



4 Conclusion

The energy levels as well as radiative data for the transitions of E1, E2, M1, and M2 among the lowest level 205 fine structure levels for C-like W are reported in this work. In the calculations, two separate codes, GRASP and FAC, are used and the outcomes of both

Fig. 7 Line strength (S_n) against $\log_{10}(S_n/S_{n+1})$ for $n = 5$ for $M2$ transitions of C-like W



codes are compared. The discrepancy between our GRASP energies and current theoretical and experimental data in the literature is explained thoroughly. We believe our findings are extensive and new and will be beneficial in identifying and studying fusion plasmas, astrophysical and diagnosis of solar and fusion plasmas that require appropriate atomic data for the analysis.

Acknowledgements We appreciate the support and better facilities provided by Delhi Technological University.

Data Availability Statement This manuscript has associated data in a data repository. [Authors' comment: The data used to support the findings of this study are included within the article and are cited at relevant places within the text as references.]

References

1. G. Tachiev, C.F. Fischer, Breit-Pauli energy levels and transition rates for the carbonlike sequence. *Can. J. Phys.* **79**, 955–976 (2001). <https://doi.org/10.1139/cjp-79-7-955>
2. A. Al-Modlej, R.A.B. Alraddadi, N.B. Nessib, Energy levels and oscillator strengths for carbon isoelectronic sequence from C I to Ne V. *Eur. Phys. J. Plus.* (2018). <https://doi.org/10.1140/epjp/i2018-12192-9>
3. P.R. Young, U. Feldman, A. Lobel, Forbidden and intercombination lines of RR Telescopii: wavelength measurements and energy levels. *Astrophys. J. Suppl. Ser.* (2011). <https://doi.org/10.1088/0067-0049/196/2/23>
4. J.P. Mosnier, E.T. Kennedy, J.M. Bizau, D. Cubaynes, S. Guilhaud, C. Blancard, B.M. McLaughlin, Photoionization cross-sections of carbon-like n near the k-edge (390–440 eV). *Atoms* **9**, 1–18 (2021). <https://doi.org/10.3390/atoms9020027>
5. W.D. Chen, J. Xiao, Y. Shen, Y.Q. Fu, F.C. Meng, C.Y. Chen, B.H. Zhang, Y.J. Tang, R. Hutton, Y. Zou, Precise studies on resonant energies of the first intershell (KLL) dielectronic recombination processes for He- up to O-like xenon. *Phys. Plasmas*. (2008). <https://doi.org/10.1063/1.2967486>
6. U. Feldman, W. Curdt, E. Landi, K. Wilhelm, Identification of spectral lines in the 500–1600 Å wavelength range of highly ionized Ne, Na, Mg, Ar, K, Ca, Ti, Cr, Mn, Fe Co, and Ni emitted by flares ($T_e \geq 3 \times 10^6$ K) and their potential use in plasma diagnostics. *Astrophys. J.* **544**, 508–521 (2000). <https://doi.org/10.1086/317203>
7. J.M. Bizau, D. Cubaynes, S. Guilhaud, M.M. Alshorman, M.F. Gharaibeh, I.Q. Ababneh, C. Blancard, B.M. McLaughlin, K-shell photoionization of O^+ and O^{2+} ions: experiment and theory. *Phys. Rev. A At. Mol. Opt. Phys.* **92**, 1–14 (2015). <https://doi.org/10.1103/PhysRevA.92.023401>
8. K.P. Dere, G. Del Zanna, P.R. Young, E. Landi, R.S. Sutherland, CHIANTI—an atomic database for emission lines. XV. version 9, improvements for the X-ray satellite lines. *Astrophys. J. Suppl. Ser.* **241**, 22 (2019). <https://doi.org/10.3847/1538-4365/ab05cf>
9. J.K. Rudolph, S. Bernitt, S.W. Epp, R. Steinbrügge, C. Beilmann, G.V. Brown, S. Eberle, A. Graf, Z. Harman, N. Hell, M. Leutenegger, A. Müller, K. Schlage, H.C. Wille, H. Yavaş, J. Ullrich, J.R.C. López-Urrutia, X-ray resonant photoexcitation: linewidths and energies of $K\alpha$ transitions in highly charged Fe ions. *Phys. Rev. Lett.* **111**, 1–6 (2013). <https://doi.org/10.1103/PhysRevLett.111.103002>
10. B. Edl , Comparison of theoretical and experimental level values of the $n = 2$ configurations in the nitrogen isoelectronic sequence. *Phys. Scr.* **30**, 125–145 (1984). <https://doi.org/10.1088/0031-8949/30/2/007>
11. J.Y. Liao, S.N. Zhang, Y. Yao, Wavelength measurements of k transitions of oxygen, neon, and magnesium with X-ray absorption lines. *Astrophys. J.* (2013). <https://doi.org/10.1088/0004-637X/774/2/116>
12. K.J. McCarthy, N. Tamura, S.K. Combs, R. Garcia, J.H. Sánchez, M. Navarro, N. Panadero, I. Pastor, A. Soletto, Identification of S VIII through S XIV emission lines between 17.5 and 50 nm in a magnetically confined plasma. *Phys. Scr.* (2018). <https://doi.org/10.1088/1402-4896/aaa22c>
13. M. Lestinsky, N.R. Badnell, D. Bernhardt, D. Bing, M. Grieser, M. Hahn, J. Hoffmann, B. Jordon-Thaden, C. Krantz, O. Novotný, D.A. Orlov, R. Repnow, A. Shornikov, A. Müller, S. Schippers, A. Wolf, D.W. Savin, Electron-ion recombination of Mg^{6+} forming Mg^{5+} and of Mg^{7+} forming Mg^{6+} : laboratory measurements and theoretical calculations. *Astrophys. J.* (2012). <https://doi.org/10.1088/0004-637X/758/1/40>
14. Y.A. Podpaly, J.D. Gillaspay, J. Reader, Y. Ralchenko, EUV measurements of Kr XXI–Kr XXXIV and the effect of a magnetic-dipole line on allowed transitions. *J. Phys. B At. Mol. Opt. Phys.* (2014). <https://doi.org/10.1088/0953-4075/47/9/095702>
15. E. Tr bert, M. Grieser, R. Hahn, C. Krantz, R. Repnow, A. Wolf, M1 and E2 decay-dependent lifetime of the lowest $1S\ 0$ level in C-like ions up to Ne^{4+} measured at a heavy-ion storage ring. *New J. Phys.* (2012). <https://doi.org/10.1088/1367-2630/14/2/023061>
16. K. Wang, D.F. Li, H.T. Liu, X.Y. Han, B. Duan, C.Y. Li, J.G. Li, X.L. Guo, C.Y. Chen, J. Yan, Systematic calculations of energy levels and transition rates of C-like Ions with $Z = 13$ –36. *Astrophys. J. Suppl. Ser.* **215**, 1–14 (2015). <https://doi.org/10.1088/0067-0049/215/2/26>

17. N.W. Zheng, T. Wang, Systematical study on the ionization potential of excited states in carbon-like sequence. *Chem. Phys. Lett.* **376**, 557–565 (2003). [https://doi.org/10.1016/S0009-2614\(03\)01021-2](https://doi.org/10.1016/S0009-2614(03)01021-2)
18. K.M. Aggarwal, F.P. Keenan, A.Z. Msezane, Oscillator strengths for transitions in C-like ions between K XIV and MN XX. *Astron. Astrophys.* **401**, 377–383 (2003). <https://doi.org/10.1051/0004-6361:20030117>
19. J.E. Sansonetti, W.C. Martin, Handbook of basic atomic spectroscopic data. *J. Phys. Chem. Ref. Data.* **34**, 1559–2259 (2005). <https://doi.org/10.1063/1.1800011>
20. G.C. Rodrigues, P. Indelicato, J.P. Santos, P. Páté, F. Parente, Systematic calculation of total atomic energies of ground state configurations. *At. Data Nucl. Data Tables.* **86**, 117–233 (2004). <https://doi.org/10.1016/j.adt.2003.11.005>
21. B.C. Fawcett, Wavelengths and classifications of emission energy levels for the above isoelectronic. *Science* **164**, 135–164 (1975). <https://doi.org/10.1103/PhysRevA.88.042504>
22. C. Chen, Energies, radial expectation values, hyperfine structures of the ground state and highly excited states for C and O²⁺. *Int. J. Mod. Phys. B.* (2020). <https://doi.org/10.1142/S0217979220501970>
23. C. Nazé, S. Verdebout, P. Rynkun, G. Gaigalas, M. Godefroid, P. Jönsson, Isotope shifts in beryllium-, boron-, carbon-, and nitrogen-like ions from relativistic configuration interaction calculations. *At. Data Nucl. Data Tables.* **100**, 1197–1249 (2014). <https://doi.org/10.1016/j.adt.2014.02.004>
24. H.L. Zhang, C.J. Fontes, Relativistic distorted-wave collision strengths and oscillator strengths for the 185 $\Delta n = 0$ transitions with $n = 2$ in C-like ions with $9 \leq Z \leq 54$. *At. Data Nucl. Data Tables.* **63**, 275–314 (1996). <https://doi.org/10.1006/adnd.1996.0014>
25. H.L. Zhang, C.J. Fontes, Relativistic distorted-wave collision strengths and oscillator strengths for the 185 $\Delta n = 0$ transitions with $n = 2$ in the 67 C-like ions with $26 \leq Z \leq 92$. *At. Data Nucl. Data Tables.* **101**, 41–142 (2015). <https://doi.org/10.1016/j.adt.2014.08.001>
26. M.F. Gu, Energies of 1s22lq ($1 \leq q \leq 8$) states for $Z \leq 60$ with a combined configuration interaction and many-body perturbation theory approach. *At. Data Nucl. Data Tables.* **89**, 267–293 (2005). <https://doi.org/10.1016/j.adt.2005.02.004>
27. D. Ray, P.K. Mukherjee, Radiative transitions in highly-stripped carbon-like ions. *Phys. Scr.* **51**, 81 (1995). <https://doi.org/10.1088/0031-8949/51/1/013>
28. C.C. Sang, Z.B. Chen, Y. Sun, X.Z. Shen, F. Hu, J. Ma, X.L. Wang, Hyperfine structure and 2s–2p transition in C-like Fe, Co and Ni. *J. Electron. Spectros. Relat. Phenom.* **230**, 26–32 (2019). <https://doi.org/10.1016/j.elspec.2018.11.001>
29. G.V. Shpatakovskaya, Patterns of the ionization potentials of multicharged ions of heavy elements. *JETP Lett.* **114**, 737–741 (2021). <https://doi.org/10.1134/S0021364021240073>
30. C.F. Fischer, H.P. Saha, Multiconfiguration hartree-fock results with breit-pauli corrections for transitions in the carbon sequence. *Phys. Scr.* **32**, 181–194 (1985). <https://doi.org/10.1088/0031-8949/32/3/004>
31. C.F. Fischer, G. Tachiev, Breit-Pauli energy levels, lifetimes, and transition probabilities for the beryllium-like to neon-like sequences. *At. Data Nucl. Data Tables.* **87**, 1–184 (2004). <https://doi.org/10.1016/j.adt.2004.02.001>
32. P. Palmeri, P. Quinet, C. Mendoza, M.A. Bautista, J. García, M.C. Witthoef, T.R. Kallman, Atomic decay data for modeling K lines of iron peak and light odd-Z elements. *Astron. Astrophys.* **543**, 1–9 (2012). <https://doi.org/10.1051/0004-6361/201219438>
33. P. Jönsson, G. Gaigalas, P. Rynkun, L. Radziute, J. Ekman, S. Gustafsson, H. Hartman, K. Wang, M. Godefroid, C.F. Fischer, I. Grant, T. Brage, G. Del Zanna, Multiconfiguration dirac-hartree-fock calculations with spectroscopic accuracy: applications to astrophysics. *Atoms* **5**, 1–24 (2017). <https://doi.org/10.3390/atoms5020016>
34. F. Li, G.Y. Liang, G. Zhao, Soft X-ray emission lines of S VII–S XIV in procyon. *Astrophys. J.* (2013). <https://doi.org/10.1088/0004-637X/762/1/53>
35. B. Tu, J. Xiao, K. Yao, X. Wang, Y. Shen, Y. Yang, D. Lu, L. Huang, C. Zhen, Y. Fu, B. Wei, R. Hutton, Y. Zou, Photorecombination studies of highly charged tungsten ions at Shanghai EBIT. *J. Phys. Conf. Ser.* (2017). <https://doi.org/10.1088/1742-6596/875/2/012003>
36. B. Tu, J. Xiao, Y. Shen, Y. Yang, D. Lu, T.H. Xu, W.X. Li, C.Y. Chen, Y. Fu, B. Wei, C. Zheng, L.Y. Huang, R. Hutton, X. Wang, K. Yao, Y. Zou, B.H. Zhang, Y.J. Tang, KLL dielectronic recombination resonant strengths of He-like up to O-like tungsten ions. *Phys. Plasmas.* (2016). <https://doi.org/10.1063/1.4948420>
37. M.B. Trzhaskovskaya, V.K. Nikulin, Radiative recombination and photoionization data for tungsten ions. *Electron structure of ions in plasmas. Atoms* **3**, 86–119 (2015). <https://doi.org/10.3390/atoms3020086>
38. H. Liu, G. Jiang, F. Hu, C.K. Wang, Z.B. Wang, J.M. Yang, Intercombination transitions of the carbon-like isoelectronic sequence. *Chin. Phys. B.* (2013). <https://doi.org/10.1088/1674-1056/22/7/073202>
39. P. Beiersdorfer, M.J. May, J.H. Scofield, S.B. Hansen, Atomic physics and ionization balance of high-Z Ions: critical ingredients for characterizing and understanding high-temperature plasmas. *High Energy Density Phys.* **8**, 271–283 (2012). <https://doi.org/10.1016/j.hedp.2012.03.003>
40. U. Feldman, J.F. Seely, E. Landi, Y. Ralchenko, Bright EUV lines emitted by highly ionized tungsten ions as diagnostic indicators of the tungsten transport in ITER core plasmas (Te > 7 keV). *Nucl. Fusion.* (2008). <https://doi.org/10.1088/0029-5515/48/4/045004>
41. A.E. Kramida, J. Reader, Ionization energies of tungsten ions: W2⁺ through W71⁺. *At. Data Nucl. Data Tables.* **92**, 457–479 (2006). <https://doi.org/10.1016/j.adt.2006.03.002>
42. J. Huang, G. Jiang, Q. Zhao, Ground-state ionization potentials for lithium through neon isoelectronic sequences with $Z = 37$ –82. *Chin. Phys. Lett.* **23**, 69–72 (2006). <https://doi.org/10.1088/0256-307X/23/1/021>
43. U.I. Safronova, Z.B. Rudzikas, Perturbation theory for the relativistic energy of atomic systems. *J. Phys. B At. Mol. Phys.* **9**, 1989–2001 (1976). <https://doi.org/10.1088/0022-3700/9/12/011>
44. T.A. Carlson, C.W. Nestor, N. Wasserman, J.D. McDowell, Calculated ionization potentials for multiply charged ions. *At. Data Nucl. Data Tables.* **2**, 63–99 (1970). [https://doi.org/10.1016/S0092-640X\(70\)80005-5](https://doi.org/10.1016/S0092-640X(70)80005-5)
45. I.P. Grant, B.J. McKenzie, P.H. Norrington, D.F. Mayers, N.C. Pyper, An atomic multiconfigurational Dirac-Fock package. *Comput. Phys. Commun.* **21**, 207–231 (1980). [https://doi.org/10.1016/0010-4655\(80\)90041-7](https://doi.org/10.1016/0010-4655(80)90041-7)
46. R. Sharma, R. Pajjwar, Spectroscopic study of EUV and SXR spectral lines with partition function and level population of W LVI. *Can. J. Phys.* **99**, 657–669 (2021). <https://doi.org/10.1139/cjp-2020-0497>
47. M.F. Gu, The flexible atomic code. *Can. J. Phys.* **86**, 675–689 (2008). <https://doi.org/10.1139/p07-197>
48. A. Kramida, Yu. Ralchenko, J. Reader, and NIST ASD Team, <https://physics.nist.gov/asd> for NIST Atomic Spectra Database (ver. 5.6.1) (2019).

Springer Nature or its licensor (e.g. a society or other partner) holds exclusive rights to this article under a publishing agreement with the author(s) or other rightsholder(s); author self-archiving of the accepted manuscript version of this article is solely governed by the terms of such publishing agreement and applicable law.

Spectroscopic study of EUV and SXR spectral lines with partition function and level population of W LVI

Rinku Sharma and Paijwar Richa

Abstract: We present a comprehensive and elaborate study of W LVI (K-like W^{55+}) by using multi-configuration Dirac-Fock method (MCDF). We have included relativistic corrections, QED (quantum electrodynamics) and Breit corrections in our computation. We have reported energy levels and radiative data for multipole transitions (i.e., electric dipole (E1), electric quadrupole (E2), magnetic dipole (M1), and magnetic quadrupole (M2)) within the lowest 142 fine-structure levels and predicted soft X-ray transition (SXR) and extreme ultraviolet transitions (EUV) from higher excited states to the ground state. We have compared our calculated data with energy levels compiled by NIST and other available results in the literature and the small discrepancies found with them are discussed. Because only a few of the lowest levels are available in the literature, for checking excitation energies of higher excited states we have performed the same calculations with the distorted wave method. Furthermore, we have also provided relative population for the first five excited states, with both the partition function and thermodynamic quantities for W LVI and studied their variations with temperature. We believe that our reported new atomic data of W LVI may be useful in identification and analysis of spectral lines from various astrophysical and fusion plasma sources and may also be beneficial in plasma modeling.

Key words: EUV, SXR, partition function, atomic data, level population.

Résumé : Nous présentons une étude élaborée et exhaustive du W LVI (W^{55+} de type K) en utilisant une méthode de Dirac-Fock multi-configurations (DFMC/MCDF). Ces calculs incluent les corrections relativistes de EDQ/QED (électrodynamique quantique) et de Breit. Nous présentons ici les niveaux d'énergie et les données radiatives pour plusieurs transitions multipolaires (i.e., dipolaires électriques (E1), quadripolaires électriques (E2), dipolaires magnétiques (M1) et quadripolaires magnétiques (M2)) dans les 146 niveaux les plus bas de structure fine, avec les transitions à rayons X mous et UV extrêmes entre les états excités et le fondamental. Nous comparons nos résultats de calcul avec les données sur les niveaux d'énergie compilées par NIST et d'autres résultats trouvés dans la littérature et nous discutons les petites divergences. Parce que peu de niveaux sont disponibles dans la littérature et afin de vérifier les énergies des niveaux de plus haute excitation, nous avons refait le calcul à l'aide de la méthode des ondes distordues. De plus, nous donnons les populations relatives pour les cinq plus bas niveaux excités, avec la fonction de partition et les quantités thermodynamiques pour les deux modèles de W LVI et étudions leurs variations avec la température. Nous estimons que ces nouveaux résultats pour W LVI peuvent être utiles dans l'identification de lignes spectrales en astrophysique et dans des sources de plasma de fusion et être bénéfiques en modélisation de plasma. [Traduit par la Rédaction]

Mots-clés : UV extrêmes, rayons X mous, données atomiques, population des niveaux.

1. Introduction

Specific physical properties of tungsten (W), such as its highest melting point and lower vapor pressure of all metals, position it as a potential candidate in fusion agency. Tungsten as a favorable material for plasma-covering components in development of a magnetic confinement fusion reactor is gaining interest due to its maximum tensile strength at temperatures over 1650 °C [1, 2]. Tungsten has been desirable as a plasma-covering material for the ITER (International Thermonuclear Experiment Reactor) tokamak [3]. Consequently, the atomic properties of tungsten and plasma kinetics are critical to understand generation of radiative losses over wide temperature ranges will take place in ITER [1–3].

In the past few decades, forbidden transitions have been used to collect information about plasma parameters, accurate determination of electron density, and temperature diagnostics in

several astronomical objects as well as laboratory tokamak plasmas [4–12]. Experimentally, some spectra of K-like ions have been studied and forbidden transitions in these spectra have also been analyzed [13–15]. Furthermore, accurate and sufficient atomic data including energy levels, transition wavelengths, collision strengths, and radiative data, for tungsten ions are also needed to establish plasma parameters for plasma diagnosis. Therefore, there have been several estimations and theoretical studies on frequent charge states of tungsten in the literature, but still fewer data are available on forbidden transitions of K-like W. Therefore, in the present work, we have provided radiative data of forbidden transitions of K-like W.

In recent years, much improvement in the experimental observations of atomic data of tungsten ions has been made [16]. The thorough study of extreme ultraviolet (EUV) and soft X-ray (SXR) ionized high-Z ions has become a matter of significant research due to their applications in laser physics, plasma physics, and

Received 13 September 2020. Accepted 29 December 2020.

R. Sharma and P. Richa. Department of Applied Physics, Delhi Technological University, Delhi 110042, India.

Corresponding author: Rinku Sharma (email: rinkusharma@dtu.ac.in).

Copyright remains with the author(s) or their institution(s). Permission for reuse (free in most cases) can be obtained from copyright.com.

astrophysics. The wavelengths of spectral lines radiated by the sun within EUV and SXR are compelling and vital keys to understanding the physical processes in Earth's upper atmosphere and ionosphere [17].

In the past few decades, numerous studies of W LVI have become available in the literature using different theoretical methods as well as experimental techniques, but are limited to only a few energy levels [18–26]. Beiersdorfer et al. [27] have presented detailed description of tungsten and gold ions including W LVI. Trzhaskovskaya et al. [28] have calculated radiative recombination and photoionization cross sections as well as radiated power loss coefficients for 54 tungsten ions W^{6+} – W^{71+} including W LVI by using Dirac–Fock electron wavefunctions. Priti et al. [29] have reported electron impact excitation for M- and L-shell transitions for tungsten ions W^{44+} – W^{66+} including W LVI with the help of the fully relativistic distorted wave (DW) method. Guo et al. [30] have presented wavelengths and transition probabilities for transitions in the ground state configuration of tungsten and other ions including W LVI by using second-order relativistic many-body perturbation theory (RMBPT) and relativistic configuration interaction (RCI). Dipti et al. [31] have studied electron impact excitation and polarization for Fe-like W to Al-like W ions using the fully relativistic DW method. Xu et al. [32] have listed excitation energies and wavelengths for nine isoelectronic sequences of tungsten ions for the lowest few levels by utilizing the multi-configuration Dirac–Fock (MCDf) method. Fischer et al. [33] have reported excitation energies of tungsten ions for ground configurations by using GRASP2K code. Zhao et al. [34] have reported atomic data of ground configurations $3d^k$ ($k = 1$ – 9) for highly charged ions with nuclear charge ranging from 72 to 83 by employing the multi-configuration Dirac–Hartree–Fock method. But most of the work available in the literature is only for a few levels of W LVI and there is a scarcity in complete, consistent, and precise atomic data for this ion. Therefore, in the present work, our fundamental objective is to present the energies for levels of higher excited states along with the radiative data for multipole transitions (electric dipole (E1), electric quadrupole (E2), magnetic dipole (M1), and magnetic quadrupole (M2)) for WLVI.

The partition function has several applications, such as the study of thermodynamic parameters of ions and neutral atoms, diagnosis and modeling of plasmas, and computation of levels in stellar and interstellar plasmas with the help of Saha's equation of state. Due to computational limitations, it has become very cumbersome for experimentalists to consider a large number of excited states in their calculations of the partition function, specifically at higher temperatures. Therefore, in the past few decades, several theoretical methods and techniques have been developed in the study of the partition function [35–39]. A few methods in the literature have adopted criteria of cut-off condition for simplicity and according to availability of data and computational limitations. Some tables, such as NASA, Russian, and Drawin–Felenbok, available in the literature have taken into account only a few of the lowest states in their calculations [40–43]. The Planck–Larkin partition function has also been adopted in the study of high-temperature plasmas in the past. But this gives total partition functions near to zero at high temperature and hence violates the basic condition that total partition function of the system cannot be less than unity. Another model that has gained popularity in the last few years is the three-group model, presented in the literature [44]. This method divides the chosen levels into exactly three groups, namely, ground state, middle levels, and higher excited levels. The limitation of this method is that it does not calculate the contribution of individual levels to the partition function and thus may yield inaccurate results. We have overcome these difficulties and limitations in our present fine-structure model.

2. Theoretical methods

2.1. MCDf method

For the study of highly charged potassium-like tungsten ion considered in this paper, the fully relativistic MCDf method, which was revised by Norrington and earlier developed by Grant et al. [45], is executed in our calculations. Detailed explanation of this method has been presented in the literature [45–49], therefore, we discuss it only briefly here. It includes high-order relativistic corrections arising due to Breit interactions and quantum electrodynamics (QED) effects (vacuum polarization and self-energy). To evaluate radial wavefunctions at the time of self-consistent field operation, we have opted to use the extended average level in which weighted trace of the Hamiltonian matrix is minimized.

Energy levels of an atomic ion with N electrons are obtained by diagonalizing the relativistic Hamiltonian H

$$H = \sum_{i=1}^N H_D(i) + \sum_{i<j}^N \frac{1}{r_{ij}} \quad (1)$$

where $H_D(i)$ is the single-electron Dirac Hamiltonian. For an N -electron atom or ion system, an atomic state function is an estimation of the specific wavefunction of an atomic state.

The configuration state functions are anti-symmetrized linear combinations of products of relativistic orbitals

$$\Phi(\gamma_i P J) = \frac{1}{r} \begin{bmatrix} P_{nk}(r) \chi_{km} \\ i Q_{nk}(r) \chi_{-km}(\hat{r}) \end{bmatrix} \quad (2)$$

where k is the relativistic angular quantum number, P_{nk} and $Q_{nk}(r)$ are the large and small components of the radial wavefunction, respectively, and $\chi_{-km}(\hat{r})$ is a spinor spherical harmonic.

The atomic state function is a linear combination of N electronic configuration state functions, and is expressed as

$$\Psi(\gamma P J) = \sum_{i=1}^N c_i \Phi(\gamma_i P J) \quad (3)$$

Here γ_i denotes the configuration together with the angular coupling tree; P is parity; J is the final angular quantum number; and c_i are the expansion coefficients, achieved through diagonalization of the Dirac–Coulomb–Hamiltonian.

2.2. Flexible atomic code (FAC)

To evaluate and ensure the exactness of our results, we have executed complementary calculation by using the DW method by way of FAC. FAC was developed by Gu [50] at Stanford University and can be found at <http://kipac-tree.stanford.edu/fac>. FAC is a fully relativistic code and the power of FAC is that it is extremely efficient to run and mostly yields results comparable to those collected with other methods.

A detailed explanation of the calculation approach of this method can be found in the literature [50–52]. The difference between the two fully relativistic codes is that in FAC, a local central field is adopted in calculations, while MCDf performs minimization of energy for a given set of states. The local potential used in the FAC includes the contribution from nuclear charge and electron–electron interaction. The nuclear potential is

$$V^N = \begin{cases} \frac{Z}{2} \left(\frac{r}{R_N} \right) \left[3 - \left(\frac{r}{R_N} \right)^2 \right] & r \leq R_N \\ \frac{Z}{r} & r > R_N \end{cases}$$

where R_N is the radius of the nucleus.

To obtain better results, we have included configurations in steps and optimized average energy. We have applied the same

optimization process in both methods. In step 1, we have taken only configurations obtained by single-electron excitation within Hartree–Fock orbitals, while in step 2, we have included configurations obtained by one-electron excitation to $n = 4$ orbitals, and in the final step, we have taken double and triple electron excitations from $n = 3$ orbitals to $n = 3$ and $n = 4$ orbitals and considered only those configurations whose contribution is larger and neglected other configurations to save computational time in optimization of the average energy. This helps in choosing the highest-contribution and most important configurations and also reduces the cost of personnel as well as machinery.

In the next section, we provide the final 37 configurations included in our calculations from both MCDF and FAC. We also discuss the minor discrepancy between the results from both codes.

3. Results and discussion

3.1. Energy levels

In present paper, we have listed the lowest 142 fine-structure levels belonging to the configurations $3s^2 3p^6 3d$, $3s^2 3p^5 3d^2$, and $3s^2 3p^6 3d^3$ from MCDF and DW both in Table 1. In our calculations, we included 37 configurations, namely, $3s^2 3p^6 3d$, $3s^2 3p^5 3d^2$, $3s 3p^6 3d^2$, $3s^2 3p^4 3d^3$, $3s 3p^5 3d^3$, $3p^6 3d^3$, $3s^2 3p^3 3d^4$, $3s 3p^4 3d^4$, $3p^5 3d^4$, $3s^2 3p^6 4l$ ($l = 0-3$), $3s 3p^6 3d 4l$ ($l = 0-3$), $3s^2 3p^5 3d 4l$ ($l = 0-3$), $3s^1 3p^5 3d^2 4l$ ($l = 0-3$), $3s^2 3p^4 3d^2 4l$ ($l = 0-3$), $3p^6 3d^2 4l$ ($l = 0-3$), and $3p^5 3d^3 4l$ ($l = 0-3$).

From Table 1, we observe that the contribution of QED is less than that of Breit and is very small for levels 2, 42, and 63. In the case of W LVI, QED effects are less significant for some levels. We have compared our calculated data from MCDF and DW with NIST [26] and the maximum discrepancies of MCDF and DW results with results compiled by NIST are 0.45% and 0.25%, respectively, for $3s^2 3p^5 3d^2$ (3F_2) $^2G_{7/2}$. In Table 1, we show the percentage difference of MCDF with DW under the column “ ΔE ”,

$$\Delta E = \frac{|E_{\text{FAC}} - E_{\text{GRASP}}|}{E_{\text{FAC}}} \times 100\% \quad (4)$$

The maximum value of ΔE is 0.43%. This shows that our results from the two independent calculations for most of the levels are in reasonable agreement and verifies that our results are accurate. The small differences for some levels in MCDF and DW energies mainly arise due to different ways of calculating electron wavefunctions for radial orbitals and re-coupling schemes of the angular parts.

We have also compared our results with other available results in the literature and discussed the discrepancies with them in the following sections.

3.1.1. Comparison with Quinet [25]

Quinet [25] has calculated fine-structure level energies of only the first excited state $3s^2 3p^6 3d$ $^2D_{5/2}$ by using the fully relativistic MCDF method. There is a very small discrepancy of 0.008 Ryd between our MCDF results and Quinet [25] and this shows that additional configurations in calculations from the same method have not introduced correlation effects on $3s^2 3p^6 3d$ $^2D_{5/2}$.

3.1.2. Comparison with Priti et al. [28]

Priti et al. [28] have presented excitation energies of two levels, $3s^2 3p^5 3d^2$ $^2F_{5/2}$ and $3s^2 3p^5 3d^2$ $^2D_{3/2}$, which are levels 42 and 63 in Table 1. The discrepancies between our MCDF results and those of Priti et al. [28] are 0.0977 and 0.24 Ryd for $3s^2 3p^5 3d^2$ $^2D_{3/2}$ and $3s^2 3p^5 3d^2$ $^2F_{5/2}$, respectively. The reason behind the small discrepancy may be the different configurations and techniques adopted by Priti et al. [28]. They have included six configurations $3s^2 3p^6 3d$, $3s^2 3p^5 3d^2$, $3s 3p^6 3d^2$, $3p^6 3d^3$, $3s^2 3p^5 4p 4d$, and $3s 3p^5 3d^3$ for the initial and final target state wavefunctions while in our calculations we have taken 37 configurations by considering single, double, and

triple (SDT) excitations from $3s$ and $3p$ orbitals and one-electron excitation from $3d$ to $n = 4$ orbitals. Our MCDF results are close to the results from Priti et al. [28] and ensure the reliability and authenticity of excitation energies of higher excited states.

3.1.3. Comparison with Clementson et al. [54]

Clementson et al. [54] have presented theoretically calculated and experimentally measured energies for W LVI. They have performed the experiment by employing superEBIT at Lawrence Livermore National Laboratory (LLNL). For theoretical calculations, they have adopted GRASP and FAC. The discrepancies between our MCDF results and their experimental, FAC, and GRASP results are 0.09, 0.055, and 0.139 Ryd, respectively. This difference between our MCDF results and their GRASP and FAC results is mainly due to the choice of different configuration sets. In their FAC calculations, they have opted for $2s^2 2p^6 3l^9$, $2s^2 2p^6 3l^8 4l$ ($l = 0-3$), $2s^2 2p^6 3l^8 5l$ ($l = 0-3$), $2s^2 2p^5 3s^2 3p^6 3dnl$ ($n = 3, 4, 5; l = 0$ to $n - 1$), and $2s 2p^6 3s^2 3p^6 3dnl$ ($n = 3, 4, 5; l = 0$ to $n - 1$) while in their GRASP calculations, they chose $3s^2 3p^6 3d$, $3s^2 3p^5 3d^2$, and $3s 3p^6 3d^2$. So it is clear that they have included only three configurations in GRASP and have missed some important configurations, which have significant contribution to the total atomic wavefunction of $3s^2 3p^5 3d^2$, while in FAC, they have taken a large number of configurations, which is not possible in GRASP as it will increase computational time and make calculations cumbersome with very little improvement in excitation energies of higher excited states. So, we have considered important configurations with SDT excitations in both MCDF and DW, but it will be a topic of future research to explore the contribution of configurations containing more than five electrons in the $3d$ orbital. Hence, we found that our results are in good agreement with experimental and theoretical results of Clementson et al. [55] with minimal difference.

3.1.4. Comparison with Guo et al. [30]

Guo et al. [30] have presented excitation energies only for two fine-structure levels of the $3s^2 3p^6 3d$ configuration for WLVI using second-order RMBPT and RCI. The small discrepancy of our MCDF results with the RMBPT results of Guo et al. [30] is 0.025 Ryd for level 2. This is because, in their RMBPT calculations, they have taken single excitation up to $n = 125$ and double excitations with one electron to $n = 65$ and other electrons to $n = 125$, but in MCDF, it is not possible to include so many configurations, as we have stated in the previous section.

But the discrepancy of our MCDF results with their RCI results is 0.001 for level 2. Guo et al. [30] have only included interaction within $n = 3$ orbitals but still our MCDF energy and their GRASP energy for this level is exactly same, which implies that effect of correlations from other configurations included by us is almost negligible on level 2 and a similar effect is also shown in Section 3.1.1.

3.1.5. Comparison with Fischer et al. [33]

Fischer et al. [33] have also listed excitation energy only for the first excited state of configuration $3s^2 3p^6 3d$ $^2D_{5/2}$ by using GRASP2K. They have considered core–valence and core–core correlations by taking single- and double-electron excitations from $n = 2$ orbitals but they have included orbitals up to $n = 6$, while in our calculations we have considered SDT excitations within $n = 3$ and single-electron excitation from $n = 3$ orbitals to $n = 4$. Therefore, there is a small discrepancy of 0.02 Ryd between our MCDF results and those of Fischer et al. [33] for level 2, which shows that our results match well with the results reported by Fischer et al. [33].

3.1.6 Comparison with Zhao et al. [34]

Zhao et al. [34] have also reported excitation energy for the ground state configuration $3s^2 3p^6 3d$ using second-order RMBPT

Table 1. Energies (in Ryd) of lowest 142 fine-structure levels of W LVI.

Level	Configuration	Parity	MCDF				DW	Other	ΔE
			DC	BREIT	QED	Total			
1	$3s^2 3p^6 3d^1 ({}^2D_1) {}^4D_{3/2}$	Even	0.0000	—	—	0.0000	0	0.000	0.36
2	$3s^2 3p^6 3d^1 ({}^2D_1) {}^2D_{5/2}$	Even	5.8279	−0.1440	0.00006	5.6840	5.7044	5.709 ^a 5.692 ^b 5.709 ^c 5.683 ^d 5.704 ^e 5.700 ^f 5.709 ^g 5.708 ^h	0.20
3	$3s^2 3p^5 3d^2 ({}^3F_2) {}^4F_{3/2}$	Odd	18.9125	−0.0490	−0.0362	18.8273	18.7898		0.19
4	$3s^2 3p^5 3d^2 ({}^3F_2) {}^4D_{1/2}$	Odd	19.0699	−0.0684	−0.0362	18.9653	18.9289		0.20
5	$3s^2 3p^5 3d^2 ({}^3F_2) {}^4F_{5/2}$	Odd	19.4914	−0.0969	−0.0361	19.3584	19.3198		0.20
6	$3s^2 3p^5 3d^2 ({}^3F_2) {}^2G_{7/2}$	Odd	19.7178	−0.1240	−0.0361	19.5582	19.5182	19.470	0.18
7	$3s^2 3p^5 3d^2 ({}^3P_2) {}^4P_{5/2}$	Odd	21.2442	−0.0332	−0.0362	21.1748	21.1366		0.06
8	$3s^2 3p^5 3d^2 ({}^3F_2) {}^4D_{5/2}$	Odd	24.2967	−0.1940	−0.0361	24.0667	24.0520		0.07
9	$3s^2 3p^5 3d^2 ({}^3F_2) {}^4G_{9/2}$	Odd	24.7714	−0.2800	−0.0359	24.4559	24.4392		0.06
10	$3s^2 3p^5 3d^2 ({}^3F_2) {}^4F_{7/2}$	Odd	24.9369	−0.2510	−0.0360	24.6496	24.6340		0.06
11	$3s^2 3p^5 3d^2 ({}^3F_2) {}^4D_{3/2}$	Odd	25.1631	−0.2120	−0.0361	24.9154	24.8996		0.06
12	$3s^2 3p^5 3d^2 ({}^3P_2) {}^4P_{5/2}$	Odd	25.3353	−0.2320	−0.0361	25.0675	25.0518		0.32
13	$3s^2 3p^5 3d^2 ({}^3P_2) {}^4D_{7/2}$	Odd	25.6359	−0.2710	−0.0361	25.3283	25.2468		0.19
14	$3s^2 3p^5 3d^2 ({}^1G_2) {}^2H_{11/2}$	Odd	25.6596	−0.3600	−0.0359	25.2632	25.3113		0.06
15	$3s^2 3p^5 3d^2 ({}^3P_2) {}^2S_{1/2}$	Odd	25.9931	−0.1810	−0.0362	25.7761	25.7599		0.06
16	$3s^2 3p^5 3d^2 ({}^1G_2) {}^2F_{7/2}$	Odd	26.4409	−0.2610	−0.0361	26.1436	26.1269		0.07
17	$3s^2 3p^5 3d^2 ({}^3P_2) {}^4D_{5/2}$	Odd	26.4977	−0.1930	−0.0362	26.268	26.2505		0.06
18	$3s^2 3p^5 3d^2 ({}^3P_2) {}^4S_{3/2}$	Odd	26.6911	−0.1610	−0.0362	26.4936	26.4765		0.07
19	$3s^2 3p^5 3d^2 ({}^1G_2) {}^2G_{9/2}$	Odd	26.8793	−0.2990	−0.0361	26.5439	26.5264		0.09
20	$3s^2 3p^5 3d^2 ({}^3P_2) {}^2D_{3/2}$	Odd	27.9527	−0.2210	−0.0357	27.6958	27.6707		0.09
21	$3s^2 3p^5 3d^2 ({}^1D_2) {}^2F_{5/2}$	Odd	28.5622	−0.2590	−0.0360	28.2676	28.2417		0.10
22	$3s^2 3p^5 3d^2 ({}^3P_2) {}^2P_{1/2}$	Odd	29.073	−0.1930	−0.0357	28.8441	28.8158		0.02
23	$3s^2 3p^5 3d^2 ({}^3F_2) {}^4G_{11/2}$	Odd	30.6462	−0.4470	−0.0358	30.1632	30.1690		0.02
24	$3s^2 3p^5 3d^2 ({}^1D_2) {}^2D_{5/2}$	Odd	31.0555	−0.3650	−0.0361	30.6542	30.6609		0.02
25	$3s^2 3p^5 3d^2 ({}^3F_2) {}^2G_{9/2}$	Odd	31.381	−0.4050	−0.0360	30.9400	30.9452		0.02
26	$3s^2 3p^5 3d^2 ({}^1D_2) {}^2F_{7/2}$	Odd	31.5175	−0.3790	−0.0359	31.1022	31.1072		0.02
27	$3s^2 3p^5 3d^2 ({}^1D_2) {}^2P_{1/2}$	Odd	31.9677	−0.3260	−0.0363	31.6055	31.6111		0.001
28	$3s^2 3p^5 3d^2 ({}^3F_2) {}^2F_{7/2}$	Odd	33.1857	−0.3700	−0.0360	32.7792	32.7795		0.01
29	$3s^2 3p^5 3d^2 ({}^1S_0) {}^2P_{3/2}$	Odd	33.7114	−0.2860	−0.0362	33.3887	33.3924		0.02
30	$3s^2 3p^5 3d^2 ({}^3F_2) {}^2D_{5/2}$	Odd	34.3384	−0.3750	−0.0356	33.9278	33.9223		0.01
31	$3s^2 3p^5 3d^2 ({}^1D_2) {}^2D_{3/2}$	Odd	34.63	−0.3210	−0.0355	34.2737	34.2710		0.31
32	$3s^2 3p^4 3d^3 ({}^4F_3) {}^6D_{3/2}$	Even	39.0056	−0.0731	−0.0723	38.8603	38.7412		0.30
33	$3s^2 3p^4 3d^3 ({}^4F_3) {}^6D_{1/2}$	Even	39.0677	−0.0946	−0.0724	38.9007	38.7845		0.31
34	$3s^2 3p^4 3d^3 ({}^4F_3) {}^6F_{5/2}$	Even	39.6263	−0.1170	−0.0726	39.4371	39.3150		0.31
35	$3s^2 3p^4 3d^3 ({}^2P_3) {}^4D_{7/2}$	Even	39.7533	−0.1490	−0.0721	39.5324	39.4099		0.32
36	$3s^2 3p^4 3d^3 ({}^4F_3) {}^4F_{3/2}$	Even	41.1739	−0.0742	−0.0721	41.0276	40.8978		0.21
37	$3s^2 3p^4 3d^3 ({}^4F_3) {}^6D_{5/2}$	Even	43.8465	−0.2230	−0.0721	43.5516	43.4623		0.21
38	$3s^2 3p^4 3d^3 ({}^4F_3) {}^6G_{9/2}$	Even	44.3709	−0.3100	−0.0719	43.9888	43.8966		0.21
39	$3s^2 3p^4 3d^3 ({}^4F_3) {}^6F_{7/2}$	Even	44.386	−0.2850	−0.0725	44.0288	43.9378		0.21
40	$3s^2 3p^4 3d^3 ({}^4F_3) {}^4F_{3/2}$	Even	44.4654	−0.2330	−0.0725	44.1598	44.0688		0.21
41	$3s^2 3p^4 3d^3 ({}^2P_3) {}^4H_{7/2}$	Even	44.7383	−0.2800	−0.0721	44.3861	44.2942		0.02
42	$3s^2 3p^5 3d^2 ({}^3F_2) {}^2F_{5/2}$	Odd	44.8664	−0.4290	−0.0067	44.4312	44.4387	44.340 44.191 ⁱ 44.341 ^j 44.376 ^k 44.292 ^l	0.20
43	$3s^2 3p^5 3d^2 ({}^4P_3) {}^6P_{5/2}$	Even	44.918	−0.2640	−0.0724	44.5816	44.4905		0.21
44	$3s^2 3p^4 3d^3 ({}^2G_3) {}^4G_{11/2}$	Even	45.0578	−0.3990	−0.0720	44.5872	44.4950		0.21
45	$3s^2 3p^4 3d^3 ({}^2G_3) {}^4G_{9/2}$	Even	45.1194	−0.3780	−0.0724	44.6689	44.5774		0.25
46	$3s^2 3p^4 3d^3 ({}^4F_3) {}^4F_{3/2}$	Even	45.3177	−0.2600	−0.0751	44.9825	44.8708		0.17
47	$3s^2 3p^4 3d^3 ({}^2G_3) {}^2H_{11/2}$	Even	45.4566	−0.4200	−0.0719	44.9645	44.8864		0.21
48	$3s^2 3p^4 3d^3 ({}^2G_3) {}^4H_{13/2}$	Even	45.5505	−0.4680	−0.0718	45.0108	44.9163		0.21
49	$3s^2 3p^4 3d^3 ({}^2H_3) {}^4G_{5/2}$	Even	45.6964	−0.3150	−0.0753	45.3066	45.2107		0.21
50	$3s^2 3p^4 3d^3 ({}^4F_3) {}^4D_{1/2}$	Even	46.1151	−0.2280	−0.0731	45.8144	45.7169		0.20
51	$3s^2 3p^4 3d^3 ({}^4P_3) {}^6P_{7/2}$	Even	46.2618	−0.2900	−0.0722	45.8995	45.8066		0.22
52	$3s^2 3p^4 3d^3 ({}^4F_3) {}^4F_{5/2}$	Even	46.4061	−0.2310	−0.0722	46.1025	46.0004		0.20

Table 1 (continued).

Level	Configuration	Parity	MCDF				DW	Other	ΔE
			DC	BREIT	QED	Total			
53	$3s^2 3p^4 3d^3 ({}^4P_3) {}^6D_{9/2}$	Even	46.5724	-0.3230	-0.0721	46.1774	46.0847		0.22
54	$3s^2 3p^4 3d^3 ({}^4F_3) {}^4P_{3/2}$	Even	46.8829	-0.2060	-0.0721	46.605	46.5024		0.22
55	$3s^2 3p^4 3d^3 ({}^4F_3) {}^6F_{1/2}$	Even	47.1397	-0.2120	-0.0717	46.8564	46.7520		0.22
56	$3s^2 3p^4 3d^3 ({}^4F_3) {}^4G_{5/2}$	Even	47.3995	-0.2770	-0.0718	47.0503	46.9447		0.22
57	$3s^2 3p^4 3d^3 ({}^2G_3) {}^4F_{3/2}$	Even	47.4365	-0.2640	-0.0721	47.1000	46.9947		0.21
58	$3s^2 3p^4 3d^3 ({}^2G_3) {}^2G_{7/2}$	Even	47.5023	-0.3020	-0.0721	47.1279	47.0281		0.21
59	$3s^2 3p^4 3d^3 ({}^2G_3) {}^2G_{9/2}$	Even	47.7203	-0.3290	-0.0723	47.3192	47.2188		0.22
60	$3s^2 3p^4 3d^3 ({}^2F_3) {}^4F_{3/2}$	Even	47.7836	-0.2730	-0.0719	47.4385	47.3326		0.18
61	$3s^2 3p^5 3d^2 ({}^3P_2) {}^4D_{1/2}$	Odd	47.8654	-0.3460	-0.0074	47.512	47.4274		0.04
62	$3s^2 3p^5 3d^2 ({}^2G_3) {}^4F_{5/2}$	Even	47.8812	-0.2730	-0.0719	47.5367	47.5163		0.19
63	$3s^2 3p^5 3d^2 ({}^3F_2) {}^2D_{3/2}$	Odd	48.0631	-0.3880	-0.0079	47.6677	47.5782	47.502 ^a 47.570 ⁱ 47.497 ^j 47.605 ^k 47.767 ^l	0.04
64	$3s^2 3p^4 3d^3 ({}^2H_3) {}^4G_{7/2}$	Even	48.0825	-0.3260	-0.0720	47.6844	47.6664		0.23
65	$3s^2 3p^5 3d^2 ({}^4P_3) {}^4P_{1/2}$	Odd	48.1026	-0.2300	-0.0721	47.8009	47.6890		0.35
66	$3s^2 3p^4 3d^3 ({}^4P_3) {}^2S_{1/2}$	Even	48.3365	-0.2230	-0.0745	48.0390	47.8716		0.16
67	$3s^2 3p^5 3d^2 ({}^2G_3) {}^4H_{7/2}$	Even	48.376	-0.3200	-0.0720	47.9840	47.9081		0.17
68	$3s^2 3p^4 3d^3 ({}^2H_3) {}^4H_{9/2}$	Even	48.4625	-0.3710	-0.0722	48.0197	47.9380		0.21
69	$3s^2 3p^4 3d^3 ({}^2D_1) {}^2D_{5/2}$	Even	49.3789	-0.2300	-0.0723	49.0769	48.9763		0.13
70	$3s^2 3p^4 3d^3 ({}^4F_3) {}^6G_{11/2}$	Even	49.8344	-0.4800	-0.0718	49.2829	49.2190		0.21
71	$3s^2 3p^4 3d^3 ({}^2F_3) {}^4D_{3/2}$	Even	49.9893	-0.2450	-0.0720	49.6721	49.5672		0.06
72	$3s^2 3p^5 3d^2 ({}^3F_2) {}^4F_{7/2}$	Odd	50.1427	-0.5760	-0.0067	49.5604	49.5915		0.43
73	$3s^2 3p^4 3d^3 ({}^2F_3) {}^4F_{5/2}$	Even	50.1855	-0.2540	-0.0723	49.8592	49.6445		0.05
74	$3s^2 3p^4 3d^3 ({}^2F_3) {}^4F_{5/2}$	Odd	50.2685	-0.5350	-0.0069	49.7265	49.7502		0.14
75	$3s^2 3p^4 3d^3 ({}^2F_3) {}^6D_{7/2}$	Even	50.318	-0.4180	-0.0723	49.8273	49.7575		0.11
76	$3s^2 3p^4 3d^3 ({}^4F_3) {}^6G_{13/2}$	Even	50.3618	-0.5830	-0.0717	49.7074	49.7637		0.13
77	$3s^2 3p^4 3d^3 ({}^4F_3) {}^2G_{9/2}$	Even	50.5824	-0.4230	-0.0723	50.0873	50.0229		0.13
78	$3s^2 3p^4 3d^3 ({}^2D_3) {}^5D_{5/2}$	Even	50.585	-0.3880	-0.0724	50.1250	50.0610		0.06
79	$3s^2 3p^5 3d^2 ({}^3P_2) {}^4D_{3/2}$	Odd	50.6636	-0.5010	-0.0070	50.1559	50.1868		0.06
80	$3s^2 3p^5 3d^2 ({}^3P_2) {}^4D_{1/2}$	Odd	50.7978	-0.4590	-0.0071	50.3321	50.3635		0.14
81	$3s^2 3p^4 3d^3 ({}^2G_3) {}^2F_{5/2}$	Even	50.94	-0.4130	-0.0750	50.4521	50.3828		0.18
82	$3s^2 3p^4 3d^3 ({}^2D_3) {}^4P_{1/2}$	Even	51.0116	-0.3530	-0.0739	50.5851	50.4936		0.15
83	$3s^2 3p^4 3d^3 ({}^3F_2) {}^2G_{9/2}$	Odd	51.2503	-0.6470	-0.0067	50.5963	50.5195		0.14
84	$3s^2 3p^4 3d^3 ({}^2H_3) {}^4I_{15/2}$	Even	51.2859	-0.6550	-0.0717	50.5588	50.6275		0.13
85	$3s^2 3p^5 3d^2 ({}^1G_2) {}^2H_{9/2}$	Even	51.3092	-0.4890	-0.0720	50.7478	50.6826		0.13
86	$3s^2 3p^4 3d^3 ({}^2F_3) {}^4G_{11/2}$	Even	51.375	-0.5440	-0.0718	50.7597	50.6931		0.13
87	$3s^2 3p^4 3d^3 ({}^4P_3) {}^4D_{7/2}$	Even	51.4904	-0.4250	-0.0733	50.9921	50.9235		0.14
88	$3s^2 3p^4 3d^3 ({}^2D_3) {}^2P_{3/2}$	Even	51.8673	-0.3910	-0.0745	51.4013	51.3285		0.14
89	$3s^2 3p^4 3d^3 ({}^2D_3) {}^4F_{9/2}$	Even	52.0559	-0.4700	-0.0720	51.5136	51.4408		0.28
90	$3s^2 3p^4 3d^3 ({}^2D_3) {}^4P_{3/2}$	Even	52.1678	-0.3720	-0.0739	51.7224	51.5764		0.13
91	$3s^2 3p^4 3d^3 ({}^2F_3) {}^2F_{7/2}$	Even	52.2138	-0.4670	-0.0738	51.6731	51.6039		0.003
92	$3s^2 3p^4 3d^3 ({}^2H_3) {}^4H_{11/2}$	Even	52.2504	-0.5310	-0.0719	51.6473	51.6491		0.14
93	$3s^2 3p^4 3d^3 ({}^4F_3) {}^4D_{5/2}$	Even	52.3979	-0.4260	-0.0742	51.8974	51.8246		0.14
94	$3s^2 3p^4 3d^3 ({}^4F_3) {}^4F_{7/2}$	Even	52.422	-0.4270	-0.0729	51.9220	51.8483		0.31
95	$3s^2 3p^4 3d^3 ({}^2H_3) {}^4G_{9/2}$	Even	52.9476	-0.4760	-0.0728	52.3984	52.2378		0.02
96	$3s^2 3p^4 3d^3 ({}^2H_3) {}^4H_{13/2}$	Even	52.9878	-0.6020	-0.0718	52.3137	52.3233		0.04
97	$3s^2 3p^5 3d^2 ({}^3F_2) {}^2D_{5/2}$	Odd	53.0435	-0.5380	-0.0079	52.4979	52.5210		0.15
98	$3s^2 3p^4 3d^3 ({}^4P_3) {}^4D_{7/2}$	Even	53.1461	-0.3950	-0.0722	52.6789	52.6013		0.27
99	$3s^2 3p^5 3d^2 ({}^1G_2) {}^2F_{7/2}$	Odd	53.1682	-0.3250	-0.0724	52.7712	52.6274		0.09
100	$3s^2 3p^4 3d^3 ({}^4F_3) {}^6D_{5/2}$	Even	53.1696	-0.3930	-0.0718	52.705	52.6552		0.13
101	$3s^2 3p^4 3d^3 ({}^2D_1) {}^4D_{3/2}$	Even	53.2083	-0.5720	-0.0075	52.6289	52.6985		0.15
102	$3s^2 3p^4 3d^3 ({}^2F_3) {}^2G_{9/2}$	Even	53.3887	-0.4860	-0.0733	52.8291	52.7517		0.15
103	$3s^2 3p^4 3d^3 ({}^4P_3) {}^4P_{1/2}$	Even	53.6566	-0.3800	-0.0719	53.2052	53.1275		0.15
104	$3s^2 3p^5 3d^2 ({}^3P_2) {}^4D_{3/2}$	Odd	53.7308	-0.4420	-0.0719	53.2166	53.1343		0.04
105	$3s^2 3p^4 3d^3 ({}^2P_3) {}^2F_{7/2}$	Even	53.7341	-0.4940	-0.0076	53.2327	53.2520		0.14
106	$3s^2 3p^4 3d^3 ({}^4P_3) {}^4P_{5/2}$	Odd	53.8127	-0.4100	-0.0716	53.3314	53.2563		0.40
107	$3s^2 3p^4 3d^3 ({}^2F_3) {}^4D_{3/2}$	Even	53.9904	-0.3990	-0.0727	53.5188	53.3079		0.10
108	$3s^2 3p^4 3d^3 ({}^2F_3) {}^4G_{11/2}$	Even	54.0041	-0.5470	-0.0717	53.3854	53.4400		0.14
109	$3s^2 3p^4 3d^3 ({}^2F_3) {}^4D_{1/2}$	Even	54.1855	-0.3450	-0.0734	53.7672	53.6899		0.17
110	$3s^2 3p^4 3d^3 ({}^4P_3) {}^4D_{3/2}$	Even	54.2509	-0.3820	-0.0722	53.7963	53.7062		0.33
111	$3s^2 3p^4 3d^3 ({}^2D_3) {}^2D_{5/2}$	Even	54.3294	-0.3700	-0.0721	53.8876	53.7115		0.03

Table 1 (concluded).

Level	Configuration	Parity	MCDF				DW	Other	ΔE
			DC	BREIT	QED	Total			
112	$3s^23p^43d^3(^2G_3)^4G_{9/2}$	Even	54.3556	-0.4910	-0.0719	53.7929	53.8071		0.15
113	$3s^23p^43d^3(^2H_3)^2H_{11/2}$	Even	54.5313	-0.5400	-0.0719	53.9196	53.8371		0.14
114	$3s^23p^43d^3(^2F_3)^2F_{5/2}$	Even	54.5437	-0.3680	-0.0723	54.1038	54.0290		0.14
115	$3s^23p^43d^3(^2F_3)^2F_{7/2}$	Even	54.6833	-0.4110	-0.0726	54.1994	54.1249		0.16
116	$3s^23p^43d^3(^2F_3)^4F_{7/2}$	Even	55.0491	-0.4470	-0.0723	54.5302	54.4452		0.15
117	$3s^23p^43d^3(^2F_3)^4F_{9/2}$	Even	55.1164	-0.5000	-0.0718	54.5445	54.4616		0.15
118	$3s^23p^43d^3(^2F_3)^2F_{5/2}$	Even	55.1238	-0.4140	-0.0721	54.6373	54.5547		0.15
119	$3s^23p^43d^3(^2D_1)^2D_{3/2}$	Even	55.2814	-0.3700	-0.0724	54.8387	54.7543		0.21
120	$3s^23p^43d^3(^2D_1)^4P_{1/2}$	Even	55.3662	-0.3540	-0.0731	54.9390	54.8229		0.08
121	$3s^23p^43d^3(^2H_3)^4G_{5/2}$	Even	55.3789	-0.4020	-0.0720	54.9053	54.8625		0.16
122	$3s^23p^43d^3(^2F_3)^2D_{3/2}$	Even	55.4584	-0.3740	-0.0715	55.0128	54.9275		0.15
123	$3s^23p^43d^3(^2G_3)^2G_{7/2}$	Even	55.6465	-0.4340	-0.0721	55.1407	55.0585		0.16
124	$3s^23p^43d^3(^2D_1)^2D_{5/2}$	Even	55.941	-0.4260	-0.0728	55.4426	55.3546		0.22
125	$3s^23p^43d^3(^2D_1)^2D_{3/2}$	Even	55.9483	-0.3390	-0.0724	55.5367	55.4159		0.12
126	$3s^23p^53d^2(^3F_2)^4D_{7/2}$	Odd	56.0252	-0.6550	-0.0072	55.3631	55.4312		0.10
127	$3s^23p^43d^3(^2H_3)^2G_{7/2}$	Even	56.0767	-0.4880	-0.0722	55.5162	55.4603		0.07
128	$3s^23p^43d^3(^2G_3)^4H_{13/2}$	Even	56.3362	-0.6800	-0.0716	55.5842	55.5464		0.21
129	$3s^23p^43d^3(^2D_3)^2P_{1/2}$	Even	56.551	-0.3790	-0.0726	56.0996	55.9820		0.13
130	$3s^23p^53d^2(^3F_2)^2G_{9/2}$	Odd	56.6727	-0.7360	-0.0069	55.9296	56.0034		0.09
131	$3s^23p^53d^2(^1D_2)^2P_{3/2}$	Odd	56.6963	-0.6220	-0.0073	56.0674	56.1207		0.09
132	$3s^23p^53d^2(^1D_2)^2F_{5/2}$	Odd	57.0833	-0.6650	-0.0071	56.4113	56.4640		0.08
133	$3s^23p^43d^3(^2F_3)^4D_{7/2}$	Even	57.3147	-0.5600	-0.0737	56.6805	56.6327		0.09
134	$3s^23p^43d^3(^2P_3)^2P_{3/2}$	Even	58.0044	-0.4860	-0.0732	57.4452	57.3925		0.16
135	$3s^23p^43d^3(^2F_3)^2D_{3/2}$	Even	58.2205	-0.4180	-0.0728	57.7297	57.6394		0.09
136	$3s^23p^43d^3(^4F_3)^4F_{9/2}$	Even	58.5148	-0.6130	-0.0729	57.8289	57.7785		0.03
137	$3s^23p^53d^2(^1S_0)^2P_{1/2}$	Odd	58.6635	-0.5670	-0.0073	58.0890	58.0703		0.03
138	$3s^23p^43d^3(^2G_3)^4G_{11/2}$	Even	58.8326	-0.6380	-0.0715	58.1230	58.1410		0.08
139	$3s^23p^43d^3(^2D_1)^4D_{7/2}$	Even	59.1947	-0.5320	-0.0730	58.5899	58.5451		0.08
140	$3s^23p^43d^3(^2D_1)^4F_{9/2}$	Even	59.2751	-0.5500	-0.0719	58.6535	58.6081		0.09
141	$3s^23p^43d^3(^2P_3)^4P_{5/2}$	Even	59.7575	-0.5420	-0.0732	59.1427	59.0897		0.08
142	$3s^23p^43d^3(^2D_1)^2P_{1/2}$	Even	59.9032	-0.4900	-0.0740	59.3396	59.2904		0.36

^a[26], ^b[25], ^cRMBPT [30], ^dRCI [30], ^e[33], ^fRCI [34], ^gRMBPT [34], ^h[53], ⁱ[28], ^jExperimental [54], ^kFAC [54], ^lGRASP [54].

and RCI. The discrepancy between our MCDF results and the RMBPT results of Zhao et al. [34] is 0.025 Ryd for level 2, which is very small. This may be because in their RMBPT calculations, they have taken single excitation up to $n = 125$ and double excitations with one electron to $n = 65$ and other electrons to $n = 125$. But the discrepancy between our MCDF results and their RCI results is 0.016 for level 2, which is less than the discrepancy with their RMBPT results because they have only included interaction within $n = 3$ orbitals but not considered correlation with higher orbitals. So, it is observed that consideration of correlations by taking one excitation to higher orbitals is affecting the fine-structure energies of the ground state configuration. But because the difference is very small, therefore, inclusion of SDT excitations within $n = 3$ and single excitations to higher orbitals is necessary for correlation for higher excited states.

So from the above discussions, we finally deduced that inclusion of a large configuration set is not notably affecting the fine-structure splitting of $3s^23p^63d$ and all fully relativistic codes and methods producing nearly the same excitation energies for low-lying levels for a small configuration set.

3.2. Radiative data

Radiative rate A_{ji} (in s^{-1}) and absorption oscillator strength f_{ij} for a transition $i \rightarrow j$ are correlated as

$$f_{ij} = \frac{mc\lambda_{ji}^2}{8\pi^2e^2} \frac{\omega_j}{\omega_i} A_{ij} \tag{5}$$

where c , m , e are the velocity of light, electron mass, and electron charge, respectively, and ω_i , ω_j , and λ_{ij} represent upper and lower

levels of statistical weights and transition wavelength (in Å), respectively. The oscillator strength (f_{ij}) and line strength (S_{ij}) can be connected by the following:

E1 transitions:

$$A_{ji} = \frac{2.0261 \times 10^{18}}{\omega_j \lambda_{ji}^3} S_{ij} \quad \text{and} \quad f_{ij} = \frac{303.75}{\lambda_{ji} \omega_i} S_{ij} \tag{6}$$

M1 transitions:

$$A_{ji} = \frac{2.6974 \times 10^{13}}{\omega_j \lambda_{ji}^3} S_{ij} \quad \text{and} \quad f_{ij} = \frac{4.044 \times 10^{-3}}{\lambda_{ji} \omega_i} S_{ij} \tag{7}$$

E2 transitions:

$$A_{ji} = \frac{1.1199 \times 10^{13}}{\omega_j \lambda_{ji}^5} S_{ij} \quad \text{and} \quad f_{ij} = \frac{167.89}{\lambda_{ji}^3 \omega_i} S_{ij} \tag{8}$$

M1 transitions:

$$A_{ji} = \frac{1.4910 \times 10^{13}}{\omega_j \lambda_{ji}^5} S_{ij} \quad \text{and} \quad f_{ij} = \frac{2.236 \times 10^{-3}}{\lambda_{ji}^3 \omega_i} S_{ij} \tag{9}$$

Transition wavelengths (λ_{ij} in Å), line strengths (S_{ij} in a.u.), radiative rates (A_{ij} in s^{-1}), and oscillator strengths (f_{ij} , dimensionless) are reported from the ground state for E1, E2, M1, and M2 in Tables 2–5, respectively. We have found 29 E1, 68 E2, 51 M1, and

Table 2. Radiative data for E1 transitions in W LVI.

S. No.	Transition		λ (Å)	A_{ji} (s ⁻¹)	f_{ij}	S_{ij} (a.u.)
	Lower level	Upper level				
1	1	3	48.402	2.4338E+09	8.5480E-04	5.4483E-04
2	1	4	48.049	1.0365E+10	1.7938E-03	1.1350E-03
3	1	5	47.074	5.5148E+09	2.7481E-03	1.7035E-03
4	1	7	43.036	1.0967E+09	3.0450E-04	1.7256E-04
5	1	8	37.864	3.5621E+07	1.1484E-05	5.7263E-06
6	1	11	36.575	1.4394E+10	2.8867E-03	1.3903E-03
7	1	12	36.353	1.2075E+09	3.5883E-04	1.7177E-04
8	1	15	35.353	1.3710E+08	1.2845E-05	5.9799E-06
9	1	17	34.691	4.8991E+09	1.3259E-03	6.0570E-04
10	1	18	34.396	1.1446E+05	2.0300E-08	9.1949E-09
11	1	20	32.903	7.4878E+11	1.2153E-01	5.2655E-02
12	1	21	32.237	1.0246E+12	2.3944E-01	1.0165E-01
13	1	22	31.593	1.1756E+12	8.7956E-02	3.6592E-02
14	1	24	29.727	1.8423E+09	3.6612E-04	1.4332E-04
15	1	27	28.833	1.1348E+10	7.0717E-04	2.6850E-04
16	1	29	27.293	2.0486E+08	2.2878E-05	8.2223E-06
17	1	30	26.859	2.7455E+10	4.4540E-03	1.5753E-03
18	1	31	26.588	3.5129E+08	3.7229E-05	1.3035E-05
19	1	42	20.510	8.6149E+11	8.1492E-02	2.2009E-02
20	1	61	19.180	3.1208E+12	8.6055E-02	2.1735E-02
21	1	63	19.117	5.6834E+12	3.1140E-01	7.8392E-02
22	1	74	18.326	1.0633E+08	8.0300E-06	1.9378E-06
23	1	79	18.169	7.7716E+10	3.8461E-03	9.2019E-04
24	1	80	18.105	4.3648E+07	1.0725E-06	2.5570E-07
25	1	97	17.358	2.5351E+09	1.7177E-04	3.9264E-05
26	1	105	17.119	1.7693E+10	7.7733E-04	1.7523E-04
27	1	131	16.253	1.9043E+09	7.5416E-05	1.6141E-05
28	1	132	16.154	1.0316E+09	6.0538E-05	1.2878E-05
29	1	137	15.687	3.5470E+10	6.5432E-04	1.3517E-04

38 M2 SXR transitions and 1 E2 and 1 M1 EUV transitions from higher excited states to the ground state. The transition data of E1, E2, M1, and M2 transitions among the lowest 142 levels is provided as supplementary material¹. In Table 6, we have compared our GRASP transition wavelengths from theoretically calculated [31, 54] and experimentally measured wavelengths [31]. We have also compared our calculated oscillator strengths with theoretically calculated oscillator strengths [31]. We found that our transition data compared in Table 6 are in good agreement with Dipti et al. [31] and Clementson et al. [54] with a very small difference. This shows that our presented radiative data for W LVI are reliable and can be used further for identification of spectral lines observed experimentally.

3.3. Partition function and thermodynamic parameters

The generalized formula for partition function (Q) is given by

$$Q = g_0 + \sum_{i=1}^{n-1} g_i \exp\left(-\frac{\varepsilon_i}{kT}\right) \quad (10)$$

thermodynamic quantities, internal energy and specific heat, can be obtained using standard expressions [55]

$$U = \frac{1}{Q} \sum_{i=1}^{n-1} g_i \left(\frac{\varepsilon_i}{kT}\right) \exp\left(-\frac{\varepsilon_i}{kT}\right) \quad (11)$$

$$C = \frac{1}{Q} \left[\sum_{i=1}^{n-1} g_i \left(\frac{\varepsilon_i}{kT}\right)^2 \exp\left(-\frac{\varepsilon_i}{kT}\right) \right] - (U)^2 \quad (12)$$

In eqs. (10)–(12), g_0 and g_i are statistical weight of ground state and i th levels, respectively, ε_i is fine-structure energy of the i th level with respect to ground state, and n is the number of levels considered in calculations.

In Table 7, we have presented partition function (Q), internal energy, and specific heat for K-like W. From Table 7, we can see that as temperature increases, partition function and thermodynamic quantities increase, which also satisfies the basic requirement of the partition function.

In Figs. 1a–1c, we show the variation of partition function, internal energy, and specific heat as a function of thermodynamic temperature. It is observed that change in partition function is almost negligibly the same below 10^6 K for K-like W, but after that increases rapidly due to the contribution of higher excited states. We have predicted maxima for both internal energy and specific heat for both O-like W in Figs. 1b and 1c, respectively. It is also predicted that the position of the highest peak of O-like W for internal energy and specific heat is nearly at the same position but the width of the internal energy peak is greater than that of specific heat. A similar pattern can also be seen in Fig. 2.

In Fig. 2, we have plotted the variation of internal energy and specific heat with partition function for temperature 10^4 – 10^{10} K for K-like W. We predicted that internal energy and specific heat attain maximum values approximately at the same value of partition function but the fall of specific heat is very rapid compared to that of internal energy and similarly the rise of specific heat is also fast as compared to that of internal energy.

The partition function can be used in the determination of probability of occupancy of levels and also line intensity of

¹Supplementary data are available with the article at <https://doi.org/10.1139/cjp-2020-0497>.

Table 3. Radiative data for E2 transitions in W LVI.

S. No.	Transition		λ (Å)	A_{ji} (s ⁻¹)	f_{ij}	S_{ij} (a.u.)
	Lower level	Upper level				
1	1	2	160.320	5.2988E+02	3.0627E-09	3.0069E-04
2	1	32	23.450	3.0063E+04	2.4784E-09	7.6141E-07
3	1	33	23.426	2.5262E+04	1.0391E-09	3.1825E-07
4	1	34	23.107	2.0332E+05	2.4412E-08	7.1757E-06
5	1	35	23.051	7.0505E+03	1.1233E-09	3.2779E-07
6	1	36	22.211	5.9561E+03	4.4052E-10	1.1500E-07
7	1	37	20.924	4.8419E+03	4.7670E-10	1.0404E-07
8	1	39	20.697	1.4054E+04	1.8052E-09	3.8131E-07
9	1	40	20.636	4.8925E+04	3.1234E-09	6.5390E-07
10	1	41	20.531	2.8571E+04	3.6109E-09	7.4446E-07
11	1	43	20.440	2.7774E+04	2.6095E-09	5.3096E-07
12	1	46	20.258	4.1487E+05	2.5526E-08	5.0560E-06
13	1	49	20.113	2.1454E+06	1.9518E-07	3.7836E-05
14	1	50	19.890	2.8243E+05	8.3757E-09	1.5703E-06
15	1	51	19.854	9.7740E+04	1.1551E-08	2.1537E-06
16	1	52	19.766	1.5264E+04	1.3411E-09	2.4675E-07
17	1	54	19.553	3.5683E+04	2.0452E-09	3.6426E-07
18	1	55	19.448	6.8151E+04	1.9322E-09	3.3862E-07
19	1	56	19.368	1.4075E+03	1.1873E-10	2.0552E-08
20	1	57	19.348	8.1804E+04	4.5907E-09	7.9211E-07
21	1	58	19.336	1.2173E+04	1.3646E-09	2.3504E-07
22	1	60	19.209	3.8570E+03	2.1337E-10	3.6034E-08
23	1	62	19.170	2.2961E+00	1.8974E-13	3.1845E-11
24	1	64	19.110	2.6522E-01	2.9043E-14	4.8292E-12
25	1	65	19.064	1.4819E+05	4.0371E-09	6.6639E-07
26	1	66	18.969	1.5917E+06	4.2933E-08	6.9819E-06
27	1	67	18.991	5.6148E+03	6.0718E-10	9.9082E-08
28	1	69	18.568	1.1537E+05	8.9447E-09	1.3643E-06
29	1	71	18.346	2.9447E+04	1.4858E-09	2.1858E-07
30	1	73	18.277	8.3390E+04	6.2642E-09	9.1117E-07
31	1	75	18.289	1.6612E+05	1.6659E-08	2.4279E-06
32	1	78	18.180	1.6698E+05	1.2411E-08	1.7767E-06
33	1	81	18.062	2.3847E+06	1.7495E-07	2.4561E-05
34	1	82	18.015	1.4923E+06	3.6302E-08	5.0563E-06
35	1	87	17.871	8.4575E+05	8.0987E-08	1.1012E-05
36	1	88	17.729	1.7983E+06	8.4737E-08	1.1249E-05
37	1	90	17.618	3.0241E+05	1.4073E-08	1.8337E-06
38	1	91	17.635	6.6529E+05	6.2038E-08	8.1065E-06
39	1	93	17.559	1.1668E+02	8.0901E-12	1.0435E-09
40	1	94	17.551	4.8215E+04	4.4531E-09	5.7355E-07
41	1	98	17.299	8.6422E+03	7.7541E-10	9.5628E-08
42	1	99	17.268	7.7472E+05	3.4634E-08	4.2489E-06
43	1	100	17.290	2.9100E+04	1.9563E-09	2.4090E-07
44	1	103	17.127	1.2547E+05	2.7591E-09	3.3027E-07
45	1	104	17.124	1.5063E+03	1.3243E-10	1.5842E-08
46	1	106	17.087	4.5335E+05	2.9765E-08	3.5378E-06
47	1	107	17.027	6.6534E+05	2.8919E-08	3.4012E-06
48	1	109	16.948	1.1842E+06	2.5498E-08	2.9574E-06
49	1	110	16.939	5.8341E+04	2.5097E-09	2.9062E-07
50	1	111	16.911	7.7110E+04	4.9587E-09	5.7131E-07
51	1	114	16.843	4.1178E+05	2.6270E-08	2.9905E-06
52	1	115	16.813	9.8851E+05	8.3786E-08	9.4876E-06
53	1	116	16.711	4.9908E+04	4.1791E-09	4.6466E-07
54	1	118	16.679	1.1757E+05	7.3546E-09	8.1294E-07
55	1	119	16.617	6.7060E+04	2.7761E-09	3.0349E-07
56	1	120	16.587	1.9611E+06	4.0445E-08	4.3973E-06
57	1	121	16.597	7.3143E+05	4.5309E-08	4.9352E-06
58	1	122	16.565	2.4869E+05	1.0230E-08	1.1078E-06
59	1	123	16.526	7.7470E+05	6.3440E-08	6.8221E-06
60	1	124	16.436	3.1796E+05	1.9316E-08	2.0434E-06
61	1	125	16.408	1.8741E+05	7.5647E-09	7.9620E-07
62	1	127	16.414	4.2508E+02	3.4341E-11	3.6184E-09
63	1	129	16.244	4.4954E+04	8.8914E-10	9.0794E-08

Table 3 (concluded).

S. No.	Transition		λ (Å)	A_{ji} (s^{-1})	f_{ij}	S_{ij} (a.u.)
	Lower level	Upper level				
64	1	133	16.077	1.5098E+05	1.1702E-08	1.1585E-06
65	1	134	15.863	7.5152E+04	2.8352E-09	2.6964E-07
66	1	135	15.785	7.7278E+02	2.8867E-11	2.7051E-09
67	1	139	15.553	9.9552E+04	7.2208E-09	6.4727E-07
68	1	141	15.408	1.1467E+05	6.1218E-09	5.3351E-07
69	1	142	15.357	5.8087E+03	1.0269E-10	8.8602E-09

Table 4. Radiative data for M1 transitions in W LVI.

S. No.	Transition		λ (Å)	A_{ji} (s^{-1})	f_{ij}	S_{ij} (a.u.)
	Lower level	Upper level				
1	1	2	160.320	2.5832E+06	1.4931E-05	2.3677E+00
2	1	32	23.450	1.9683E+04	1.6227E-09	3.7636E-05
3	1	33	23.426	2.5033E+04	1.0297E-09	2.3858E-05
4	1	34	23.107	1.2611E+04	1.5142E-09	3.4607E-05
5	1	36	22.211	2.0712E+03	1.5318E-10	3.3653E-06
6	1	37	20.924	4.1714E+02	4.1069E-11	8.4993E-07
7	1	40	20.636	5.4779E+02	3.4971E-11	7.1378E-07
8	1	43	20.440	1.4622E+02	1.3739E-11	2.7776E-07
9	1	46	20.258	1.5550E+03	9.5671E-11	1.9170E-06
10	1	49	20.113	5.7076E+01	5.1924E-12	1.0330E-07
11	1	50	19.890	3.1196E+04	9.2514E-10	1.8201E-05
12	1	52	19.766	5.3078E+03	4.6634E-10	9.1171E-06
13	1	54	19.553	1.7988E+04	1.0310E-09	1.9939E-05
14	1	55	19.448	1.7797E+04	5.0457E-10	9.7058E-06
15	1	56	19.368	1.9235E+04	1.6226E-09	3.1082E-05
16	1	57	19.348	7.1180E+03	3.9945E-10	7.6440E-06
17	1	60	19.209	3.3399E+03	1.8476E-10	3.5105E-06
18	1	62	19.170	1.8035E+04	1.4904E-09	2.8259E-05
19	1	65	19.064	1.1590E+03	3.1573E-11	5.9533E-07
20	1	66	18.969	2.6157E+04	7.0555E-10	1.3238E-05
21	1	69	18.568	1.4897E+04	1.1550E-09	2.1212E-05
22	1	71	18.346	3.3914E+04	1.7112E-09	3.1050E-05
23	1	73	18.277	3.1309E+04	2.3519E-09	4.2516E-05
24	1	78	18.180	1.7694E+03	1.3151E-10	2.3647E-06
25	1	81	18.062	2.1783E+02	1.5981E-11	2.8550E-07
26	1	82	18.015	3.3565E+03	8.1650E-11	1.4548E-06
27	1	88	17.729	1.1552E+03	5.4433E-11	9.5449E-07
28	1	90	17.618	2.0618E+02	9.5947E-12	1.6720E-07
29	1	93	17.559	2.7244E-01	1.8890E-14	3.2806E-10
30	1	99	17.268	1.8045E+02	8.0669E-12	1.3778E-07
31	1	100	17.290	6.5173E+02	4.3813E-11	7.4926E-07
32	1	103	17.127	4.7761E+03	1.0502E-10	1.7791E-06
33	1	106	17.087	5.1953E+03	3.4110E-10	5.7648E-06
34	1	107	17.027	4.5222E+03	1.9656E-10	3.3102E-06
35	1	109	16.948	2.1358E+03	4.5987E-11	7.7090E-07
36	1	110	16.939	5.1062E+01	2.1966E-12	3.6802E-08
37	1	111	16.911	6.6507E+01	4.2769E-12	7.1535E-08
38	1	114	16.843	3.9032E+02	2.4900E-11	4.1482E-07
39	1	118	16.679	1.8636E+03	1.1658E-10	1.9231E-06
40	1	119	16.617	2.1374E+03	8.8484E-11	1.4543E-06
41	1	120	16.587	6.3194E+03	1.3033E-10	2.1381E-06
42	1	121	16.597	7.5574E+02	4.6815E-11	7.6851E-07
43	1	122	16.565	3.5370E+03	1.4550E-10	2.3838E-06
44	1	124	16.436	7.3490E+02	4.4646E-11	7.2580E-07
45	1	125	16.408	1.8928E+02	7.6400E-12	1.2399E-07
46	1	129	16.244	2.7016E+03	5.3434E-11	8.5850E-07
47	1	134	15.863	5.2412E+02	1.9773E-11	3.1024E-07
48	1	135	15.785	1.8891E+03	7.0569E-11	1.1018E-06
49	1	141	15.408	3.9228E+02	2.0943E-11	3.1916E-07
50	1	142	15.357	7.2668E+02	1.2846E-11	1.9512E-07

Table 5. Radiative data for M2 transitions in W LVI.

S. No.	Transition		λ (Å)	A_{ji} (s ⁻¹)	f_{ij}	S_{ij} (a.u.)
	Lower level	Upper level				
1	1	3	48.402	8.4721E+01	2.9755E-11	6.0374E-03
2	1	4	48.049	8.9934E+01	1.5564E-11	3.0895E-03
3	1	5	47.074	5.9930E-01	2.9864E-13	5.5742E-05
4	1	6	46.593	1.9356E+01	1.2599E-11	2.2803E-03
5	1	7	43.036	1.0766E+02	2.9892E-11	4.2633E-03
6	1	8	37.864	1.5895E+04	5.1248E-09	4.9781E-01
7	1	10	36.969	5.6630E+02	2.3206E-10	2.0980E-02
8	1	11	36.575	4.9222E+04	9.8714E-09	8.6421E-01
9	1	12	36.353	3.5082E+04	1.0426E-08	8.9621E-01
10	1	13	35.978	4.7796E+04	1.8551E-08	1.5459E+00
11	1	15	35.353	6.9698E+04	6.5298E-09	5.1629E-01
12	1	16	34.856	1.7160E+04	6.2513E-09	4.7372E-01
13	1	17	34.691	6.4903E+03	1.7565E-09	1.3122E-01
14	1	18	34.396	9.9863E+03	1.7712E-09	1.2897E-01
15	1	20	32.903	2.6909E+03	4.3673E-10	2.7836E-02
16	1	21	32.237	4.2742E+02	9.9888E-11	5.9882E-03
17	1	22	31.593	1.7631E+02	1.3191E-11	7.4433E-04
18	1	24	29.727	4.7536E-01	9.4467E-14	4.4407E-06
19	1	26	29.299	6.0515E+02	1.5576E-10	7.0102E-03
20	1	27	28.833	8.7524E+02	5.4541E-11	2.3392E-03
21	1	28	27.800	1.6481E+03	3.8192E-10	1.4683E-02
22	1	29	27.293	7.3772E+02	8.2384E-11	2.9970E-03
23	1	30	26.859	1.9280E+03	3.1279E-10	1.0845E-02
24	1	31	26.588	3.3414E+03	3.5413E-10	1.1910E-02
25	1	42	20.510	4.2852E+04	4.0536E-09	6.2577E-02
26	1	61	19.180	3.2390E+04	8.9314E-10	1.1276E-02
27	1	63	19.117	3.0700E+03	1.6820E-10	2.1028E-03
28	1	72	18.387	9.8586E+04	9.9937E-09	1.1116E-01
29	1	74	18.326	2.2059E+05	1.6659E-08	1.8346E-01
30	1	79	18.169	2.7474E+05	1.3597E-08	1.4592E-01
31	1	80	18.105	2.8021E+05	6.8851E-09	7.3118E-02
32	1	97	17.358	6.3314E+04	4.2900E-09	4.0149E-02
33	1	101	17.315	2.5766E+05	2.3162E-08	2.1516E-01
34	1	105	17.119	2.6524E+04	1.1653E-09	1.0460E-02
35	1	126	16.460	1.2232E+04	9.9364E-10	7.9289E-03
36	1	131	16.253	8.7392E+01	3.4610E-12	2.6590E-05
37	1	132	16.154	3.5880E+02	2.1055E-11	1.5882E-04
38	1	137	15.687	1.5153E+03	2.7954E-11	1.9311E-04

Table 6. Comparison of transition wavelength (λ in Å) and oscillator strength (f in a.u.) for W LVI.

Transition		λ_{GRASP}	λ [31]	λ_{exp} [54]	λ [54]	f_{GRASP}	f [31]
Upper level	Lower level						
21	1	32.237	32.376	32.469	32.382	0.2394	0.2866
20	1	32.903	33.089	33.107	33.082	0.1215	0.1418
22	1	31.593	31.830	31.814	31.733	0.0879	0.0967
17	1	34.691	35.116	34.850	34.883	0.0013	0.0013

Table 7. Partition function (Q), internal energy (U/kT), and specific heat (C/k) in LSJ coupling for K-like W.

S. No.	logT (K)	LSJ		
		Q	U/kT	C/k
1	4	4.0000	1.40E-38	1.29E-36
2	5	4.0006	1.38E-03	1.27E-02
3	6	9.7476	1.668731	4.000631
4	7	465.5805	0.694324	4.06E-02

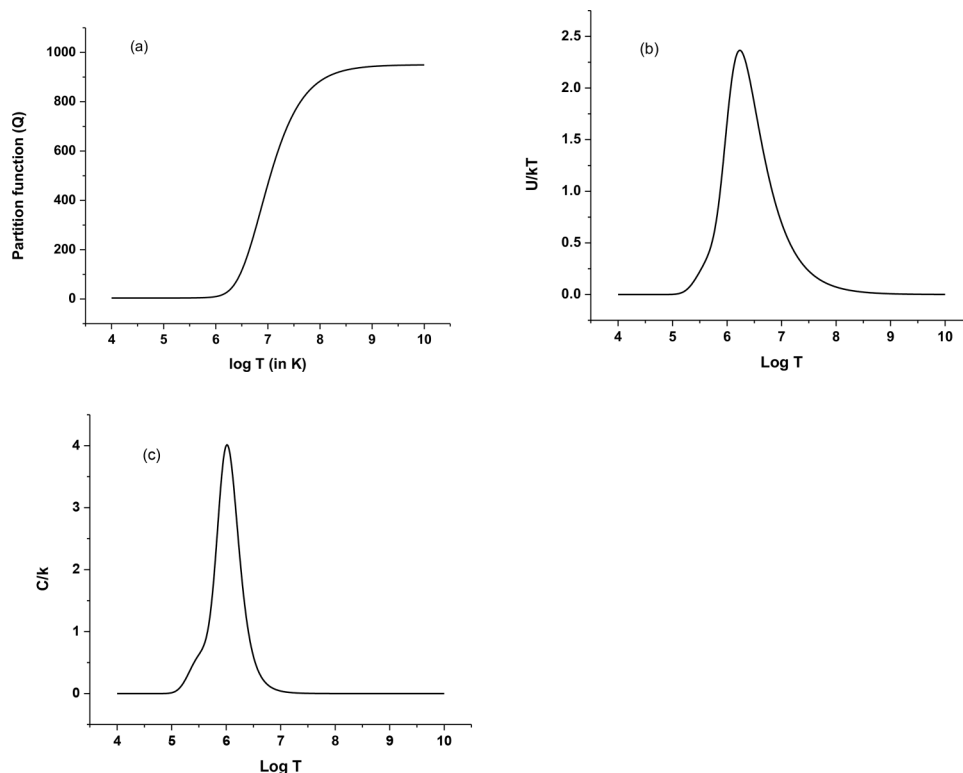
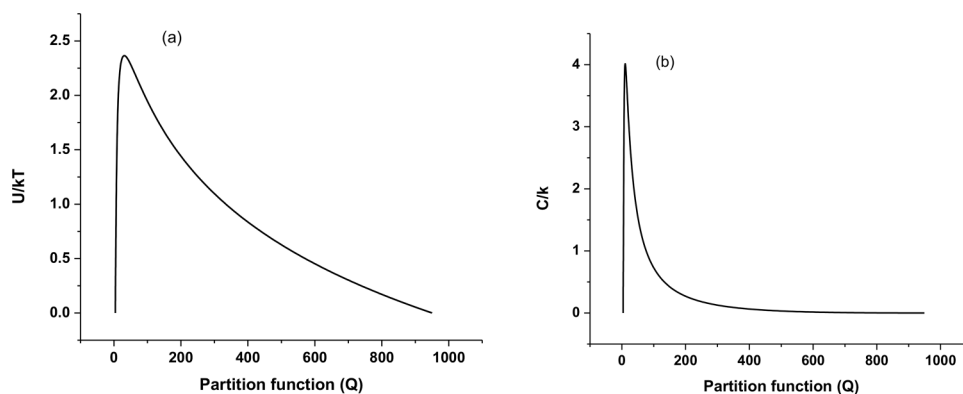
spectral lines. Therefore, we have studied population of the levels relative to the ground state in the next section.

3.4. Relative population

According to the Boltzmann distribution, population of level j for an ionization stage z can be calculated from the following formula:

$$n_j = \frac{N}{Q} g_j \exp\left(-\frac{\epsilon_j}{kT}\right) \tag{13}$$

where n_j is population of level j for ionization stage z , Q is the partition function, N is total number of ions in z , ϵ_j is energy of the j th level, and g_j is statistical weight of the j th level.

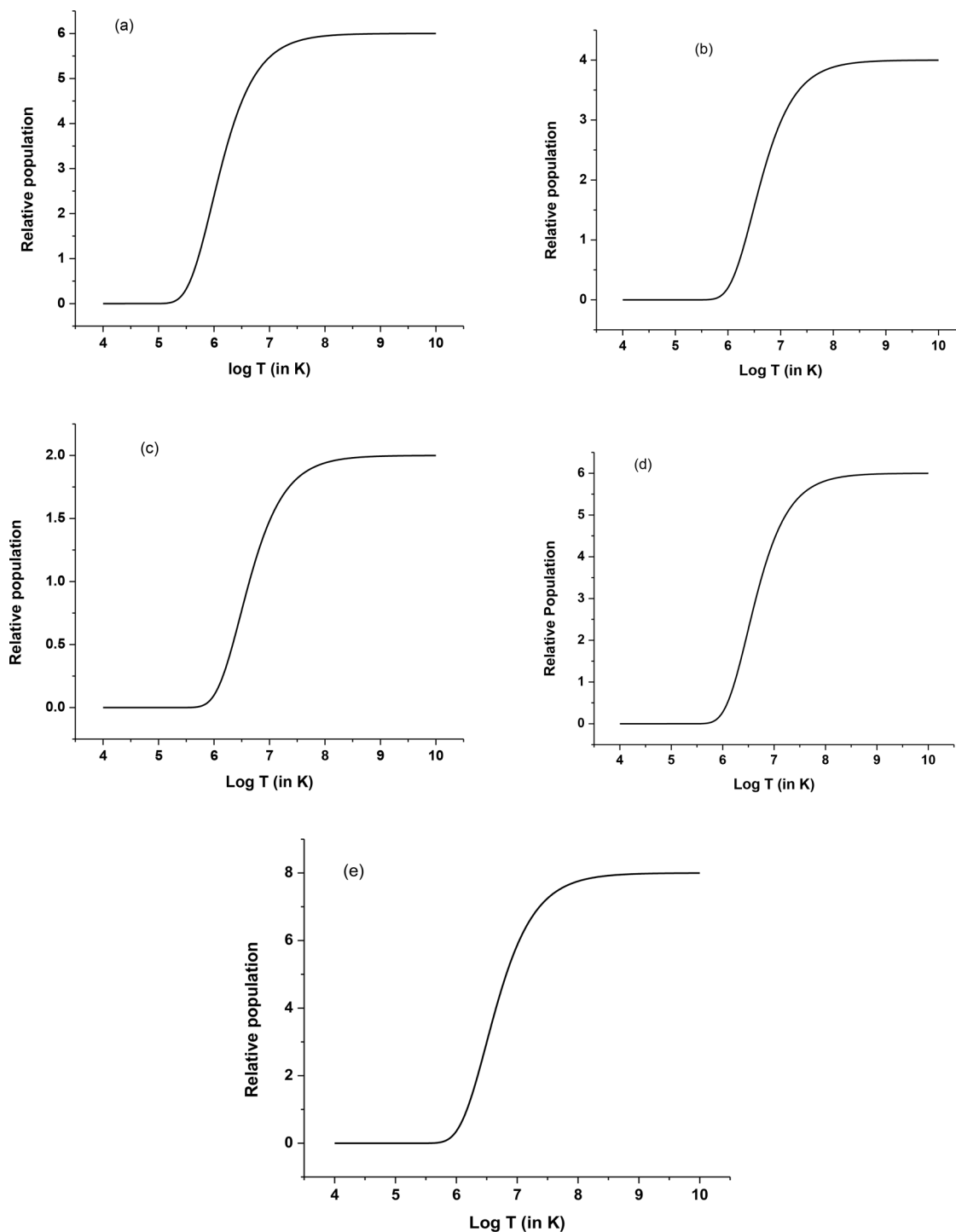
Fig. 1. Variation of (a) partition function (b) internal energy and (c) specific heat with temperature for K-like W.**Fig. 2.** Variation of (a) internal energy and (b) specific heat with partition function for K-like W.

We have calculated the population of the first five excited states relative to the ground state for a single K-like W ion for temperature ranges from 10^4 to 10^{10} K by employing Boltzmann statistics. Therefore, in eq. (13), we have taken $N = 1$ and the partition function of the ground state. In Figs. 3a–3e, we have plotted variation of relative population of the first five excited levels with temperature. From Fig. 3, we can see that for the second to fifth excited states below 10^6 K, the population is almost negligible as compared to the ground state. But for the first excited state, the temperature at which relative population is negligible is similar at $10^{5.5}$ K. From Fig. 3e, it is also evident that relative population of the fifth excited state of K-like W is the highest at above 10^7 K. Since relative population of the first five excited states is large above 10^6 K, therefore we can achieve population inversion for all five excited states for K-like W above 10^6 .

4. Conclusion

In the current paper, we have presented energy levels and radiative data for E1, E2, M1, and M2 transitions among the lowest 142 fine-structure levels for K-like W. MCDF and DW, two independent codes, are executed in calculations and the discrepancy in the results from both codes are provided. The discrepancy of our MCDF energies with the available theoretical and experimental data in the literature is discussed in detail. We have also predicted SXR and EUV transitions from ground state in W LVI and found most of the transitions towards the ground state lie in the SXR region. Further, we have also studied variation of the partition function and thermodynamic quantities within temperature range 10^4 – 10^{10} K. We have also shown the variation of relative population of the first five excited states with respect to the ground state using Boltzmann statistics and discussed their variations with temperature.

Fig. 3. Variation of relative population of (a) first (b) second (c) third (d) fourth and (e) fifth excited states with temperature for K-like W.



Overall, we conclude that our results are extensive and new and will be useful in identification and analysis of spectral lines in experimental spectra, microscopic imaging, and in plasma physics.

Acknowledgement

We are thankful to Delhi Technological University for their support and giving us better facilities.

References

1. R. Neu, R. Dux, and A. Kallenbach, et al. Nucl. Fusion, **45**, 209 (2005). doi:[10.1088/0029-5515/45/3/007](https://doi.org/10.1088/0029-5515/45/3/007).
2. K. Ikeda. Nucl. Fusion, **50**, 014002 (2010). doi:[10.1088/0029-5515/50/1/014002](https://doi.org/10.1088/0029-5515/50/1/014002).
3. M. Merolaa, D. Loesserb, and A. Martina, et al. Fusion Eng. Des. **85**, 2312 (2010). doi:[10.1016/j.fusengdes.2010.09.013](https://doi.org/10.1016/j.fusengdes.2010.09.013).
4. T. Das, Y.A. Podpaly, J. Reader, J.D. Gillaspay, and Y. Ralchenko. Eur. Phys. J. D, **72**, 124 (2018). doi:[10.1140/epjd/e2018-90118-7](https://doi.org/10.1140/epjd/e2018-90118-7).
5. M.J. Seaton. Adv. Atom. Mol. Phys. **4**, 331 (1968).
6. A.H. Gabriel and C. Jordan. Mon. Not. R. Astron. Soc. **145**, 241 (1969). doi:[10.1093/mnras/145.2.241](https://doi.org/10.1093/mnras/145.2.241).

7. D.E. Osterbrock. Astrophysics of gaseous nebulae. Freeman, San Francisco (1974).
8. D.E. Osterbrock. Astrophysics of gaseous nebulae and active galactic nuclei. University Science Books, Mill Valley, Calif. (1989).
9. S. Suckewer and E. Hinnov. Phys. Rev. A, **20**, 578 (1979). doi:10.1103/PhysRevA.20.578.
10. E. Hinnov and S. Suckewer. Phys. Lett. A, **79**, 298 (1980). doi:10.1016/0375-9601(80)90352-7.
11. S. Suckewer, R. Fonck, and E. Hinnov. Phys. Rev. A, **21**, 924 (1980). doi:10.1103/PhysRevA.21.924.
12. B. Edlén. Phys. Scr. **1983** (T3), 5 (1983). doi:10.1088/0031-8949/1983/T3/001.
13. V. Kaufman, J. Sugar, and W.L. Rowan. J. Opt. Soc. Am. B, **6** (3), 142 (1989). doi:10.1364/JOSAB.6.000142.
14. K.B. Fournier, W.H. Goldstein, M. May, and M. Finkenthal. Phys. Rev. A, **53** (2), 709 (1996). doi:10.1103/PhysRevA.53.709.
15. M. Wang, F. O'Reilly, P. Dunne, A. Arnesen, F. Heijenskjöld, R. Hallin, and G. O'Sullivan. J. Phys. B: At. Mol. Opt. Phys. **30**, 4175 (1997). doi:10.1088/0953-4075/30/19/009.
16. M. Wang, R. Faulkner, and F. O'Reilly, et al. J. Phys. B: At. Mol. Opt. Phys. **32**, 5299 (1999). doi:10.1088/0953-4075/32/22/308.
17. A.K. Singh, A. Goyal, I. Khatri, S. Aggarwal, R. Sharma, and M. Mohan. At. Data Nucl. Data Tables, **109–110**, 339 (2016). doi:10.1016/j.adt.2015.12.003.
18. T.A. Carlson, C.W. Nestor, N. Wasserman, and J.D. McDowell. At. Data Nucl. Data Tables, **2**, 63 (1970).
19. L. Yang, L. Liu, and J.-M. Li. Chin. Phys. Lett. **7**, 121 (1990).
20. M.A. Ali and Y.-K. Kim. J. Opt. Soc. Am. B, **9**, 185 (1992). doi:10.1364/JOSAB.9.000185.
21. E. Behar, A. Peleg, R. Doron, P. Mandelbaum, and J.L. Schwob. J. Quant. Spectrosc. Radiat. Transfer, **58**, 449 (1997). doi:10.1016/S0022-4073(97)00052-6.
22. G.C. Rodrigues, P. Indelicato, J.P. Santos, P. Patté, and F. Parente. At. Data Nucl. Data Tables, **86**, 117 (2004). doi:10.1016/j.adt.2003.11.005.
23. A.E. Kramida and J. Reader. At. Data Nucl. Data Tables, **92**, 457 (2006). doi:10.1016/j.adt.2006.03.002.
24. A.E. Kramida and T. Shirai. At. Data Nucl. Data Tables, **95**, 305 (2009). doi:10.1016/j.adt.2008.12.002.
25. P. Quinet. J. Phys. B: At. Mol. Opt. Phys. **44**, 195007 (2011). doi:10.1088/0953-4075/44/19/195007.
26. A. Kramida. Can. J. Phys. **89** (5), 551 (2011). doi:10.1139/p11-045.
27. P. Beiersdorfer, M.J. May, J.H. Scofield, and S.B. Hansen. High Energy Dens. Phys. **8**, 271 (2012). doi:10.1016/j.hedp.2012.03.003.
28. Dipti Priti, L. Sharma, and R. Srivastava. Atoms, **3**, 53 (2015). doi:10.3390/atoms3020053.
29. M.B. Trzhaskovskaya and V.K. Nikulin. Atoms, **3**, 86 (2015). doi:10.3390/atoms3020086.
30. X.L. Guo, M. Huang, and J. Yan, et al. J. Phys. B, **48**, 144020 (2015).
31. T. Das, L. Sharma, and R. Srivastava. Can. J. Phys. **93** (8), 888 (2015). doi:10.1139/cjp-2014-0636.
32. M. Xu, G. Jiang, M. Wu, X. Li, G. Bian, and F. Hu. Can. J. Phys. **94** (3), 563 (2016). doi:10.1139/cjp-2015-0772.
33. C.F. Fischer, G. Gaigalas, and P. Jönsson. Atoms, **5**, 7 (2017). doi:10.3390/atoms5010007.
34. Z.L. Zhao, K. Wang, S. Li, R. Si, C.Y. Chen, Z.B. Chen, J. Yan, and Yu. Ralchenko. At. Data Nucl. Data Tables, **119**, 314 (2018). doi:10.1016/j.adt.2017.01.002.
35. G. Colonna and M. Capitelli. Spectrochim. Acta Part B, **64**, 863 (2009). doi:10.1016/j.sab.2009.07.002.
36. G. D'Ammando, G. Colonna, L.D. Pietanza, and M. Capitelli. Spectrochim. Acta Part B, **65**, 603 (2010). doi:10.1016/j.sab.2010.05.002.
37. O. Cardona, E. Simmoneau, and L. Crivellari. Rev. Mex. Fis. **51**, 476 (2005).
38. O. Cardona, E. Simmoneau, and L. Crivellari. ApJ, **690**, 1378 (2009). doi:10.1088/0004-637X/690/2/1378.
39. O. Cardona, M. Martinez-Arroyo, and M.A.L. Opez-Castillo. ApJ, **711**, 239 (2010). doi:10.1088/0004-637X/711/1/239.
40. S. Gordon and B.J. McBride. Computer program for calculation of complex chemical equilibrium compositions, rocket performance, incident and reflected shocks, and Chapman-Jouguet detonations. Technical Report No. SP-273. NASA (1976).
41. B.J. McBride, S. Gordon, and M.A. Reno. Coefficients for calculating thermodynamic and transport properties of individual species. Technical Memorandum No. TM-4513. NASA (1993).
42. L.V. Gurvich, I.V. Veyts, C.B. Alcock, and V.S. Iorish. Thermodynamic properties of individual substances. CRC, Boca Raton, Fla. (1994).
43. H.W. Drawin and P. Felenbok. Data for plasmas in local thermodynamic equilibrium. Gauthier-Villars (1965).
44. G. D'Ammando, G. Colonna, and M. Capitelli. Phys. Plasmas, **20**, 032108 (2013). doi:10.1063/1.4794286.
45. I.P. Grant, B.J. McKenzie, P.H. Norrington, D.F. Mayers, and N.C. Pyper. Comput. Phys. Commun. **21**, 207 (1980). doi:10.1016/0010-4655(80)90041-7.
46. F.A. Parpia, C.F. Fischer, and I.P. Grant. Comput. Phys. Commun. **94**, 249 (1996). doi:10.1016/0010-4655(95)00136-0.
47. J. Olsen, M.R. Godefroid, P. Jönsson, P.A. Malmqvist, and C.F. Fischer. Phys. Rev. E, **52**, 4499 (1995). doi:10.1103/PhysRevE.52.4499.
48. P. Jönsson, X. He, C.F. Fischer, and I.P. Grant. Comput. Phys. Commun. **177**, 597 (2007). doi:10.1016/j.cpc.2013.02.016.
49. B. Fricke. Phys. Scr. **T8**, 129 (1986). doi:10.1088/0031-8949/1984/T8/021.
50. M.F. Gu. Can. J. Phys. **86** (5), 675 (2008).
51. Z.B. Chen, K. Ma, H.W. Hu, and K. Wang. Phys. Plasmas, **25**, 052105 (2018).
52. Z.B. Chen, H.W. Hu, K. Ma, X.B. Liu, X.L. Guo, S. Li, B.H. Zhu, L. Huang, and K. Wang. Phys. Plasmas, **25**, 032108 (2018).
53. Yu. Ralchenko, I.N. Draganic, D. Osin, J.D. Gillaspay, and J. Reader. Phys. Rev. A, **83**, 032517 (2011). doi:10.1103/PhysRevA.83.032517.
54. J. Clementson and P. Beiersdorfer. Phys. Rev. A, **81**, 052509 (2010). doi:10.1103/PhysRevA.81.052509.
55. M. Capitelli, G. Colonna, and A. D'Angola. Fundamental aspects of plasma chemical physics: thermodynamics. Springer (2012).



Theoretical study of the atomic parameters, plasma parameters and photoionization of W LXIV

Richa Paijwar^a, Rinku Sharma

Department of Applied Physics, Delhi Technological University, New Delhi, Delhi 110042, India

Received: 21 June 2023 / Accepted: 27 November 2023

© The Author(s), under exclusive licence to Società Italiana di Fisica and Springer-Verlag GmbH Germany, part of Springer Nature 2023

Abstract We have presented atomic data including energies, transition wavelengths, radiative rates and oscillator strengths, which are evaluated for W LXIV, for the lowest 100 fine structure levels and multipole transitions ($E1$, $E2$, $M1$ and also for $M2$). For W LXIV, we identified the 21 in electric dipole, 33 in electric quadrupole, 28 in magnetic dipole and 21 in magnetic quadrupole soft x-ray (SXR) transitions, as well as 1 in electric dipole extreme ultraviolet (EUV) transitions from the ground state. Furthermore, we have analysed the photoionization cross section and ionization potential of $3s$, $3p$ and $3d$ levels of Na-like W at five different photoelectron energies by employing the FAC code. Line intensity ratios and electron density for W LXIV have also been reported, which will be useful and necessary for plasma diagnostics, including modelling for future International Thermonuclear Experimental Reactor (ITER) investigations. We assume that our observations will be useful for cell biology, biophysics, fusion plasma research, as well as astrophysical studies and their applications.

1 Introduction

The majority of attention in the field of fusion research has been on tungsten since it will serve as a plasma-facing material in impending massive tokamaks among future fusion reactors [1]. The ionization of multielectron tungsten ions during modern thermonuclear plasma investigations has been investigated because the thermonuclear reactor ITER uses tungsten as a material for its plasma-facing components [2]. Photoionization of tungsten atoms and ions is still of importance in the context of plasma, although it is not directly relevant to fusion research since it can reveal information about the spectroscopic properties of tungsten that are necessary for plasma diagnostics [3]. When there are a lot of strongly interacting, singly excited channels accessible to an outgoing electron, it might be challenging to calculate the photoionization cross section of an open-shell atom [4]. A highly sensitive spectroscopic method for examining the function of intermediate multiple excited states in photon–ion interactions, with implications for electron–ion recombination and the ionization processes, is the use of photoionization observations together with thorough theoretical computations [5]. The photon–ion merged-beams technology was used to measure the experimental cross sections on an absolute scale and large-scale close-coupling simulations using the Dirac–Coulomb R-matrix approximations provided the theoretical data for W-ion have been investigated by Muller et al. In our article on the outcomes for W + ions, we provide a thorough explanation of the procedure used to photoionize tungsten ions.

On Na-like W, some theoretical calculations and experimental measurements have been made in the past using a variety of experimental and theoretical methodologies. At the ASDEX upgrade to Tokamak, Pütterich et al. [6] performed an experimental study of tungsten ions. Tokamak. The ionization energies of the tungsten ions: W^{2+} through W^{71+} have been experimentally examined by E. Kramida et al. [7] using a semi-empirical technique based on scaled Hartree–Fock estimates of electron binding energies. Similarly, Kramida et al. [8] assembled experimental data between W^{2+} – W^{73+} to demonstrate the energy levels as well as spectral lines. Additionally, the theoretical and experimental work on tungsten spectroscopy has been reviewed by Kramida et al. [9]. Safronova et al. [10] used the relativistic Hartree–Fock approach of Cowan, relativistic many-body perturbation theory techniques, as well as relativistic multiconfiguration processes, which are employed at the Hebrew University Lawrence Livermore Atomic Code to calculate the energy levels, autoionization rates, radiative transition probabilities, dielectronic recombination rates and dielectronic satellite lines for excited states of Na-like to Ne-like W. Also, to use the hard x-ray spectra of Na-like W generated by dielectronic recombination, Safronova et al. [11] have explored the polarization of L-shell dielectronic satellite lines. Using Dirac–Fock electron wave functions, Trzhaskovskaya et al. [12] calculated the cross sections for photoionization and radiative recombination, including power loss rate coefficients in plasmas of W^{6+} – W^{71+} ions. In order to evaluate the energy balance of high-temperature plasmas, Beiersdorfer et al. [13] plasmas use dielectronic recombination resonances to illustrate the ionization balance among high Z ions or the

^a e-mail: richagautam2001@gmail.com (corresponding author)

fractional abundance of various charge states of a specific element. Similarly, by using the relativistic multireference Møller–Plesset method, Beiersdorfer et al. [14] have studied the $n = 3$ and $n = 2$ L-shell x-ray transitions using high-resolution crystal spectroscopy of neon-like W^{64+} . Li et al. [15] used the flexible atomic code to perform ab initio calculations on the dielectronic recombination rate coefficients of tungsten that are similar to those of Ne, Pd and Ag and these calculations included determining energy levels, radiative transition probabilities and autoionization rates. Large-scale estimation of the $n = 3-3$ transition energies for Ne- to Ar-like W was done by Chen et al. [16] used the relativistic no-pair Hamiltonian as a basis function, as well as finite B-spline orbitals in a cavity. QED with mass polarization corrections was also considered. In order to calculate the excitation cross sections for an electric and magnetic dipole for the quadrupole transitions for these ions, Dipti et al. [17] electron impact excitations from the ground-state L-shell, in particular $n = 2$ to $n = 3$ transitions in Mg via O-like tungsten. With the use of multiconfiguration Dirac–Fock and relativistic configuration interaction computations, including the Breit interaction calculations, Hu et al. [18] have presented energy levels as well as transition probabilities. The M- and L-shell transition cross sections for the tungsten ions W^{n+} ($n = 44-66$) have been estimated by Priti et al. [19] using a fully relativistic distorted wave technique.

Due to their astrophysical interest, high Z ion transitions in the extreme ultraviolet (EUV) and soft X-rays (SXR) have become the subject of real study interest [20]. They give detailed information about the sun and the coronal atmosphere. The interval between EUV (50 to 1200) Å as well as SXR (1–50) Å is where high Z ion lines generate the maximum number of lines. The ultraviolet (UV) to EUV along with soft x-ray emission lines from multiple charged ions are helpful because they provide an in-depth understanding of the coronal atmosphere [21] using methodologies of laser blow-off as well as impurity pellet injection [22]. EUV and SXR zones also have continuum emission from radiative recombination (free-bound) as well as bremsstrahlung (free–free), in addition to emission lines.

The importance of EUV and SXR transitions and their applications are described in many previous research papers. Every planet in the solar system, along with the dwarf planet Pluto as well as comets, has all been studied using EUV irradiance, which is widely utilized in planetary science [23]. Controlling the thermodynamics and chemistry of the Earth's upper atmosphere involves SXR and EUV bands [24]. Applying up to almost ten times higher gas pressures through a newly created piezoelectric valve resulted in increased target densities and consequently, higher laser energy conversion efficiencies into SXR and EUV radiation [25]. Zhang [26] made use of the multiple wavelength observations from the Atmospheric Imaging Assembly (AIA) on board the Solar Dynamics Observatory (SDO) in the EUV passbands. Microscopy at EUV or even shorter SXR wavelengths is quite popular because it directly enhances spatial resolution in photon-based imaging systems by reducing the illuminating wavelength [27–31]. EUV along with SXR reflect their multi-thermal structures [32]. Our knowledge of objects in universe, such as emission measurements, space structure, physical environment, morphology, heating mechanisms and other factors, has been greatly aided by EUV missions (such as Hinode, Chandra, XMM-Newton and SDO for solar physics) [33]. The experimental setups were equipped with EUV/SXR collectors for focusing the radiation onto the gas to be ionized, or the gas was injected nearby the laser-produced plasma (LPP) [34]. For instance, the National Aeronautics and Space Administration (NASA) uses EUV and SXR in its solar physics missions to investigate the Sun. Furthermore, a EUV microscope can capture images with nanometer-scale spatial resolution in just a few seconds. Looking at the physics of the laser interaction with the target, conversion effectiveness, debris generation and the procedures used to produce SXR and EUV radiation can help you understand how plasma is formed [35].

Tungsten ions that penetrate deep into the plasma would not be completely stripped due to the high Z element of tungsten ($Z = 74$), even with a hot core. Our second goal is to generate calculations when analysing the variation in plasma parameters among line intensity ratios, as W LXIV is critical for plasma diagnostics. Furthermore, there is no information in the literature about the photoionization cross section of W^{63+} and W^{64+} at the different photoelectron energies. Therefore, due to a lack of atomic data, modelling and characterizing plasma properties as well as making a comparison to existing experimental data is particularly challenging. In the future, these calculations should help analyse additional information from astrophysical sources as well as fusion plasma.

2 Theoretical procedure

2.1 Atomic structure calculations

FAC merges the advantages of these already-existing atomic codes with improvements in numerical techniques established to increase the potential, efficiency, as well as robustness of the programmes [36]. By M.F.Gu, fac is developed and it is based on Dirac–Hartree–Fock–Slater (DHFS). The source code and documentation are accessible to the general public at <http://kipac-tree.stanford.edu/fac>. With this approach, we used non-local exchange potential in place of potential. When the behaviour of the particles is in local potential, the interaction remains constant, whereas in non-local potential, particle behaviour also influences the interaction. Nuclear charge and electron–electron interaction contribute to the local potential involved in the FAC.

The Dirac–Coulomb Hamiltonian in the MCDF (multiconfiguration Dirac–Fock) technique can be represented for only an N electron atom or an ion as follows:

$$H = \sum_{i=1}^N H_D(i) + \sum_{i=1}^N \frac{1}{r_{ij}} \quad (1)$$

The single-electron Dirac Hamiltonian is $H_D(i)$ and an ASF (atomic state function) is used to estimate the specific wave function such an atomic state for an N electron atom or ion system in Eq. (1).

The linear combination of n electronic configuration state functions yields an atomic state function (ASF) for N electron atoms or ions that describes various fine structural states (CSFs).

$$|\Psi_\alpha(PJM)\rangle = \sum_{i=1}^N c_i(\alpha) |\gamma_i(PJM)\rangle \quad (2)$$

in which the ASFs satisfy the orthonormality criterion. α indicates the coupling, orbital occupation numbers, etc. CSFs called γ_i (PJM) specify a specific state with a specific parity. Also, (J, M) specified as angular momentum.

2.2 Photoionization cross section

One of the most fundamental interactions between radiation and matter is the photoionization of atoms, which plays a role in different scientific fields. More specifically, photoionization from excited states has several uses in radiative recombination, controlled thermonuclear research plasma, radiation protection and stellar atmospheres. As a result, measuring photoionization cross sections accurately from excited atomic states is a considerably more stimulating mission. In the presence of radiation emitted from the sun, processes such as photoexcitation, photoionization and recombination occur naturally all the time [37].

Being a highly charged ion and a simple electronic configuration of sodium their computed numbers may represent the background cross sections, their computation must go beyond a few core-ion excitations to show the behaviour at the core-ion thresholds on the background. The photoionization cross section should contain the same resonances, as the related or inverse processes impact excitation recombination. For a proper treatment of the photoionization process, several approaches of increasing sophistication have been adopted over the years. Photoionization cross sections calculated mainly in the hydrogenic or central field approximation accounted for the background cross section but not resonance [38].

The differential cross section ($\frac{d\sigma}{d\Omega}$) is the ratio of energy absorbed dP to the incident flux ($(1/4\pi)$) in the solid angle element ($d\Omega$), i.e.

$$\frac{d\sigma}{d\Omega} = \frac{dP}{(1/4\pi)d\Omega} = \frac{4\pi^3 c^2}{n_w w_{ij}^2} \frac{dT_{ij}}{d\Omega} \quad (3)$$

The partial photoionization cross section for a transition from level j of the $(N+1)$ electron system to level i of the N electron system in terms of weighted differential oscillator strength is derived using the relativistic distorted wave technique as:

$$\sigma_{PI} = 2\pi\alpha \frac{df}{dE} \quad (4)$$

where α stands for the fine structure constant.

Calculating the Dirac equation using the Dirac–Fock–Slater potential obtains all bound and free orbitals [39].

Rydberg series of levels play a crucial role in atomic processes.

$$\text{Rydberg formula } E_{\text{res}} = E_c - z^2/v_c^2 = E_c - \frac{z^2}{(n - \mu_I)^2} \quad (5)$$

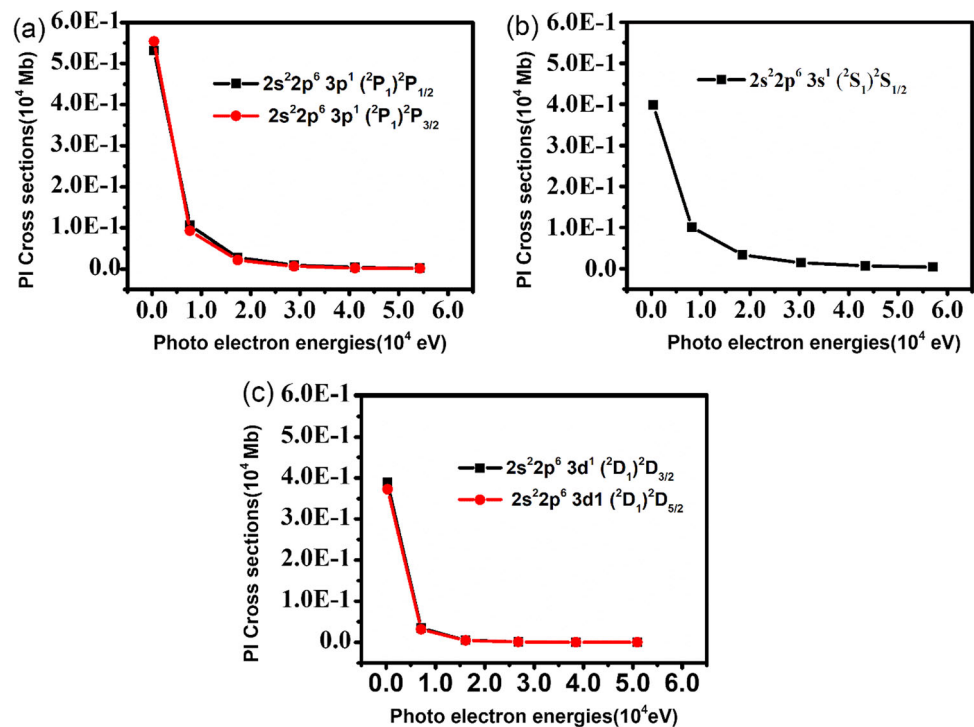
where E_c is an excited state of the residual ion X_c , also referred to as the ‘core’ ion, left behind as the doubly excited autoionizing state breaks up. For all atoms and ions, provided the outer electron is in sufficiently high- n state, i.e. sufficiently far away from all the inner electrons so as to experience only the residual charge z . However, the amount of screening depends on the orbital symmetry via the orbital angular momentum. Assuming that there are no other potentials involved, μ is a unique positive constant for each l .

The states of an electron in or with an atom to be bound, when the ground or excited discrete energies are negative, that is, lie below the first ionization threshold or energy of the ground state of the ionized core. Excited state ionization energies E_i are measured relative to the ionization threshold $E = 0$, when the electron has zero energy and becomes free. The ionization energies of the outermost electron(s) in excited states are lower than those of the ground state. Excitation of a bound state to another bound state may occur due to impact by other particles or photons. The bound electron(s) in the ion may be excited, or ionized, by the free electrons. Since the ionized electron may have any energy, there is an infinite continuum of positive (kinetic) energies $E > 0$ above the ionization threshold at $E = 0$, where no ‘pure’ bound states can exist. Here, the meaning of the term ‘continuum state’ of an (e + ion) system, with a free electron and an ion, needs to be understood. The state refers to a continuum of kinetic energies, which the free electron may have, but the total (e + ion) energy is relative to a specific bound state of the ion, usually the ground state (38).

Table 1 Photoionization cross section (in 10^2 Mb) and ionization potential (I.P. in eV) of Na-like W at five photoelectron energies (in 10^4 eV), from which the ground state of W^{64+} is $1s^2 2s^2 2p^6$

Energies (10^4 eV) \rightarrow	0.0356	0.8162	1.8449	3.0372	4.3354	5.7048	Ionization potential (eV) \downarrow	Ionization potential (eV) NIST \downarrow
$2s^2 2p^6 3s^1 ({}^2S_1) {}^2S_{1/2}$	3.98E-01	1.01E-01	3.36E-02	1.40E-02	6.87E-03	3.75E-03	7131.0	7131.0
Energies (10^4 eV) \rightarrow	0.0392	0.7673	1.7405	2.8751	4.1156	5.4275	–	–
$2s^2 2p^6 3p^1 ({}^2P_1) {}^2P_{1/2}$	5.31E-01	1.06E-01	2.77E-02	9.28E-03	3.75E-03	1.75E-03	6971.1	6970.4
$2s^2 2p^6 3p^1 ({}^2P_1) {}^2P_{3/2}$	5.54E-01	9.26E-02	2.15E-02	6.63E-02	2.25E-03	1.12E-03	6597.2	6596
Energies (10^4 eV) \rightarrow	0.0318	0.7091	1.6157	2.6809	3.8516	5.0942	–	–
$2s^2 2p^6 3d^1 ({}^2D_1) {}^2D_{3/2}$	3.89E-01	3.50E-02	5.06E-03	1.08E-03	3.08E-04	1.08E-04	6410.2	6409.3
$2s^2 2p^6 3d^1 ({}^2D_1) {}^2D_{5/2}$	3.72E-01	3.16E-02	4.41E-03	9.14E-04	2.53E-04	8.73E-05	6325.2	6324.4

Fig. 1 Graph between photoionization cross section (in 10^2 Mb) at five different photoelectron energies (in 10^4 eV)



In Table 1, we have analysed the photoionization cross section and ionization potential of $3s$, $3p$ and $3d$ levels of Na-like W at five different photoelectron energies by employing the FAC code and compare our estimated ionization potential from the FAC code with the ionization potential from the National Institute of Standards and Technology (NIST) database of Na-like W. FAC calculates cross sections in a single-channel approximations which cannot produce the naturally existing resonances. In the absence of consideration of any coupling of channels resulting in mixing resonant features in photoionization cross-sections are not expected to provide the precise values. Figure 1 represents the graph between photoionization cross section (10^2 Mb) at five different photoelectron energies (10^4 eV).

2.3 Computation procedure

In order to obtain accurate results for W^{63+} (Na-like tungsten) as we have chosen the following method:

Firstly, we have provided energy for levels $2p^5 3l nl'$ with $3 \leq n \leq 5$, $2p^5 4l 4l'$ excitations among one electron as of the $2p$ subshell to additional high subshells and $2s2p^6 3l nl'$ with $3 \leq n \leq 5$, $2s2p^6 4l 4l'$ excitations of one electron as of the $2s$ subshell to additional high subshell configurations accompanying oscillator strengths, transition wavelengths, line strengths, as well as transition probabilities for magnetic ($M1$) and electric ($E1$) dipole transitions from the ground state for W LXIV.

3 Results and discussion

3.1 Energy levels

For highly stripped ions, electronic interaction is required to determine precise and comprehensive atomic data, such as energy levels, transition wavelength and oscillator strength. A carefully selected configuration expansion depends on the calculation of accuracy. Since there have only been a few theoretical and experimental research on the photoionization of W ions up till now, the theoretical investigation and analysis of the atomic properties as well as the spectra of the W^{63+} ion are particularly interesting and significant for the curiosity in the investigation of tungsten ions. The atomic characteristics of the W^{63+} ion were therefore examined in this work. A comparison between our calculated energy values with other literature energies and NIST (in Ryd) is shown in Table 2, and the energies (in Ryd.) with spectroscopic notation of lowest 100 fine structure levels of W LXIV are shown in Table 3. We used atomic modelling with 12 configurations in our VV correlation generated in the form of $2p^6 nl$ ($3 \leq n \leq 5$ and $0 \leq l \leq 4$) and 21 levels are included in this process. Additionally, for CV correlation we have taken $2p^5 3l nl'$ with $3 \leq n \leq 5$, $2p^5 4l 4l'$, $2s2p^6 3l nl'$ with $3 \leq n \leq 5$, $2s2p^6 4l 4l'$ configurations are taken into account and generated 2700 fine structure levels, which are obtained by single as well as double excitations from the ground state. We have limited the modelling of configurations to $n = 5$ orbitals for conciseness.

Table 2 A comparison between our calculated energy values with other literature energies and NIST (in Ryd)

Level	Configurations	NIST [50]	FAC	GRASP REF [46]	FAC REF [46]	MCDF REF [47]	MCDF REF [8]	RBMT REF [4]	HULLAC REF [48]	COWAN REF [49]
1	$2s^2 2p^6 3s^1$ (2S_1) $^2S_{1/2}$	0.0000	0.0000	0.0000	0.0000	0.0000	0.0000	0.0000	0.0000	0.0000
2	$2s^2 2p^6 3p^1$ (2P_1) $^2P_{1/2}$	11.7280	11.7493	11.8989	11.7457	11.7370	11.7238	11.7371	11.8918	10.9897
3	$2s^2 2p^6 3p^1$ (2P_1) $^2P_{3/2}$	39.189	39.2334	39.3365	39.2218	39.2267	39.1927	39.2068	39.3315	39.8862
4	$2s^2 2p^6 3d^1$ (2D_1) $^2D_{3/2}$	52.969	52.9815	53.1127	52.9352	53.0081	52.9545	52.9674	53.1316	52.3155
5	$2s^2 2p^6 3d^1$ (2D_1) $^2D_{5/2}$	59.210	59.2312	59.3372	59.1730	59.2605	59.2393	59.2288	59.3547	58.9189
6	$2s^2 2p^6 4s^1$ (2S_1) $^2S_{1/2}$	239.1	239.0101	239.0661	238.9973	239.2723				
7	$2s^2 2p^6 4p^1$ (2P_1) $^2P_{1/2}$	243.9	243.8679	243.9788	243.8505	244.0685				
8	$2s^2 2p^6 4p^1$ (2P_1) $^2P_{3/2}$	255.2	255.1180	255.2154	255.0981	255.3387				
9	$2s^2 2p^6 4d^1$ (2D_1) $^2D_{3/2}$	260.4	260.3343	260.4510	260.3002	260.5362				
10	$2s^2 2p^6 4s^1$ (2D_1) $^2D_{5/2}$	263.1	263.0348	263.1426	262.9954	263.2625				
11	$2s^2 2p^6 4f^1$ (2F_1) $^2F_{5/2}$	265.9	265.7614	265.8618	265.7361	266.0983				
12	$2s^2 2p^6 4f^1$ (2F_1) $^2F_{7/2}$	267.1	266.9432	267.0446	266.9176	267.2928				
13	$2s^2 2p^6 5s^1$ (2S_1) $^2S_{1/2}$	–	345.3396	345.5593	345.3305	–				
14	$2s^2 2p^6 5p^1$ (2P_1) $^2P_{1/2}$	–	347.7801	348.0234	347.7664	–				
15	$2s^2 2p^6 5p^1$ (2P_1) $^2P_{3/2}$	–	353.4352	353.6728	353.4209	–				
16	$2s^2 2p^6 5d^1$ (2D_1) $^2D_{3/2}$	–	355.9884	356.2383	355.9695	–				
17	$2s^2 2p^6 5d^1$ (2D_1) $^2D_{5/2}$	357.5	357.3798	357.6240	357.3573	357.7642				
18	$2s^2 2p^6 5f^1$ (2F_1) $^2F_{5/2}$	358.8	358.7291	358.9640	358.7180	359.0589				
19	$2s^2 2p^6 5f^1$ (2F_1) $^2F_{7/2}$	359.5	359.3365	359.5722	359.3256	359.6882				
20	$2s^2 2p^6 5g^1$ (2G_1) $^2G_{7/2}$	359.8	359.5308	359.7585	359.5057	359.9799				
21	$2s^2 2p^6 5g^1$ (2G_1) $^2G_{9/2}$	360.1	359.8911	360.1191	359.8662	360.3447				

3.2 Radiative rates (wavelengths, oscillator strengths and transition rates)

For various radiative channels, the line strength (S_{ij}) and oscillator strength (f_{ij}) are as follows:

$$\text{for } E1 \text{ transitions : } A_{ji} = \frac{2.0261 \times 10^{18}}{\omega_j \lambda_{ji}^3} S_{ij} \text{ and } f_{ij} = \frac{303.75}{\lambda_{ji} \omega_i} S_{ij}, \quad (6)$$

$$\text{for } M1 \text{ transitions : } A_{ji} = \frac{2.6974 \times 10^{13}}{\omega_j \lambda_{ji}^3} S_{ij} \text{ and } f_{ij} = \frac{4.044 \times 10^{-3}}{\lambda_{ji} \omega_i} S_{ij}, \quad (7)$$

Table 3 Energies (in Ryd.) of lowest 100 fine structure levels of W LXIV

Level	Configurations	Parity	FAC(Ryd)	NIST(Ryd) [50]	ΔE
1	$2s^2 2p^6 3s^1 ({}^2S_1) {}^2S_{1/2}$	Even	0.0000	0.0000	0.00
2	$2s^2 2p^6 3p^1 ({}^2P_1) {}^2P_{1/2}$	Odd	11.7493	11.7280	1.06
3	$2s^2 2p^6 3p^1 ({}^2P_1) {}^2P_{3/2}$	Odd	39.2334	39.189	0.21
4	$2s^2 2p^6 3d^1 ({}^2D_1) {}^2D_{3/2}$	Even	52.9815	52.969	0.20
5	$2s^2 2p^6 3d^1 ({}^2D_1) {}^2D_{5/2}$	Even	59.2312	59.210	0.13
6	$2s^2 2p^6 4s^1 ({}^2S_1) {}^2S_{1/2}$	Even	239.0101	239.1	0.04
7	$2s^2 2p^6 4p^1 ({}^2P_1) {}^2P_{1/2}$	Odd	243.8679	243.9	0.06
8	$2s^2 2p^6 4p^1 ({}^2P_1) {}^2P_{3/2}$	Odd	255.1180	255.2	0.05
9	$2s^2 2p^6 4d^1 ({}^2D_1) {}^2D_{3/2}$	Even	260.3343	260.4	0.06
10	$2s^2 2p^6 4s^1 ({}^2D_1) {}^2D_{5/2}$	Even	263.0348	263.1	0.05
11	$2s^2 2p^6 4f^1 ({}^2F_1) {}^2F_{5/2}$	Odd	265.7614	265.9	0.04
12	$2s^2 2p^6 4f^1 ({}^2F_1) {}^2F_{7/2}$	Odd	266.9432	267.1	0.04
13	$2s^2 2p^6 5s^1 ({}^2S_1) {}^2S_{1/2}$	Even	345.3396	–	0.04
14	$2s^2 2p^6 5p^1 ({}^2P_1) {}^2P_{1/2}$	Odd	347.7801	–	0.05
15	$2s^2 2p^6 5p^1 ({}^2P_1) {}^2P_{3/2}$	Odd	353.4352	–	0.05
16	$2s^2 2p^6 5d^1 ({}^2D_1) {}^2D_{3/2}$	Even	355.9884	–	0.05
17	$2s^2 2p^6 5d^1 ({}^2D_1) {}^2D_{5/2}$	Even	357.3798	357.5	0.05
18	$2s^2 2p^6 5f^1 ({}^2F_1) {}^2F_{5/2}$	Odd	358.7291	358.8	0.05
19	$2s^2 2p^6 5f^1 ({}^2F_1) {}^2F_{7/2}$	Odd	359.3365	359.5	0.05
20	$2s^2 2p^6 5g^1 ({}^2G_1) {}^2G_{7/2}$	Even	359.5308	359.8	0.04
21	$2s^2 2p^6 5g^1 ({}^2G_1) {}^2G_{9/2}$	Even	359.8911	360.1	0.04
22	$2s^2 2p^5 3s^2 ({}^1S_0) {}^2P_{3/2}$	Odd	606.9790		
23	$2s^2 2p^5 3s^1 3p^1 ({}^2P_1) {}^4P_{3/2}$	Even	616.1585		
24	$2s^2 2p^5 3s^1 3p^1 ({}^2P_1) {}^4D_{5/2}$	Even	617.2351		
25	$2s^2 2p^5 3s^1 3p^1 ({}^2P_1) {}^2D_{3/2}$	Even	617.6222		
26	$2s^2 2p^5 3s^1 3p^1 ({}^2P_1) {}^2P_{3/2}$	Even	617.8084		
27	$2s^2 2p^5 3p^2 ({}^3P_2) {}^4D_{3/2}$	Odd	629.6193		
28	$2s^2 2p^5 3s^1 3p^1 ({}^2P_1) {}^4D_{7/2}$	Even	643.4528		
29	$2s^2 2p^5 3s^1 3p^1 ({}^2P_1) {}^4S_{3/2}$	Even	644.0812		
30	$2s^2 2p^5 3s^1 3p^1 ({}^2P_1) {}^4P_{5/2}$	Even	644.5490		
31	$2s^2 2p^5 3s^1 3p^1 ({}^2P_1) {}^2S_{1/2}$	Even	645.3077		
32	$2s^2 2p^5 3s^1 3p^1 ({}^2P_1) {}^2D_{5/2}$	Even	646.6930		
33	$2s^2 2p^5 3s^1 3p^1 ({}^2P_1) {}^2P_{3/2}$	Even	647.2673		
34	$2s^2 2p^5 3s^1 3p^1 ({}^2P_1) {}^2S_{1/2}$	Even	650.1377		
35	$2s^2 2p^5 3p^2 ({}^3P_2) {}^4P_{1/2}$	Odd	655.7743		
36	$2s^2 2p^5 3p^2 ({}^3P_2) {}^4P_{5/2}$	Odd	655.8282		
37	$2s^2 2p^5 3p^2 ({}^1D_2) {}^2F_{7/2}$	Odd	655.8962		
38	$2s^2 2p^5 3p^2 ({}^1D_2) {}^2P_{3/2}$	Odd	655.9289		
39	$2s^2 2p^5 3p^2 ({}^1D_2) {}^2D_{5/2}$	Odd	656.7224		
40	$2s^2 2p^5 3p^2 ({}^3P_2) {}^2D_{3/2}$	Odd	656.8221		
41	$2s^2 2p^5 3s^1 3d^1 ({}^2D_1) {}^4P_{1/2}$	Odd	657.4354		
42	$2s^2 2p^5 3s^1 3d^1 ({}^2D_1) {}^2D_{3/2}$	Odd	658.2976		
43	$2s^2 2p^5 3s^1 3d^1 ({}^2D_1) {}^4P_{3/2}$	Odd	658.4006		
44	$2s^2 2p^5 3s^1 3d^1 ({}^2D_1) {}^2P_{1/2}$	Odd	658.6996		
45	$2s^2 2p^5 3s^1 3d^1 ({}^2D_1) {}^4F_{7/2}$	Odd	659.0358		
46	$2s^2 2p^5 3s^1 3d^1 ({}^2D_1) {}^2D_{3/2}$	Odd	659.7364		
47	$2s^2 2p^5 3s^1 3d^1 ({}^2D_1) {}^2F_{5/2}$	Odd	659.8185		
48	$2s^2 2p^5 3p^2 ({}^1D_2) {}^2P_{1/2}$	Odd	661.9999		

Table 3 continued

Level	Configurations	Parity	FAC(Ryd)	NIST(Ryd) [50]	ΔE
49	$2s^2 2p^5 3s^1 3d^1 (^2D_1) ^4F_{9/2}$	Odd	663.9801		
50	$2s^2 2p^5 3s^1 3d^1 (^2D_1) ^4P_{5/2}$	Odd	664.8790		
51	$2s^2 2p^5 3s^1 3d^1 (^2D_1) ^4D_{7/2}$	Odd	665.3981		
52	$2s^2 2p^5 3s^1 3d^1 (^2D_1) ^2D_{3/2}$	Odd	665.7569		
53	$2s^2 2p^5 3s^1 3d^1 (^2D_1) ^2F_{7/2}$	Odd	665.8743		
54	$2s^2 2p^5 3s^1 3d^1 (^2D_1) ^2D_{5/2}$	Odd	666.7686		
55	$2s^2 2p^5 3p^1 3d^1 (^2D_1) ^4D_{1/2}$	Even	667.7302		
56	$2s^2 2p^5 3s^1 3d^1 (^2D_1) ^2P_{3/2}$	Odd	668.0052		
57	$2s^2 2p^5 3p^1 3d^1 (^2D_1) ^4D_{3/2}$	Even	668.3914		
58	$2s^2 2p^5 3s^1 3d^1 (^2D_1) ^2P_{1/2}$	Odd	668.3984		
59	$2s^2 2p^5 3p^1 3d^1 (^2D_1) ^4G_{7/2}$	Even	668.4765		
60	$2s^2 2p^5 3s^1 3d^1 (^2D_1) ^4F_{5/2}$	Even	668.8146		
61	$2s^2 2p^5 3p^1 3d^1 (^2D_1) ^4P_{1/2}$	Even	670.6091		
62	$2s^2 2p^5 3p^1 3d^1 (^2D_1) ^4F_{5/2}$	Even	671.0050		
63	$2s^2 2p^5 3p^1 3d^1 (^2D_1) ^4D_{3/2}$	Even	671.3865		
64	$2s^2 2p^5 3p^1 3d^1 (^2D_1) ^4D_{7/2}$	Even	675.6948		
65	$2s^2 2p^5 3p^1 3d^1 (^2D_1) ^4G_{9/2}$	Even	676.0153		
66	$2s^2 2p^5 3p^1 3d^1 (^2D_1) ^2P_{3/2}$	Even	676.2796		
67	$2s^2 2p^5 3p^1 3d^1 (^2D_1) ^2F_{5/2}$	Even	676.4676		
68	$2s^2 2p^5 3p^1 3d^1 (^2D_1) ^4P_{5/2}$	Even	676.9706		
69	$2s^2 2p^5 3p^1 3d^1 (^2D_1) ^2F_{7/2}$	Even	677.2248		
70	$2s^2 2p^5 3p^1 3d^1 (^2D_1) ^2P_{1/2}$	Even	679.1841		
71	$2s^2 2p^5 3p^1 3d^1 (^2D_1) ^2D_{3/2}$	Even	679.2955		
72	$2s^2 2p^5 3p^2 (3p^1) ^2S_{1/2}$	Odd	684.4237		
73	$2s^2 2p^5 3p^2 (3p^1) ^4D_{7/2}$	Odd	684.4358		
74	$2s^2 2p^5 3p^2 (^3P_2) ^2D_{5/2}$	Odd	684.4758		
75	$2s^2 2p^5 3p^2 (^1S_0) ^2P_{3/2}$	Odd	686.4124		
76	$2s^2 2p^5 3p^2 (^3P_2) ^2P_{3/2}$	Odd	688.4842		
77	$2s^2 2p^5 3p^1 3d^1 (^2D_1) ^4P_{3/2}$	Even	696.6554		
78	$2s^2 2p^5 3p^1 3d^1 (^2D_1) ^2P_{1/2}$	Even	697.0092		
79	$2s^2 2p^5 3p^1 3d^1 (^2D_1) ^4D_{5/2}$	Even	697.1176		
80	$2s^2 2p^5 3p^1 3d^1 (^2D_1) ^4F_{7/2}$	Even	697.1226		
81	$2s^2 2p^5 3p^1 3d^1 (^2D_1) ^2F_{5/2}$	Even	697.4420		
82	$2s^2 2p^5 3p^1 3d^1 (^2D_1) ^2D_{3/2}$	Even	697.5096		
83	$2s^2 2p^5 3p^1 3d^1 (^2D_1) ^2G_{9/2}$	Even	697.5959		
84	$2s^2 2p^5 3p^1 3d^1 (^2D_1) ^4D_{3/2}$	Even	698.4236		
85	$2s^2 2p^5 3p^1 3d^1 (^2D_1) ^4D_{5/2}$	Even	698.6454		
86	$2s^2 2p^5 3p^1 3d^1 (^2D_1) ^4P_{1/2}$	Even	698.6805		
87	$2s^2 2p^5 3p^1 3d^1 (^2D_1) ^2F_{7/2}$	Even	698.7712		
88	$2s^2 2p^5 3p^1 3d^1 (^2D_1) ^4G_{1/2}$	Even	701.8904		
89	$2s^2 2p^5 3p^1 3d^1 (^2D_1) ^2D_{3/2}$	Even	702.5486		
90	$2s^2 2p^5 3p^1 3d^1 (^2D_1) ^2F_{7/2}$	Even	702.7298		
91	$2s^2 2p^5 3p^1 3d^1 (^2D_1) ^2D_{5/2}$	Even	703.2169		
92	$2s^2 2p^5 3p^1 3d^1 (^2D_1) ^4F_{9/2}$	Even	703.6215		
93	$2s^2 2p^5 3p^1 3d^1 (^2D_1) ^4D_{7/2}$	Even	703.8673		
94	$2s^2 2p^5 3p^1 3d^1 (^2D_1) ^2P_{3/2}$	Even	704.0300		
95	$2s^2 2p^5 3p^1 3d^1 (^2D_1) ^2G_{9/2}$	Even	704.6175		
96	$2s^2 2p^5 3p^1 3d^1 (^2D_1) ^2P_{1/2}$	Even	704.9477		

Table 3 continued

Level	Configurations	Parity	FAC(Ryd)	NIST(Ryd) [50]	ΔE
97	$2s^2 2p^5 3p^1 3d^1 (^2D_1) ^4D_{7/2}$	Even	705.1930		
98	$2s^2 2p^5 3p^1 3d^1 (^2D_1) ^2D_{5/2}$	Even	705.7649		
99	$2s^2 2p^5 3p^1 3d^1 (^2D_1) ^2P_{3/2}$	Even	706.5673		
100	$2s^2 2p^5 3p^1 3d^1 (^2D_1) ^2D_{5/2}$	Even	707.1703		

Table 4 The radiative data of $E1$, $E2$, $M1$ and $M2$ transitions of W LXIV

Transitions	Lower level (i)	Upper level (j)	λ_{ji} (in Å)	A_{ji} (in s^{-1})	f_{ij}	S_{ij} (in a.u.)	Vel/len
E1	1	2	76.747	4.4554E+10	3.9343E-02	1.9881E-02	0.960
E1	1	3	23.178	1.7543E+12	2.8259E-01	4.3126E-02	1.000
E1	1	7	3.735	6.3048E+13	1.3182E-01	3.2414E-03	1.000
E1	1	8	3.570	3.9237E+13	1.4996E-01	3.5250E-03	1.000
E1	1	14	2.619	3.5715E+13	3.6724E-02	6.3325E-04	0.970
E1	1	15	2.577	2.5350E+13	5.0480E-02	8.5656E-04	0.940
E1	1	22	1.502	1.1244E+14	7.6023E-02	7.5167E-04	0.990
E1	1	27	1.447	1.1757E+12	7.3815E-04	7.0330E-06	1.000
E1	1	35	1.389	1.0951E+12	3.1689E-04	2.8987E-06	1.000
E1	1	38	1.389	2.8606E+13	1.6551E-02	1.5138E-04	0.990
E1	1	40	1.387	8.0418E+12	4.6402E-03	4.2383E-05	0.980
E1	1	41	1.386	1.1583E+13	3.3361E-03	3.0445E-05	0.980
E1	1	42	1.384	3.0323E+13	1.7420E-02	1.5877E-04	0.980
E1	1	44	1.383	8.8377E+13	2.5355E-02	2.3094E-04	0.990
E1	1	46	1.381	1.6360E+12	9.3580E-04	8.5103E-06	0.970
E1	1	48	1.376	2.0595E+14	5.8485E-02	5.2999E-04	0.970
E1	1	52	1.369	2.7912E+13	1.5673E-02	1.4123E-04	0.990
E1	1	56	1.364	2.7490E+15	1.5338E+00	1.3777E-02	0.980
E1	1	58	1.363	2.5475E+15	7.0969E-01	6.3698E-03	0.980
E1	1	72	1.331	1.4429E+13	3.8338E-03	3.3606E-05	0.970
E1	1	75	1.328	1.1814E+11	6.2423E-05	5.4561E-07	0.670
E1	1	76	1.324	3.4509E+12	1.8124E-03	1.5793E-05	1.100
E2	1	4	17.166	1.4053E+08	1.2417E-05	7.4823E-04	1.000
E2	1	5	15.364	2.5612E+08	2.7193E-05	1.1749E-03	1.000
E2	1	9	3.498	4.3608E+11	1.6003E-03	8.1625E-04	1.000
E2	1	10	3.463	4.3340E+11	2.3372E-03	1.1560E-03	1.000
E2	1	16	2.559	2.1579E+11	4.2354E-04	8.4502E-05	0.880
E2	1	17	2.549	2.2623E+11	6.6089E-04	1.3033E-04	0.880
E2	1	23	1.479	3.1670E+11	2.0769E-04	8.0031E-06	0.990
E2	1	24	1.476	8.6218E+11	8.4518E-04	3.2397E-05	0.990
E2	1	25	1.475	6.5200E+11	4.2558E-04	1.6283E-05	0.990
E2	1	29	1.415	9.9118E+10	5.9495E-05	2.0074E-06	0.990
E2	1	30	1.414	7.7802E+11	6.9950E-04	2.3551E-05	0.990
E2	1	32	1.409	1.5462E+11	1.3809E-04	4.6031E-06	1.000
E2	1	33	1.408	7.3562E+11	4.3722E-04	1.4536E-05	0.990
E2	1	57	1.363	4.2367E+07	2.3602E-08	7.1205E-10	1.200
E2	1	60	1.362	1.0880E+09	9.0801E-07	2.7342E-08	1.000
E2	1	62	1.358	4.7445E+09	3.9339E-06	1.1730E-07	1.000
E2	1	63	1.357	1.1397E+09	6.2924E-07	1.8731E-08	0.990
E2	1	66	1.347	1.1239E+07	6.1164E-09	1.7816E-10	1.300
E2	1	67	1.347	4.1307E+07	3.3701E-08	9.8086E-10	0.780
E2	1	68	1.346	1.9403E+09	1.5807E-06	4.5902E-08	1.000
E2	1	71	1.341	1.7261E+08	9.3102E-08	2.6760E-09	2.200

Table 4 continued

Transitions	Lower level (<i>i</i>)	Upper level (<i>j</i>)	λ_{ji} (in Å)	A_{ji} (in s^{-1})	f_{ij}	S_{ij} (in a.u.)	Vel/len
E2	1	77	1.308	1.3554E+08	6.9511E-08	1.8524E-09	1.100
E2	1	79	1.307	5.2172E+08	4.0082E-07	1.0660E-08	0.930
E2	1	81	1.306	1.4802E+09	1.1361E-06	3.0175E-08	1.100
E2	1	82	1.306	3.4839E+08	1.7820E-07	4.7295E-09	1.000
E2	1	84	1.305	4.8202E+08	2.4597E-07	6.5053E-09	0.960
E2	1	85	1.304	1.1516E+08	8.8081E-08	2.3270E-09	0.880
E2	1	89	1.297	1.4218E+08	7.1664E-08	1.8606E-09	1.400
E2	1	91	1.296	1.9374E+08	1.4629E-07	3.7906E-09	1.200
E2	1	94	1.294	1.2902E+09	6.4794E-07	1.6731E-08	1.000
E2	1	98	1.291	1.6724E+09	1.2536E-06	3.2132E-08	1.200
E2	1	99	1.290	2.1006E+09	1.0474E-06	2.6756E-08	0.970
E2	1	100	1.289	1.2428E+09	9.2795E-07	2.3644E-08	0.710
M1	1	4	17.166	1.4712E+04	1.2999E-09	1.1035E-05	
M1	1	6	3.811	5.8203E+07	1.2675E-07	2.3890E-04	
M1	1	9	3.498	8.1552E+05	3.3597E-09	5.8128E-06	
M1	1	13	2.638	6.5816E+07	6.8646E-08	8.9542E-05	
M1	1	16	2.559	1.1779E+06	2.3120E-09	2.9254E-06	
M1	1	23	1.479	1.9008E+10	1.2466E-05	9.1173E-03	
M1	1	25	1.475	1.1398E+10	7.4400E-06	5.4287E-03	
M1	1	26	1.475	2.8236E+10	9.2095E-06	6.7178E-03	
M1	1	29	1.415	8.4942E+09	5.0986E-06	3.5676E-03	
M1	1	31	1.412	1.1438E+10	3.4198E-06	2.3883E-03	
M1	1	33	1.408	5.7384E+08	3.4106E-07	2.3747E-04	
M1	1	34	1.402	8.6983E+08	2.5620E-07	1.7760E-04	
M1	1	55	1.364	2.9979E+06	8.3672E-10	5.6459E-07	
M1	1	57	1.363	1.2265E+06	6.8325E-10	4.6058E-07	
M1	1	61	1.359	8.8377E+07	2.4455E-08	1.6430E-05	
M1	1	63	1.357	3.1638E+06	1.7468E-09	1.1723E-06	
M1	1	66	1.347	7.0480E+06	3.8356E-09	2.5555E-06	
M1	1	70	1.342	1.0365E+07	2.7964E-09	1.8552E-06	
M1	1	71	1.341	3.7020E+05	1.9968E-10	1.3245E-07	
M1	1	77	1.308	4.5800E+06	2.3489E-09	1.5192E-06	
M1	1	78	1.307	7.3445E+05	1.8815E-10	1.2163E-07	
M1	1	82	1.306	5.1443E+06	2.6312E-09	1.6995E-06	
M1	1	84	1.305	1.0770E+06	5.4960E-10	3.5458E-07	
M1	1	86	1.304	1.0297E+07	2.6246E-09	1.6924E-06	
M1	1	89	1.297	2.5492E+05	1.2849E-10	8.2386E-08	
M1	1	94	1.294	2.2367E+06	1.1233E-09	7.1894E-07	
M1	1	96	1.293	2.1280E+07	5.3296E-09	3.4067E-06	
M1	1	99	1.290	1.0619E+04	5.2948E-12	3.3767E-09	
M2	1	3	23.178	3.6324E+05	5.8511E-08	6.5184E-01	
M2	1	8	3.570	3.3835E+08	1.2931E-06	5.2647E-02	
M2	1	11	3.427	7.5974E+03	4.0140E-11	1.4459E-06	
M2	1	15	2.577	4.1691E+08	8.3021E-07	1.2713E-02	
M2	1	18	2.539	3.6919E+03	7.8056E-12	1.1432E-07	
M2	1	22	1.502	5.2225E+09	3.5311E-06	1.0698E-02	
M2	1	27	1.447	1.5910E+07	2.2546E-08	6.1124E-05	
M2	1	36	1.389	1.2562E+07	1.0903E-08	2.6149E-05	
M2	1	38	1.389	1.5591E+09	9.0207E-07	2.1634E-03	
M2	1	39	1.388	6.6038E+07	5.7177E-08	1.3664E-04	
M2	1	40	1.387	8.5484E+07	4.9325E-08	1.1781E-04	

Table 4 continued

Transitions	Lower level (<i>i</i>)	Upper level (<i>j</i>)	λ_{ji} (in Å)	A_{ji} (in s^{-1})	f_{ij}	S_{ij} (in a.u.)	Vel/len
M2	1	42	1.384	1.3263E+09	7.6192E-07	1.8079E-03	
M2	1	43	1.384	6.3659E+07	5.4842E-08	1.3008E-04	
M2	1	46	1.381	2.6312E+09	1.5050E-06	3.5480E-03	
M2	1	47	1.381	1.9916E+09	1.7083E-06	4.0255E-03	
M2	1	50	1.371	1.1575E+11	9.7792E-05	2.2526E-01	
M2	1	52	1.369	1.1122E+11	6.2455E-05	1.4321E-01	
M2	1	54	1.367	5.8300E+08	4.8974E-07	1.1185E-03	
M2	1	56	1.364	1.1031E+09	6.1551E-07	1.3979E-03	
M2	1	74	1.331	3.3615E+07	2.6792E-08	5.6550E-05	
M2	1	75	1.328	1.7976E+07	9.4980E-09	1.9879E-05	
M2	1	76	1.324	3.5272E+08	1.8524E-07	3.8419E-04	

$$\text{for } E2 \text{ transitions : } A_{ji} = \frac{1.1199 \times 10^{18}}{w_j \lambda_{ji}^5} S_{ij} \text{ and } f_{ij} = \frac{167.89}{\lambda_{ji}^3 \omega_i} S_{ij}, \quad (8)$$

$$\text{for } M2 \text{ transitions : } A_{ji} = \frac{1.4910 \times 10^{13}}{\omega_j \lambda_{ji}^5} S_{ij} \text{ and } f_{ij} = \frac{2.236 \times 10^{-3}}{\lambda_{ji}^3 \omega_i} S_{ij}. \quad (9)$$

In Eqs. (6, 7, 8 and 9), transition wavelength is λ_{ij} in Å and ω_j and ω_i stand for the upper and lower levels of statistical weight, accordingly. For W LXIV, we identified 21 *E1*, 33 *E2*, 28 *M1* and 21 *M2* SXR transitions from Table 4, as well as 1 EUV transition to the ground state from higher excited states. We have also compared our transitional parameters with available values in the literature and at NIST website in Table 5. Radiative data for W LXIV that we have provided are accurate and can be utilized to further identify the spectral lines observed experimentally.

The computed transition rates for *E1* and *E2* transitions in two gauges, namely length and velocity gauge, differ from each other for the multiconfiguration model and will be in agreement when the large electronic interaction will be considered. To check the accuracy of computed radiative data, we have presented the ratio vel/len of absorption oscillator strengths in the last column of Table 4. For allowed dipole transitions or *E1*, *E2* transitions ($\Delta J = 0, \pm 1$ except for $J = 0 \rightarrow J' = 0$; $\Delta S = 0$, $\Delta L = 0, \pm 1$ except for $L = 0 \rightarrow L' = 0$), length and velocity forms should agree. We note that for strong and allowed transitions, agreement between the length and velocity form of the oscillator strength is better than 10%. For intercombination lines or spin forbidden lines, the selection rule is same as for the allowed transitions except for $\Delta S = 0$. For spin forbidden lines or indeed for others weak lines, only the length form should be used [40]. One can observe that, in most of the transitions, the ratio is unity or near to unity. This ensures vel/len ratio of oscillator strength reaffirms the accuracy of our calculations for Na-like W.

4 Line intensity ratio and plasma parameters

If the plasma has a thin optical layer and is also in local thermodynamic equilibrium (LTE), the diagnosis of elemental composition using different experimental spectroscopic techniques becomes easy as well as straightforward (LTE). The optically thick line is the reason for this saturation with self-absorption, as seen in the line profile, which results in an asymmetrical or asymmetrical peak in the spectrum. As a result, the electron density and plasma temperature are measured wrongly and inappropriately. Increased kinematic excitement, or perhaps the movement of electrons, arises at higher temperatures. LTE can be easily accomplished due to the increase in the number of collisions with an electron at higher temperatures. The effect of plasma temperature upon line intensity ratio in addition to the limiting value of electron density has been studied in ongoing research to understand more about the features of optically thin plasma.

Two spectral lines from the same atom or ion are measured by line intensity ratio as follows:

$$R = \frac{I_1}{I_2} = \frac{\lambda_2}{\lambda_1} \frac{A_1}{A_2} \frac{g_1}{g_2} \exp \left[-\frac{E_1 - E_2}{KT} \right] \quad (10)$$

In Eq. (10), λ is the wavelength, A is the transition probability, I indicates intensity, g denotes the lower level of transition of the statistical weight, K denotes the Boltzmann constant and the value of K is 8.6173×10^{-5} eV/K, T denotes the excitation temperature in Kelvin (K) and E represents the energy of the upper stage of transition in (eV) [41, 42]. According to Eq. (10), the exponential term significantly impacts the line intensity ratio of two spectral lines. In Hot Dense Plasma, the line intensity ratio and electron density calculations, opted as $1 [1s^2 2s^2 2p^6 3s (^2S_{1/2}) - 1s^2 2s^2 2p^6 3p (^2P_{1/2}^0)]$, $2 [1s^2 2s^2 2p^6 3s (^2S_{1/2}) - 1s^2 2s^2 2p^6 3p (^2P_{3/2}^0)]$

Table 5 Comparisons of the transitional parameters with available values in the literature and at NIST website

Lower Level (i)	Upper Level (j)	λ_{ji} (in Å)	λ_{ji} (in Å) [46]	λ_{ji} [NIST] (in Å)	A_{ji} (in s^{-1}) [E1]	A_{ji} (in s^{-1}) [E1][46]	A_{ji} (in s^{-1}) [E2]	A_{ji} (in s^{-1}) [E2][46]	A_{ji} (in s^{-1}) [M1]	A_{ji} (in s^{-1}) [M1][46]	A_{ji} (in s^{-1}) [M2]	A_{ji} (in s^{-1}) [M2][46]	f_{ij} [E1]	f_{ij} [E1][46]	S_{ij} (in a.u.) [E1]	S_{ij} (in a.u.) [E1] [46]
1	2	7.658+01	7.658+01	7.674+01	4.45+10	4.50+10	0	0	0	0	0	0	3.96-02	3.96-02	1.98-02	1.99-02
1	3	2.317+01	2.317+01	2.317+01	1.75+12	1.76+12	0	0	0	0	0	0	2.82-01	2.84-01	4.31-02	4.33-02
1	4	1.716+01	1.716+01		0	0	1.41+08	1.41+08	1.47+04	1.50+04	3.63+05	3.65+05	0	0	0	0
1	5	1.536+01	1.536+01		0	0	2.58+08	2.58+08	0	0	0	0	0	0	0	0
1	6	3.811+00	3.812+00		0	0	0	0	5.82+07	5.44+07	0	0	0	0	0	0
1	7	3.735+00	3.735+00		6.30+13	6.19+13	0	0	0	0	0	0	1.31-01	1.29-01	3.24-03	3.18-03
1	8	3.570+00	3.571+00		3.92+13	3.83+13	0	0	0	0	3.38+08	3.30+08	1.49-01	1.46-01	3.52-03	3.44-03
1	9	3.498+00	3.499+00		0	0	4.36+11	4.32+11	8.15+05	8.37+05	0	0	0	0	0	0
1	10	3.463+00	3.463+00		0	0	4.33+11	4.29+11	0	0	0	0	0	0	0	0
1	11	3.427+00	3.428+00		0	0	0	0	0	0	7.57+03	7.56+03	0	0	0	0
1	13	2.638+00	2.637+00		0	0	0	0	6.58+07	6.49+07	0	0	0	0	0	0
1	14	2.619+00	2.618+00		3.57+13	3.36+13	0	0	0	0	0	0	3.67-02	3.46-02	6.33-04	5.97-04
1	15	2.577+00	2.577+00		2.53+13	2.34+13	0	0	0	0	4.16+08	3.86+08	5.04-02	4.65-02	8.56-04	7.90-04
1	16	2.559+00	2.558+00		0	0	2.15+11	1.93+11	1.77+06	1.17+06	0	0	0	0	0	0
1	17	2.549+00	2.548+00		0	0	2.26+11	2.02+11	0	0	0	0	0	0	0	0
1	18	2.539+00	2.539+00		0	0	0	0	0	0	3.69+03	3.62+03	0	0	0	0

Table 6 Line intensity ratio and electron density (in cm^{-3}) as a function of plasma temperature (in K) for W LXIV

Index	Plasma temperature (in K)	Line intensity ratio (R)	Number of electron density (ne in cm^{-3})	λ_2 (Å) $1s^2 2s^2 2p^6 3s$ ($^2S_{1/2}$)— $1s^2 2s^2 2p^6 3p$ ($^2P_{1/2}^0$) [1, 2]	λ_1 (Å) $1s^2 2s^2 2p^6 3s$ ($^2S_{1/2}$)— $1s^2 2s^2 2p^6 3p$ ($^2P_{3/2}^0$) [1–3]	g1 and g2	A_1 (s^{-1})	A_2 (s^{-1})	ΔE ($= E_1 - E_2$) eV
1	2×10^6	14.95	1.177×10^{23}	7.674×10^1	2.317×10^1	2	1.754×10^{12}	4.454×10^{10}	373.38
2	4×10^6	44.15	1.665×10^{23}	7.674×10^1	2.317×10^1	2	1.754×10^{12}	4.454×10^{10}	373.38
3	6×10^6	63.35	2.041×10^{23}	7.674×10^1	2.317×10^1	2	1.754×10^{12}	4.454×10^{10}	373.38
4	8×10^6	75.89	2.355×10^{23}	7.674×10^1	2.317×10^1	2	1.754×10^{12}	4.454×10^{10}	373.38
5	1×10^7	84.57	2.633×10^{23}	7.674×10^1	2.317×10^1	2	1.754×10^{12}	4.454×10^{10}	373.38
6	1×10^8	124.90	8.328×10^{23}	7.674×10^1	2.317×10^1	2	1.754×10^{12}	4.454×10^{10}	373.38
7	1×10^9	129.87	2.633×10^{24}	7.674×10^1	2.317×10^1	2	1.754×10^{12}	4.454×10^{10}	373.38
8	1×10^{10}	130.37	8.328×10^{29}	7.674×10^1	2.317×10^1	2	1.754×10^{12}	4.454×10^{10}	373.38

Fig. 2 For Na-like W, the line intensity ratio for spectral lines 1 $[1s^2 2s^2 2p^6 3s(^2S_{1/2}) - 1s^2 2s^2 2p^6 3p(^2P_{1/2}^0)]$ and 2 $[1s^2 2s^2 2p^6 3s(^2S_{1/2}) - 1s^2 2s^2 2p^6 3p(^2P_{3/2}^0)]$ varies with plasma temperature

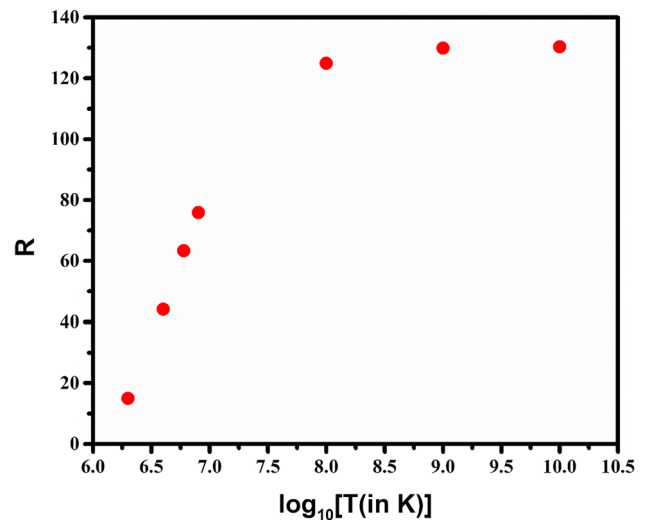
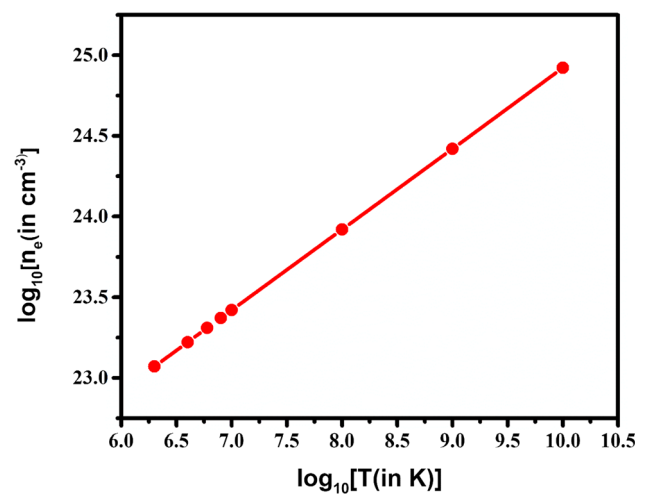


Fig. 3 Limiting electron density for Na-like W for spectral lines 1 $[1s^2 2s^2 2p^6 3s(^2S_{1/2}) - 1s^2 2s^2 2p^6 3p(^2P_{1/2}^0)]$ and 2 $[1s^2 2s^2 2p^6 3s(^2S_{1/2}) - 1s^2 2s^2 2p^6 3p(^2P_{3/2}^0)]$ varies with plasma temperature



which signifies the two spectral lines. For Na-like W at high temperatures, we have presented the line intensity ratio (R) in Table 6. The International Thermonuclear Experimental Reactor (ITER) has started using various heating techniques to raise the plasma temperature to the optimal level value of 1.5×10^8 °C or 4×10^{10} K [43]. As a result, we specified 10^{10} K as the maximum plasma temperature in our calculations. As is observable, the exponential term becomes extremely small for the lowest values of $\Delta E (= E_1 - E_2)$, which leads the line intensity ratio between two spectral lines to become too small. This led to calculating the line intensity ratio between two spectral transitions. From Fig. 2 and Table 6, it is possible to determine how the line intensity ratio behaves with plasma temperature. According to our observations, the line intensity ratio rises as the plasma temperature T rises, especially when T is more than or equivalent to 10^9 K. This demonstrates the saturation of the line intensity ratio or the negligible effect of rising temperatures on the line intensity ratio.

By comparing their estimated line intensity ratio with the measured ratio for various delay times, researchers may pinpoint the timeframe window only when plasma is already in LTE as well as optically thin.

The overall number of electron collisions must be high to achieve LTE. For plasmas as being in partial local thermodynamic equilibrium (LTE), it is possible to predict the lowest principal quantum number that meets the criterion of being within 10% of its Saha-Boltzmann value [44]. The McWhirter criterion [45] establishes the minimal or limiting value of electron density for this purpose.

$$n_e \geq 1.6 \times 10^{12} T^{(1/2)} (\Delta E)^3 \quad (11)$$

where T is the plasma temperature in Kelvin, the electron density is n_e and $\Delta E = (E_1 - E_2)$ eV. The limiting electron density at various plasma temperature levels is also mentioned. 10^{20} cm^{-3} is the electron density order because of its occurrence in several types of stars, including white dwarf stars. Plasma throughout this density range is particularly well known, as are inertial confinement fusion plasmas. In Fig. 3 and Table 6, it can be deduced that the value of the limiting electron density for Na-like W demonstrates

that the number of collisions in the plasma rises as the plasma temperature rises. Therefore, this knowledge may be useful for experimenters who want to produce optically thin plasma for Na-like W ions in LTE at significantly higher temperatures.

5 Conclusion

In the current work, we have provided theoretical research as well as analysis regarding the atomic parameters of multipole transitions of W ions for 100 fine structure levels for Na-like which is inspired by demand. We have investigated the photoionization cross section and ionization potential of $3s$, $3p$ and $3d$ levels of Na-like W at five different photoelectron energies. Our computing process uses the FAC approach, and the discrepancy between the findings and the available theoretical as well as experimental data is explained. Furthermore, we estimated the line intensity ratio and electron density for W LXIV and evaluated how they behaved under high plasma temperatures. Our predicted results will be useful for fusion plasma, astrophysical plasma and modelling plasma.

Acknowledgements We express our sincere gratitude to Delhi Technological University in gratitude for their support and for enhancing our services and facilities.

Data Availability Statement This manuscript has associated data in a data repository. [Authors' comment: All data used in the manuscript are included within the article and all citation references with (DOI) are mentioned or texted as references at relevant places.]

References

1. R. Aymar, P. Barabaschi, Y. Shimomura, The ITER design. *Plasma Phys. Control. Fusion* **44**, 519–565 (2002). <https://doi.org/10.1088/0741-3335/44/5/304>
2. A.V. Demura, M.B. Kadomtsev, V.S. Lisitsa, V.A. Shurygin, Electron impact ionization of tungsten ions in a statistical model. *JETP Lett.* **101**, 85–88 (2015). <https://doi.org/10.1134/S0021364015020058>
3. A. Müller, S. Schippers, J. Hellhund, A.L.D. Kilcoyne, R.A. Phaneuf, B.M. McLaughlin, Photoionization of tungsten ions: experiment and theory for W5+. *J. Phys. B At. Mol. Opt. Phys.* **52**, 195005 (2019). <https://doi.org/10.1088/1361-6455/ab39c8>
4. J.J. Boyle, Z. Altun, H.P. Kelly, Photoionization cross-section calculation of atomic tungsten. *Phys. Rev. A* **47**, 4811–4830 (1993). <https://doi.org/10.1103/PhysRevA.47.4811>
5. O. Physics, Photoionization of tungsten ions : experiment and theory for and Manuscript version : Accepted Manuscript Photoionization of tungsten ions : experiment and, (2016) 0–16.
6. T. Pütterich, R. Neu, R. Dux, A.D. Whiteford, M.G. O'Mullane, Modelling of measured tungsten spectra from ASDEX Upgrade and predictions for ITER. *Plasma Phys. Control. Fusion.* (2008). <https://doi.org/10.1088/0741-3335/50/8/085016>
7. A.E. Kramida, J. Reader, Ionization energies of tungsten ions: W2+ through W71+. *At. Data Nucl. Data Tables* **92**, 457–479 (2006). <https://doi.org/10.1016/j.adt.2006.03.002>
8. A.E. Kramida, T. Shirai, Energy levels and spectral lines of tungsten, W III through W LXXIV. *At. Data Nucl. Data Tables* **95**, 305–474 (2009). <https://doi.org/10.1016/j.adt.2008.12.002>
9. A. Kramida, Recent progress in spectroscopy of tungsten. *Can. J. Phys.* **89**, 551–570 (2011). <https://doi.org/10.1139/p11-045>
10. U.I. Safronova, A.S. Safronova, P. Beiersdorfer, Excitation energies, radiative and autoionization rates, dielectronic satellite lines, and dielectronic recombination rates for excited states of Na-like W from Ne-like W. *At. Data Nucl. Data Tables* **95**, 751–785 (2009). <https://doi.org/10.1016/j.adt.2009.04.001>
11. A.S. Safronova, A. Stafford, A.K. Gill, R.R. Childers, Polarization of hard X-ray dielectronic satellite lines from Na-like W ions. *J. Quant. Spectrosc. Radiat. Transf.* **272**, 107788 (2021). <https://doi.org/10.1016/j.jqsrt.2021.107788>
12. M.B. Trzhaskovskaya, V.K. Nikulin, Radiative recombination and photoionization data for tungsten ions. *Electron Struct. Ions Plasmas Atoms*. **3**, 86–119 (2015). <https://doi.org/10.3390/atoms3020086>
13. P. Beiersdorfer, M.J. May, J.H. Scofield, S.B. Hansen, Atomic physics and ionization balance of high-Z Ions: critical ingredients for characterizing and understanding high-temperature plasmas. *High Energy Density Phys.* **8**, 271–283 (2012). <https://doi.org/10.1016/j.hedp.2012.03.003>
14. P. Beiersdorfer, J.K. Lepson, M.B. Schneider, M.P. Bode, L-shell x-ray emission from neonlike W64+. *Phys. Rev. A At. Mol. Opt. Phys.* **86**, 1–11 (2012). <https://doi.org/10.1103/PhysRevA.86.012509>
15. B. Li, G. O'Sullivan, C. Dong, X. Chen, Dielectronic recombination of tungsten ions. *J. Phys. B At. Mol. Opt. Phys.* **49**, 1–15 (2016). <https://doi.org/10.1088/0953-4075/49/15/155201>
16. W.D. Chen, J. Xiao, Y. Shen, Y.Q. Fu, F.C. Meng, C.Y. Chen, B.H. Zhang, Y.J. Tang, R. Hutton, Y. Zou, Precise studies on resonant energies of the first intershell (KLL) dielectronic recombination processes for He- up to O-like xenon. *Phys. Plasmas* (2008). <https://doi.org/10.1063/1.2967486>
17. T. Dipti, L. Das, R. Sharma, Srivastava, L-shell electron excitations of Mg- through O-like tungsten ions. *Phys. Scr.* (2014). <https://doi.org/10.1088/0031-8949/89/8/085403>
18. J. Huang, G. Jiang, Q. Zhao, Ground-state ionization potentials for lithium through neon isoelectronic sequences with $Z = 37$ –82. *Chin. Phys. Lett.* **23**, 69–72 (2006). <https://doi.org/10.1088/0256-307X/23/1/021>
19. D. Priti, L. Sharma, R. Srivastava, Fully relativistic electron impact excitation cross-section and polarization for tungsten ions. *Atoms* **3**, 53–75 (2015). <https://doi.org/10.3390/atoms3020053>
20. W. Eckstein, J. Bohdansky, J. Roth, Atomic and plasma material interaction data for fusion. *Nucl. Fusion* **1**, 51 (1991)
21. R.K. Pandey, Spectroscopic study of EUV and SXR transitions of Ba XLVI. *J. At. Mol. Condens. Nano Phys.* **5**, 18–39 (2018). <https://doi.org/10.26713/jamcnp.v5i1.836>
22. M. Klapisch, P. Mandelbaum, A. Zigler, C. Bauche-Arnoult, J. Bauche, The unresolved 3d-4f transitions in the x-ray spectra of highly ionized tin to iron from laser produced plasma. *Phys. Scr.* **34**, 51–57 (1986). <https://doi.org/10.1088/0031-8949/34/1/009>
23. E.M.B. Thiemann, F.G. Eparvier, V. Knoer, A. Al Muharrami, R.J. Lillis, Solar extreme ultraviolet irradiance uncertainties for planetary studies. *J. Geophys. Res. Sp. Phys.* (2021). <https://doi.org/10.1029/2020JA028184>

24. V.S. Airapetian, J. Allred, Forward modeling of synthetic EUV/SXR emission from solar coronal active regions: Case of AR 11117. (2014). <http://arxiv.org/abs/1409.3866>.
25. J. Holburg, M. Müller, K. Mann, S. Wieneke, Brilliance improvement of laser-produced extreme ultraviolet and soft x-ray plasmas based on pulsed gas jets. *J. Vac. Sci. Technol. A* **37**, 031303 (2019). <https://doi.org/10.1116/1.5089201>
26. Q.M. Zhang, H.S. Ji, A swirling flare-related EUV jet. *Astron. Astrophys.* **561**, 1–7 (2014). <https://doi.org/10.1051/0004-6361/201322616>
27. P.W. Wachulak, A. Bartnik, M. Skorupka, J. Kostecki, R. Jarocki, M. Szczurek, L. Węgrzynski, T. Fok, H. Fiedorowicz, Water-window microscopy using a compact, laser-plasma SXR source based on a double-stream gas-puff target. *Appl. Phys. B Lasers Opt.* **111**, 239–247 (2013). <https://doi.org/10.1007/s00340-012-5324-y>
28. A. Bartnik, H. Fiedorowicz, P. Wachulak, T. Fok, Temporal measurements of extreme ultraviolet (EUV) emission, from low temperature, EUV-induced plasmas. *Laser Part. Beams* **36**, 286–292 (2018). <https://doi.org/10.1017/S0263034618000319>
29. P. Wachulak, A. Torrisi, M. Ayele, A. Bartnik, J. Czwartos, Ł. Węgrzyński, T. Fok, H. Fiedorowicz, Nanoimaging using soft X-ray and EUV laser-plasma sources. *EPJ Web Conf.* **167**, 1–5 (2018). <https://doi.org/10.1051/epjconf/201816703001>
30. P. Wachulak, A. Torrisi, M. Ayele, J. Czwartos, A. Bartnik, Ł. Węgrzyński, T. Fok, T. Parkman, Š. Salačová, J. Turňová, M. Odstrčil, H. Fiedorowicz, Bioimaging using full field and contact EUV and SXR microscopes with nanometer spatial resolution. *Appl. Sci.* (2017). <https://doi.org/10.3390/app7060548>
31. A. Torrisi, P.W. Wachulak, A. Bartnik, Ł. Węgrzyński, T. Fok, H. Fiedorowicz, Biological and material science applications of EUV and SXR nanoscale imaging systems based on double stream gas puff target laser plasma sources. *Nucl. Instrum. Methods Phys. Res. Sect B Beam Interact. Mater. Atoms.* **411**, 29–34 (2017). <https://doi.org/10.1016/j.nimb.2017.01.035>
32. L.H. Yang, Y.C. Jiang, J.Y. Yang, Y. Bi, R.S. Zheng, J.C. Hong, Observations of EUV and soft X-ray recurring jets in an active region. *Res. Astron. Astrophys.* **11**, 1229–1242 (2011). <https://doi.org/10.1088/1674-4527/11/10/010>
33. G.Y. Liang, F. Li, F.L. Wang, Y. Wu, J.Y. Zhong, G. Zhao, X-Ray and euv spectroscopy of various astrophysical and laboratory plasmas: collisional, photoionization and charge-exchange plasmas. *Astrophys. J.* (2014). <https://doi.org/10.1088/0004-637X/783/2/124>
34. A. Bartnik, W. Skrzeczanowski, H. Fiedorowicz, P. Wachulak, T. Fok, EUV induced plasmas created in atomic and molecular gases, (n.d.) 502.
35. J.B. Spencer, D.A. Alman, D.N. Ruzic, B.E. Jurczyk, Dynamics of a laser produced plasma for soft x-ray production. *Emerg. Lithogr. Technol. IX.* **5751**, 798 (2005). <https://doi.org/10.1117/12.598543>
36. M.F. Gu, The Flexible Atomic Code, 2004. <http://kipac-tree.stanford.edu/fac..>
37. M.A. Baig, Measurement of photoionization cross-section for the excited states of atoms: a review. *Atoms* (2022). <https://doi.org/10.3390/atoms10020039>
38. Atomic Astrophysics and spectroscopy, A.K. Pradhan, S.N. Nahar, www.cambridge.org, ISBN 978-0-521-82536-8.
39. D.H. Sampson, H.L. Zhang, A.K. Mohanty, R.E.H. Clark, *Phys. Rev. A* **40**, 604 (1989)
40. N. Singh, A.K.S. Jha, M. Mohan, Breit-Pauli energy levels and radiative lifetimes in neutral chlorine. *Eur. Phys. J. D* **38**, 285–291 (2006). <https://doi.org/10.1140/epjd/e2006-00068-4>
41. T. An, P. Yuan, G. Lu, J. Che, X. Wing, M. Zhang, Y. An, The radius and temperature distribution along radial direction of lightning plasma channel. *Phys. Plasmas* **26**, 013506 (2019). <https://doi.org/10.1063/1.5059363>
42. A.K. Singh, M. Dimri, D. Dawra, A.K. Jha, M. Mohan, Relativistic atomic structure calculations and study of plasma parameters for Na-like Se XXIV. *Phys. Plasmas* **26**, 062704 (2019). <https://doi.org/10.1063/1.5100565>
43. C. Aragón, J.A. Aguilera, Characterization of laser induced plasmas by optical emission spectroscopy: a review of experiments and methods. *Spectrochim. Acta Part B At. Spectrosc.* **63**, 893–916 (2008). <https://doi.org/10.1016/j.sab.2008.05.010>
44. T. Fujimoto, R.W.P. Mc Whirter, Validity criteria for local thermodynamic equilibrium in plasma spectroscopy. *Phys. Rev. A* **42**, 6588 (1990). <https://doi.org/10.1103/PhysRevA.42.6588>
45. R.W.P. McWhirter (1965). *Plasma Diagnostic Techniques* (Huddleston, R. H.; Leonard S. L., Eds). New York: Academic.
46. K.M. Aggarwal, F.P. Keenan, Radiative rates for E1, E2, M1, and M2 transitions in S-like to F-like tungsten ions (W LIX to W LXVI). *At. Data Nucl. Data Tables* **111–112**, 187–279 (2016). <https://doi.org/10.1016/j.adt.2016.02.004>
47. F. Hu, C. Wang, J. Yang, G. Jiang, L. Hao, Multiconfiguration Dirac–Fock calculations of transition probabilities of some tungsten ions. *Phys. Scr.* (2011). <https://doi.org/10.1088/0031-8949/84/01/015302>
48. M.D. Turkington, C.P. Ballance, A. Hibbert, C.A. Ramsbottom, Benchmarking a modified version of the civ3 nonrelativistic atomic-structure code within Na-like-tungsten R-matrix calculations. *Phys. Rev. A* **94**, 1–9 (2016). <https://doi.org/10.1103/PhysRevA.94.022508>
49. M. Xu, G. Jiang, M. Wu, X. Li, G. Bian, F. Hu, Multiconfiguration dirac-fock calculations of excitation energies and wavelengths in highly charged tungsten ions. *Can. J. Phys.* **94**, 563–568 (2016). <https://doi.org/10.1139/cjp-2015-0772>
50. A. Kramida, Yu. Ralchenko, J. Reader, and NIST ASD Team, <https://physics.nist.gov/asd> for NIST Atomic Spectra Database (ver. 5.6.1) (2019).

Springer Nature or its licensor (e.g. a society or other partner) holds exclusive rights to this article under a publishing agreement with the author(s) or other rightsholder(s); author self-archiving of the accepted manuscript version of this article is solely governed by the terms of such publishing agreement and applicable law.

Relativistic atomic structure calculations of KIX with plasma parameters

Cite as: Phys. Plasmas **29**, 092702 (2022); <https://doi.org/10.1063/5.0095476>

Submitted: 11 April 2022 • Accepted: 27 June 2022 • Published Online: 01 September 2022

 Richa Pajwar,  Rinku Sharma and  Alok K. Singh Jha



[View Online](#)



[Export Citation](#)



[CrossMark](#)

Physics of Plasmas

Special Topic: Plasma Physics
of the Sun in Honor of Eugene Parker

Submit Today!



Relativistic atomic structure calculations of KIX with plasma parameters

Cite as: Phys. Plasmas **29**, 092702 (2022); doi: [10.1063/5.0095476](https://doi.org/10.1063/5.0095476)

Submitted: 11 April 2022 · Accepted: 27 June 2022 ·

Published Online: 1 September 2022



View Online



Export Citation



CrossMark

Richa Paijwar,¹  Rinku Sharma,^{1,a)}  and Alok K. Singh Jha^{2,a)} 

AFFILIATIONS

¹Department of Applied Physics, Delhi Technological University, Delhi 110042, India

²School of Physical Sciences, Jawaharlal Nehru University, Delhi 110044, India

^{a)}Authors to whom correspondence should be addressed: rinkusharma@dtu.ac.in and aloksinghjha@gmail.com

ABSTRACT

Systematic calculations for energy levels, lifetimes, and radiative data for the KIX are reported, including oscillator strengths, transition wavelengths, line strengths, and radiative rates of electric dipole (E1) transition, electric quadrupole (E2) transition, magnetic dipole (M1) transition, and magnetic quadrupole (M2) transition, using GRASP. Quantum electrodynamics and Breit correction have been considered in our calculations. The importance and effect of valence valence and core valence correlations on the excitation energies have been discussed in graphical and tabular forms. Analogous calculations using flexible atomic code (FAC) and the large-scale configuration interaction technique have also been done to confirm the accuracy of energy levels. The calculated results are in close agreement with NIST compiled data and other available results. The influence of plasma temperature (2×10^6 – 1×10^{10} K) on the line intensity ratio with the number of electron density has been studied for the hot dense plasma (HDP) graph for KIX. Our reported results will be valuable or beneficial for the characterization of HDP, astrophysical plasmas, and plasma modeling.

Published under an exclusive license by AIP Publishing. <https://doi.org/10.1063/5.0095476>

I. INTRODUCTION

Due to its prospective applications in plasma diagnostics, inertial confinement fusion (ICF), magnetic confinement fusion, and atomic spectroscopy of highly charged ions have attracted significant interest.^{1–3} Modeling and research into low and high-temperature plasmas using inertial and magnetic confinement thermonuclear fusion demand very accurate atomic data and plasma parameters such as the line intensity ratio, plasma temperature, and electron density.⁴ Because the adjacent neon-like stage of ionization is necessary for x-ray laser modeling, atomic data on Na-like ions are essential for studying high-temperature plasma.^{5,6} Inertial confinement fusion, magnetic confinement fusion, and plasma diagnostics are important for atomic spectroscopy of highly charged ions. Highly charged sodium-like ions were found in laboratory sources such as high-voltage vacuum spark tokamak and laser-produced plasmas. In astrophysical plasmas, for example, Cu XIX (sodium-like copper ion) spectra were observed in a solar spectrum obtained at the White Sands Missile Range.⁷

Potassium was chosen for the current investigation because the absolute abundance of potassium has been calculated using x-ray solar flare line and continuum spectra. Phillips *et al.*⁸ have assumed flare plasma is coronal and potassium is significant in the continuing debate concerning the nature of the coronal/photospheric element abundance

ratios, which are usually considered to be dependent on first ionization potential, as it has the lowest FIP (FIPs $n < 10$ eV) of any common element in the Sun. The RESIK crystal spectrometer on the Coronas-F spacecraft was used to make the measurements. Using high-resolution spectra gathered with FLAMES at the ESO—very large telescope, Mucciarelli *et al.*⁹ have determined the potassium abundances in red-giant-branch stars in the Galactic globular clusters. GCs have revealed large and correlated star-to-star inhomogeneities in the abundance of various light elements, including C, N, Na, O, Mg, Al, and He, in chemical composition.

A. Experimental and theoretical work on Na-like ions

Edlen *et al.* published a complete list of the potassium lines detected in their spectrograms, including 230 lines varying between 230 and 41 Å, nearly half of which are classified in spectra including between KVII and KXII. Cohen *et al.*¹⁰ investigated the seven spectra from KIX to Mn XV, determining series limits, presenting adopted wavelengths, derived energy levels, and term splitting. Recently, Trabert *et al.*¹¹ identified 3p–3d transitions in singly excited Na-like ions in the ³⁹K beam foil spectrum. Jupen *et al.*,¹² using Cowan code, found the most prominent line of the multiplet, $2p^5 3s3p^4 D^o_{7/2} - 2p^5 3s3d^4 F^o_{9/2}$, in the spectra of various Na-like ions. To compute the oscillator strengths for the E1

transition in the sodium isoelectronic sequence, Seigal *et al.*¹³ used the theoretical single configuration Dirac–Fock technique (Na I–Ca X). Yonis *et al.*¹⁴ calculated the fine structure energy levels, transition probabilities, and oscillator strengths of Na-like ions using the configuration interaction approach CIV3. Ivanov *et al.*¹⁵ used a model potential technique for Na-like series with ($Z = 25\text{--}80$) nuclear charge. With 71 Na-like ions in the $Z = 22\text{--}92$ range, Sampson *et al.*¹⁶ observed relativistic distorted wave collision strengths as well as oscillator strengths. Kim *et al.*¹⁷ also used the Dirac–Fock technique to find the resonance transition energies of Na-like ions. Moreover, Johnson *et al.*¹⁸ calculated E1 transition amplitudes for Na-like ions using third-order many-body perturbation theory. Similarly, to determine the transition probability of allowed transition for KIX, Johnson *et al.* employed the third-order many-body perturbation theory. For 67 Na-like and F-like as well as Li-like transitions between the region of $26 \leq Z \leq 92$, the relativistic distorted-wave collision intensities for all possible $\Delta n = 0$ in the region of $26 \leq Z \leq 92$ were calculated by Fontes *et al.*¹⁹ Safronova *et al.*²⁰ evaluated the relativistic many-body perturbation theory by taking neon-like Dirac–Fock potential. Furthermore, for $2p^5 3s 3p^4 D^{\circ}_{7/2} - 2p^5 3s 3d^4 F^{\circ}_{9/2}$, Jupen *et al.* observed a wavelength of 423.05(5) Å along the isoelectronic sequence using the interpolation method. Furthermore, Sansonetti *et al.*²¹ compiled the energy levels using experimental wavelengths of Cohen and Behring’s²² and Edlen and Boden.²³ Moreover, using relativistic many-body perturbation theory, Gillaspay *et al.*²⁴ determined the transition energies of D lines for Na-like ions. Last but not least, Fisher *et al.*²⁵ calculated the energy levels and oscillator strength of Na-like ions by using the multi-configuration Hartree–Fock (MCHF) technique with non-orthogonal spline CI methods. There is a considerable previous experimental as well as theoretical work on KIX, mostly restricted to low-lying states. The principal objective of our work is to upgrade the atomic database for KIX ions in the form of energy levels, wavelengths, oscillator strength, and line strengths. The transitions of radiative rates are presented as E1 (electric dipole) and E2 (electric quadrupole), also M1 (magnetic dipole) and M2 (magnetic quadrupole). The effect of quantum electrodynamics correction with Breit interaction correction on energy levels has been studied. We have done additional independent calculations using flexible atomic code (FAC) to ensure the correctness of our multi-configuration Dirac–Fock (MCDF) results. Furthermore, the configuration interaction (CIV3) approach has also been used to determine the fine structural energy levels of KIX.

We have used two alternative sets of configurations based on valence–valence (VV) and core–valence (CV) correlations in our present calculations. While doing calculations with the VV correlations, we have taken configuration namely, as $2p^6 n l$ with $3 \leq n \leq 5$ and $0 \leq l \leq 4$, where one electron excitation from the valence to another high subshell is involved. In the case of core valence correlation, however, the configuration has been included as $2p^5 3l n l'$ with $3 \leq n \leq 5$, $2p^5 4l'$ excitations among one electron as of the $2p$ subshell to additional high subshells and $2s 2p^6 3l n l'$ with $3 \leq n \leq 5$, $2s 2p^6 4l'$ excitations of one electron as of the $2s$ subshell to additional high subshells. $1s^2 2s^2 2p^6$ core gets set for valence calculation, while $1s^2$ core remains unchangeable for calculation of core valence correlation.

Plasma characterization and modeling help to understand the multiple atomic processes that occur in plasmas. Consequently, we have analyzed the various plasma characteristics, line intensity ratios, and electron density of the hot-dense plasma in local thermodynamic

equilibrium (LTE). We believe that KIX calculations should help examine or observe the new valuable data from a variety of plasma sources, where plasma diagnostics, including modeling studies, were always inhabited by a scarcity of precise atomic data and future astrophysical sources.

This paper is divided into four sections, as demonstrated in Sec. II, where we provide the theoretical method used in our calculations. In Sec. III, we have evaluated and compared our calculated results using the NIST database²⁶ or previously published results. Finally, Sec. IV presents the entire conclusive summary of KIX.

II. THEORETICAL METHOD

A. Multi-configuration Dirac–Fock method (MCDF)

In our calculations for fully relativistic, we used the multi-configuration Dirac–Fock (MCDF) technique, which was modified by Norrington and established by Grant *et al.*²⁷ Because a thorough explanation of this method can be found in the literature, we will only cover it briefly. These are all included in the Breit interactions, quantum electrodynamics (QED) effects, and high-order relativistic corrections (vacuum polarization and self-energy). An extended average level that minimizes a Hamiltonian matrix’s weighted trace is preferred when evaluating radial wave functions during self-consistent field (SCF) operation. For an N -electron atom or ion, the Dirac–Coulomb Hamiltonian

$$H = \sum_{i=1}^N H_D(i) + \sum_{i=1}^N \sum_{j=1}^N \frac{1}{r_{ij}}. \quad (1)$$

Through diagonalizing a relativistic Hamiltonian H , the energy levels of an atomic ion having N electrons can also be determined. For a single electron, the Hamiltonian Dirac is $H_D(i)$. An atomic state function calculates the particular wave function for an N electron atom or ion system. CSFs (configuration state functions) are the sum of four-component spin-orbital products, which are stated as follows:

$$\mathcal{O}_{nkm} = \frac{1}{r} \begin{pmatrix} P_{nk}(r) \chi_{km}(\theta, \phi, \sigma) \\ -iQ_{nk}(r) \chi_{-km}(\theta, \phi, \sigma) \end{pmatrix}, \quad (2)$$

where (P_{nk}) is large and (Q_{nk}) is small component radial wave functions, respectively. It fulfills the coupled Dirac equation for a local central field and may be explained using a self-consistent field standard technique, n is a principal quantum number, k is the Dirac angular quantum number, whereas the spinor spherical harmonic χ_{km} is given as

$$\chi_{km}(\theta, \phi) = \sum_{\sigma=\pm\frac{1}{2}} \left\langle l m - \sigma \frac{1}{2} \sigma \middle| l \frac{1}{2} j m \right\rangle Y_l^{m-\sigma}(\theta, \phi) \varphi^{\sigma}. \quad (3)$$

Linear combination of n electronic configuration state functions (CSFs) gives rise to atomic state function (ASF) and is defined as

$$|\Psi_{\alpha}(PJM)\rangle = \sum_{i=1}^N c_i(\alpha) |\gamma_i(PJM)\rangle. \quad (4)$$

CSFs, which specify a particular state, are $\gamma_i(PJM)$, where P denotes parity, and the angular quantum is given by (J, M) . For each CSF, the expansion mixing coefficients $c_i(\alpha)$ follow the formula:

$$(C_i(\alpha) + C_j(\alpha) = \delta_{ij}). \quad (5)$$

B. The FAC method

To check the accuracy of our results, we also did analogous calculations by using FAC, developed by Gu.²⁸ FAC calculates local central potential by performing a self-consistent Dirac Slater iteration on such a fictitious mean configuration. Dirac–coulomb Hamiltonian is being used to evaluate the relativistic effects. For considering the high order quantum electrodynamics (QED) effects, the Breit interaction is used in vacuum polarization effects, hydrogenic approximations for self-energy and zero energy limit for the exchanged photon. The present calculations have been performed by taking 2700 fine structure levels from $(2 \times 8) \times 1$ and $(2 \times 7) \times 2, 4 \times 2, 3 \times 1, 4 \times 1, 3 \times 1 \times 5 \times 1$ configurations, where $3 \leq n \leq 10$ and $n \times q$ given all possible distributions of q electrons (without restriction to orbital angular momentum) as one of the shells described by their principal quantum number, which are shown in Table I.

C. Configuration interaction method

Hibbert's configuration interaction approach CIV3²⁹ has been used in the present calculations. The atomic state functions (ASFs) of the configuration interaction (CI) are expressed as in the intermediate LSJ-coupling scheme

$$\Psi_i(J) = \sum_{j=1}^M a_{ij} \phi_j(\alpha_j L_j S_j J), \quad (6)$$

where $\{\phi_j\}$ stands for a set of single configuration wave functions, and coupling of an orbital L_j and spin S_j angular momenta is defined by α_j , which produces the total angular momentum J . To obtain the mixing coefficients of a_{ij} , the Breit–Pauli Hamiltonian matrix is diagonalized with a basis $\{\phi_j\}$. A linear combination of normalized Slater–type orbitals is used to expand the radial functions $P_{nl}(r)$

$$P_{nl}(r) = \sum_{j=1}^k C_{jnl} \chi_{jnl}(r). \quad (7)$$

C_{jnl} denotes the Clementi-type coefficients and

$$\chi_{jnl}(r) = \frac{(2\xi_{jnl})^{I_{jnl} + \frac{1}{2}}}{[(2I_{jnl})!]^{\frac{1}{2}}} r^{I_{jnl}} \exp(-\xi_{jnl} r), \quad (8)$$

with $I_{jnl} \geq l + 1$ as an integer.

Meanwhile, the parameters C_{jnl} and ξ_{jnl} are obtained variationally in the process of optimization through minimizing one or more Hamiltonian matrix's energy eigenvalues, whereas the parameters of I_{jnl} remain constant. In current calculations, 21 orthonormal one-electron orbitals, namely, 1s, 2s, 2p, 3s, 3p, 3d, 4s, 4p, 4d, 4f, 5s, 5p, 5d, 5f, 5g, 6s, 6p, 6d, 6f, and 6g has been used, in which 1s, 2s, and 2p are defined as the Hartree–Fock functions of KIX where ground state is $1s^2 2s^2 2p^6 3s^1$, as defined by Clementi and Roetti. The 3p, 3d, 4s, 4p, 4d, 4f, 5s, 5p, 5d, 5f, 5g, 6s, 6p, 6d, 6f, and 6g are spectroscopic orbitals and $2p^6 3p$, $2p^6 3d$, $2p^6 4s$, $2p^6 4p$, $2p^6 4d$, $2p^6 4f$, $2p^6 5s$, $2p^6 5p$, $2p^6 5d$, $2p^6 5f$, $2p^6 5g$, $2p^6 6s$, $2p^6 6p$, $2p^6 6d$, $2p^6 6f$, and $2p^6 6g$ optimized based on the excited states. On the ground state $2p^6 3s$, the 3s orbital is optimized. Table II displays the optimized radial function parameters.

The overall energy of each LS coupled term in CIV3 is affected by the inclusion of spin-independent Darwin and the relativistic mass-

TABLE I. Energy levels for the $2p^6 nl$ ($n \leq 10$) fine-structure levels for KIX (in Ryd).

Index	Configuration	Level	FAC3	NIST
1	$2p^6 3s$	$^2S_{1/2}$	0.0000	0.000 000
2	$2p^6 3p$	$^2P_{1/2}^0$	1.4340	1.432 078
3	$2p^6 3p$	$^2P_{3/2}^0$	1.4680	1.466 352
4	$2p^6 3d$	$^2D_{3/2}$	3.4172	3.416 039
5	$2p^6 3d$	$^2D_{5/2}$	3.4192	3.418 63
6	$2p^6 4s$	$^2S_{1/2}$	6.3513	6.368 78
7	$2p^6 4p$	$^2P_{1/2}^0$	6.8948	6.9098
8	$2p^6 4p$	$^2P_{3/2}^0$	6.9074	6.9228
9	$2p^6 4d$	$^2D_{3/2}$	7.6063	7.6261
10	$2p^6 4d$	$^2D_{5/2}$	7.6072	7.6273
11	$2p^6 4f$	$^2F_{5/2}^0$	7.8287	7.884 63
12	$2p^6 4f$	$^2F_{7/2}^0$	7.8290	7.845 00
13	$2p^6 5s$	$^2S_{1/2}$	8.9303	8.9575
14	$2p^6 5p$	$^2P_{1/2}^0$	9.1920	9.2176
15	$2p^6 5p$	$^2P_{3/2}^0$	9.1980	9.2239
16	$2p^6 5d$	$^2D_{3/2}$	9.5309	9.5596
17	$2p^6 5d$	$^2D_{5/2}$	9.5315	9.5604
18	$2p^6 5f$	$^2F_{5/2}^0$	9.6442	9.6722
19	$2p^6 5f$	$^2F_{7/2}^0$	9.6444	9.6723
20	$2p^6 5g$	$^2G_{7/2}$	9.6557	
21	$2p^6 5g$	$^2G_{9/2}$	9.6558	
22	$2p^6 6s$	$^2S_{1/2}$	10.2335	10.2655
23	$2p^6 6p$	$^2P_{1/2}^0$	10.3791	10.4104
24	$2p^6 6p$	$^2P_{3/2}^0$	10.3825	10.4135
25	$2p^6 6d$	$^2D_{3/2}$	10.5674	10.6003
26	$2p^6 6d$	$^2D_{5/2}$	10.5677	10.6009
27	$2p^6 6f$	$^2F_{5/2}^0$	10.6328	10.6657
28	$2p^6 6f$	$^2F_{7/2}^0$	10.6329	10.6658
29	$2p^6 6g$	$^2G_{7/2}$	10.6391	10.6328
30	$2p^6 6g$	$^2G_{9/2}$	10.6392	10.6329
31	$2p^6 6h$	$^2H_{9/2}^0$	10.6418	
32	$2p^6 6h$	$^2H_{11/2}^0$	10.6419	
33	$2p^6 7s$	$^2S_{1/2}$	10.9836	11.0185
34	$2p^6 7p$	$^2P_{1/2}^0$	11.0727	11.1082
35	$2p^6 7p$	$^2P_{3/2}^0$	11.0748	11.1082
36	$2p^6 7d$	$^2D_{3/2}$	11.1882	11.2233
37	$2p^6 7d$	$^2D_{5/2}$	11.1884	11.2235
38	$2p^6 7f$	$^2F_{5/2}^0$	11.2293	11.2644
39	$2p^6 7f$	$^2F_{7/2}^0$	11.2293	11.2647
40	$2p^6 7g$	$^2G_{7/2}$	11.2330	
41	$2p^6 7g$	$^2G_{9/2}$	11.2331	
42	$2p^6 7h$	$^2H_{9/2}^0$	11.2347	
43	$2p^6 7h$	$^2H_{11/2}^0$	11.2347	
44	$2p^6 7i$	$^2I_{11/2}$	11.2360	
45	$2p^6 7i$	$^2I_{13/2}$	11.2360	
46	$2p^6 8s$	$^2S_{1/2}$	11.4547	
47	$2p^6 8p$	$^2P_{1/2}^0$	11.5131	11.5493

TABLE I. (Continued.)

Index	Configuration	Level	FAC3	NIST
48	2p ⁶ 8p	2P _{3/2} ⁰	11.5145	11.5493
49	2p ⁶ 8d	2D _{3/2}	11.5890	11.6257
50	2p ⁶ 8d	2D _{5/2}	11.5892	11.6258
51	2p ⁶ 8f	2F _{5/2} ⁰	11.6166	11.6538
52	2p ⁶ 8f	2F _{7/2} ⁰	11.6166	11.6538
53	2p ⁶ 8g	2G _{7/2}	11.6189	
54	2p ⁶ 8g	2G _{9/2}	11.6190	
55	2p ⁶ 8h	2H _{9/2} ⁰	11.6200	
56	2p ⁶ 8h	2H _{11/2} ⁰	11.6200	
57	2p ⁶ 8i	2I _{11/2}	11.6209	
58	2p ⁶ 8i	2I _{13/2}	11.6209	
59	2p ⁶ 8k	2K _{13/2} ⁰	11.6216	
60	2p ⁶ 8k	2K _{15/2} ⁰	11.6216	
61	2p ⁶ 9s	2S _{1/2}	11.7698	
62	2p ⁶ 9p	2P _{1/2} ⁰	11.8103	11.8480
63	2p ⁶ 9p	2P _{3/2} ⁰	11.8112	11.8480
64	2p ⁶ 9d	2D _{3/2}	11.8628	11.8987
65	2p ⁶ 9d	2D _{5/2}	11.8629	11.8893
66	2p ⁶ 9f	2F _{5/2} ⁰	11.8822	11.9194
67	2p ⁶ 9f	2F _{7/2} ⁰	11.8822	11.9194
68	2p ⁶ 9g	2G _{7/2}	11.8837	
69	2p ⁶ 9g	2G _{9/2}	11.8838	
70	2p ⁶ 9h	2H _{9/2}	11.8844	
71	2p ⁶ 9h	2H _{11/2} ⁰	11.8844	
72	2p ⁶ 9i	2I _{11/2}	11.8851	
73	2p ⁶ 9i	2I _{13/2}	11.8851	
74	2p ⁶ 9k	2K _{13/2} ⁰	11.8856	
75	2p ⁶ 9k	2K _{15/2} ⁰	11.8856	
76	2p ⁶ 9l	2L _{15/2}	11.8860	
77	2p ⁶ 9l	2L _{17/2}	11.8860	
78	2p ⁶ 10s	2S _{1/2}	11.9911	
79	2p ⁶ 10p	2P _{1/2} ⁰	12.0202	
80	2p ⁶ 10p	2P _{3/2} ⁰	12.0208	
81	2p ⁶ 10d	2D _{3/2}	12.0581	12.0956
82	2p ⁶ 10d	2D _{5/2}	12.0582	
83	2p ⁶ 10f	2F _{5/2} ⁰	12.0722	
84	2p ⁶ 10f	2F _{7/2} ⁰	12.0722	
85	2p ⁶ 10g	2G _{7/2}	12.0733	
86	2p ⁶ 10g	2G _{9/2}	12.0733	
87	2p ⁶ 10h	2H _{9/2}	12.0737	
88	2p ⁶ 10h	2H _{11/2} ⁰	12.0737	
89	2p ⁶ 10i	2I _{11/2}	12.0742	
90	2p ⁶ 10i	2I _{13/2}	12.0742	
91	2p ⁶ 10k	2K _{13/2} ⁰	12.0745	
92	2p ⁶ 10k	2K _{15/2} ⁰	12.0746	
93	2p ⁶ 10l	2L _{15/2}	12.0749	
94	2p ⁶ 10l	2L _{17/2}	12.0749	

TABLE I. (Continued.)

Index	Configuration	Level	FAC3	NIST
95	2p ⁶ 10m	2M _{17/2} ⁰	12.0752	
96	2p ⁶ 10m	2M _{19/2} ⁰	12.0752	

correction components, while spin–spin (SS) and one-body spin–orbit (SO) as well as two-body spin–other-orbit (SOO) terms divide the LS states into J-dependent levels. The SO operator in the modified form is as follows:

$$H'_{SO} = \frac{\alpha^2}{2} Z \sum_{i=1}^N \frac{\zeta(l)}{r_i^3} (l.s). \quad (9)$$

III. RESULTS AND DISCUSSION

The fine structure energy levels of KIX have been calculated using the fully relativistic GRASP algorithm. For orbital optimization, the “extended average level” (EAL) option has been chosen, which reduces the weighted proportional to $(2j+1)$ trace of a Hamiltonian matrix. Two sets of calculations were performed using the valence–valence (VV) correlation and core valence (CV) correlation to explore the effect of correlation on energy levels. We employed an atomic model with 12 configurations in our MCDF1 calculation in the form of $2p^6nl$ ($3 \leq n \leq 5$ and $0 \leq l \leq 4$) there are a total of 21 fine-structure energy levels as a result of this process. Table III and Fig. 1 show the impact of electron correlations of KIX, for the lowest 21 fine structure energy configurations. The CSF has been generated by taking excitations from the reference configuration $2p^63s^1$ to orbitals with $n=3, 4, 5$, and 6, respectively. To predict the electronic correlation effects systematically, configuration spaces were extended layer by layer. In Table III, the difference in correlation energies between two neighboring principal quantum numbers decreases as the principal quantum number increases. In our MCDF2 calculations, additional configurations of $2p^5 3l n'l'$ with $3 \leq n \leq 5$, $2p^5 4l 4l'$, $2s2p^6 3l n'l'$ with $3 \leq n \leq 5$, $2s2p^6 4l 4l'$ are taken into account, resulting in a total of 2700 levels. Table IV shows 21 fine-structure energy levels calculated from (MCDF1, MCDF2) methods, NIST values, and other relevant references. Our two sets of energy (using the MCDF1 and MCDF2 methods) differ by 0.0409 Ryd. Most of the energies level have been lowered by using a larger CI in the MCDF2 calculations. The relative fluctuations between MCDF1 and MCDF2 energies are shown in Fig. 2. Because of the inclusion of larger CI, one can see that most of the levels have converged the energy. Furthermore, our calculated energies using the MCDF2 method well match with those of NIST (Fig. 3), wherein an average difference of 0.22% whereas a maximum difference of 0.86% for the $2p^6 3p$ ($2P_{1/2}^0$) state. For the lowest 21 energy levels of KIX, the significance of both BI and QED correlations on MCDF2 energies has been evaluated. In Fig. 4, it is shown that the BI and QED effects alter the energies quite significantly, BI + QED correlations reduce them by around 0.0123 Ryd.

We have also done three independent calculations by using the FAC code. In our present calculations of FAC1, we have included the configurations that are used in the MCDF1 and FAC2 includes the CI as in MCDF2 but without the angular momentum constraints.

TABLE II. Optimized radial function parameters for KIX orbitals, where $\{\xi_{jnl}\}$ are variables in the Breit–Pauli Hamiltonian matrix elements that depends on the interacting electrons l -value. $\xi(s) = 0.0$, $\xi(p) = 0.98$, and $\xi(d) = 0.39$.

Index	Orbitals	Expansion coefficient (C_{jnl})	Power of r (I_{jnl})	Exponents (ξ_{jnl})
1	3s	0.161 76	1	15.121 42
2		−0.688 62	2	6.135 65
3		1.244 16	3	3.640 32
4	3p	0.439 14	2	7.522 27
5		−1.072 53	3	3.277 88
6	3d	0.985 36	3	3.340 45
7		0.02931	3	1.330 72
8	4s	0.091 12	1	15.989 15
9		−0.885 10	2	4.343 89
10		1.704 96	3	3.809 74
11		−1.463 05	4	2.444 21
12	4p	0.293 38	2	7.399 23
13		−2.250 01	3	2.512 08
14		2.688 62	4	2.467 79
15	4d	1.208 71	3	3.126 65
16		−0.945 17	3	2.103 47
17		−0.69516	4	2.024 10
18	4f	0.996 99	4	2.263 88
19		0.004 43	4	1.255 00
20	5s	0.066 40	1	15.421 87
21		−0.351 44	2	5.637 62
22		3.083 47	3	2.430 66
23		−4.8871	4	2.415 70
24		2.568 06	5	1.957 87
25	5p	0.207 93	2	7.343 90
26		−3.085 84	3	2.127 19
27		6.167 03	4	2.113 83
28		−3.765 58	5	1.928 48
29	5d	−8.776 42	3	2.769 96
30		10.146 75	3	2.742 26
31		−3.361 11	4	2.22715
32		2.510 54	4	1.529 56
33	5f	0.000 44	4	16.099 14
34		0.140 35	4	3.611 60
35		1.033 29	5	2.615 48
36		−1.515 41	5	1.710 92
37	5g	0.000 25	5	4.207 99
38		0.999 90	5	1.800 092
39	6s	0.050 53	1	14.910 64
40		−0.237 34	2	5.976 60
41		2.293 75	3	2.360 95
42		−8.337 59	4	1.953 61
43		10.796 26	5	1.828 30
44		−5.0116	6	1.637 08
45	6p	0.154 60	2	7.357 32
46		−4.776 72	3	1.740 27

TABLE II. (Continued.)

Index	Orbitals	Expansion coefficient (C_{jnl})	Power of r (I_{jnl})	Exponents (ξ_{jnl})
47		15.2788	4	1.734 47
48		16.208 15	5	1.733 39
49		6.065 90	6	1.586 47
50	6d	−1.617 89	3	3.159 00
51		1.231 57	3	2.979 53
52		−0.970 78	4	2.396 59
53		9.222 02	4	1.571 32
54		−15.959 91	5	1.547 70
55		8.425 15	6	1.511 33
56	6f	0.000 02	4	9.750 67
57		0.182 84	4	3.292 74
58		5.268 00	5	2.142 67
59		−681 061	5	1.923 43
60		2.087 75	6	1.386 12
61	6g	0.000 01	5	6.792 84
62		1.855 76	5	1.630 32
63		−2.240 40	6	1.475 90

^aFischer *et al.*²⁵ and the values without superscript in column 10 denotes the data taken from NIST.²⁶

Although we did extensive FAC3 calculations, we only recorded energies for the lowest 96 fine-structure levels, which all belong to $2p^6nl$ configurations with $n \leq 10$, 2700 fine-structure levels generated in FAC2, using all possible values. The maximum disagreement between both MCDF2 and FAC2 is predicted to be around 0.0266 Ryd. This disagreement arises from distinctions in the algorithms of the codes and the central potential calculation. Higher $2p^6nl$ configurations ($n > 10$) could not be incorporated because of the computational limitations of the code. For a few levels, inserting more CI into the FAC calculations (Table I) changes the energy by up to 0.0080 Ryd. As a result, it is possible to conclude that including additional CI in FAC calculations is enough to achieve reliable results. Furthermore, as shown in Tables I and IV, no intense mixing exists, so there is no uncertainty in identifying the $2p^6nl$ levels.

The *ab initio* calculations for the CIV3 column in Table II were performed by including $2p^6nl$ with $3 \leq n \leq 5$ and $0 \leq l \leq 4$, $2p^5 3l n'l'$ with $3 \leq n \leq 5$, $2p^5 4l 4l'$, $2s2p^6 3l n'l'$ with $3 \leq n \leq 5$, $2s2p^6 4l 4l'$ configurations which are generated by particular arrangements of 2700 fine-structure energy levels. We achieved a good agreement with NIST on the majority of calculated energies. We have also compared our calculated energy to Fischer *et al.* in Table IV. It is worth noting that the results presented for all approaches are not just in good agreement with all accessible data, but they are also in good agreement with one another, and they are getting closer to those of NIST.

A. Radiative rates (wavelengths, oscillator strengths, and transition rates)

For KIX, we calculated the radiative rates (A_{ij} in s^{-1}), transition wavelengths (λ_{ij} in Å), line strengths (S_{ij} in a.u.) also, and oscillator strengths (f_{ij} is dimensionless) which are tabulated in Table V.

TABLE III. The MCDF method to calculate fine structure energy (in Ryd) as a component of rising active sets of orbitals for the lowest 21 levels of KIX.

Index	Configuration	J	Term	n = 3	n = 4	n = 5	n = 6	NIST
1	2p ⁶ 3s	1/2	² S	0.000 000	0.000 000	0.000 000	0.000 000	0.000 000
2	2p ⁶ 3p	1/2	² P ^o	1.434 004	1.434 209	1.434 293	1.434 323	1.432 078
3	2p ⁶ 3p	3/2	² P ^o	1.467 905	1.468 091	1.468 165	1.468 192	1.466 352
4	2p ⁶ 3d	3/2	² D	3.418 47	3.418 428	3.418 45	3.418 466	3.416 039
5	2p ⁶ 3d	5/2	² D	3.420 51	3.420 481	3.420 50	3.420 52	3.418 63
6	2p ⁶ 4s	1/2	² S		6.342 41	6.341 59	6.341 29	6.368 78
7	2p ⁶ 4p	1/2	² P ^o		6.8847	6.8839	6.8837	6.9098
8	2p ⁶ 4p	3/2	² P ^o		6.8974	6.8967	6.8964	6.9228
9	2p ⁶ 4d	3/2	² D		7.6003	7.5993	7.5990	7.6261
10	2p ⁶ 4d	5/2	² D		7.6011	7.6003	7.6000	7.6273
11	2p ⁶ 4f	5/2	² F ^o		7.809 57	7.808 41	7.807 98	7.884 63
12	2p ⁶ 4f	7/2	² F ^o		7.8100	7.8088	7.808 41	7.845 00
13	2p ⁶ 5s	1/2	² S			8.922 14	8.921 76	8.9575
14	2p ⁶ 5p	1/2	² P ^o			9.1831	9.1827	9.2176
15	2p ⁶ 5p	3/2	² P ^o			9.1892	9.1888	9.2239
16	2p ⁶ 5d	3/2	² D			9.5246	9.5242	9.5596
17	2p ⁶ 5d	5/2	² D			9.5251	9.5248	9.5604
18	2p ⁶ 5f	5/2	² F ^o			9.6331	9.6389	9.6722
19	2p ⁶ 5f	7/2	² F ^o			9.6333	9.6390	9.6723
20	2p ⁶ 5g	5/2	² G			9.6432	9.6432	
21	2p ⁶ 5g	7/2	² G			9.6433	9.6433	
22	2p ⁶ 6s	1/2	² S				10.2268	10.2655
23	2p ⁶ 6p	1/2	² P ^o				10.3718	10.4104
24	2p ⁶ 6p	3/2	² P ^o				10.3753	10.4135
25	2p ⁶ 6d	3/2	² D				10.5618	10.6003
26	2p ⁶ 6d	5/2	² D				10.5621	10.6009
27	2p ⁶ 6f	5/2	² F ^o				10.6248	10.6657
28	2p ⁶ 6f	7/2	² F ^o				10.6289	10.6658
29	2p ⁶ 6g	5/2	² G				10.6328	10.6328
30	2p ⁶ 6g	7/2	² G				10.6329	10.6329

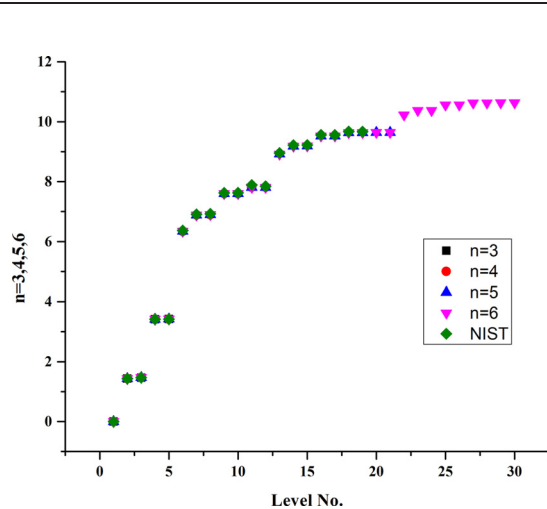
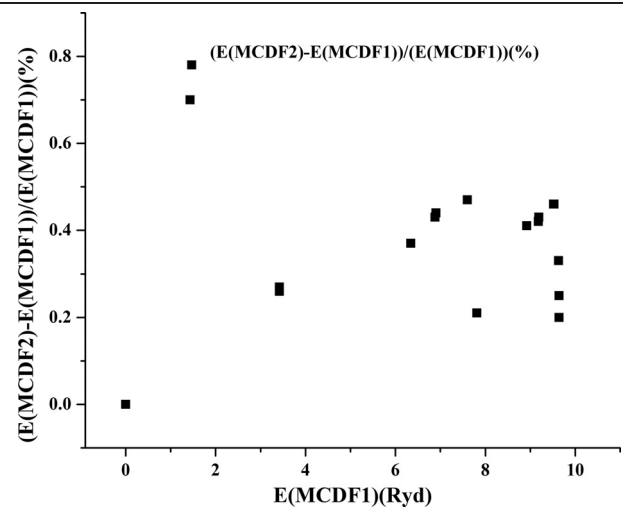
**FIG. 1.** Variations of increasing active sets of orbitals (in Ryd) using the MCDF approach for the lowest 21 levels of KIX.**FIG. 2.** Using MCDF, the influence of correlations on the energy of the lowest 21 levels of KIX.

TABLE IV. Comparison of the lowest 21 fine-structure levels of KIX calculated by us including threshold energies from many other sources.

Index	Configuration	J	Term	MCDF1	MCDF2	CIV-3	FAC1	FAC2	NIST	Lifetime (MCDF1)	Lifetime (Fisher <i>et al.</i>)
1	2p ⁶ 3s	1/2	² S _{1/2}	0.0000	0.0000	0.0000	0.0000	0.0000	0.0000	0.0000	0.0000
2	2p ⁶ 3p	1/2	² P ^O	1.4342	1.4446	1.4585	1.4345	1.4362	1.4320 1.4356 ^a	3.289 × 10 ⁻¹⁰	3.490 × 10 ⁻¹⁰
3	2p ⁶ 3p	3/2	² P ^O	1.4681	1.4785	1.4858	1.4684	1.4702	1.4663 1.4710 ^a	3.058 × 10 ⁻¹⁰	3.232 × 10 ⁻¹⁰
4	2p ⁶ 3d	3/2	² D	3.4184	3.4242	3.4603	3.4171	3.4211	3.4160 3.4329 ^a	1.095 × 10 ⁻¹⁰	1.136 × 10 ⁻¹⁰
5	2p ⁶ 3d	5/2	² D	3.4205	3.4262	3.4618	3.4191	3.4231	3.4186 3.4355 ^a	1.136 × 10 ⁻¹⁰	1.181 × 10 ⁻¹⁰
6	2p ⁶ 4s	1/2	² S	6.3415	6.3624	6.3575	6.3513	6.3529	6.3687 6.3841 ^a	2.109 × 10 ⁻¹¹	2.018 × 10 ⁻¹¹
7	2p ⁶ 4p	1/2	² P ^O	6.8839	6.9120	6.9050	6.8956	6.8985	6.9098 6.9268 ^a	3.374 × 10 ⁻¹¹	3.198 × 10 ⁻¹¹
8	2p ⁶ 4p	3/2	² P ^O	6.8967	6.9246	6.9181	6.9080	6.9110	6.9228 6.9402 ^a	3.569 × 10 ⁻¹¹	3.268 × 10 ⁻¹¹
9	2p ⁶ 4d	3/2	² D	7.5993	7.6317	7.6309	7.7063	7.6129	7.6261 7.6473 ^a	3.267 × 10 ⁻¹¹	3.198 × 10 ⁻¹¹
10	2p ⁶ 4d	5/2	² D	7.6003	7.6327	7.6317	7.6073	7.6139	7.6273 7.6487 ^a	3.231 × 10 ⁻¹¹	3.061 × 10 ⁻¹¹
11	2p ⁶ 4f	5/2	² F ^O	7.8084	7.8210	7.8277	7.8286	7.8239	7.8846 7.8701 ^a	0.998 × 10 ⁻¹¹	1.006 × 10 ⁻¹¹
12	2p ⁶ 4f	7/2	² F ^O	7.8088	7.8214	7.8277	7.8290	7.8243	7.8450 7.8707 ^a	1.000 × 10 ⁻¹¹	1.007 × 10 ⁻¹¹
13	2p ⁶ 5s	1/2	² S	8.9221	8.9564	8.9416	8.9305	8.9349	8.9575	2.911 × 10 ⁻¹¹	
14	2p ⁶ 5p	1/2	² P ^O	9.1831	9.2202	9.2061	9.1928	9.1984	9.2176	4.422 × 10 ⁻¹¹	
15	2p ⁶ 5p	3/2	² P ^O	9.1892	9.2262	9.2123	9.1987	9.2044	9.2239	5.181 × 10 ⁻¹¹	
16	2p ⁶ 5d	3/2	² D	9.5246	9.5655	9.5568	9.5311	9.5389	9.5596	4.195 × 10 ⁻¹¹	
17	2p ⁶ 5d	5/2	² D	9.5251	9.5660	9.5573	9.5316	9.5394	9.5604	3.933 × 10 ⁻¹¹	
18	2p ⁶ 5f	5/2	² F ^O	9.6331	9.6624	9.6549	9.6443	9.6477	9.6722	1.840 × 10 ⁻¹¹	
19	2p ⁶ 5f	7/2	² F ^O	9.6333	9.6626	9.6550	9.6556	9.6479	9.6723	1.842 × 10 ⁻¹¹	
20	2p ⁶ 5g	5/2	² G	9.6432	9.6674	9.6616	9.6556	9.6546		3.571 × 10 ⁻¹¹	
21	2p ⁶ 5g	7/2	² G	9.6433	9.6675	9.6616	9.6557	9.6548		3.571 × 10 ⁻¹¹	

The absorption oscillator strength f_{ij} for a transition $i \rightarrow j$ is obtained from the radiative rate A_{ji} (in s^{-1}), using the following relation:

$$f_{ij} = \frac{mc\lambda_{ji}^2 \omega_j}{8\pi^2 e^2 \omega_i} A_{ij} = 1.49 \times 10^{-16} \lambda_{ji}^2 \frac{\omega_j}{\omega_i} A_{ji}, \quad (10)$$

where c is the speed of the light and m, e denotes the charge of an electron, λ_{ij} is the transition wavelength (\AA), w_i is the upper, whereas w_j is a lower level of statistical weights correspondingly, while transition probability is A_{ij} (in s^{-1}). The relationship between oscillator strength (f_{ij}) and line strength (S_{ij}) for the E1, M1, E2, and M2 transitions can be represented by

$$\text{for E1 transitions: } A_{ji} = \frac{2.0261 \times 10^{18}}{\omega_j \lambda_{ji}^3} S_{ij} \quad \text{and} \quad f_{ij} = \frac{303.75}{\lambda_{ji} \omega_i} S_{ij}, \quad (11)$$

for M1 transitions:

$$A_{ji} = \frac{2.6974 \times 10^{13}}{\omega_j \lambda_{ji}^3} S_{ij} \quad \text{and} \quad f_{ij} = \frac{4.044 \times 10^{-3}}{\lambda_{ji} \omega_i} S_{ij}, \quad (12)$$

for E2 transitions:

$$A_{ji} = \frac{1.1199 \times 10^{18}}{\omega_j \lambda_{ji}^5} S_{ij} \quad \text{and} \quad f_{ij} = \frac{167.89}{\lambda_{ji}^3 \omega_i} S_{ij}, \quad (13)$$

for M1 transitions:

$$A_{ji} = \frac{1.4910 \times 10^{13}}{\omega_j \lambda_{ji}^5} S_{ij} \quad \text{and} \quad f_{ij} = \frac{2.236 \times 10^{-3}}{\lambda_{ji}^3 \omega_i} S_{ij}. \quad (14)$$

B. Lifetimes

By taking the inverse of a sum of transition probabilities from the radiative transition from level (i), the lifetime (τ) of a level (j) is calculated as

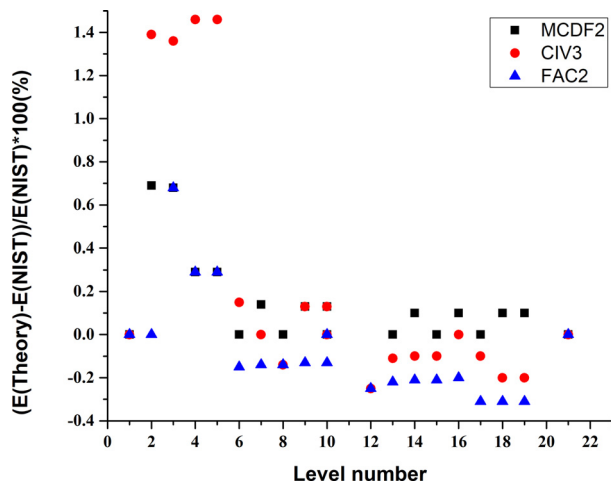


FIG. 3. For lowest 21 levels of KIX, the percentage differences among appropriate theoretical energies as well as NIST values were calculated.

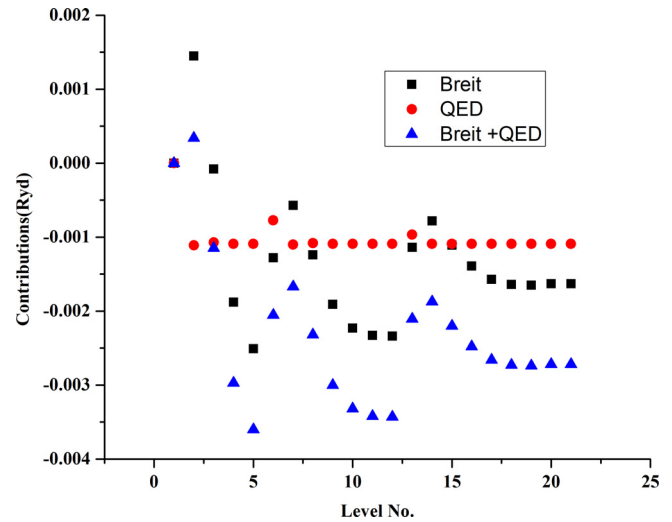


FIG. 4. At the lowest 21 levels, BI and QED contribute to MCDF2 energy for KIX.

TABLE V. Radiative rates (A_{ji} in s^{-1}), transition wavelengths (λ_{ij} in \AA), line strengths (S in atomic units), and also oscillator strengths (f_{ij} , dimensionless) of KIX for E1, E2, M1, as well as M2. $R(E1)$ is the ratio of the velocity and length forms of A -values for E1 transitions within last column.

I	J	λ_{ij}	A_{ji}^{E1}	f_{ij}^{E1}	S^{E1}	A_{ji}^{E2}	A_{ji}^{M1}	A_{ji}^{M2}	R^{E1}
1	2	6.35×10^2	3.04×10^9	1.84×10^{-1}	7.69×10^{-1}	0.00×10	0.00×10	0.00×10	1.00×10
1	3	6.21×10^2	3.27×10^9	3.77×10^{-1}	1.54×10	0.00×10	0.00×10	9.36×10^{-1}	1.00×10
1	4	2.67×10^2	0.00×10	0.00×10	0.00×10	2.73×10^5	3.90×10^{-3}	0.00×10	0.00×10
1	5	2.66×10^2	0.00×10	0.00×10	0.00×10	2.74×10^5	0.00×10	0.00×10	0.00×10
1	6	1.44×10^2	0.00×10	0.00×10	0.00×10	0.00×10	7.05×10^{-1}	0.00×10	0.00×10
1	7	1.32×10^2	1.70×10	4.46×10^{-2}	3.89×10^{-2}	0.00×10	0.00×10	0.00×10	9.80×10^{-1}
1	8	1.32×10^2	1.63×10	8.56×10^{-2}	7.44×10^{-2}	0.00×10	0.00×10	1.03×10^2	9.80×10^{-1}
1	9	1.20×10^2	0.00×10	0.00×10	0.00×10	4.60×10^6	6.16×10^{-4}	0.00×10	0.00×10
1	10	1.20×10^2	0.00×10	0.00×10	0.00×10	9.90×10^{-1}	0.00×10	0.00×10	0.00×10
1	11	1.17×10^2	0.00×10	0.00×10	0.00×10	0.00×10	0.00×10	2.50×10^{-6}	0.00×10
1	13	1.20×10^2	0.00×10	0.00×10	0.00×10	0.00×10	7.71×10^{-1}	0.00×10	0.00×10
1	14	9.92×10	1.03×10	1.53×10^{-2}	9.97×10^{-3}	0.00×10	0.00×10	0.00×10	9.80×10^{-1}
1	15	9.92×10	1.00×10	2.95×10^{-2}	1.93×10^{-3}	0.00×10	0.00×10	1.13×10^8	9.80×10^{-1}
1	16	9.57×10	0.00×10	0.00×10	0.00×10	9.80×10^{-1}	2.36×10^{-3}	0.00×10	0.00×10^{-1}
1	17	9.57×10^1	0.00×10	0.00×10	0.00×10	9.80×10^{-1}	0.00×10	0.00×10	0.00×10
1	18	9.46×10^1	0.00×10	0.00×10	0.00×10	0.00×10	0.00×10	1.78×10^{-6}	0.00×10
2	3	2.69×10^4	0.00×10	0.00×10	0.00×10	2.97×10^5	4.62×10^{-1}	0.00×10	0.00×10
2	4	4.59×10^2	7.67×10^9	4×10^{-1}	1.47×10	0.00×10	0.00×10	1.61×10^{-1}	1.10×10
2	5	5.59×10^2	0.00×10	0.00×10	0.00×10	0.00×10	0.00×10	1.51×10	0.00×10
2	6	1.86×10^2	1.57×10	8.10×10^{-2}	9.90×10^{-2}	0.00×10	0.00×10	0.00×10	1.00×10
2	7	1.66×10^2	0.00×10	0.00×10	0.00×10	0.00×10	1.54×10^{-1}	0.00×10	0.00×10
2	8	1.66×10^2	0.00×10	0.00×10	0.00×10	0.00×10	2.58×10^1	0.00×10	0.00×10
2	9	1.48×10^2	2.39×10	1.57×10^{-1}	1.53×10^{-1}	0.00×10	0.00×10	4.84×10	9.50×10^{-1}
2	10	1.48×10^2	0.00×10^{-1}	0.00×10	0.00×10	0.00×10^1	0.00×10	3.43×10^1	0.00×10
2	11	1.43×10^2	0.00×10	0.00×10	0.00×10	9.46×10^6	0.00×10	0.00×10	0.00×10
2	13	1.22×10^2	6.68×10^9	1.48×10^{-2}	1.19×10^{-2}	0.00×10	0.00×10	0.00×10	1.00×10

TABLE V. (Continued.)

I	J	λ_{ij}	A_{ji}^{E1}	f_{ij}^{E1}	S^{E1}	A_{ji}^{E2}	A_{ji}^{M1}	A_{ji}^{M2}	R^{E1}
2	14	1.18×10^2	0.00×10	0.00×10	0.00×10	0.00×10	1.7×10^{-1}	0.00×10	0.00×10
2	15	1.18×10^2	0.00×10	0.00×10	0.00×10	7.51×10^5	1.73×10^1	0.00×10	0.00×10
2	16	1.13×10^2	1.66×10	6.33×10^{-2}	4.70×10^{-2}	0.00×10	0.00×10	5.79×10	9.50×10^{-1}
2	17	1.13×10^2	0.00×10	0.00×10	0.00×10	0.00×10	0.00×10	4.11×10^1	0.00×10
2	18	1.11×10^2	0.00×10	0.00×10	0.00×10	2.69×10^6	0.00×10	0.00×10	0.00×10
3	4	4.67×10^2	1.46×10^9	4.78×10^{-2}	2.94×10^{-1}	0.00×10	0.00×10	0.00×10	1.10×10
3	5	4.67×10^2	8.80×10^9	4.31×10^{-1}	2.65×10	0.00×10	0.00×10	5.78×10	1.10×10
3	6	1.87×10^2	3.17×10	8.31×10^{-2}	2.05×10^{-1}	0.00×10	0.00×10	1.00×10^2	1.00×10
3	7	1.68×10^2	0.00×10	0.00×10	0.00×10	2.76×10^6	5.83×10^1	0.00×10	0.00×10
3	8	1.68×10^2	0.00×10	0.00×10	0.00×10	1.38×10^6	9.30×10^{-1}	0.00×10	0.00×10
3	9	1.49×10^2	4.88×10^9	1.62×10^{-2}	3.16×10^{-2}	0.00×10	0.00×10	0.00×10	9.50×10^{-1}
3	10	1.49×10^2	2.92×10	1.45×10^{-1}	2.84×10^{-1}	0.00×10	0.00×10	1.89×10^2	9.50×10^{-1}
3	11	1.44×10^2	0.00×10	0.00×10	0.00×10	2.67×10^6	2.54×10^{-2}	0.00×10	0.00×10
3	12	1.44×10^2	0.00×10	0.00×10	0.00×10	1.20×10^7	0.00×10	0.00×10	0.00×10
3	13	1.22×10^2	1.35×10	1.51×10^{-2}	2.43×10^{-2}	0.00×10	0.00×10	9.95×10^1	1.00×10
3	14	1.18×10^2	0.00×10	0.00×10	0.00×10	1.48×10^6	4.07×10	0.00×10	0.00×10
3	15	1.18×10^2	0.00×10	0.00×10^{-2}	0.00×10	7.41×10^5	1.05×10	0.00×10	0.00×10
3	16	1.13×10^2	3.37×10^9	6.46×10^{-3}	9.62×10^{-3}	0.00×10	0.00×10	0.00×10	9.50×10^{-1}
3	17	1.13×10^2	2.02×10	5.80×10^{-2}	8.64×10^{-2}	0.00×10	0.00×10	2.26×10^2	9.50×10^{-1}
3	18	1.12×10^2	0.00×10	0.00×10	0.00×10	7.49×10^5	1.85×10^{-2}	0.00×10	0.00×10
3	19	1.12×10^2	0.00×10	0.00×10	0.00×10	3.37×10^6	0.00×10	0.00×10	0.00×10
3	20	1.12×10^2	0.00×10	0.00×10	0.00×10	0.00×10	0.00×10	1.29×10^{-6}	0.00×10
4	5	4.44×10^5	0.00×10	0.00×10	0.00×10	6.65×10^{-12}	1.24×10^{-4}	0.00×10	0.00×10
4	6	3.12×10^2	0.00×10	0.00×10	0.00×10	1.95×10^5	2.53×10^{-9}	0.00×10	0.00×10
4	7	2.63×10^2	1.12×10	5.79×10^{-2}	2.01×10^{-1}	0.00×10	0.00×10	7.13×10^{-1}	1.10×10
4	8	2.62×10^2	1.10×10^9	1.14×10^{-2}	3.92×10^{-2}	0.00×10	0.00×10	0.00×10	1.10×10
4	9	0.00×10	0.00×10^2	0.00×10	0.00×10	4.88×10^5	1.25×10^{-1}	0.00×10	0.00×10
4	10	0.00×10	0.00×10	0.00×10	0.00×10	1.39×10^5	4.68×10^{-2}	0.00×10	0.00×10
4	11	2.08×10^2	9.35×10	9.06×10^{-1}	2.48×10	0.00×10	0.00×10	5.70×10^1	9.90×10^{-1}
4	12	2.08×10^2	0.00×10	0.00×10	0.00×10	0.00×10	0.00×10	7.30×10^1	0.00×10^2
4	13	1.66×10^2	0.00×10	0.00×10	0.00×10	6.95×10^4	1.19×10^{-6}	0.00×10	0.00×10
4	14	1.58×10^2	4.20×10^9	7.86×10^{-3}	1.64×10^{-2}	0.00×10	0.00×10	7.42×10^{-1}	1.10×10
4	15	1.58×10^2	4.15×10^8	1.55×10^{-3}	3.23×10^{-3}	0.00×10	0.00×10	0.00×10	1.10×10
4	16	1.49×10^2	0.00×10	0.00×10	0.00×10	2.27×10^5	1.37×10^{-1}	0.00×10	0.00×10
4	17	1.49×10^2	0.00×10	0.00×10	0.00×10	1.49×10^2	2.92×10^2	0.00×10	0.00×10
4	18	1.47×10^2	3.55×10	1.72×10^{-1}	3.32×10^{-1}	0.00×10	0.00×10	4.34×10^1	9.90×10^{-1}
4	19	1.47×10^2	0.00×10	0.00×10	0.00×10	0.00×10	0.00×10	55.56×10^1	0.00×10
4	20	1.46×10^2	0.00×10	0.00×10	0.00×10	5.49×10^6	0.00×10	0.00×10	0.00×10
5	6	3.12×10^2	0.00×10	0.00×10	0.00×10	2.19×10^5	0.00×10	0.00×10	0.00×10
5	7	2.63×10^2	0.00×10	0.00×10	0.00×10	0.00×10	0.00×10	7.61×10	0.00×10
5	8	2.62×10^2	9.94×10^9	6.83×10^{-2}	3.54×10^1	0.00×10	0.00×10	2.07×10^1	1.10×10
5	9	2.18×10^2	0.00×10	0.00×10	0.00×10	2.09×10^5	2.47×10^{-1}	0.00×10	0.00×10
5	10	2.18×10^2	0.00×10	0.00×10	0.00×10	5.57×10^5	4.23×10^{-1}	0.00×10	0.00×10
5	11	2.08×10^2	6.68×10^9	4.32×10^{-2}	1.77×10^{-1}	0.00×10	0.00×10	0.00×10	9.90×10^{-1}
5	12	2.08×10^2	1.00×10^{11}	8.64×10^{-1}	3.54×10	0.00×10	0.00×10	5.03×10^2	9.90×10^{-1}
5	13	1.66×10^2	0.00×10	0.00×10	0.00×10	1.04×10^5	0.00×10	0.00×10	0.00×10
5	14	1.58×10^2	0.00×10	0.00×10	0.00×10	0.00×10	0.00×10	7.90×10	0.00×10
5	15	1.58×10^2	3.74×10^9	9.32×10^{-3}	2.91×10^2	0.00×10	0.00×10	2.14×10^1	1.10×10
5	16	1.49×10^2	0.00×10	0.00×10	0.00×10	9.71×10^4	2.03×10^{-1}	0.00×10	0.00×10

TABLE V. (Continued.)

I	J	λ_{ij}	A_{ji}^{E1}	f_{ij}^{E1}	S^{E1}	A_{ji}^{E2}	A_{ji}^{M1}	A_{ji}^{M2}	R^{E1}
5	17	1.49×10^2	0.00×10	0.00×10	0.00×10	2.59×10^5	4.60×10^{-1}	0.00×10	0.00×10
5	18	1.47×10^2	2.54×10^9	8.18×10^{-3}	2.37×10^{-2}	0.00×10	0.00×10	0.00×10	9.90×10^{-1}
5	19	1.47×10^2	3.80×10	1.64×10^{-1}	4.74×10^{-1}	0.00×10	0.00×10	3.82×10^2	9.90×10^{-1}
5	20	1.47×10^2	0.00×10	0.00×10	0.00×10	6.10×10^{-5}	5.14×10^{-3}	0.00×10	0.00×10
5	21	1.47×10^2	0.00×10	0.00×10	0.00×10	6.10×10^{-5}	0.00×10	0.00×10	0.00×10

$$\tau_j(s) = \frac{1}{\sum_i A_{ji}(S^{-1})}. \quad (15)$$

Table IV contains lifetime information for the lowest 21 fine structure levels of KIX, taking into account all possible transitions such as E1 and E2 and M1 and M2. We tried to compare our lifetime calculations with available results. Fisher *et al.*²³ have given the lifetime for the level $1s^2 2p^6 3s$, $1s^2 2p^6 3p$, $1s^2 2p^6 3d$, $1s^2 2p^6 4s$, $1s^2 2p^6 4p$, $1s^2 2p^6 4d$, and $1s^2 2p^6 4f$. Our calculated lifetimes for these levels are in close agreement with Fisher *et al.* Furthermore, we have also predicted the lifetime for the levels $1s^2 2p^6 5s$, $1s^2 2p^6 5p$, $1s^2 2p^6 5d$, $1s^2 2p^6 5f$, and $1s^2 2p^6 5g$ where no other data are available for comparison.

C. Line intensity ratio and plasma parameters

The plasma parameters are influenced by changes in spectroscopic parameters, like transition wavelength and transition probability. Characterizing and analyzing hot dense plasma (HDP) appears easy and uncomplicated only when plasma is treated as optically thin in the local thermodynamic equilibrium (LTE). Because of saturation as well as self-absorption as in line profile, the optically thick line implements an asymmetrical rather than distorted peak in the spectrum. This causes the electron density and plasma temperature both are measured incorrectly and inaccurately. Variations in spectroscopic parameters cause changes in plasma temperature. The increasing number of collisions between electrons increases as kinematic excitation, at higher values of temperatures, and hence, LTE is easily accomplished at high temperatures. As a result, we explored plasma temperature in the line intensity ratio in optically thin plasma. In HDP, any two spectral lines of the line intensity ratio are

$$R = \frac{I_1}{I_2} = \frac{\lambda_2 A_1 g_1}{\lambda_1 A_2 g_2} \exp \left[-\frac{E_1 - E_2}{KT} \right], \quad (16)$$

where λ and A are the wavelength and transition probability, I is the intensity, g is the statistical weight of the lower level of transition, K is the Boltzmann constant, T is the excitation temperature in Kelvin, and E is the energy of the upper level of transition in eV. In HDP, for the line intensity ratio and electron density calculations, opted 1 [$1s^2 2s^2 2p^6 3s (^2S_{1/2}) - 1s^2 2s^2 2p^6 3p (^2P_{3/2})$] and 2 [$1s^2 2s^2 2p^6 3s (^2S_{1/2}) - 1s^2 2s^2 2p^6 3p (^2P_{1/2})$] which signifies the two spectral lines.

For HDP, using McWhirter criteria, the lowest or limiting value of electron density given by

$$n_e \geq 1.6 \times 10^{12} T^{(1/2)} (\Delta E)^3. \quad (17)$$

Here, T indicates plasma temperature (Kelvin), n_e is the electron density, and $\Delta E (= E_1 - E_2)$ is in eV.

The line intensity ratio for various plasma temperature and electron density values is tabulated in Table VI. Figure 5 illustrates how the line intensity ratio varies with plasma temperature. For temperatures up to 10^8 K or 10 keV, the variation is exponential, but there is no visible change in the line intensity ratio for $T > 10^8$ K. In Fig. 6, we can see that the value of limiting electron increases when plasma temperature density for Na-like K increases. One can also see that number of collisions in plasma increases as the temperature of the plasma increases. Thus, this knowledge of the Na-like K ion may be helpful in experiments for generating an optically thin plasma in LTE at higher temperatures.

IV. CONCLUSION

We present energy levels, oscillator strengths, lifetimes, and radiative rates for KIX using the MCDF approach. We also included the radiative rates for E1, E2 transitions and M1, M2 transitions. The energy level gets significantly lowered by the inclusion of Breit and QED interaction. Two codes have been employed, and a discrepancy in the results for specific configuration effects is studied. The configuration interaction technique (CIV3) is also used to confirm the accuracy of energy levels further. Furthermore, we investigated the impact of plasma temperature on specific parameters for hot dense plasma under LTE conditions. We observed that the line intensity ratio and other HDP parameters follow the same increasing pattern with temperature. The coupling constant is used to justify the criteria for hot dense as well as weakly coupled plasma. Finally, we found our results agree well with those of NIST as well as other currently available data

TABLE VI. The electron density (n_e in cm^{-3}) and line intensity ratio (R) for KIX are shown against plasma temperature (T in K).

Index	Temperature (K)	Line intensity ratio (R)	Number of electron density (n_e in cm^{-3})
1	2×10^6	1.098 23	0.22×10^{15}
2	4×10^6	1.099 74	0.31×10^{15}
3	6×10^6	1.100 19	0.38×10^{15}
4	8×10^6	1.100 43	0.44×10^{15}
5	1×10^7	1.100 58	0.49×10^{15}
6	1×10^8	1.101 11	0.15×10^{19}
7	1×10^9	1.101 16	0.49×10^{19}
8	1×10^{10}	1.101 17	0.15×10^{20}

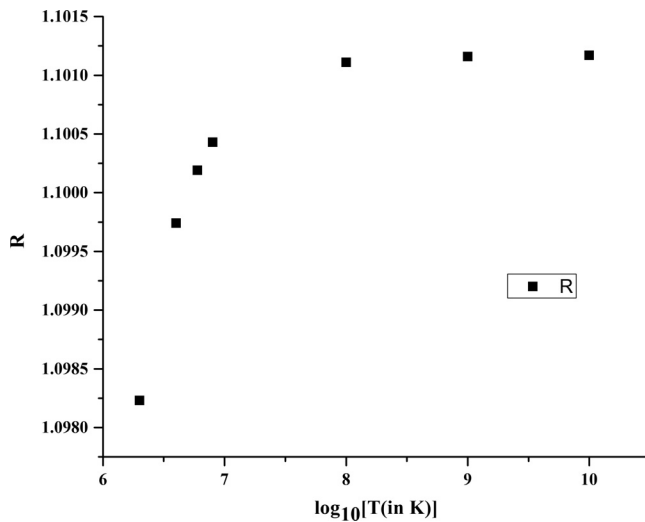


FIG. 5. Line intensity ratios for spectral lines 1 and 2 as a function of plasma temperature for KIX.

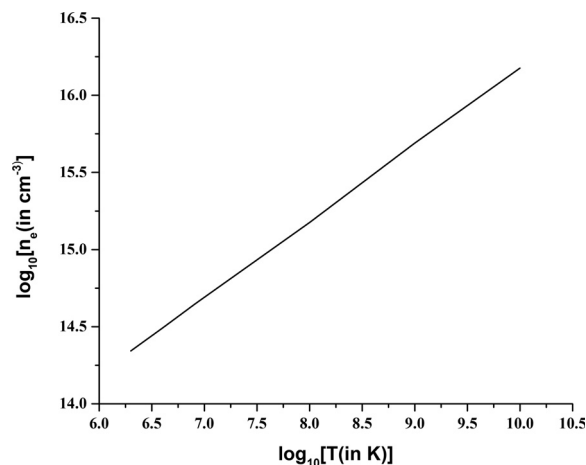


FIG. 6. For spectral lines 1 and 2, KIX electron density varies with plasma temperature.

for the Na-like ion. Our predicted results will be advantageous for fusion, astrophysical, and modeling plasma.

ACKNOWLEDGMENTS

We acknowledge sincere gratitude to Delhi Technological University and Jawaharlal Nehru University to appreciate their help and enhance our services and facilities.

AUTHOR DECLARATIONS

Conflict of Interest

The authors have no conflicts to disclose.

Author Contributions

Richa Paijwar: Conceptualization (lead); Data curation (lead); Formal analysis (lead); Investigation (lead); Methodology (lead); Writing – original draft (lead); Writing – review and editing (lead). **Rinku Sharma:** Conceptualization (equal); Data curation (equal); Formal analysis (equal); Funding acquisition (equal); Investigation (equal); Methodology (equal); Resources (lead); Software (lead); Supervision (lead); Validation (equal); Writing – review and editing (equal). **Alok K. S. Jha:** Conceptualization (equal); Data curation (equal); Formal analysis (equal); Investigation (equal); Supervision (equal); Validation (equal); Writing – review and editing (equal).

DATA AVAILABILITY

The data that support the findings of this study are available within the article.

REFERENCES

- A. K. Singh, M. Dimri, D. Dawra, A. K. Jha, and M. Mohan, *Phys. Plasmas* **26**, 062704 (2019).
- I. Martinson, *Nucl. Instrum. Methods Phys. Res., Sec. B* **43**, 323–332 (1989).
- H. Fiedorowicz, A. Bartnik, and Z. Patron, *Appl. Phys. Lett.* **62**, 2778 (1993).
- N. Singh, A. Goyal, and M. Mohan, *J. Electron Spectrosc. Related Phenom.* **229**, 94 (2018).
- A. K. Singh, M. Dimri, D. Dawra, A. K. Jha, N. Verma, and M. Mohan, *Radiat. Phys. Chem.* **156**, 174–192 (2019).
- G. G. Konan and L. Ozdemir, *Chin. J. Phys.* **54**, 433 (2016).
- A. K. Singh, M. Dimri, D. Dawra, A. K. S. Jha, and M. Mohan, *Can. J. Phys.* **97**(4), 436–442 (2019).
- K. J. H. Phillips, J. Sylwester, B. Sylwester, and E. Landi, *Astrophys. J.* **589**, L113–L116 (2003).
- A. Mucciarelli, T. Merle, and M. Bellazzini, *Astron. Astrophys.* **600**, A104 (2017).
- S. Goldsmith, U. Feldman, L. Oren, and L. Cohen, *Astrophys. J.* **174**, 209–214 (1972).
- E. Träbert, *Atoms* **7**, 103 (2019).
- C. Jupen, L. Engstrom, R. Hutton, and E. Trabert, *J. Phys. B* **21**, L347 (1988).
- W. Siegel, J. Migdalek, and Y. K. Kim, *At. Data Nucl. Data Tables* **68**, 303–322 (1998).
- W. O. Younis, S. H. Allam, and T. El-Sherbini, *At. Data Nucl. Data Tables* **92**, 187–105 (2006).
- L. N. Ivanov and E. P. Ivanova, *At. Data Nucl. Data Tables* **24**, 95–109 (1979).
- D. H. Sampson, H. L. Zhang, and C. J. Fontes, *At. Data Nucl. Data Tables* **44**, 209–227 (1990).
- Y. K. Kim, D. H. Baik, and P. Indelicato, *Phys. Rev. A* **44**(1), 148 (1991).
- W. R. Johnson, Z. W. Liu, and A. J. Sapirstein, *At. Data Nucl. Data Tables* **64**, 279–300 (1996).
- C. J. Fontes and H. L. Zhang, *At. Data Nucl. Data Tables* **113**, 293–315 (2016).
- U. I. Safronova, W. R. Johnson, and M. S. Safronova, *Phys. Rev. A* **66**, 042506 (2002).
- J. E. Sansonetti, *Phys. Chem. Ref. Data* **37**(1), 7–96 (2008).
- L. Cohen and W. E. Behring, *J. Opt. Soc. Am.* **66**(9), 899–904 (1976).
- B. Edlen and E. Boden, *Phys. Scr.* **14**, 31–38 (1976).
- J. D. Gillaspay, D. Osin, Y. Ralchenko, J. Reader, and S. A. Blundell, *Phys. Rev. A* **87**, 062503 (2013).
- C. Froese Fischer, G. Tachiev, and A. Irimia, *At. Data Nucl. Data Tables* **92**, 607–812 (2006).
- A. Kramida, Y. Ralchenko, J. Reader, and NIST ASD Team, NIST Atomic Spectra Database, version 5.6.1 (2019), <https://physics.nist.gov/asd>.
- I. P. Grant, B. J. McKenzie, P. H. Norrington, D. F. Mayers, and N. C. Pyper, *Comput. Phys. Commun.* **21**, 207 (1980).
- M. F. Gu, *Can. J. Phys.* **86**, 675 (2008).
- A. Hibbert, *Comput. Phys. Commun.* **9**, 141 (1975).